LIÈGE université
Sciences Appliquées

Orbital propagation around irregular celestial bodies using the harmonic balance method

A thesis submitted in partial fulfillment of the requirements
for the degree of Doctor of Philosophy (PhD) in Engineering Science

by

Nicolas Leclère

Supervisor: Gaëtan KERSCHEN

DOCTORAL COLLEGE IN AEROSPACE AND MECHANICS

OCTOBER 2025

Members of the examination committee

President
Prof. Loïc Salles
University of Liège

Supervisor
Prof. Gaëtan Kerschen
University of Liège

Members
Prof. Jérôme Daquin
University of Toulon

Dr. Lamberto Dell'Elce
INRIA Sophia Antipolis

Prof. Gregor Rauw
University of Liège

Dr. Ghislain Raze
University of Liège

Orbital propagation around irregular celestial bodies using the harmonic balance method

Nicolas Leclère

Abstract

This thesis presents a frequency-domain framework for the computation and analysis of periodic and quasi-periodic orbits in astrodynamics. The harmonic balance method is adapted to autonomous and conservative systems to compute periodic solutions efficiently while providing direct access to their stability and bifurcations. The method's performance is first validated on a benchmark two degrees of freedom system and then applied to the circular restricted three-body problem, where it reproduces classical families of periodic orbits and reveals new connections between resonant branches through bifurcation analysis.

The approach is then extended to the gravitational environment of asteroid 433 Eros, modeled using the polyhedron method. A dense map of periodic families, comprising over one hundred bifurcations, is established, offering new insights into the resonance structure and transitions between orbital modes. The multi-harmonic balance method is further introduced to compute quasi-periodic orbits, enabling the study of multi-frequency dynamics directly in the frequency domain.

Finally, the method is extended to more realistic scenarios by incorporating solar radiation pressure and binary gravitational effects, demonstrated through the Didymos–Dimorphos system. The results confirm that the harmonic balance framework provides a powerful, efficient, and insightful alternative to classical time-domain techniques for orbital propagation around irregular celestial bodies.

Acknowledgements

Je tiens à remercier en premier celui sans qui ce travail n'aurait jamais pu voir le jour, mon promoteur, Gaëtan Kerschen. C'est grâce à ta patience, ton écoute et ta guidance que cette thèse a pu arriver à son terme. En six ans, j'ai eu le temps de douter, mais ta confiance suffisait à remettre le coup de boost nécessaire pour y arriver.

J'aimerais également adresser mes remerciements au jury qui a accepté de relire ce travail, et en particulier à mon comité de thèse, Lamberto Dell'Elce et Gregor Rauw, pour leur suivi annuel ainsi que leurs remarques constructives.

Cette thèse n'aurait pas été possible sans l'opportunité d'être assistant dans le département A&M. J'ai eu l'occasion d'encadrer les cours non seulement de Gaëtan, mais également de Maarten Arnst et de Koen Hillewaert. Certains de ces cours étaient en partie nouveaux pour moi, et je tiens à les remercier pour leur confiance et leur soutien lors des laboratoires et séances d'exercices. Je remercie aussi tous les rouages essentiels du département, toujours présents pour répondre aux questions administratives ou pour maintenir un lieu de travail sain et propre.

Durant les six ans que j'ai pu passer dans l'équipe du S3L, j'ai eu l'occasion de fréquenter de nombreux collègues qui m'ont tous aidé et apporté à leur manière. Gaëtan, Jenni, Tong, Sam, Martin, Thibaut, Ghislain, Alexandre, François, et même la relève que je n'ai pas eu l'occasion de connaître aussi bien, Louise et Grégoire, merci. Parmi ces personnes, il y en a trois qui méritent une mention particulière. Thibaut, qui négocie son assistance à coups de *pool party* chez mes parents, mais qui trouve le signe négatif fautif de tant de cheveux arrachés. Ghislain, dont la gentillesse n'a d'égal que son intellect, toujours disponible pour aider. Je ne suis pas sûr que j'y serais arrivé sans ton aide précieuse. Et enfin Martin, le premier jour de mon contrat à l'université s'est terminé par une partie de Mario Kart dans son bureau. L'amitié ne pouvait pas mieux démarrer. Pour tout ça, merci. Je voudrais aussi remercier Norman, bien que dans une autre équipe, le doctorat avait la même saveur que les études avec toi, que ce soit ingénieur ou HEC. Ne recommence pas des études, s'il te plaît; je vais me sentir obligé de te suivre.

Je remercie mes parents de m'avoir donné l'opportunité de suivre les études qui m'ont mené là où j'en suis. Merci aussi à mes amis pour tous les moments qui permettent de souffler durant cette thèse.

Et enfin, un grand merci à Carla d'avoir toujours cru en moi. Merci pour les kits de survie quand je devais travailler tard pour respecter une échéance. Merci d'avoir géré les petits tracas de la maison lorsque j'étais en train de rédiger. Merci pour tout.

Contents

Chapter 1

Introduction

Context

The study of periodic and quasi-periodic motion lies at the heart of celestial mechanics. From the earliest analytical treatments of the two-body problem to the modern numerical exploration of complex multi-body environments, the search for recurrent trajectories has remained a cornerstone of astrodynamics. Periodic orbits, in particular, provide the backbone of the dynamical structure surrounding celestial bodies: they organize the flow in phase space, define regions of stability, and often serve as the foundation for mission design and station-keeping strategies.

However, when the gravitational potential departs from the idealized spherical or point-mass model, as is the case near irregular asteroids or binary systems, the dynamics become considerably more intricate. The loss of symmetry introduces strong nonlinearities that challenge both analytical and numerical approaches. In such environments, classical time-domain methods, though reliable, may struggle with sensitivity to initial conditions, numerical stiffness, and the high computational cost of long-term integrations.

These limitations have motivated the search for alternative formulations capable of describing periodic motion more efficiently. Among them, the harmonic balance method (HBM) offers an appealing perspective. By reformulating the equations of motion directly in the frequency domain, the method enforces periodicity intrinsically and provides immediate access to the stability and bifurcation properties of the solutions. Originally developed in the field of nonlinear electrical circuits [1], HBM has seen growing interest for its ability to capture steady-state oscillations in strongly nonlinear systems with remarkable efficiency.

Transposing this approach to celestial mechanics opens new opportunities. Around small and irregular bodies, where gravitational fields are highly nonlinear and resonances are dense, the frequency-domain formulation allows the systematic construction of families of periodic and quasi-periodic orbits without time integration. It also enables the detection of bifurcations and the continuation of emerging branches, offering a global view of the system's dynamical organization.

In this context, the present work explores how the harmonic balance framework can be adapted and extended to astrodynamics. It aims to demonstrate that this method

provides not only a computationally efficient alternative to traditional approaches but also a novel way to interpret the complex dynamical behavior around irregular celestial bodies, paving the way toward more comprehensive and automated exploration of their orbital environments.

Contributions of the Thesis

The central objective of this thesis is to introduce and validate a new approach for the computation of periodic solutions in orbital propagation problems, with particular attention to motion around irregular celestial bodies. The harmonic balance method, operating directly in the frequency domain, enforces the periodicity of the solutions by construction while providing an efficient and low-cost framework for stability and bifurcation analysis. A second major goal is to construct a comprehensive map of periodic orbits around the asteroid 433 Eros, tracing the numerous bifurcations that connect families of solutions. This global view of the dynamical environment highlights the complex resonant structure surrounding irregular bodies. The third contribution extends the harmonic balance formulation to the computation of quasi-periodic solutions. This extension, referred to as the multi-harmonic balance method, allows the characterization of multi-frequency oscillations and provides a frequency-domain perspective on quasi-periodic motion around asteroids. Finally, the thesis demonstrates that the proposed methodology can be generalized to more realistic dynamical scenarios, including external perturbations such as solar radiation pressure and the gravitational influence of additional bodies. This establishes the transferability of the method beyond idealized models toward practical applications in mission analysis and trajectory design.

The thesis is organized as follows. Chapter 2 introduces the theoretical foundations of the harmonic balance method for nonlinear autonomous and conservative systems. Particular emphasis is placed on stability analysis and bifurcation tracking, with validation carried out on a two-degree-of-freedom system. The chapter concludes with the introduction of the multi-harmonic balance method, applied to a simple example to illustrate its potential for capturing quasi-periodic behavior.

In Chapter 3, the method is applied to the classical circular restricted three-body problem. Despite the extensive literature on this problem, the harmonic balance method offers a renewed perspective by enforcing periodicity directly in the frequency domain. The results are validated against the software `AUTO`, and a schematic map of the Earth–Moon periodic solutions is constructed, highlighting bifurcations and the emergence of secondary branches. The bifurcation analysis also uncovers previously unreported connections between resonant families. To further demonstrate the flexibility of the approach, an alternative continuation parameter is introduced.

Chapter 4 forms the core of the thesis. The gravitational environment of asteroid 433 Eros is modeled using the polyhedron method to capture its nonlinear potential. For the first time, a dense bifurcation map comprising roughly one hundred distinct bifurcations among periodic families is established. The stability of the solutions is examined, and a detailed spectral analysis provides new insight into the evolution of harmonics across resonances. The full potential of the harmonic balance framework is realized here with the computation of quasi-periodic orbits around Eros.

In Chapter 5, the study is extended to perturbed and more realistic dynamical environments. The first part introduces solar radiation pressure in the vicinity of Eros, including the development of an eclipse model. The resulting resonant orbits are analyzed and compared with those obtained through classical time-domain integration. The second part shifts focus to the binary asteroid system Didymos–Dimorphos, assessing the method's ability to handle the additional complexity induced by a secondary body.

The final chapter gathers the main conclusions of the work, summarizes the contributions of the thesis and outlines the perspectives for future research and applications.

Chapter 2

Harmonic Balance Method

2.1 Introduction

The study of periodic motion is key to many dynamical systems from mechanical vibration of large structures like satellites [2, 3] to celestial dynamics [4]. Two distinct angles exist to compute periodic solutions that consist of either working in the time domain or in the frequency domain. In the time domain, the two main approaches consist of the shooting method and the collocation method. The shooting method transforms the problem of finding a periodic orbit into a boundary value problem, where an initial condition is iteratively adjusted so that the solution after one period matches the starting point [5],[6]. This approach is conceptually simple and computationally efficient for systems with a moderate number of degrees of freedom. However, its performance can degrade in stiff systems or when the solution is highly sensitive to initial conditions. The collocation method, by contrast, discretizes the time domain into subintervals and seeks a solution that satisfies the governing differential equations at selected points, known as collocation points. This strategy allows for a more robust handling of complex dynamics, including stiff and highly nonlinear behavior. It reformulates the original problem into a system of nonlinear algebraic equations, which can be solved using established numerical techniques while enforcing periodicity explicitly as a constraint [7]. Most of the software packages that exist for the computation of periodic solutions are based on this method, like MATCONT [8], AUTO [9] or COCO [10].

In the frequency domain, the main method is the harmonic balance method (HBM) that offers significant advantages for systems with smooth periodic solutions dominated by low-order harmonics. By formulating the problem directly in the frequency domain, harmonic balance avoids transient integration and efficiently captures steady-state behavior. The method assumes that the periodic solution can be approximated by a truncated Fourier series and substitutes this expansion into the governing differential equations. The resulting expressions are then projected onto the basis of harmonic functions, yielding a system of nonlinear algebraic equations for the Fourier coefficients. This makes it particularly attractive for applications in electrical and mechanical oscillatory systems. However, its effectiveness diminishes when strong nonlinearities generate rich harmonic content, requiring many terms in the Fourier expansion to maintain accuracy. A comparative study of the HBM and the collocation method on stiff systems was produced by Karkar in 2014 [11]. A review of the recent developments around the harmonic balance is proposed by Yan [12].

Many cases of application of the HBM for forced or autonomous systems are found in the literature [13, 14]. However, unlike forced systems, where the periodicity is externally defined, autonomous systems have their phase inherently indeterminate and requiring explicit specification. This is typically achieved by formulating an augmented system that incorporates a phase constraint [15, 16]. This fixes the issue related to the phase but creates an over-constrained system that can be fixed with the introduction of a fictitious energy [17].

Stability plays a central role in understanding complex nonlinear behaviors. Hill's method offers a powerful approach for analyzing the stability of linear differential equations with periodic coefficients. The method approximates the Floquet exponents, allowing the identification of stability regions [18]. Bifurcation theory complements this analysis by describing qualitative changes in system dynamics as parameters vary. Bifurcations mark critical thresholds where the number or stability of solutions changes, often giving rise to new dynamical regimes such as periodic, quasi-periodic, or chaotic motion. The interplay between Hill's method and bifurcation analysis provides valuable insights of the dynamics of the system.

A quasi-periodic orbit is characterized by the interaction of multiple frequencies, which requires adapting the classical HBM to account for this complexity. The first adaptation of the HBM for multi-frequency systems was developed in 1981 for electrical circuits by Chua and colleagues [19]. Several years later, the method was improved through coupling with the alternating frequency–time domain method (AFT) [20]. Guillot extended the approach further by enabling the continuation of quasi-periodic solutions involving two frequencies using the asymptotic numerical method (ANM) [21]. More recently, Wang proposed an efficient adaptation of the reconstruction-based HBM for handling multiple frequencies [22]. A detailed analysis of the quasi-periodic responses of a single-degree-of-freedom harmonically forced Duffing oscillator, as well as a two-degree-of-freedom system using the MHBM, along with their respective stability properties, was provided by Liao [23].

This chapter presents the methodology for computing periodic solutions in autonomous and conservative systems, with a focus on their stability analysis and bifurcation tracking using the HBM. Section 2.2 reviews the core components of the general algorithm, including key concepts specific to autonomous systems, such as the phase condition and fictitious energy, along with a discussion of Hill's method for stability analysis. Given their substantial influence on system behavior, bifurcations in the frequency response are examined in detail in Section 2.3. The extension of the HBM to the MHBM for the computation of quasi-periodic solutions is presented in Section 2.4. Section 2.5 then explores the emergence of new solution branches originating from branch points. In Section 2.6, a simple two-degree-of-freedom system is used as a reference case to validate the proposed approach. The chapter concludes with a summary of the main findings in Section 2.7.

2.2 Harmonic balance for autonomous and conservative systems

An autonomous nonlinear dynamical system with n degrees of freedom (DOFs) is considered, governed by the equations of motion shown in Eq. (2.1):

$$\mathbf{M}\ddot{\mathbf{x}} + \mathbf{C}\dot{\mathbf{x}} + \mathbf{K}\mathbf{x} = \mathbf{f}_{nl}\left(\mathbf{x}\right) \tag{2.1}$$

Here, $\mathbf{M}$, $\mathbf{C}$ and $\mathbf{K}$ represent the mass, damping, and stiffness matrices, respectively. The displacement vector $\mathbf{x}$ corresponds to the n DOFs, and $\mathbf{f}_{nl}$ denotes the nonlinear force vector, which may depend on both displacement and velocity. Time derivatives are indicated by dots. The system is autonomous, as there is no explicit time dependence in the equations of motion. It is also conservative if the damping matrix $\mathbf{C}$ is zero. It is retained in the formulation for generality, despite being null in the present context.

2.2.1 Computation of periodic solution in the frequency domain

Periodic solutions are approximated using truncated Fourier series up to the N^{th} harmonic. Two such expansions are applied to the displacement vector $\mathbf{x}$ and the nonlinear force vector $\mathbf{f}_{nl}$ from Eq. (2.1):

$$\mathbf{x}(t) = \frac{\mathbf{c_0^x}}{\sqrt{2}} + \sum_{j=1}^{N_H} \left(\mathbf{s_j^x}\sin(j\omega t) + \mathbf{c_j^x}\cos(j\omega t)\right) \tag{2.2}$$

$$\mathbf{f}_{nl}(t) = \frac{\mathbf{c_0^f}}{\sqrt{2}} + \sum_{j=1}^{N_H} \left(\mathbf{s_j^f}\sin(j\omega t) + \mathbf{c_j^f}\cos(j\omega t)\right) \tag{2.3}$$

Here, $\mathbf{s_j}$ and $\mathbf{c_j}$ denote the vectors of Fourier coefficients associated with the sine and cosine terms, respectively, with the superscripts $^{\mathbf{x}}$ and $^{\mathbf{f}}$ indicating displacement and force. For compact representation, these coefficients are assembled into vectors $\mathbf{z}$ and $\mathbf{b}$, respectively. The accuracy of this truncated representation relies on the fact that, for sufficiently smooth and strictly periodic solutions, the Fourier coefficients associated with higher harmonics decay rapidly, making their contribution negligible beyond a finite number of terms. The corresponding trigonometric functions, sine and cosine components across harmonics, are collected into a time dependent vector $\mathbf{Q}(t)$.

$$\mathbf{z} = \left[(\mathbf{c_0^x})^T(\mathbf{s_1^x})^T(\mathbf{c_1^x})^T \ldots \left(\mathbf{s_{N_H}^x}\right)^T\left(\mathbf{c_{N_H}^x}\right)^T\right]^T \tag{2.4}$$

$$\mathbf{b} = \left[\left(\mathbf{c_0^f}\right)^T\left(\mathbf{s_1^f}\right)^T\left(\mathbf{c_1^f}\right)^T \ldots \left(\mathbf{s_{N_H}^f}\right)^T\left(\mathbf{c_{N_H}^f}\right)^T\right]^T \tag{2.5}$$

$$\mathbf{Q}(t) = \left[\frac{1}{\sqrt{2}}\sin\left(\omega t\right)\cos\left(\omega t\right)\ldots\sin\left(N_H\omega t\right)\cos\left(N_H\omega t\right)\right] \tag{2.6}$$

By applying the Kronecker tensor product, along with the identity matrix $\mathbb{I}_n$ of dimension $(n \times n)$, Eq.(2.2) and Eq.(2.3) are written in a more compact form as Eq.(2.7) and (2.8), respectively:

$$\mathbf{x}(t) = (\mathbf{Q}(t) \otimes \mathbb{I}_n)\, \mathbf{z} \tag{2.7}$$

$$\mathbf{f}_{nl}(t) = (\mathbf{Q}(t) \otimes \mathbb{I}_n)\, \mathbf{b} \tag{2.8}$$

This compact formulation makes it straightforward to derive expressions for velocity and acceleration directly from the vector $\mathbf{Q}(t)$:

$$\dot{\mathbf{x}}(t) = \left(\dot{\mathbf{Q}}(t) \otimes \mathbb{I}_n\right) \mathbf{z} = (\mathbf{Q}(t)\nabla \otimes \mathbb{I}_n)\, \mathbf{z} \tag{2.9}$$

$$\ddot{\mathbf{x}}(t) = \left(\ddot{\mathbf{Q}}(t) \otimes \mathbb{I}_n\right) \mathbf{z} = \left(\mathbf{Q}(t)\nabla^2 \otimes \mathbb{I}_n\right) \mathbf{z} \tag{2.10}$$

where ∇ is defined as the matrix

$$\nabla = \begin{bmatrix} 0 & & & & \\ & \ddots & & & \\ & & \omega\nabla_j & & \\ & & & \ddots & \\ & & & & \omega\nabla_{NH} \end{bmatrix}, \nabla^2 = \begin{bmatrix} 0 & & & & \\ & \ddots & & & \\ & & \omega^2\nabla_j^2 & & \\ & & & \ddots & \\ & & & & \omega^2\nabla_{NH}^2 \end{bmatrix} \tag{2.11}$$

with

$$\nabla_j = \begin{bmatrix} 0 & -j \\ j & 0 \end{bmatrix}, \nabla_j^2 = \begin{bmatrix} -j^2 & 0 \\ 0 & -j^2 \end{bmatrix} \tag{2.12}$$

By substituting Eq. (2.7), (2.8), (2.9) and (2.10) into the equation of motion, Eq. (2.1), we obtain

$$\mathbf{M}\left(\left(\mathbf{Q}(t)\nabla^2\right) \otimes \mathbb{I}_n\right) \mathbf{z} + \mathbf{C}\left((\mathbf{Q}(t)\nabla) \otimes \mathbb{I}_n\right) \mathbf{z} + \mathbf{K}\left(\mathbf{Q}(t) \otimes \mathbb{I}_n\right) \mathbf{z} = \left(\mathbf{Q}(t) \otimes \mathbb{I}_n\right) \mathbf{b} \tag{2.13}$$

Thanks to the mixed-product property of the Kronecker product, $(\mathbf{A} \otimes \mathbf{B})\,(\mathbf{C} \otimes \mathbf{D}) = (\mathbf{AC}) \otimes (\mathbf{BD})$, this expression can be rearranged into a more convenient form

$$\left(\left(\mathbf{Q}(t)\nabla^2\right) \otimes \mathbf{M}\right) \mathbf{z} + \left((\mathbf{Q}(t)\nabla) \otimes \mathbf{C}\right) \mathbf{z} + \left(\mathbf{Q}(t) \otimes \mathbf{K}\right) \mathbf{z} = \left(\mathbf{Q}(t) \otimes \mathbb{I}_n\right) \mathbf{b} \tag{2.14}$$

To eliminate the time dependence in Eq. (2.14), a Galerkin procedure is applied, resulting in:

$$\left(\nabla^2 \otimes \mathbf{M}\right) \mathbf{z} + \left(\nabla \otimes \mathbf{C}\right) \mathbf{z} + \left(\mathbb{I}_{2N_H+1} \otimes \mathbf{K}\right) \mathbf{z} = \left(\mathbb{I}_{2N_H+1} \otimes \mathbb{I}_n\right) \mathbf{b} \tag{2.15}$$

Finally, the system can be expressed in its most compact form within the Harmonic Balance framework as:

$$\mathbf{h}(\mathbf{z}, \omega) = \mathbf{A}(\omega)\mathbf{z} - \mathbf{b}(\mathbf{z}) = \mathbf{0} \tag{2.16}$$

Here, $\mathbf{h}(\mathbf{z}, \omega)$ denotes the residual, while the matrix $\mathbf{A}(\omega)$ encapsulates the linear dynamics of the system. Two equivalent expressions for $\mathbf{A}(\omega)$ are provided in Eqs. (2.17) and (2.18).

$$\mathbf{A} = \nabla^2 \otimes \mathbf{M} + \nabla \otimes \mathbf{C} + \mathbb{I}_{2N_H+1} \otimes \mathbf{K} \tag{2.17}$$

$$\mathbf{A} = \begin{bmatrix} \mathbf{K} & & & & & \\ & \mathbf{K}-\omega^2\mathbf{M} & -\omega\mathbf{C} & & & \\ & \omega\mathbf{C} & \mathbf{K}-\omega^2\mathbf{M} & & & \\ & & & \ddots & & \\ & & & & \mathbf{K}-(N_H\omega)^2\mathbf{M} & -N_H\omega\mathbf{C} \\ & & & & N_H\omega\mathbf{C} & \mathbf{K}-(N_H\omega)^2\mathbf{M} \end{bmatrix} \tag{2.18}$$

Equation (2.16) is nonlinear, and solving it requires the use of an iterative approach. Several methods are available for this purpose, with Newton–Raphson being the most commonly used [24], though alternatives like Powell's hybrid method also exist [25]. In this thesis, we focus on Newton's method.

2.2.2 Newton's method and alternating frequency-time method

The core idea behind Newton's method is to begin with an initial guess, $\mathbf{z}_0$, and iteratively refine it using derivative information. At each step, the next approximation $\mathbf{z}_{j+1}$ is computed using the current estimate $\mathbf{z}_j$, the residual $\mathbf{h}(\mathbf{z}_j, \omega)$, and the Jacobian with respect to $\mathbf{z}$, denoted $\mathbf{h}_\mathbf{z}(\mathbf{z}_j, \omega)$:

$$\mathbf{z}_{j+1} = \mathbf{z}_j - \frac{\mathbf{h}(\mathbf{z}_j, \omega)}{\mathbf{h}_\mathbf{z}(\mathbf{z}_j, \omega)} \tag{2.19}$$

One of the main challenges in applying this method lies in computing the Jacobian of Eq. (2.16), particularly due to the nonlinear force terms. In many cases, these forces are not explicitly defined as functions of $\mathbf{z}$, which complicates the derivation. To address this, the alternating frequency–time (AFT) method can be employed to evaluate the nonlinear part of the Jacobian, specifically $\mathbf{b}(\mathbf{z})$ [26]. The AFT method leverages the discrete Fourier transform (DFT): the nonlinear forces, typically expressed in the time domain as $\mathbf{f}_{nl}(\mathbf{x}, \dot{\mathbf{x}})$, are evaluated there and then transformed back into the frequency domain to complete the computation.

$$\mathbf{z} \xrightarrow{FFT^{-1}} \mathbf{x}(t) \rightarrow \mathbf{f}_{nl}(\mathbf{x}) \xrightarrow{FFT} \mathbf{b}(\mathbf{z})$$

Several approaches can be used to compute the Jacobian matrix $\mathbf{h}_\mathbf{z}$. The most straightforward is the finite difference method, which is easy to implement but can be computationally expensive, especially for large systems. A more elegant and computationally efficient alternative involves interpreting the inverse Fourier transform (DFT^{-1}) as a linear operator, denoted by $\mathbf{\Gamma}(\omega)$. To reconstruct the time-domain response from its frequency-domain representation, the periodic solution (with period T) must be discretized into N time steps, with a uniform time interval $\Delta t = \frac{T}{N}$. The resulting time vector is

$$\mathbf{t} = [t_1, t_2, \ldots, t_N], \quad \text{with} \quad t_1 = 0, t_2 = \Delta t, \ldots, t_N = T - \Delta t$$

The operator $\mathbf{\Gamma}(\omega)$ then takes the form:

$$\mathbf{\Gamma}(\omega) = \begin{bmatrix} \mathbb{I}_n \otimes \begin{bmatrix} 1/\sqrt{2} \\ 1/\sqrt{2} \\ \vdots \\ 1/\sqrt{2} \end{bmatrix} & \mathbb{I}_n \otimes \begin{bmatrix} \sin(\omega t_1) \\ \sin(\omega t_2) \\ \vdots \\ \sin(\omega t_N) \end{bmatrix} & \mathbb{I}_n \otimes \begin{bmatrix} \cos(\omega t_1) \\ \cos(\omega t_2) \\ \vdots \\ \cos(\omega t_N) \end{bmatrix} & \dots \\ & \mathbb{I}_n \otimes \begin{bmatrix} \sin(N_H \omega t_1) \\ \sin(N_H \omega t_2) \\ \vdots \\ \sin(N_H \omega t_N) \end{bmatrix} & \mathbb{I}_n \otimes \begin{bmatrix} \cos(N_H \omega t_1) \\ \cos(N_H \omega t_2) \\ \vdots \\ \cos(N_H \omega t_N) \end{bmatrix} & \end{bmatrix} \tag{2.20}$$

or as the simple equation that links discretized time domain and frequency domain:

$$\tilde{\mathbf{x}} = \mathbf{\Gamma}(\omega)\mathbf{z} \tag{2.21}$$

The time-domain vector $\tilde{\mathbf{x}}$, of size nN, is constructed by stacking the N time samples for each degree of freedom sequentially. Specifically, it is ordered as the time discretization of the first degree of freedom, followed by the second, and so on up to the n^{th}, yielding:

$$\tilde{\mathbf{x}} = [x_1(t_1) \dots x_1(t_N) \dots x_n(t_1) \dots x_n(t_N)]$$

The inverse of Eq.(2.21), i.e., the direct Fourier transform, provides the relationship:

$$\mathbf{z} = (\mathbf{\Gamma}(\omega))^+ \tilde{\mathbf{x}} \tag{2.22}$$

Here, the superscript $^+$ denotes the Moore–Penrose pseudo-inverse, given by $\mathbf{\Gamma}^+ = \mathbf{\Gamma}^\top \left(\mathbf{\Gamma}\mathbf{\Gamma}^\top\right)^{-1}$. This operator is also used to transform the nonlinear force vector, evaluated in the time domain, back into the frequency domain to compute

$$\mathbf{b}(\mathbf{z}) = (\mathbf{\Gamma}(\omega))^+ \tilde{\mathbf{f}} \tag{2.23}$$

Using Eqs. (2.22) and (2.23), the Jacobian $\mathbf{h}_\mathbf{z}(\mathbf{z}_j, \omega)$ is conveniently expressed as:

$$\mathbf{h}_\mathbf{z} = \frac{\partial \mathbf{h}}{\partial \mathbf{z}} = \mathbf{A} - \frac{\partial \mathbf{b}}{\partial \mathbf{z}} = \mathbf{A} - \frac{\partial \mathbf{b}}{\partial \tilde{\mathbf{f}}} \frac{\partial \tilde{\mathbf{f}}}{\partial \tilde{\mathbf{x}}} \frac{\partial \tilde{\mathbf{x}}}{\partial \mathbf{z}} = \mathbf{A} - \mathbf{\Gamma}^+ \frac{\partial \tilde{\mathbf{f}}}{\partial \tilde{\mathbf{x}}} \mathbf{\Gamma} \tag{2.24}$$

The term $\frac{\partial \tilde{\mathbf{f}}}{\partial \tilde{\mathbf{x}}}$—the Jacobian of the nonlinear forces with respect to the state in the time domain—is assumed to be analytically defined.

At this point, all components required to solve the harmonic balance equation (2.16) are in place. However, since the dynamical systems studied in this thesis are autonomous, additional care must be taken to ensure that the periodic solutions computed are nontrivial (i.e., $\mathbf{z} \neq \mathbf{0}$) and suitable for continuation. To this end, a phase condition is introduced.

2.2.3 Phase condition

Solutions of autonomous nonlinear systems exhibit time-translation invariance. That is, if $x(t)$ is a solution to an autonomous system with an initial condition $x(\Delta t) = x_0$, then the time-shifted function $x(t + \Delta t)$ is also a valid solution with initial condition $x(0) = x_0$. However, since the HBM operates in the frequency domain, this invariance

must be expressed in terms of Fourier coefficients. If $\hat{\mathbf{z}}$ denotes the vector of Fourier coefficients associated with a solution $x(t)$, then the time-translated solution $x(t+\Delta t)$ corresponds to a new vector of coefficients, denoted $\hat{\mathbf{z}}(\mathbf{z}, \Delta t)$. In this context, the Fourier decomposition of the time-shifted solution takes the form

$$\begin{aligned} \mathbf{x}(t+\Delta t) &= \frac{\hat{\mathbf{c}}_{\mathbf{0}}^{\mathbf{x}}}{\sqrt{2}} + \sum_{j=1}^{N_H} \left(\hat{\mathbf{s}}_{\mathbf{j}}^{\mathbf{x}} \sin(j\omega t) + \hat{\mathbf{c}}_{\mathbf{j}}^{\mathbf{x}} \cos(j\omega t) \right) \\ &= (\mathbf{Q}(t) \otimes \mathbb{I}_n)\, \hat{\mathbf{z}} \end{aligned} \tag{2.25}$$

$$\begin{aligned} \mathbf{x}(t+\Delta t) &= \frac{\mathbf{c}_{\mathbf{0}}^{\mathbf{x}}}{\sqrt{2}} + \sum_{j=1}^{N_H} \left(\mathbf{s}_{\mathbf{j}}^{\mathbf{x}} \sin(j\omega(t+\Delta t)) + \mathbf{c}_{\mathbf{j}}^{\mathbf{x}} \cos(j\omega(t+\Delta t)) \right) \\ &= \frac{\mathbf{c}_{\mathbf{0}}^{\mathbf{x}}}{\sqrt{2}} + \sum_{j=1}^{N_H} (\mathbf{s}_{\mathbf{j}}^{\mathbf{x}} (\cos(j\omega t)\cos(j\omega\Delta t) - \sin(j\omega t)\sin(j\omega\Delta t)) \\ &+ \mathbf{c}_{\mathbf{j}}^{\mathbf{x}} (\cos(j\omega t)\cos(j\omega\Delta t) + \sin(j\omega t)\sin(j\omega\Delta t))) \\ &= (\mathbf{Q}(t) \otimes \mathbb{I}_n)\, (\mathbf{R}(\Delta t) \otimes \mathbb{I}_n)\, \mathbf{z} \end{aligned} \tag{2.26}$$

with

$$\mathbf{R}(\Delta t) = \begin{bmatrix} 1 & & & & \\ & \ddots & & & \\ & & \mathbf{Rot}_j & & \\ & & & \ddots & \\ & & & & \mathbf{Rot}_{NH} \end{bmatrix}, \mathbf{Rot}_j = \begin{bmatrix} \cos(j\omega\Delta t) & -\sin(j\omega\Delta t) \\ \sin(j\omega\Delta t) & \cos(j\omega\Delta t) \end{bmatrix}$$

Just as solutions of autonomous systems are invariant under time translations in the time domain, they exhibit a similar invariance in the frequency domain through the transformation $\hat{\mathbf{z}}$. Because the HBM assumes periodic solutions, this invariance results in a lack of uniqueness due to an undefined phase shift. In practical terms, this causes the Jacobian matrix $\mathbf{h_z}$ to become singular. The eigenvector corresponding to this singularity can be identified by examining the Jacobian under the transformation $\hat{\mathbf{z}}$.

$$\begin{aligned} \mathbf{h}_{\hat{\mathbf{z}}}|_{\Delta t=0} \left.\frac{\partial \hat{\mathbf{z}}(\mathbf{z}, \Delta t)}{\partial \Delta t}\right|_{\Delta t=0} + \mathbf{h}_{\mathbf{\Delta t}} &= 0 \\ \mathbf{h}_{\hat{\mathbf{z}}}|_{\Delta t=0} \left.\frac{\partial \hat{\mathbf{z}}(\mathbf{z}, \Delta t)}{\partial \Delta t}\right|_{\Delta t=0} &= 0 \\ \mathbf{h}_{\hat{\mathbf{z}}}|_{\Delta t=0} \left(\left.\frac{\partial \mathbf{R}(\Delta t)}{\partial \Delta t}\right|_{\Delta t=0} \otimes \mathbb{I}_n \right) \mathbf{z} &= 0 \\ \mathbf{h_z}\, (-\nabla \otimes \mathbb{I}_n)\, \mathbf{z} &= 0 \end{aligned}$$

This shows that the direction of the singularity in the solution space is given by $\varphi = (\mathrm{diag}(\mathbf{0}, \ldots, \nabla_j, \ldots, \nabla_{N_H}) \otimes \mathbb{I}_n)\, \mathbf{z}$. The factor ω found in the matrix ∇, has been omitted, since scalar multiplication does not affect the nullspace and therefore does not

alter the singularity of $\mathbf{h}_\mathbf{z}$. To restore uniqueness, a phase condition, denoted $g(\mathbf{z})$, must be imposed. The most basic approach is to fix one of the Fourier coefficients, typically by setting a component of $\mathbf{z}$ to zero (e.g., $\mathbf{z}_i = 0$), which corresponds to constraining the initial displacement or velocity. However, this strategy can result in a phase drift during continuation, which may introduce numerical inaccuracies and slow down the computation.

A more robust and general phase condition, which does not depend on the specific type of nonlinearity, is used in continuation software like AUTO [16, 27]. This condition, formulated in the time domain, is

$$g(\dot{\mathbf{x}}(t), \mathbf{x}(t)) = \int_0^T \mathbf{x}_{j-1}^T \dot{\mathbf{x}}(t) dt = 0 \tag{2.27}$$

Here, $\mathbf{x}_{j-1}$ is the displacement vector from the previous continuation step. Following the earlier approach, this condition is translated into the frequency domain as:

$$g(\mathbf{z}) = \mathbf{z}_{j-1}^T \left(\mathrm{diag}(\mathbf{0}, \ldots, \nabla_j, \ldots, \nabla_{N_H}) \otimes \mathbb{I}_n\right) \mathbf{z} = 0 \tag{2.28}$$

This condition ensures smooth progression between continuation steps by limiting abrupt changes, thus helping prevent numerical errors. Additionally, its derivative with respect to $\mathbf{z}$ aligns with the singular eigenvector φ. In other words, this phase condition effectively cancels the evolution of $\mathbf{z}$ along the null direction of the Jacobian, thereby enforcing the uniqueness of the periodic solution. The derivative of $g(\mathbf{z})$ with respect to $\mathbf{z}$ is simply:

$$\mathbf{g}_\mathbf{z} = \left(\mathrm{diag}(\mathbf{0}, \ldots, \nabla_j, \ldots, \nabla_{N_H}) \otimes \mathbb{I}_n\right) \mathbf{z}_{j-1} \tag{2.29}$$

2.2.4 Injection of fictitious energy

Adding a phase condition to the system introduces an extra constraint, which results in an overdetermined problem and a non-square Jacobian matrix. A common workaround is to use the Moore–Penrose pseudoinverse [28]. However, a more elegant and efficient strategy is to inject a fictitious, non-conservative energy term $\mathbf{E}_{\text{fic}}$, scaled by a damping parameter η, into the equations of motion

$$\mathbf{M}\ddot{\mathbf{x}} + \mathbf{C}\dot{\mathbf{x}} + \eta \mathbf{E}_{fic}(\dot{\mathbf{x}}) + \mathbf{K}\mathbf{x} = \mathbf{f}_{nl}(\mathbf{x}) \tag{2.30}$$

In order for the system to admit periodic solutions, it must be conservative when there's no external forcing. This means that the damping coefficient η should tend toward zero as the continuation progresses [17]. Accordingly, the HBM formulation (Eq. (2.16)) becomes:

$$\mathbf{h}(\mathbf{z}, \omega, \eta) = \mathbf{A}(\omega)\mathbf{z} + \eta \mathbf{P}(\mathbf{z}) - \mathbf{b}(\mathbf{z}) = \mathbf{0} \tag{2.31}$$

with $\mathbf{P}(\mathbf{z})$ the fictitious energy $\mathbf{E}_{fic}(\dot{\mathbf{x}})$ expressed in the frequency domain. Since η goes to zero during the continuation, the specific shape of $\mathbf{P}(\mathbf{z})$ is not critical, as long as it is non-conservative. That said, the choice does affect the structure of the Jacobian. Ideally, $\mathbf{P}(\mathbf{z})$ should be set as, $\mathbf{P}(\mathbf{z}) = (\nabla \otimes \mathbb{I}_n)\, \mathbf{z}_{j-1}$. With this choice, the derivative of $\mathbf{h}$ with respect to η denoted $\mathbf{h}_\eta$ becomes identical to $\mathbf{g}_\mathbf{z}$, and the singularity in the Jacobian of the augmented system is naturally resolved.

2.2.5 Initialization and continuation

The computation of a single periodic solution for a conservative autonomous system has been detailed in the previous sections. However, in practice, it is often more insightful to compute entire branches of solutions over a range of frequencies. To achieve this, various continuation techniques are available. The MANLAB package, for instance, uses the asymptotic numerical method (ANM), while arclength continuation is another well-established approach [29]. In this work, the chosen method follows the continuation scheme implemented in the MATCONT toolbox, which relies on a Moore–Penrose-based formulation [8].

The augmented system used for continuation couples the HBM equation (Eq. (2.31)) with the phase condition (Eq. (2.29))

$$\begin{bmatrix} \mathbf{h}(\mathbf{z},\omega,\eta) \\ g(\mathbf{z}) \end{bmatrix} = \begin{bmatrix} \mathbf{A}(\omega)\mathbf{z} + \eta\mathbf{P}(\mathbf{z}) - \mathbf{b}(\mathbf{z}) \\ \mathbf{z}_{j-1}^T (\nabla \otimes \mathbb{I}_n)\, \mathbf{z} \end{bmatrix} = \begin{bmatrix} \mathbf{0} \\ 0 \end{bmatrix} \tag{2.32}$$

The continuation is carried out alongside a prediction step. The method adopted here is tangent prediction, where the next point on the solution branch is estimated using the tangent vector at the previous point. Let $\mathbf{t}_i$ denote the tangent vector associated with the current solution $\mathbf{y}_i = \begin{bmatrix} \mathbf{z}_i^T & \omega_i & \eta_i \end{bmatrix}^T$. This vector is obtained by solving the linear system

$$\begin{bmatrix} \mathbf{J}(\mathbf{y}_i) \\ \mathbf{g}_\mathbf{y} \\ \mathbf{t}_{i-1}^T \end{bmatrix} \mathbf{t}_i = \begin{bmatrix} \mathbf{0} \\ 0 \\ 1 \end{bmatrix} \tag{2.33}$$

Here, $\mathbf{J}(\mathbf{y}_i) = \begin{bmatrix} \mathbf{h}_\mathbf{z} & \mathbf{h}_\omega & \mathbf{h}_\eta \end{bmatrix}$ is the Jacobian of the HBM system, and $\mathbf{g}_\mathbf{y} = [\mathbf{g}_\mathbf{z} \quad 0 \quad 0]$ is the Jacobian of the phase condition. The last row in Eq. (2.33), $\mathbf{t}_{i-1}^T \mathbf{t}_i = 1$, enforces a unit projection onto the previous tangent, preventing the predictor from reversing direction along the branch.

All the components of the Jacobian system have been defined in earlier sections, except for $\mathbf{h}_\omega$, which is the derivative of Eq. (2.31) with respect to the frequency ω, and can be obtained straightforwardly:

$$\mathbf{h}_\omega = \frac{\partial \mathbf{A}(\omega)}{\partial \omega}\mathbf{z} \tag{2.34}$$

While frequency ω is used here as the continuation parameter, the same framework readily accommodates other scalar parameters. In that case, the additional Jacobian column is simply the derivative of Eq. (2.31) with respect to the chosen parameter, for example the mass ratio μ in the circular restricted three-body problem presented in the next chapter.

The tangent vector is scaled by a step size s_i and added to the current solution to obtain the prediction for the next continuation point:

$$\mathbf{y}_{i+1} = \mathbf{y}_i + s_i \mathbf{t}_i \tag{2.35}$$

Choosing an appropriate step size is critical: an improper selection can increase computational cost, introduce phase jumps, or even cause entire solution branches to be missed during continuation [30]. A straightforward approach is to use a constant step

size, $s_i = \text{const}$, but this strategy is often suboptimal. If the value is too small, the computation becomes unnecessarily long; if too large, the discretization may miss important features or lead to convergence failure.

An improved strategy is to use an adaptive step size based on the number of iterations n_i required by the correction scheme. If n_i exceeds an upper threshold n_u, the step size is halved. If n_i falls below a lower threshold n_l, the step size is doubled. Otherwise, the step size remains unchanged. This logic is summarized by:

$$s_i = \Upsilon s_{i-1} \quad \text{with} \quad \Upsilon = \begin{cases} 0.5 & \mathrm{n}_i > \mathrm{n}_u \\ 1 & \mathrm{n}_l \leq \mathrm{n}_i \leq \mathrm{n}_u \\ 2 & \mathrm{n}_i < \mathrm{n}_l \end{cases} \tag{2.36}$$

A drawback of this method is that the thresholds n_l and n_u may need tuning depending on the system. Alternative adaptive schemes exist, including approaches based on the smallest parameterized eigenvalue of the Jacobian matrix $\mathbf{h_z}$ [31].

Once the prediction $\mathbf{y}_{i+1}$ is constructed, it must be corrected to satisfy the system of equations (Eq. (2.31)). The correction is performed using a Moore–Penrose-based method with an auxiliary optimization variable $\mathbf{v}_i$, initialized as the tangent vector $\mathbf{t}_i$. The correction update rules are:

$$\mathbf{y}_{i+1}^{j+1} = \mathbf{y}_{i+1}^{j} + \Delta\mathbf{y}_{i+1}^{j} = \mathbf{y}_{i+1}^{j} - {\mathbf{G}_\mathbf{y}}^{-1}(\mathbf{y}_{i+1}^{j}, \mathbf{v}_{i+1}^{j})\mathbf{G}(\mathbf{y}_{i+1}^{j}, \mathbf{v}_{i+1}^{j}) \tag{2.37}$$

$$\mathbf{v}_{i+1}^{j+1} = \mathbf{v}_{i+1}^{j} + \Delta\mathbf{v}_{i+1}^{j} = \mathbf{v}_{i+1}^{j} - {\mathbf{G}_\mathbf{y}}^{-1}(\mathbf{y}_{i+1}^{j}, \mathbf{v}_{i+1}^{j})\mathbf{R}(\mathbf{y}_{i+1}^{j}, \mathbf{v}_{i+1}^{j}) \tag{2.38}$$

where the residuals and Jacobians are defined as:

$$\mathbf{G}(\mathbf{y}, \mathbf{v}) = \begin{bmatrix} \mathbf{h}(\mathbf{y}) \\ g(\mathbf{y}) \\ \mathbf{0} \end{bmatrix} \tag{2.39}$$

$$\mathbf{G}_\mathbf{y}(\mathbf{y}, \mathbf{v}) = \begin{bmatrix} \mathbf{J}(\mathbf{y}) \\ \mathbf{g}_\mathbf{y}(\mathbf{y}) \\ \mathbf{v}^T \end{bmatrix} \tag{2.40}$$

$$\mathbf{R}(\mathbf{y}, \mathbf{v}) = \begin{bmatrix} \mathbf{J}(\mathbf{y})\mathbf{v} \\ \mathbf{g}_\mathbf{y}(\mathbf{y})\mathbf{v} \\ \mathbf{0} \end{bmatrix} \tag{2.41}$$

With this prediction-correction scheme, one can trace out the evolution of the families of orbits with respect to their frequency. For complex systems, unnecessary harmonics can significantly increase computation time. It is therefore essential to select the appropriate number of harmonics to balance accuracy and efficiency. One strategy is to adapt the harmonic content during continuation, using the adaptive harmonic balance method (AHBM) [32, 33].

Adaptive harmonic balance method (AHBM)

The fundamental idea behind the AHBM is to isolate the sine and cosine contributions of each harmonic and each degree of freedom, d, in the Fourier expansion of the response. For example, for a two-degree-of-freedom system, the forcing terms for each degree of freedom are collected in vectors:

$$\mathbf{b}_{x_d} = \left[\left(\mathbf{c_0^{f_{x_d}}}\right)^T \left(\mathbf{s_1^{f_{x_d}}}\right)^T \quad \left(\mathbf{c_1^{f_{x_d}}}\right)^T \quad \left(\mathbf{s_2^{f_{x_d}}}\right)^T \quad \left(\mathbf{c_2^{f_{x_d}}}\right)^T \dots \left(\mathbf{s_{N_H}^{f_{x_d}}}\right)^T \quad \left(\mathbf{c_{N_H}^{f_{x_d}}}\right)^T \right]^T \tag{2.42}$$

For each harmonic h and each degree of freedom d, the scalar quantity Φ_h^d is computed as:

$$\Phi_h^d = \sqrt{\left(s_{N_{H_h}}^{f_{x_d}}\right)^2 + \left(c_{N_{H_h}}^{f_{x_d}}\right)^2}$$

This value represents the amplitude of the h-th harmonic of the d-th degree of freedom. It is then compared to a threshold value ϵ_{AHBM}. If $\Phi_h^d > \epsilon_{\text{AHBM}}$ for any d, the harmonic h is retained; otherwise, it is discarded. This selective inclusion reduces unnecessary computation while maintaining accuracy.

A flowchart summarizing the HBM algorithm, including all previously detailed steps, is presented in Figure 2.1. The next section addresses the stability analysis of the computed periodic solutions.

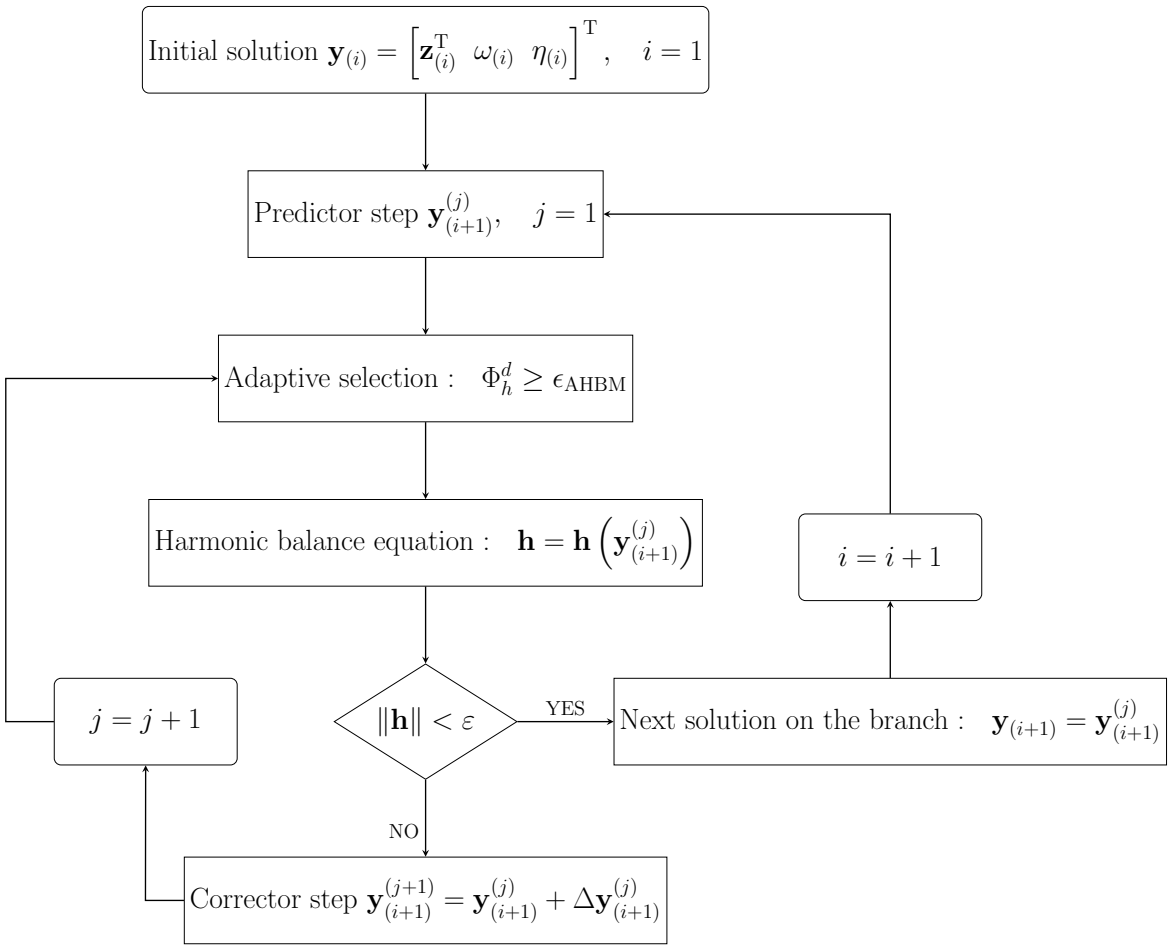

Figure 2.1: Algorithm flowchart of HBM.

2.2.6 Stability

Nonlinear systems are subject to complex dynamical behaviors, including unstable solutions and bifurcation phenomena. In the time domain, Floquet theory provides insight into the stability of periodic solutions by analyzing the eigenvalues of the monodromy matrix. In the frequency domain, an alternative approach, Hill's method, relies on the Floquet exponent, $\boldsymbol{\lambda}$, to evaluate the stability of solutions. The Floquet multipliers, $\boldsymbol{\sigma}$, are related to the exponents through the relation:

$$\sigma_i = e^{\lambda_i T} \tag{2.43}$$

A periodic solution is unstable if at least one Floquet multiplier satisfies $|\sigma_i| > 1$; otherwise, the solution is considered stable. In terms of the Floquet exponents, instability occurs if the real part of any exponent satisfies $\mathrm{Re}(\lambda_i) > 0$. A graphical representation of the stable and unstable regions for both the Floquet exponents and multipliers is provided in Figure 2.2.

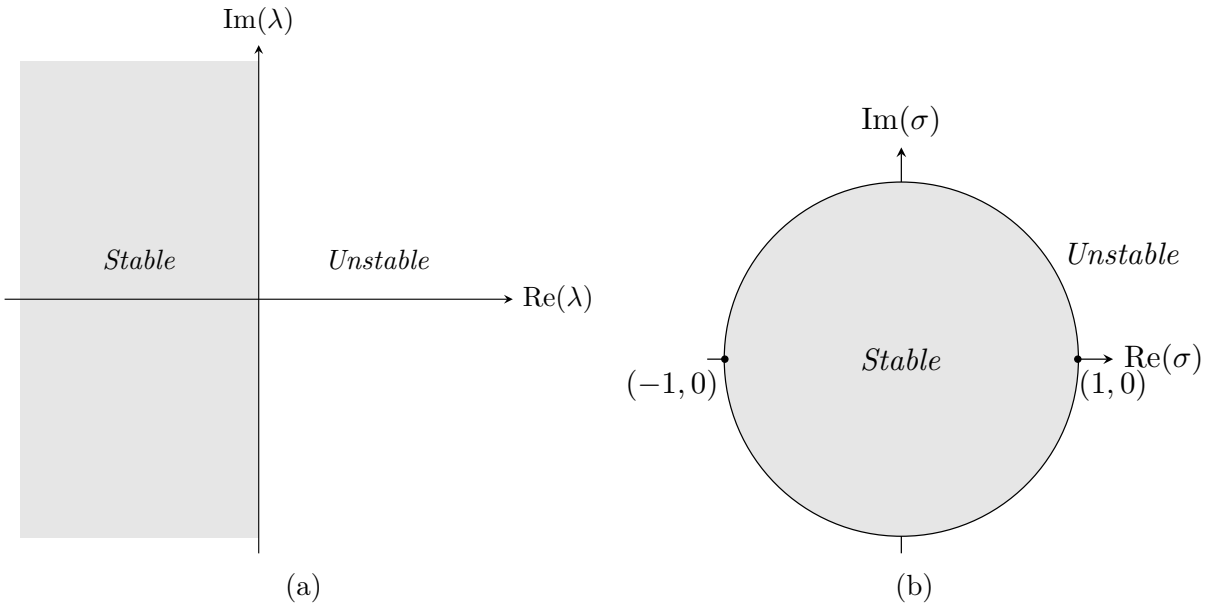

Figure 2.2: Stability with respect to the Floquet exponents (a) and Floquet multipliers (b).

Hill's method introduces a periodic perturbation, $\mathbf{s}(t)$, modulated by an exponential term, to an existing periodic solution $\mathbf{x}^*(t)$:

$$\mathbf{p}(t) = \mathbf{x}^*(t) + e^{\lambda t}\mathbf{s}(t) \tag{2.44}$$

This perturbed solution is then substituted into the equations of motion, Eq. (2.1), to assess the evolution and stability of the response.

$$\mathbf{M}\ddot{\mathbf{x}}^* + \mathbf{C}\dot{\mathbf{x}}^* + \mathbf{K}\mathbf{x}^* + \left(\lambda^2\mathbf{M}\mathbf{s} + \lambda\left(2\mathbf{M}\dot{\mathbf{s}} + \mathbf{C}\mathbf{s}\right) + \mathbf{M}\ddot{\mathbf{s}} + \mathbf{C}\dot{\mathbf{s}} + \mathbf{K}\mathbf{s}\right)e^{\lambda t} = \mathbf{f}(\mathbf{p}) \tag{2.45}$$

In the stability analysis, the fictitious energy term $\eta\mathbf{E}_{fic}$ is omitted, as it has no dynamical meaning and serves only to regularize the continuation system. Since η tends to 0 at convergence, the resulting Hill matrix corresponds strictly to the linearized physical system [34]. Using a Fourier decomposition truncated to the N^{th} order for the periodic solution $\mathbf{x}(t)$ and its perturbation $\mathbf{s}(t)$, the corresponding vectors of Fourier coefficients are denoted $\mathbf{z}$ and $\mathbf{u}$, respectively. Applying the Galerkin procedure to the perturbed equations yields:

$$\mathbf{A}\mathbf{z}^* + \left(\lambda^2\boldsymbol{\Delta}_\mathbf{2} + \lambda\boldsymbol{\Delta}_\mathbf{1} + \mathbf{A}\right)e^{\lambda t}\mathbf{u} = \mathbf{b}\left(\mathbf{z}^* + e^{\lambda t}\mathbf{u}\right) \tag{2.46}$$

where the operators $\boldsymbol{\Delta}_1$ and $\boldsymbol{\Delta}_2$ are defined as:

$$\boldsymbol{\Delta}_\mathbf{1} = \nabla \otimes 2\mathbf{M} + \mathbb{I}_{2N_H+1} \otimes \mathbf{C} \tag{2.47}$$

$$\boldsymbol{\Delta}_\mathbf{2} = \mathbb{I}_{2N_H+1} \otimes \mathbf{M} \tag{2.48}$$

To simplify Eq. (2.46), a Taylor series expansion of the right-hand side is performed:

$$\mathbf{b}\left(\mathbf{z}^* + e^{\lambda t}\mathbf{u}\right) = \mathbf{b}(\mathbf{z}^*) + \frac{\partial \mathbf{b}}{\partial \mathbf{z}}\left(e^{\lambda t}\mathbf{u}\right) \tag{2.49}$$

This makes the residual $\mathbf{Az}^* - \mathbf{b}(\mathbf{z}^*)$ appear, which vanishes by construction of the harmonic balance equation, Eq.(2.16). Substituting this expression and introducing the Jacobian matrix $\mathbf{h}_z$, defined in Eq.(2.82), leads to the following quadratic eigenvalue problem:

$$\left(\mathbf{\Delta_2}\lambda^2 + \mathbf{\Delta_1}\lambda + \mathbf{h_z}\right) e^{\lambda t}\mathbf{u} = \mathbf{0} \tag{2.50}$$

Since the exponential term is non-zero, it can be omitted, resulting in:

$$\left(\mathbf{\Delta}_2\lambda^2 + \mathbf{\Delta}_1\lambda + \mathbf{h}_z\right) \mathbf{u} = \mathbf{0} \tag{2.51}$$

This quadratic eigenvalue problem can be reformulated as a linear eigenvalue problem by increasing its dimension, typically by a factor of two [3]. Among all computed eigenvalues λ, only $2n$ are meaningful as they approximate the true Floquet exponents of the periodic solution $\mathbf{x}^*$ [35]. According to [36], the relevant exponents are those with the smallest imaginary parts in modulus, while the others are discarded due to their lack of physical significance.

It is worth noting that the accuracy of the computed Floquet exponents improves with the number of harmonics used in the Fourier decomposition. However, for autonomous systems, the Jacobian $\mathbf{h}_z$ is always singular due to time-translation invariance, resulting in two zero eigenvalues. These may affect the numerical conditioning of the stability analysis. Common remedies include shifting the null eigenvalues to a small negative value (e.g., -1), as suggested in [37], or simply discarding them, since they do not interfere with the detection of bifurcations.

2.3 Bifurcations

During the continuation process, the evolution of the Floquet multipliers along the unit circle can reveal the presence of specific points known as bifurcations. Bifurcations are often associated with changes in the stability of the system; however, a stability change is not a necessary condition for a bifurcation to occur.

In the context of this work, three particular types of bifurcations are considered, namely singular points, period doubling and Neimark-Sacker bifurcations. A more comprehensive treatment of bifurcation theory can be found in Kuznetsov [38]. The characteristic behavior of the Floquet exponents and multipliers for these three bifurcation types is illustrated in Figure 2.3.

2.3.1 Singular points

Singular points occur when the real part of a Floquet exponent changes sign while its imaginary part is zero. This is equivalent to a pair of Floquet multipliers entering or leaving the unit circle through the point $(1, 0)$. At such points, the Jacobian matrix $\mathbf{h_z}$ (Eq. (2.82)) becomes singular. Among these singular points, two types of bifurcations can arise: fold bifurcations and branch points (BP). They can be distinguished using $\mathbf{h}_\omega$ (Eq. (2.34)):

- Fold bifurcations satisfy ${\mathbf{h}_\omega}^T\mathbf{u} \neq 0$.

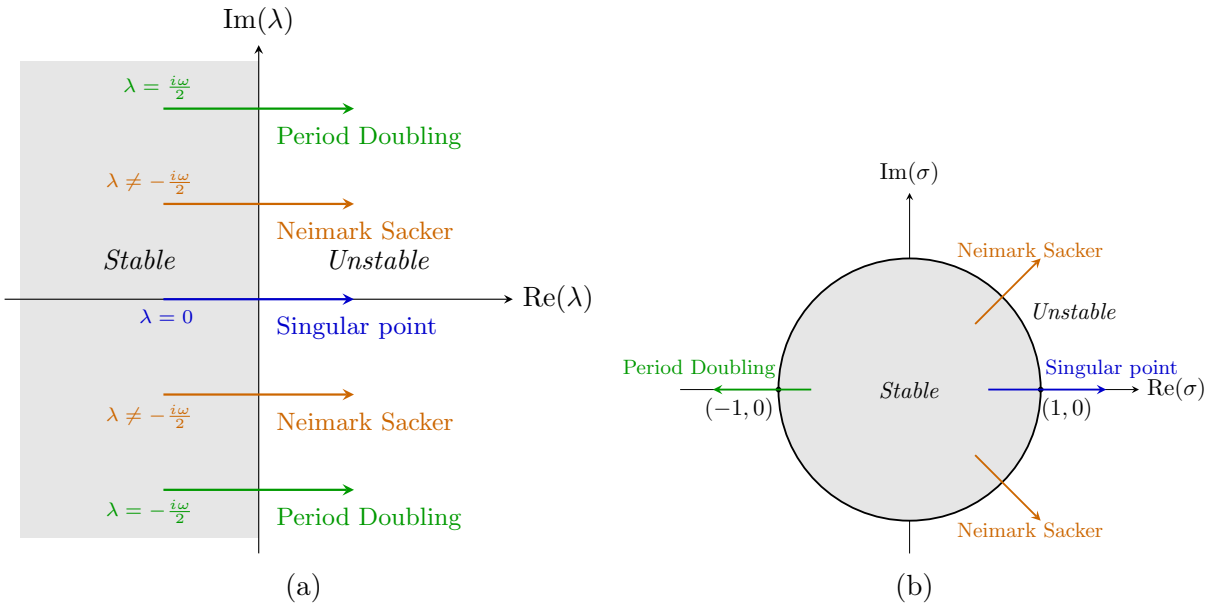

Figure 2.3: Bifurcations with respect to the Floquet exponents (a) and Floquet multipliers (b).

- Branch points satisfy ${\mathbf{h}_\omega}^T \mathbf{u} = 0$.

Fold bifurcation: Also known as limit points or saddle nodes, folds do not give rise to new branches of solutions. They are characterized by a reversal in the direction of the continuation parameter ω, typically showing an increase followed by a decrease (or vice versa). Since folds do not introduce new solution paths, their detection is not addressed in this work.

Branch point: Before a branch point, the system follows a single solution branch. After the bifurcation, multiple branches emerge. This bifurcation is often accompanied by a change in stability between the primary branch and the new one(s).

- If two branches meet and exchange stability, the phenomenon is referred to as a transcritical bifurcation.
- If a new branch emerges from the main one—either stable or unstable—along with a stability change in the main branch, the bifurcation is termed a pitchfork bifurcation.

The singularity of $\mathbf{h_z}$ at these points can be leveraged to detect folds and branch points. In both cases, the determinant of $\mathbf{h_z}$ vanishes. To distinguish between them, the rank deficiency of the Jacobian system in Eq. (2.33) is exploited, as proposed in [39]. The test function used for branch point detection is

$$\varphi_i = \det \begin{pmatrix} \mathbf{h_z} & \mathbf{h}_\omega & \mathbf{h}_\eta \\ \mathbf{g_z} & 0 & 0 \\ & \mathbf{t_{i-1}^T} & \end{pmatrix} \tag{2.52}$$

A branch point bifurcation is identified when this test function changes sign between two consecutive continuation steps, i.e, $\varphi_i . \varphi_{i+1} < 0$.

2.3.2 Period doubling

Period doubling bifurcations (PD) occur when a pair of Floquet multipliers exits or enters the unit circle through the point $(-1, 0)$ on the real axis. In terms of Floquet exponents, this corresponds to a pair of complex conjugate exponents crossing the imaginary axis at $\lambda = \pm\frac{i\omega}{2}$. At the bifurcation point, a new branch of periodic solutions emerges, with the new solutions having a period twice that of the original branch.

Several test functions are available for detecting PD bifurcations; two such methods are detailed in [40]. The first method involves substituting $\lambda = \frac{i\omega}{2}$ into Eq. (2.51) and decomposing the associated eigenvector into its real and imaginary parts as $\mathbf{u} = \mathbf{u_R} + i\mathbf{u_I}$, yielding

$$\begin{bmatrix} \mathbf{h_z} - \left(\frac{\omega}{2}\right)^2 \mathbf{\Delta_2} & \frac{\omega}{2}\mathbf{\Delta_1} \\ -\frac{\omega}{2}\mathbf{\Delta_1} & \mathbf{h_z} - \left(\frac{\omega}{2}\right)^2 \mathbf{\Delta_2} \end{bmatrix} \begin{pmatrix} \mathbf{u_R} \\ \mathbf{u_I} \end{pmatrix} = \mathbf{B} \begin{pmatrix} \mathbf{u_R} \\ \mathbf{u_I} \end{pmatrix} = \begin{pmatrix} \mathbf{0} \\ \mathbf{0} \end{pmatrix} \tag{2.53}$$

The matrix on the left-hand side of this equation, denoted as $\mathbf{B}$, becomes singular at the PD bifurcation. A simple detection method relies on monitoring the sign variation of the derivative of the determinant of $\mathbf{B}$ during the continuation. Using a finite difference approximation for the derivative, the associated test function is defined as

$$\varphi_i = \text{sign}\left(\det\left(\mathbf{B}_i\right) - \det\left(\mathbf{B}_{i-1}\right)\right) \tag{2.54}$$

The presence of a bifurcation is indicated when the test function changes sign between two consecutive steps, i.e., when $\varphi_i.\varphi_{i+1} < 0$. An alternative approach presented in [40] relies directly on the Floquet exponents. Let us define $\bar{\lambda}$ as:

$$\bar{\lambda} = \max_{j=\{1,\ldots,2n\}} \left\| e^{\frac{2\pi\lambda_j}{\omega}} \right\| \tag{2.55}$$

The corresponding test function is then given by:

$$\varphi_i = \text{sign}\left(\Re\left(\bar{\lambda}\right)\right) |\bar{\lambda}| + 1 \tag{2.56}$$

As with the previous method, a sign change in φ_i across consecutive continuation steps also signals the occurrence of a PD bifurcation. However, these methods can occasionally yield false positives in the context of autonomous systems. Therefore, it is recommended to combine them with direct monitoring of the Floquet multipliers or exponents during the continuation to enhance robustness.

A third method, also discussed in [40], involves modifying the frequency basis by explicitly incorporating subharmonics into the Fourier decomposition. In this case, the vector $\mathbf{Q}(t)$ (as defined in Eq. (2.6)) is extended as:

$$\begin{aligned} \mathbf{Q}_{PD}(t) = \Bigg[& \frac{1}{\sqrt{2}} \sin\left(\frac{\omega}{2}t\right) \cos\left(\frac{\omega}{2}t\right) \sin\left(\omega t\right) \cos\left(\omega t\right) \ldots \\ & \sin\left(N_H\omega t\right) \cos\left(N_H\omega t\right) \sin\left(\frac{\left(2N_H+1\right)\omega}{2}t\right) \cos\left(\frac{\left(2N_H+1\right)\omega}{2}t\right) \Bigg] \end{aligned} \tag{2.57}$$

This modification changes the nature of the emerging branch from a PD bifurcation. The period no longer doubles; instead, in the new frequency basis, the PD bifurcation

manifests as a branch point bifurcation [38]. Consequently, the established detection framework for branch points can be applied to reliably identify PD bifurcations. The downside of this approach is that the minimal period is extended from T to $2T$, and the number of unknowns in the system is effectively doubled. Period doubling bifurcations are detected and discussed in Chapter 3.

2.3.3 Neimark-Sacker

Neimark–Sacker (NS) bifurcations, also known as secondary Hopf bifurcations, occur when a pair of complex conjugate Floquet multipliers exit the unit circle. In terms of Floquet exponents, this corresponds to crossing the imaginary axis at values different from $\pm\frac{i\omega}{2}$. NS bifurcations give rise to a new branch of solutions characterized by quasiperiodic oscillations, defined by a combination of the fundamental frequency ω and at least one secondary frequency ω_2, such that the ratio $\frac{\omega}{\omega_2}$ is irrational. The resulting quasiperiodic branches require a dedicated formulation, and the HBM must be extended to accommodate the additional frequency. This extended formulation is referred to as the Multi-Harmonic Balance Method (MHBM). There is no explicit test function for the detection of NS bifurcations in autonomous systems. However, in the scope of this work, all observed NS bifurcations are accompanied by a change in stability. Therefore, the presence of an NS bifurcation is inferred from a stability change where $\mathrm{Im}(\lambda) \neq 0$, confirmed by the direct observation of the Floquet multipliers [41, 42]. The NS bifurcations and their associated quasiperiodic solutions are not that commonly found in simple, autonomous and conservative systems; they are studied in Chapter 4, where they are found in the vicinity of asteroid 433 Eros.

2.4 Multi-harmonic balance method

While the classical HBM effectively captures periodic motion, multiple nonlinear systems also exhibit quasi-periodic behavior, where two or more incommensurate frequencies coexist. To describe such dynamics, the formulation must be extended to account for multiple interacting frequency components. The multi-harmonic balance method (MHBM) provides this generalization by expressing the solution as a multi-dimensional Fourier expansion over several base frequencies. This approach preserves the core principles of the HBM, projection onto a harmonic basis, frequency-domain residual formulation, and continuation in parameter space, while introducing additional phase conditions to ensure uniqueness and proper handling of the multi-frequency structure. The equations of motion retain the same structure as in equation (2.30).

A quasi-periodic solution can be viewed as motion on a torus spanned by multiple independent frequencies. Each frequency introduces its own harmonic basis, and the full motion is a superposition over all combinations of harmonics of these base frequencies. To account for quasi-periodic solutions involving multiple incommensurate frequencies, the trajectory $\mathbf{x}(t)$ is expressed as a multi-harmonic Fourier series involving N_ω such frequencies ω_i:

$$\mathbf{x}(t) = \prod_{i=1}^{N_\omega} (\mathbf{Q}_i(\omega_i t) \otimes \mathbb{I}_{n_i})\, \mathbf{z} \tag{2.58}$$

Here, $\mathbf{Q}_i(\omega_i t)$ denotes the Fourier basis vector, of size $1 \times (2N_{h_i} + 1)$ associated with the i^{th} frequency component, constructed as

$$\mathbf{Q}_i(\omega_i t) = \left[\tfrac{1}{\sqrt{2}},\ \ \sin(\theta_i),\ \ \cos(\theta_i),\ \ \cdots,\ \ \sin(N_{h_i}\theta_i),\ \ \cos(N_{h_i}\theta_i)\right] \tag{2.59}$$

with the set of torus variables

$$\theta_i = \omega_i t \quad \theta_i \in [0, 2\pi] \tag{2.60}$$

The dimension n_i accounts for the nested structure of the multi-frequency expansion and is defined recursively as

$$n_i = n \prod_{k=1}^{i-1} (2N_{h_k} + 1) \tag{2.61}$$

where n is the number of degrees of freedom of the system and N_{h_k} is the number of harmonics considered for the k^{th} frequency. The Fourier coefficients vector $\mathbf{z}$ is of size n.

Time derivatives of $\mathbf{x}(t)$, the velocity $\dot{\mathbf{x}}(t)$ and the acceleration $\ddot{\mathbf{x}}(t)$, are easily expressed using the Fourier series as

$$\dot{\mathbf{x}}(t) = \sum_{i=1}^{N_\omega} \left(\prod_{j=1}^{N_\omega} (\mathbf{Q}_j(\omega_j t)\boldsymbol{\kappa}_{ji}) \otimes \mathbb{I}_{n_j} \right) \mathbf{z} \tag{2.62}$$

$$\ddot{\mathbf{x}}(t) = \sum_{i=1}^{N_\omega} \sum_{j=1}^{N_\omega} \left(\prod_{k=1}^{N_\omega} (\mathbf{Q}_k(\omega_k t)\boldsymbol{\kappa}_{kj}\boldsymbol{\kappa}_{ki}) \otimes \mathbb{I}_{n_k} \right) \mathbf{z} \tag{2.63}$$

where the derivation operator $\boldsymbol{\kappa}_{ji}$ is

$$\boldsymbol{\kappa}_{ji} = \begin{cases} \boldsymbol{\kappa}_j & \text{if } i = j \\ \mathbb{I}_{2N_{H_j}+1} & \text{if } i \neq j \end{cases}, \quad \boldsymbol{\kappa}_j = \omega_j \begin{bmatrix} 0 & & \mathbf{0} \\ & \begin{bmatrix} 1 & & \\ & \ddots & \\ & & N_{H_j} \end{bmatrix} & \\ \mathbf{0} & & \end{bmatrix} \otimes \boldsymbol{\kappa} \quad \boldsymbol{\kappa} = \begin{bmatrix} 0 & -1 \\ 1 & 0 \end{bmatrix} \tag{2.64}$$

The quasi-periodic motion can be expressed by the N_ω independent torus variables $\theta_i = \omega_i t + \theta_{i,0}$ defining the N_ω-dimensional torus $\mathbb{T}^{N_\omega} = [0, 2\pi]^{N_\omega}$. The state vector can then be regarded as a 2π-periodic function of these angles,

$$\mathbf{x}(t) = \mathbf{X}(\theta_1, \ldots, \theta_{N_\omega}). \tag{2.65}$$

If the base frequencies $\{\omega_i\}$ are rationally independent, time averages along the quasi-periodic trajectory coincide with spatial averages over the torus. Indeed, according to [43], one has

$$\lim_{T\to\infty} \frac{1}{T} \int_0^T F(\omega_1 t, \ldots, \omega_{N_\omega} t)\, dt = \frac{1}{(2\pi)^{N_\omega}} \int_{\mathbb{T}^{N_\omega}} F(\theta_1, \ldots, \theta_{N_\omega})\, d\theta_1 \cdots d\theta_{N_\omega}. \tag{2.66}$$

This equivalence allows the Galerkin procedure to be performed in the orthogonal trigonometric basis $\mathbf{Q}_i$ defined on the torus, as used in Eq. (2.67).

$$\frac{1}{\pi}\int_0^{2\pi} \mathbf{Q}_i^T(\theta_i)\mathbf{Q}_i(\theta_i)\,d\theta_i = \mathbb{I}_{2N_{h_i}+1} \tag{2.67}$$

The Galerkin procedure on the torus consists in enforcing the orthogonality of the residual with respect to all the trigonometric basis functions $\mathbf{Q}_i(\boldsymbol{\theta})$. This condition can be written as the projection integral

$$\frac{1}{(2\pi)^{N_\omega}}\int_{\mathbb{T}^{N_\omega}} \left(\prod_{i=1}^{N_\omega} \mathbf{Q}_i(\theta_i)\otimes\mathbb{I}_{n_i}\right)^T \mathbf{R}(\theta)d\theta = \mathbf{0} \tag{2.68}$$

where $R(\boldsymbol{\theta})$ denotes the residual of the governing equations (2.1). Equation (2.68) is the multidimensional counterpart of the classical Fourier–Galerkin projection used in the periodic HBM, and constitutes the formal definition of the Galerkin procedure in the MHBM framework.

Substituting the truncated Fourier expansions of the state vector and the nonlinear terms into the residual expression, and using the orthogonality of the trigonometric basis on $\mathbb{T}^{N_\omega}$, the above projection leads to a set of algebraic equations for the unknown Fourier coefficients. By arranging these equations in vector form and applying Eqs. (2.58), (2.62), (2.63), and (2.67), together with the mixed-product property of the Kronecker product, the resulting system can be written in the compact matrix form of Eq. (2.69).

$$\left[\sum_{k=1}^{N_\omega}\sum_{j=1}^{N_\omega}\left(\bigotimes_{i=N_\omega}^{1}\boldsymbol{\kappa}_{ij}\boldsymbol{\kappa}_{ik}\right)\otimes\mathbf{M} + \sum_{j=1}^{N_\omega}\left(\bigotimes_{i=N_\omega}^{1}\boldsymbol{\kappa}_{ij}\right)\otimes\mathbf{C} + \left(\bigotimes_{i=N_\omega}^{1}\mathbb{I}_{2N_{H_i}+1}\right)\otimes\mathbf{K}\right]\mathbf{z} + \eta\mathbf{P}(\mathbf{z}) - \mathbf{b}(\mathbf{z}) = 0 \tag{2.69}$$

or in the compact form,

$$\mathbf{A}(\omega_1,\ldots,\omega_{N_\omega})\mathbf{z} + \eta\mathbf{P}(\mathbf{z}) - \mathbf{b}(\mathbf{z}) = \mathbf{h}(\mathbf{z},\omega_1,\ldots,\omega_{N_\omega}) = 0 \tag{2.70}$$

The matrix of the linear dynamics for two frequencies $\mathbf{A}$ is a $n(2N_{H_1}+1)(2N_{H_2}+1)\times n(2N_{H_1}+1)(2N_{H_2}+1)$. As the number of incommensurate frequencies increases, the complexity of the multi-harmonic balance method grows rapidly. Specifically, the size of matrix $\mathbf{A}$ scales with the product of the harmonic orders, resulting in a steep rise in both computational cost and memory usage.

The presence of multiple incommensurate frequencies introduces additional considerations. The main difference lies in the need to account for more than one frequency in the formulation. While the primary frequency is treated as a continuation parameter, the secondary frequency must also be carefully controlled. Each additional frequency introduces another time-shift symmetry on the torus. A corresponding phase condition removes this degeneracy, ensuring that the quasi-periodic solution is uniquely defined. Following the approach proposed by Schilder [44] the phase condition selected minimizes the L2 norm of the difference between the current solution and that of the previous iteration, denoted by $\mathbf{z}_{j-1}$

$$g_i(\mathbf{x}) = \int_{\mathbb{T}_{N^\omega}} \left(\frac{\partial\mathbf{x}_{j-1}(\boldsymbol{\theta})}{\partial\theta_i}\right)^T \mathbf{x}(\boldsymbol{\theta})\,d\boldsymbol{\theta} = 0 \tag{2.71}$$

After the Galerkin procedure the phase condition takes the form:

$$g_i(\mathbf{z}) = \frac{1}{\omega_i}\mathbf{z}_{j-1}^T \left[\left(\bigotimes_{j=N_\omega}^{1} \boldsymbol{\kappa}_{ji}^T\right) \otimes \mathbb{I}_n\right] \mathbf{z} = \mathbf{z}_{j-1}^T \mathbf{U}_i \mathbf{z} = 0 \tag{2.72}$$

The logic behind the fictitious energy added in the classical term is kept unchanged for the MHBM to balance the number of equations and unknowns. It takes the form

$$\mathbf{P}(\mathbf{z}) = \left[\left(\bigotimes_{j=N_\omega}^{1} \boldsymbol{\kappa}_{ji}^T\right) \otimes \mathbb{I}_n\right] \mathbf{z} = \mathbf{U}_i \mathbf{z} \tag{2.73}$$

To facilitate the understanding of Eq. (2.70), and in particular the construction of $\mathbf{A}$, the different elements of equation (2.69) are separated and described for the case of two frequencies

$$\sum_{k=1}^{2}\sum_{j=1}^{2}\left(\bigotimes_{i=2}^{1} \boldsymbol{\kappa}_{ij}\boldsymbol{\kappa}_{ik}\right) \otimes \mathbf{M} = \left[\mathbb{I}_{(2N_{H2}+1)} \otimes (\boldsymbol{\kappa}_1)^2 + 2\,(\boldsymbol{\kappa}_2 \otimes \boldsymbol{\kappa}_1) + (\boldsymbol{\kappa}_2)^2 \otimes \mathbb{I}_{(2N_{H1}+1)}\right] \otimes \mathbf{M} \tag{2.74}$$

$$\sum_{j=1}^{2}\left(\bigotimes_{i=2}^{1} \boldsymbol{\kappa}_{ij}\right) \otimes \mathbf{C} = (\mathbb{I}_{(2N_{H2}+1)} \otimes \boldsymbol{\kappa}_1 + \boldsymbol{\kappa}_2 \otimes \mathbb{I}_{(2N_{H1}+1)}) \otimes \mathbf{C} \tag{2.75}$$

$$\left(\bigotimes_{i=2}^{1} \mathbb{I}_{2N_{H_i}+1}\right) \otimes \mathbf{K} = (\mathbb{I}_{(2N_{H2}+1)} \otimes \mathbb{I}_{(2N_{H1}+1)}) \otimes \mathbf{K} \tag{2.76}$$

The same continuation procedure as outlined on the classical harmonic balance method is applied to solve Eq. (2.70). The core ideas, projection, nonlinear evaluation using AFT, and continuation using pseudo-arclength remain unchanged. However, the components of those operations have to be updated to take into account the additional frequency. It translates into:

$$\boldsymbol{\Gamma}_{\mathrm{QP}} = \mathbb{I}_n \otimes (\tilde{\mathbf{Q}}_2 \otimes \tilde{\mathbf{Q}}_1) \tag{2.77}$$

with

$$\tilde{\mathbf{Q}}_i = \begin{bmatrix} \frac{1}{\sqrt{2}} & \sin(\theta_{i,1}) & \cos(\theta_{i,1}) & \cdots & \sin(N_{H_1}\theta_{i,1}) & \cos(N_{H_1}\theta_{i,1}) \\ \vdots & \vdots & \vdots & \ddots & \vdots & \vdots \\ \frac{1}{\sqrt{2}} & \sin(\theta_{i,N}) & \cos(\theta_{i,N}) & \cdots & \sin(N_{H_1}\theta_{i,N}) & \cos(N_{H_1}\theta_{i,N}) \end{bmatrix} \quad i = 1, 2$$

However, the columns of the matrix $\boldsymbol{\Gamma}_{\mathrm{QP}}$ have to be permuted so that the Fourier coefficients corresponding to each physical degree of freedom are grouped together like it was the case for the classical HBM. This is achieved by multiplying by a permutation matrix $\mathbf{P}$:

$$\boldsymbol{\Gamma}_{\mathrm{QP}} \leftarrow \boldsymbol{\Gamma}_{\mathrm{QP}}\mathbf{P}, \tag{2.78}$$

where $P \in \mathbb{R}^{nN_H \times nN_H}$ with $N_H = (2N_{H_1} + 1)(2N_{H_2} + 1)$, and whose indices are defined such that

$$\mathbf{P}_{q,p} = \begin{cases} 1, & \text{if} \quad q = (j-1)N_H + h, \quad p = (h-1)n + j \\ 0, & \end{cases} \tag{2.79}$$

with $j = 1, ..., n$ and $h = 1, ..., N_H$.

In this reordered form, $\mathbf{\Gamma}_{\mathrm{QP}}$ groups the Fourier coefficients by physical variable rather than by harmonic index, which simplifies the assembly of the harmonic balance equations. With that we retrieve the same formulation as the classical HBM. The rearranged position vector $\tilde{\mathbf{x}}$ is

$$\tilde{\mathbf{x}} = \mathbf{\Gamma}_{\mathrm{QP}}\mathbf{z} \tag{2.80}$$

This operator is similarly employed to project the nonlinear force vector, evaluated in the time domain, into the frequency domain as:

$$\mathbf{b}(\mathbf{z}) = (\mathbf{\Gamma}_{\mathrm{QP}})^{+}\,\tilde{\mathbf{f}} \tag{2.81}$$

and

$$\mathbf{h_z} = \mathbf{A} - \mathbf{\Gamma}^{+}_{\mathrm{QP}}\frac{\partial\tilde{\mathbf{f}}}{\partial\tilde{\mathbf{x}}}\mathbf{\Gamma}_{\mathrm{QP}} \tag{2.82}$$

The correction scheme, based on the Moore-Penrose presented for the HBM, to find the next solution is adapted where $\mathbf{v}_{i+1}$ is still initiated as the tangent vector $\mathbf{t}_i$ obtained by solving

$$\begin{bmatrix}\mathbf{J}(\mathbf{y}_i)\\ \mathbf{g_y}\\ \mathbf{t}_{i-1}^{T}\end{bmatrix}\mathbf{t}_i = \begin{bmatrix}\mathbf{0}\\ 0\\ 1\end{bmatrix} \tag{2.83}$$

with $\mathbf{y}_i = \begin{bmatrix}\mathbf{z}_i^T & \omega_{1_i} & \omega_{2_i} & \eta_i\end{bmatrix}^T$, $\mathbf{J}(\mathbf{y}_i) = \begin{bmatrix}\mathbf{h_z} & \mathbf{h}_{\omega_1} & \mathbf{h}_{\omega_2} & \mathbf{h}_{\eta}\end{bmatrix}$ and $\mathbf{g_y} = \begin{bmatrix}\mathbf{g_{1_z}} & 0 & 0 & 0\\ \mathbf{g_{2_z}} & 0 & 0 & 0\end{bmatrix}$

The Moore-Penrose scheme for the correction is identical to the HBM one, described in equations (2.37)-(2.41).

2.4.1 Stability

Up until recently, the stability of quasi-periodic solutions was evaluated using an extended classical monodromy matrix algorithm, which computes the Floquet multipliers [45]. However, this method can be quite time-consuming due to the need for solving a large number of eigenvalue problems, making it less efficient for large-scale systems. As an alternative, the method of Hill's equations, as presented in the previous section, can be adapted to handle quasi-periodic solutions [23].

The method involves slightly perturbing the quasi-periodic solution, $\mathbf{x}^*(t)$, with a small perturbation of the form $\mathbf{l}e^{\lambda t}$:

$$\mathbf{x}(t) = \mathbf{x}^*(t) + \mathbf{l}e^{\lambda t} \tag{2.84}$$

This newly perturbed quasi-periodic solution is reintroduced in Eq.(2.30) yields

$$\mathbf{M}\ddot{\mathbf{x}}^* + \mathbf{C}\dot{\mathbf{x}}^* + \mathbf{K}\mathbf{x}^* + \left(\lambda^2\mathbf{M}\mathbf{l} + \lambda\left(2\mathbf{M}\dot{\mathbf{l}} + \mathbf{C}\mathbf{l}\right) + \mathbf{M}\ddot{\mathbf{l}} + \mathbf{C}\dot{\mathbf{l}} + \mathbf{C}\mathbf{l}\right)e^{\lambda t} = \mathbf{f}_{nl}\left(\mathbf{x}^*(t) + \mathbf{l}e^{\lambda t}\right) \tag{2.85}$$

Using Fourier series and a Galerkin procedure as previously done Eq.(2.85) is recast in the frequency domain with $\mathbf{z}^*$ and $\mathbf{r}$ the vectors of Fourier coefficients associated to $\mathbf{x}^*$ and $\mathbf{L}$ respectively.

$$\mathbf{A}(\omega_1,\ldots,\omega_{N_\omega})\mathbf{z}^* + \left(\lambda^2\boldsymbol{\Delta}_2 + \lambda\boldsymbol{\Delta}_1 + \mathbf{A}(\omega_1,\ldots,\omega_{N_\omega})\right) e^{\lambda t}\mathbf{r}^* - \mathbf{b}\left(\mathbf{z}^* + e^{\lambda t}\mathbf{r}\right) = 0 \quad (2.86)$$

Following the same procedure as the classical Hill's method, the Hill's coefficient λ for quasi-periodic solutions are the results of the quadratic eigenvalue problem

$$\left(\lambda^2\boldsymbol{\Delta}_2 + \lambda\boldsymbol{\Delta}_1 + \mathbf{h_z}\right)\mathbf{r} = \mathbf{0} \quad (2.87)$$

where $\mathbf{h_z}$ is the Jacobian of Eq.(2.70) computed during the continuation process, and $\boldsymbol{\Delta}_2$ and $\boldsymbol{\Delta}_1$ are respectively :

$$\boldsymbol{\Delta}_2 = \mathbb{I}_{\left(2N_{H_1}+1\right)\times\left(2N_{H_2}+1\right)} \otimes \mathbf{M} \quad (2.88)$$

$$\boldsymbol{\Delta}_1 = \left(\left(\left(\mathbb{I}_{\left(2N_{H_1}+1\right)} \otimes 2\nabla_1\right) + \left(\, 2\nabla_2 \otimes \mathbb{I}_{\left(2N_{H_2}+1\right)}\right)\right) \otimes \mathbf{M}\right)\nabla + \mathbb{I}_{\left(2N_{H_1}+1\right)\times\left(2N_{H_2}+1\right)} \otimes \mathbf{C} \quad (2.89)$$

Similar to the periodic case, the quadratic eigenvalue problem can be transformed into a linear eigenvalue problem using the same approach. However, despite the problem becoming linear, the size of the eigenvalue problem is effectively doubled, which can be problematic given the already large matrix dimensions. The Floquet exponents are then determined by selecting the eigenvalues with the smallest imaginary parts.

2.5 Branching

Once a bifurcation is localized and identified, a branching technique can be applied to transition from the main branch to the secondary one. At a branch point, period doubling or Neimark-Sacker bifurcation, the uniqueness of the tangent vector $\mathbf{t}_i$, is no longer guaranteed; two distinct tangents exist, corresponding to the main and secondary branches. At this point, there exist two independent vectors $\boldsymbol{\phi} = [\boldsymbol{\phi}_1, \boldsymbol{\phi}_2]$ solutions of $\mathbf{h_y}\phi = 0$ with $\mathbf{y} = [\mathbf{z}, \omega]$ and one left eigenvector ϕ_g to $\mathbf{h_y}$ such that $\mathbf{h}_\mathbf{y}^T\phi_g = 0$ exists at the bifurcation. At a bifurcation point, the Jacobian matrix of the system becomes singular, resulting in a nontrivial nullspace. The first-order tangent vector $\mathbf{y_1}$, which satisfies $\mathbf{h_y y_1} = 0$, lies within this nullspace and corresponds to a direction in which the system is locally insensitive. However, this condition alone does not distinguish between the continuation of the original solution branch and the emergence of a secondary branch. Additionally, since $\mathbf{h_z}$ remains singular, it is regularized with respect to $\boldsymbol{\varphi}_1 = (\nabla \otimes \mathbb{I}_n)\,\mathbf{z}$ such that

$$\bar{\mathbf{h}}_\mathbf{z} = (\mathbf{h_z} + \boldsymbol{\varphi_1}\boldsymbol{\varphi}_\mathbf{1}^*)$$

To resolve this ambiguity, a second-order expansion of the solution $\mathbf{y}$ with respect to the pseudo-arclength parameter ξ is introduced:

$$\begin{aligned} \mathbf{y} &= \mathbf{y_0} + \xi\mathbf{y}_1 + \xi^2\mathbf{y}_2 \\ \mathbf{h}(\mathbf{y}) &= \mathbf{h}(\mathbf{y_0}) + \xi\bar{\mathbf{h}}_\mathbf{y}\mathbf{y}_1 + \xi^2\left(\bar{\mathbf{h}}_\mathbf{y}\mathbf{y}_2 + \bar{\mathbf{h}}_\mathbf{yy}\mathbf{y}_1\mathbf{y}_1\right) \end{aligned} \quad (2.90)$$

where $\mathbf{y}_0$ is the $(\mathbf{z}, \omega)$ at the bifurcation point, $\mathbf{y}_1$ is the first-order tangent, and $\mathbf{y}_2$ represents the curvature of the solution path. The terms of order ξ^2 are

$$\bar{\mathbf{h}}_\mathbf{y}\mathbf{y}_2 + \bar{\mathbf{h}}_\mathbf{yy}\mathbf{y}_1\mathbf{y}_1 = 0 \quad (2.91)$$

The inclusion of the second-order term is therefore essential to uniquely determine the continuation direction and ensure the trajectory departs from the original branch. Without it, the first-order information would be insufficient, as it fails to distinguish between multiple admissible paths at the bifurcation point. Equation (2.91) is multiplied by $\boldsymbol{\phi}_g^T$ resulting in

$$\boldsymbol{\phi}_g^T \left(\overline{\mathbf{h}}_{\mathbf{zz}} \mathbf{z_1} \mathbf{z_1} + \overline{\mathbf{h}}_{\mathbf{z}\omega} \mathbf{z_1} \omega_\mathbf{1} + \overline{\mathbf{h}}_{\omega\omega} \omega_1 \omega_1 \right) = 0 \tag{2.92}$$

The solution $(\mathbf{z_1}, \omega_\mathbf{1})$ is then expressed as a linear combination of two independent vectors $\boldsymbol{\phi} = (\boldsymbol{\phi}_1, \boldsymbol{\phi}_2)$, where $\boldsymbol{\phi}_1$ corresponds to the null eigenvector of the Jacobian and $\boldsymbol{\phi}_2$ is the displacement part $\Delta\mathbf{z}$ of the tangent obtained at the previous step

$$(\mathbf{z_1}, \omega_\mathbf{1}) = (\boldsymbol{\phi}_1 + \alpha \boldsymbol{\phi}_2, \alpha) \tag{2.93}$$

Substituting this expression into Eq. (2.92) yields a scalar quadratic equation in the parameter α:

$$a\alpha^2 + b\alpha + c = 0 \tag{2.94}$$

with

$$\begin{aligned} a &= \boldsymbol{\phi}_g^T \left(\left(\overline{\mathbf{h}}_\mathbf{z} \boldsymbol{\phi}_2 \right)_\mathbf{z} \boldsymbol{\phi}_2 + 2 \left(\overline{\mathbf{h}}_\mathbf{z} \boldsymbol{\phi}_2 \right)_\omega + \overline{\mathbf{h}}_{\omega\omega} \right) \\ b &= \boldsymbol{\phi}_g^T \left(\left(\overline{\mathbf{h}}_\mathbf{z} \boldsymbol{\phi}_1 \right)_\mathbf{z} \boldsymbol{\phi}_2 + \left(\overline{\mathbf{h}}_\mathbf{z} \boldsymbol{\phi}_1 \right)_\omega \right) \\ c &= \boldsymbol{\phi}_g^T \left(\overline{\mathbf{h}}_\mathbf{z} \boldsymbol{\phi}_1 \right)_\mathbf{z} \boldsymbol{\phi}_1 \end{aligned} \tag{2.95}$$

α is then simply obtained by:

$$\begin{aligned} \alpha_1 &= \frac{-b + \sqrt{b^2 - ac}}{a} \\ \alpha_2 &= \frac{-b - \sqrt{b^2 - ac}}{a} \end{aligned} \tag{2.96}$$

In the scenario where $c = 0$ the branch point is a pitchfork point, otherwise it is a transcritical point. Introducing α into Eq. (2.93) give the direction of the new tangent leading to the emerging branch.

The branching technique for the period doubling bifurcations is similar since, as stated in the previous section, the introduction of the subharmonics in the Fourier decomposition changes the nature of the bifurcation. Neimark-Sacker bifurcations are characterized by a pair of complex-conjugate Floquet exponents, λ and λ^*, for which $\Re(\lambda) = 0$ and $\frac{\partial \Re(\lambda)}{\partial \omega} \neq 0$. The eigenvector $\mathbf{v}$ associated with λ can be interpreted as the unstable mode that grows over time [46]. This allows for the construction of a predictor $\Delta\mathbf{z}$ as follows:

$$\Delta\mathbf{z} = \begin{bmatrix} \mathbf{0} \\ -\text{sign}(\Im(\lambda)) \Im(\mathbf{v}) \\ \Re(\mathbf{v}) \\ \mathbf{0} \end{bmatrix} \tag{2.97}$$

The additional frequency is then estimated by the imaginary part of λ.

2.6 Validation case - Two-degree-of-freedom system

To illustrate the results and evaluate the robustness of the approach, a simple two-degree-of-freedom autonomous and conservative system featuring cubic stiffness, shown in Fig.2.4, is selected as a test case. The system parameters, listed in Table 2.1, are chosen in alignment with values used in previous studies such as [47] and [34].

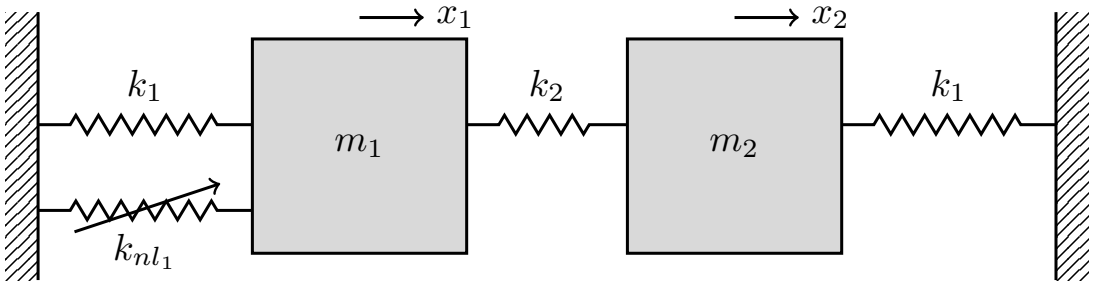

Figure 2.4: Schematic of the two-degrees-of-freedom system.

The system studied is characterized by the following matrices:

$$\mathbf{M} = \begin{bmatrix} 1 & 0 \\ 0 & 1 \end{bmatrix}, \quad \mathbf{K} = \begin{bmatrix} k_1 + k_2 & -k_2 \\ -k_2 & k_1 + k_2 \end{bmatrix} \text{ and } \mathbf{f}_{nl} = \begin{bmatrix} -k_{nl_1} x_1^3 \\ 0 \end{bmatrix}.$$

Table 2.1: Parameters for the 2 DOFs sytem.

$k_1(N/m)$	$k_2(N/m)$	$k_{nl_1}(N/m^3)$
1	1	0.5

Using the prediction–correction scheme presented in section 2.2.5, the full frequency response curve of the nonlinear autonomous system can be traced. Figure 2.5 illustrates the amplitude–frequency backbone curve of the first nonlinear normal mode (NNM) for a two-degree-of-freedom system. In the context of nonlinear dynamics, NNMs generalize the concept of classical linear normal modes to systems exhibiting nonlinear stiffness or coupling. In linear systems, normal modes represent simple harmonic oscillations at distinct natural frequencies, where all degrees of freedom move proportionally. When nonlinearities are present, this proportional motion no longer holds, and the oscillation frequency becomes amplitude-dependent. NNMs are periodic motions in which all parts of the system oscillate in a coordinated manner. The variable of interest is the amplitude of the first coordinate $\mathbf{x}_1$, obtained using $N_H = 15$ harmonics [47].

As the frequency grows, the amplitude increases up to a certain point where the solution loops on itself before increasing again. This loop corresponds to a 3:1 internal resonance, where the in-phase and out-of-phase nonlinear normal modes interact through a harmonic coupling, allowing energy exchange between them. A detailed description of this resonance mechanism and its manifestation in the frequency–energy plot can be found in Kerschen [47].

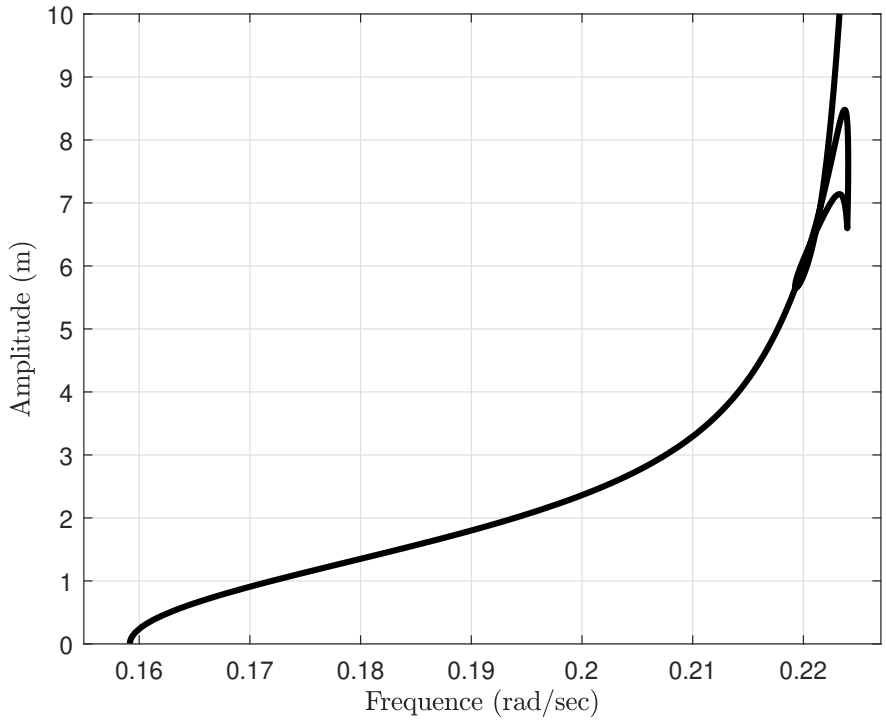

Figure 2.5: Amplitude-frequency backbone curve for the first NNM of the 2-DOF system.

Importance of the amount of harmonics

The essence of the HBM lies in the Fourier decomposition, which imposes the periodicity of the solution. However, it can suffer from accuracy loss if the number of harmonics selected, N_H, is too low. Figure 2.6 highlights the differences between five solutions computed with increasing numbers of harmonics. The cases with low harmonics, $N_H = 3$, $N_H = 5$, and $N_H = 10$, produce clearly distinct results. For $N_H = 15$ and $N_H = 20$, the curves are identical, indicating that the additional harmonics do not further improve the accuracy.

Adaptive harmonic balance method

Figure 2.7 compares the reference solution with the AHBM result using $\epsilon_{\text{AHBM}} = 10^{-4}$. The reference solution required approximately 0.128 s per converged point, whereas the AHBM solution required 0.105 s, yielding a 17% speed-up.[1] It is important to note that if ϵ_{AHBM} is set too restrictively, essential harmonics may be erroneously filtered out. This can lead to incomplete harmonic representations and ultimately prevent convergence of the solution.

Stability and bifurcation detection

Figure 2.8 illustrates the evolution of the system's stability together with the results of the bifurcation detection techniques. Three distinct branch points are identified, each corresponding to a stability change and the emergence of a new family of periodic solutions.

[1]Computation performed on MATLAB R2020a, Intel i9-9900K @ 3.60GHz, with 32GB RAM.

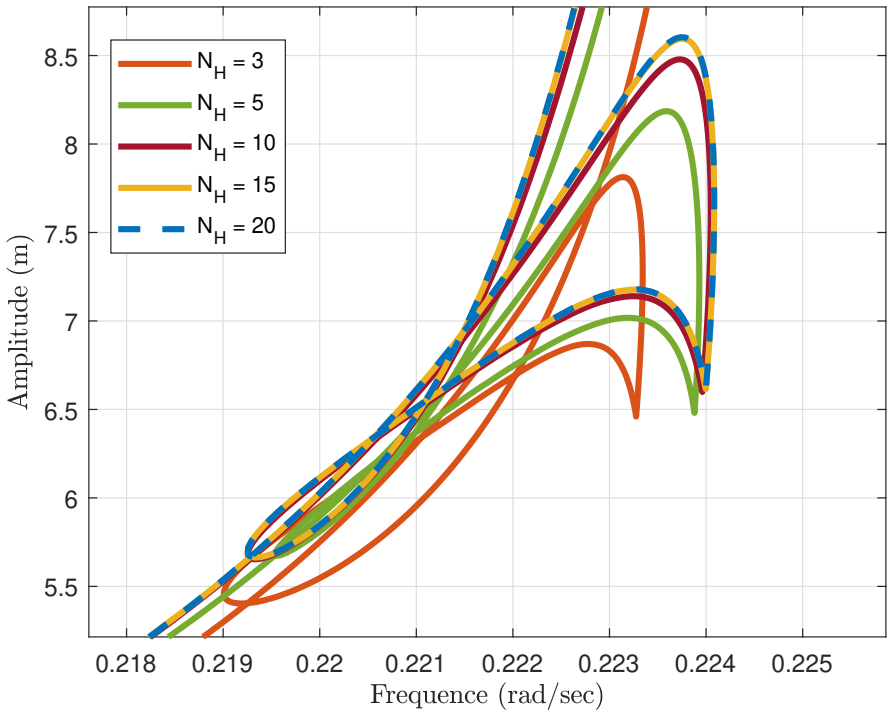

Figure 2.6: Comparison of the frequency-amplitude response for different amounts of harmonics.

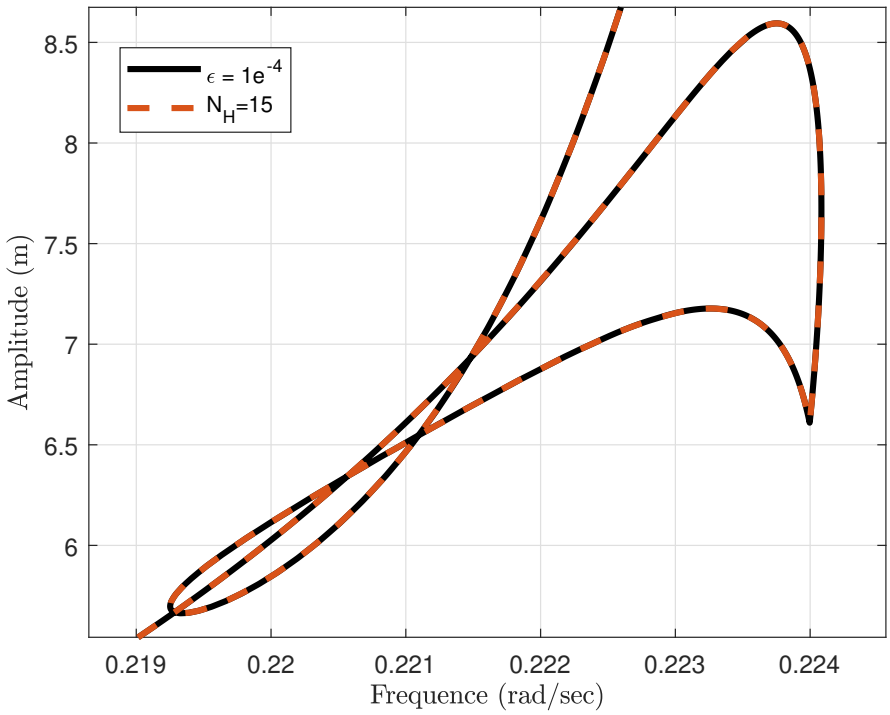

Figure 2.7: Comparison of the frequency-amplitude response with the AHBM.

Additional stability transitions are also observed, associated with fold bifurcations, which do not give rise to new branches but mark local turning points in the continuation. The

detected branch points are highlighted by blue squares in the figure.

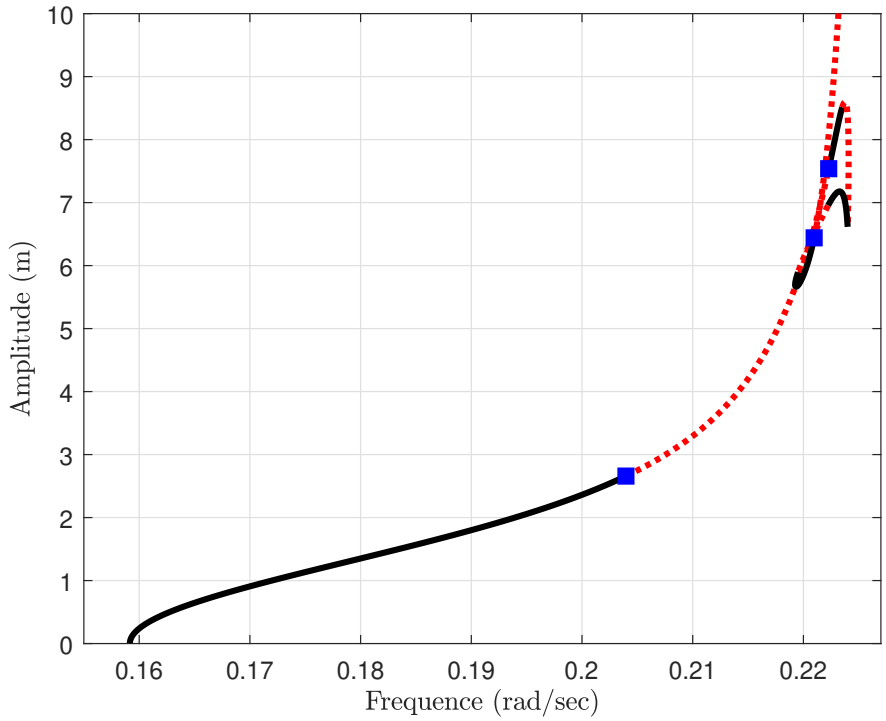

Figure 2.8: Stability (stable in black, unstable in dashed red) and bifurcations of the 2-DOF system.

Branching

The application of the branching procedure to the various branch points identified in Figure 2.8 reveals a more detailed view of the system's dynamical landscape, as illustrated in Figure 2.9. Each newly traced branch corresponds to a family of periodic solutions emerging from a detected bifurcation, thereby enriching the global map of the nonlinear response. When combined with the stability analysis, this representation provides a comprehensive picture of how stability alternates between branches along the continuation, highlighting regions of stable and unstable motion and their interconnections.

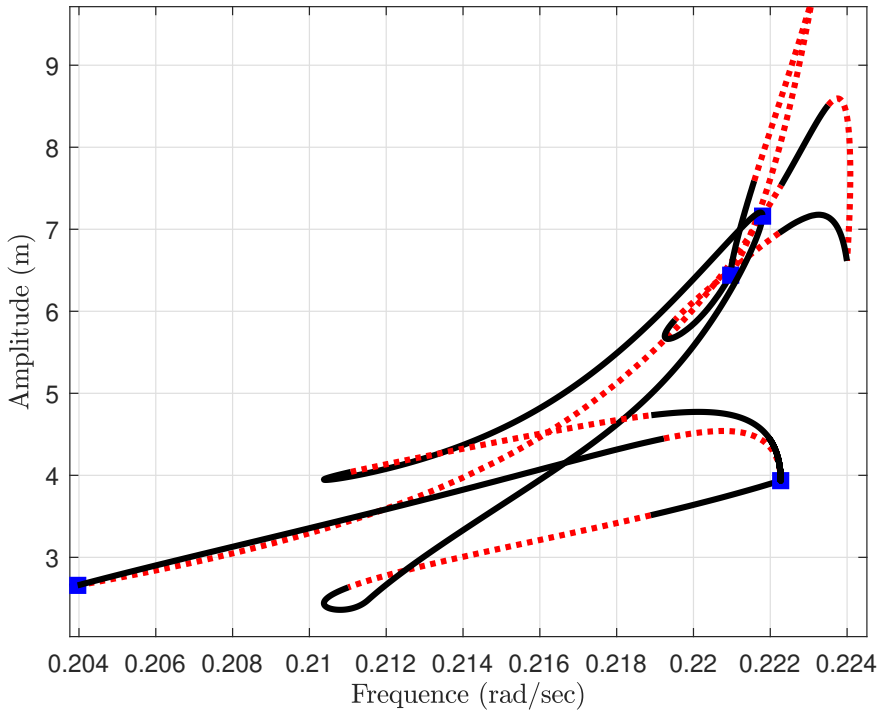

Figure 2.9: Emerging branches from the different bifurcations.

2.7 Conclusion

In this chapter, the harmonic balance method (HBM) was developed and applied to the computation of periodic solutions in autonomous and conservative nonlinear systems. Particular attention was devoted to the selection of harmonics, with an adaptive strategy introduced to retain only those contributing meaningfully to the solution throughout the continuation process. The stability of these periodic solutions was assessed using Hill's method, enabling the systematic detection of bifurcations within a representative 2-DOF mechanical system.

Among the bifurcations identified, branch points were found to generate new solution families, which were successfully explored using a dedicated branching algorithm. While period doubling and Neimark–Sacker bifurcations were not encountered during the continuation of this example, their theoretical foundation and associated branching strategies were established in anticipation of more complex systems.

The methodologies developed here, harmonic balance, adaptive harmonic selection, stability analysis via Floquet theory, and bifurcation tracking, form a robust and extensible framework. Though presented in the context of a simple mechanical system, these tools are directly transferable to higher-dimensional dynamical systems. In particular, they pave the way for the investigation of rich and intricate solution structures in astrodynamical models such as the circular restricted three-body problem (CRTBP). Chapter 2 thus serves as a foundational step toward the application of harmonic balance techniques to celestial mechanics. It establishes not only the computational tools but also the theoretical insight necessary to construct global bifurcation maps of periodic orbits in multi-body gravitational environments.

Chapter 3

Application to the circular restricted three-body problem

3.1 Introduction

The circular restricted three-body problem (CRTBP) has been a long-standing topic of interest for both mathematicians and physicists, offering a solid framework for understanding how celestial bodies move under mutual gravitational influence. Early thinkers like Newton, Euler, Lagrange, and Poincaré made key contributions that still influence current research. Newton laid out the equations for the general n-body problem, while Euler simplified things by ignoring the mass of a third body, leading to the restricted version. Lagrange identified five special equilibrium points, now named after him, and Poincaré brought a new perspective by showing that the CRTBP is not integrable, discovering periodic orbits, and laying the groundwork for dynamical systems theory [48]. These ideas, while originally theoretical, have become highly relevant with the rise of space exploration. For example, the SOHO mission uses the L_1 point between the Earth and Sun to maintain an uninterrupted view of the Sun [49]. Similarly, the James Webb Space Telescope operates near the L_2 point, where it benefits from a stable thermal environment thanks to Earth's shadow, allowing it to perform sensitive observations.

Modern computational tools have pushed CRTBP research even further. Numerical techniques like continuation methods have made it possible to explore entire families of periodic orbits [50]. Henon's classic studies [51, 52] were especially impactful, exploring different mass ratios (including Earth-Moon) and delving into stability and bifurcations. This work was continued by others who mapped out various families of orbits and how they are connected [53, 54, 55]. A more recent overview by Zhang et al. highlights just how active this area of research remains [56].

One key area of focus is understanding how periodic orbit families behave, especially their stability and how they branch off through bifurcations. Papadakis et al. [57] studied this near L_4 and L_5, while Howell and colleagues looked at the Sun-Earth/Moon setup [58]. Later on, Dichmann et al. examined the bifurcation structure around the collinear points L_1, L_2, and L_3 [59]. Tools like `AUTO` have played an important role in helping researchers trace these connections [60]. More recently, Grebow et al. improved methods for predicting initial conditions and detecting bifurcations, streamlining orbit calculations [50].

Within the broader set of periodic orbits, resonant orbits are especially interesting. Resonance occurs when orbiting bodies interact gravitationally in such a way that their orbital periods form simple ratios like $m : n$ [61]. A famous example is the Galilean moons of Jupiter: Io, Europa, and Ganymede are locked in a $1 : 2 : 4$ resonance. These types of resonances aren't just limited to our solar system; they're also found in many exoplanetary systems.

The stability of resonant orbits in the CRTBP has been extensively studied in various contexts to develop transfer orbits [62, 63, 64]. In particular, the case of a planetary $2 : 1$ resonance was examined by [65], and this work was subsequently extended to additional cases in [66]. Resonances are of significant practical interest beyond their theoretical implications, particularly in mission design and planning [67, 68, 69] For example, the extension of the IBEX (Interstellar Boundary Explorer) mission involved a maneuver to place the spacecraft in a $3 : 1$ resonance with the Moon [70]. Similarly, the TESS (Transiting Exoplanet Survey Satellite) mission currently operates in a $2 : 1$ resonant orbit with the Moon [71]. This specific orbital choice is intended to minimize exposure to high radiation doses and reduce the duration of eclipse periods.

3D resonant periodic orbits have been investigated as transfer trajectories between resonant periodic orbits and orbits associated to liberation points of the Earth-Moon system [72]. More recently, Peng et al. [73], presented an analysis on 3D 3:1 and 3:2 resonant orbits to connect L3 and L5 Lagrange points in the CRTBP. Recent studies by Pan & Hou [74, 75] demonstrated the breakup and recombination of interior and exterior resonant periodic orbits as the mass ratio μ increases, ranging from the Sun-Earth CRTBP to the Sun-Jupiter case. Additionally, [76], briefly discussed the bifurcations and stability of exterior resonant families in the Earth-Moon system. Antoniadou also performed continuation of resonant orbits for the 3:2, 5:2, 3:1, 4:1 and 5:1 resonant periodic orbits in the CRTBP and the ERTBP (Elliptic restricted three body problem) [77].

Numerical methods evolved and improved the accuracy of the results proposed during the last years. The first numerical methods were based on initial conditions of the two-body problem, which is equivalent to the CRTBP where the mass of one of the bodies is set to 0. Slightly increasing its mass allowed to obtain conclusive results [78]. Broucke et al. presented a grid search method [79] that is still relevant nowadays, with Restrepo in 2017, who provided a database of many periodic orbits obtained with the grid search [80]. Recently, Akiyama et al. presented a numerical method based on the centered manifold theorem coupled with a correction scheme to compute periodic and quasi-periodic orbits [81]. More recently, with the rise of AI in computer science, Gil et al. [82], proposed a method including neural networks to obtain periodic orbits in the CRTBP. On a side note, a modified version of the harmonic balance method (HBM), known as the reconstructed HBM, has been used to compute some periodic orbits in the CRTBP [83, 84].

This chapter introduces the dynamics of the CRTBP coupled with the HBM to the well-established astrodynamic problem. Section 3.2 outlines the equations of motion that govern the CRTBP, detailing the positions and stability of equilibrium points, as well as introducing the concept of the Jacobi constant. Periodic orbits around these equilibrium points are computed using the HBM, with results discussed in Section 3.3. This section

also revisits concepts introduced in Chapter 1, including the stability of orbits, detection of bifurcations, and branch switching. Additionally, the chapter examines switching that occurs as a result of period-doubling (PD) bifurcations. Results are compared with the ones obtained thanks to `AUTO` software, providing an efficient validation tool. Section 3.4 provides a comprehensive analysis of resonant orbits with various ratios, computed using the HBM. Finally, Section 3.6 presents the conclusions drawn from this chapter.

3.2 Problem Statement

3.2.1 Equations of motion

The CRTBP examines the motion of a small body of mass m, referred to as the tertiary, relative to two primary bodies of masses m_1 and m_2. This specific case of the three-body problem is characterized by two key assumptions:

1. The mass of the first primary is larger than that of the second, $m_1 > m_2$ while the mass m is considered negligible compared to the primaries.

2. The two primaries move in circular orbits around their common center of mass, denoted as $\mathbf{O}$.

A schematic representation of the CRTBP is shown in Figure 3.1. In this framework $\mathbf{R}$ represents the position of the tertiary relative to $\mathbf{O}$, which is defined as the origin of the rotating coordinate system $\{\mathbf{x}, \mathbf{y}, \mathbf{z}\}$. The $\mathbf{x}$ axis points towards m_2, the $\mathbf{y}$ axis lies in the orbital plane, and the $\mathbf{z}$ axis is aligned with the angular momentum vector $\mathbf{\Omega} = \omega\mathbf{z}$. Additionally, $\mathbf{R}_1$ and $\mathbf{R}_2$ denote the positions of the tertiary relative to m_1 and m_2, respectively, and the distance between the primaries is given by R_{12}. The motion of the tertiary is governed by Newton's laws of motion.

$$m\frac{d^2\mathbf{R}}{dt^2} = -\frac{Gmm_1}{\|\mathbf{R}_1\|^3}\mathbf{R}_1 - \frac{Gmm_2}{\|\mathbf{R}_2\|^3}\mathbf{R}_2 \tag{3.1}$$

where G is the universal gravitational constant. Equation (3.1) is nondimensionalized using characteristic scales for mass, length, and time. The characteristic length, L_c, is chosen as the distance between the primaries, R_{12} while the characteristic mass, M_c, is the sum of the masses of the primaries, $m_1 + m_2$. The characteristic time, t_c, is then defined in terms of these characteristic values as:

$$t_c = \sqrt{\frac{L_c^3}{GM_c}}$$

By introducing these characteristic quantities into equation (3.1), the equation can be rewritten in a dimensionless form, yielding:

$$\frac{d^2\mathbf{r}}{d\tau^2} = -\frac{1-\mu}{\|\mathbf{r}_1\|^3}\mathbf{r}_1 - \frac{\mu}{\|\mathbf{r}_2\|^3}\mathbf{r}_2 \tag{3.2}$$

where $\mu = \frac{m_2}{m_1+m_2}$ is the mass ratio, $\mathbf{r}$, $\mathbf{r}_1$, and $\mathbf{r}_2$ are the dimensionless positions, and τ is the dimensionless time. In the particular case of the Earth-Moon, $\mu = 0.01215058$.

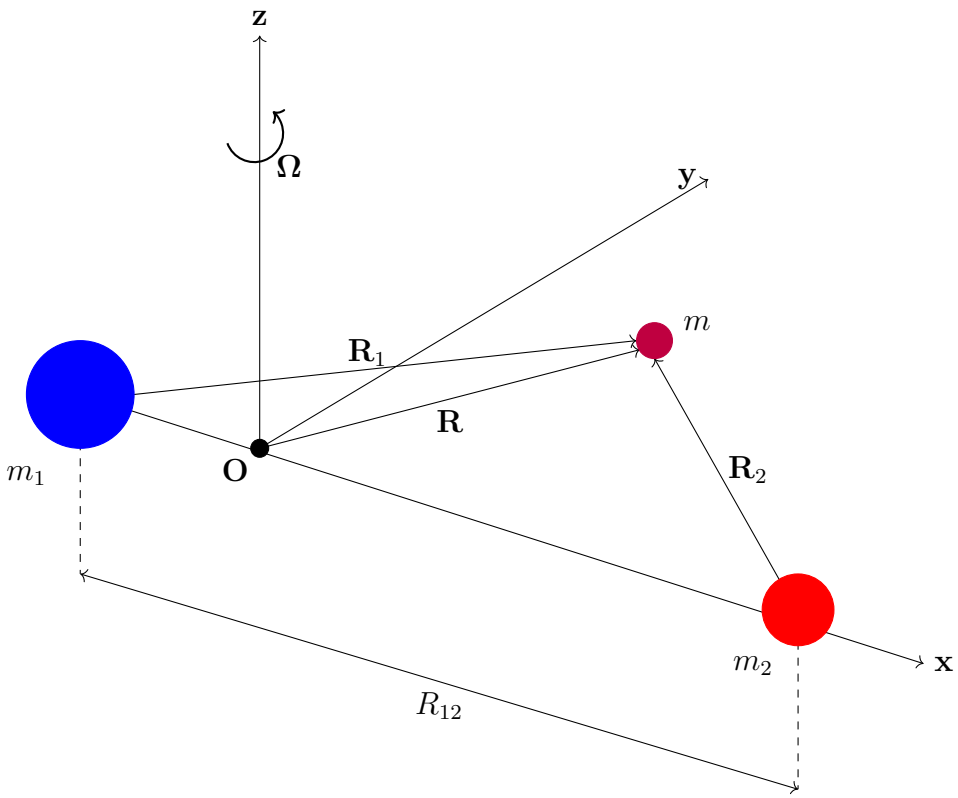

Figure 3.1: Schematic of the Circular Restricted Three-Body Problem.

The second derivative of the position with respect to the dimensionless time in the rotating frame is given by

$$\frac{d^2\mathbf{r}}{d\tau^2} = (\ddot{x} - 2\dot{y} - x)\mathbf{x} + (\ddot{y} + 2\dot{x} - y)\mathbf{y} + z\mathbf{z} \tag{3.3}$$

Since the dimensionless angular velocity Ω is equal to 1, the equations of motion of the tertiary in the rotating frame can be expressed in scalar form as shown in equations (3.4) – (3.6).

$$\ddot{x} - 2\dot{y} - x = -\frac{(1-\mu)(x+\mu)}{\|\mathbf{r}_1\|^3} - \frac{\mu(x-(1-\mu))}{\|\mathbf{r}_2\|^3} \tag{3.4}$$

$$\ddot{y} + 2\dot{x} - y = -\frac{(1-\mu)y}{\|\mathbf{r}_1\|^3} - \frac{\mu y}{\|\mathbf{r}_2\|^3} \tag{3.5}$$

$$\ddot{z} = -\frac{(1-\mu)z}{\|\mathbf{r}_1\|^3} - \frac{\mu z}{\|\mathbf{r}_2\|^3} \tag{3.6}$$

with $\|\mathbf{r}_1\| = \sqrt{(x+\mu)^2 + y^2 + z^2}$ and $\|\mathbf{r}_2\| = \sqrt{(x-(1-\mu))^2 + y^2 + z^2}$.

Equations (3.4)-(3.6) can be recast in the HBM formalism introduced in the previous chapter as

$$\mathbf{M} = \begin{bmatrix} 1 & 0 & 0 \\ 0 & 1 & 0 \\ 0 & 0 & 1 \end{bmatrix}, \quad \mathbf{C} = \begin{bmatrix} 0 & -2 & 0 \\ 2 & 0 & 0 \\ 0 & 0 & 0 \end{bmatrix}, \quad \mathbf{K} = \begin{bmatrix} -1 & 0 & 0 \\ 0 & -1 & 0 \\ 0 & 0 & 0 \end{bmatrix} \text{ and } \mathbf{f}_{nl} = \begin{bmatrix} -\frac{(1-\mu)(x+\mu)}{\|\mathbf{r}_1\|^3} - \frac{\mu(x-(1-\mu))}{\|\mathbf{r}_2\|^3} \\ -\frac{(1-\mu)y}{\|\mathbf{r}_1\|^3} - \frac{\mu y}{\|\mathbf{r}_2\|^3} \\ -\frac{(1-\mu)z}{\|\mathbf{r}_1\|^3} - \frac{\mu z}{\|\mathbf{r}_2\|^3} \end{bmatrix}.$$

3.2.2 The equilibrium points

The equations of motion (3.4) – (3.6) do not admit a general analytical solution. However, there exist five equilibrium points where both acceleration and velocity vanish. These equilibrium points, known as the Lagrange points (x_L, y_L, z_L), satisfy equations (3.7) – (3.9)

$$-x_L = -\frac{(1-\mu)(x_L+\mu)}{\|\mathbf{r}_1\|^3} - \frac{\mu(x_L-(1-\mu))}{\|\mathbf{r}_2\|^3} \tag{3.7}$$

$$-y_L = -\frac{(1-\mu)y_L}{\|\mathbf{r}_1\|^3} - \frac{\mu y_L}{\|\mathbf{r}_2\|^3} \tag{3.8}$$

$$0 = -\frac{(1-\mu)z_L}{\|\mathbf{r}_1\|^3} - \frac{\mu z_L}{\|\mathbf{r}_2\|^3} \tag{3.9}$$

From equation (3.9), the only solution is $z_L = 0$, indicating that all Lagrange points lie within the orbital plane. For equation (3.8) two cases arise, $y_L \neq 0$ and $y_L = 0$.

Case 1: $y_L \neq 0$

When $y_L \neq 0$, equation (3.8) simplifies to

$$1 = \frac{(1-\mu)}{\|\mathbf{r}_1\|^3} + \frac{\mu}{\|\mathbf{r}_2\|^3} \tag{3.10}$$

which is immediately satisfied when $\|\mathbf{r}_1\| = \|\mathbf{r}_2\| = 1$.Substituting the expressions for $\|\mathbf{r}_1\|$ and $\|\mathbf{r}_2\|$ in terms of (x_L, y_L, z_L) gives the coordinates of the two equilateral Lagrange points, L_4 and L_5

$$x_L = \frac{1}{2} - \mu, \quad y_L = \pm\frac{\sqrt{3}}{2}.$$

Case 2: $y_L \neq 0$

When $y_L = 0$, only equation (3.7) remains to be solved. This yields three solutions, L_1, L_2, L_3 referred to as the collinear Lagrange points. Their positions depend on the values of $\|\mathbf{r}_1\|^3$ and $\|\mathbf{r}_2\|^3$, which are determined numerically. The positions of these points relative to the mass ratio μ are illustrated in Figure 3.2, which shows the Lagrange points for the Earth-Moon system ($\mu = 0.01215058$)

Stability of the Lagrange points

To analyze the stability of the Lagrange points, the equations of motion are linearized around each point by introducing small perturbations:

$$\begin{aligned} x(t) &= x_L + \epsilon(t) \\ y(t) &= y_L + \eta(t) \end{aligned} \tag{3.11}$$

Substitution into the full equations of motion (3.4)–(3.5) yields:

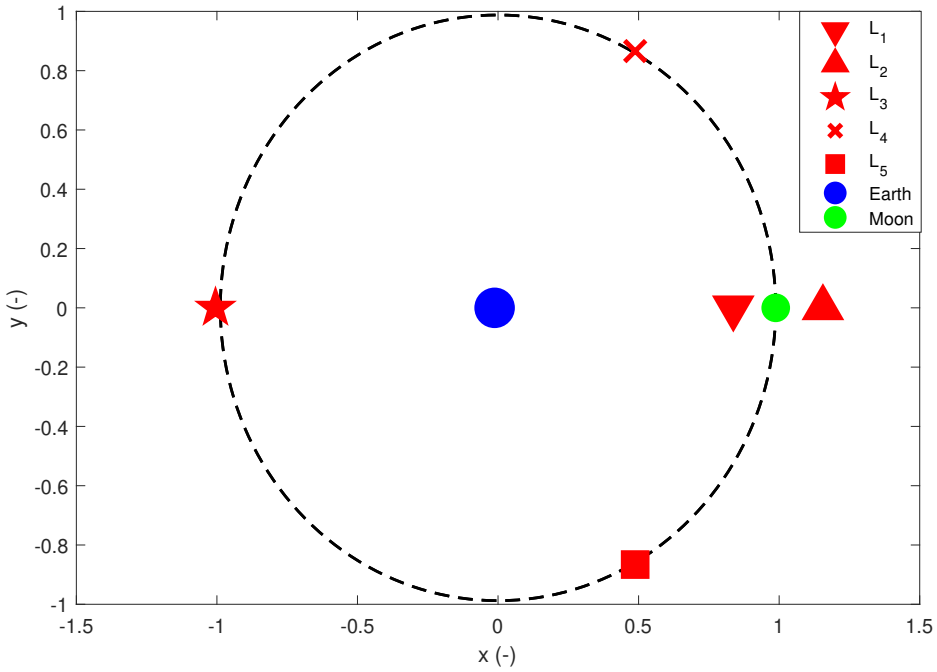

Figure 3.2: Position of the Lagrange points in the Earth-Moon CRTBP ($\mu = 0.01215058$).

$$\ddot{\epsilon} - 2\dot{\eta} = \frac{\partial \Gamma(x_L + \epsilon, y_L + \eta)}{\partial x} \tag{3.12}$$

$$\ddot{\eta} + 2\dot{\epsilon} = \frac{\partial \Gamma(x_L + \epsilon, y_L + \eta)}{\partial y} \tag{3.13}$$

where $\Gamma(x, y) = \frac{1}{2}(x^2 + y^2) + \frac{1-\mu}{\|\mathbf{r}_1\|} + \frac{\mu}{\|\mathbf{r}_2\|}$ is the effective potential (pseudo-potential) in the rotating reference frame.

Expanding the right-hand sides using a Taylor series around the equilibrium points (x_L, y_L), and retaining only first-order terms, gives:

$$\frac{\partial \Gamma(x_L + \epsilon, y_L + \eta)}{\partial x} \approx \frac{\partial \Gamma(x_L, y_L)}{\partial x} + \frac{\partial^2 \Gamma(x_L, y_L)}{\partial x^2}\epsilon + \frac{\partial^2 \Gamma(x_L, y_L)}{\partial xy}\eta \tag{3.14}$$

$$\frac{\partial \Gamma(x_L + \epsilon, y_L + \eta)}{\partial y} \approx \frac{\partial \Gamma(x_L, y_L)}{\partial y} + \frac{\partial^2 \Gamma(x_L, y_L)}{\partial xy}\epsilon + \frac{\partial^2 \Gamma(x_L, y_L)}{\partial y^2}\eta \tag{3.15}$$

At the Lagrange points, the gradient of Γ vanishes by definition, resulting in the linearized system:

$$\ddot{\epsilon} - 2\dot{\eta} = \frac{\partial^2 \Gamma(x_L, y_L)}{\partial x^2}\epsilon + \frac{\partial^2 \Gamma(x_L, y_L)}{\partial xy} \tag{3.16}$$

$$\ddot{\eta} + 2\dot{\epsilon} = \frac{\partial^2 \Gamma(x_L, y_L)}{\partial xy}\epsilon + \frac{\partial^2 \Gamma(x_L, y_L)}{\partial y^2} \tag{3.17}$$

This second-order system can be written as a first-order system by defining the state vector, $\mathbf{u} = [\epsilon, \eta, \dot{\epsilon}, \dot{\eta}]^T$ resulting in the system of equations:

$$\frac{d}{dt}\begin{pmatrix}\xi\\ \eta\\ \dot{\xi}\\ \dot{\eta}\end{pmatrix} = \begin{pmatrix} 0 & 0 & 1 & 0\\ 0 & 0 & 0 & 1\\ \frac{\partial^2\Gamma(x_L,y_L)}{\partial x^2} & \frac{\partial^2\Gamma(x_L,y_L)}{\partial xy} & 0 & 2\\ \frac{\partial^2\Gamma(x_L,y_L)}{\partial xy} & \frac{\partial^2\Gamma(x_L,y_L)}{\partial y^2} & -2 & 0\end{pmatrix}\begin{pmatrix}\xi\\ \eta\\ \dot{\xi}\\ \dot{\eta}\end{pmatrix} \tag{3.18}$$

The eigenvalues of this matrix determine the local linear stability of the corresponding Lagrange point. If all eigenvalues are purely imaginary or have negative real parts, the perturbations remain bounded and the point is considered linearly stable. In contrast, the presence of any eigenvalue with a positive real part indicates exponential divergence and instability. For the collinear Lagrange points, (L_1, L_2, L_3) the linearized matrix always possesses at least one eigenvalue with a positive real part, implying instability regardless of the mass ratio μ. In contrast, the equilateral points L_4 and L_5 are linearly stable when the mass parameter satisfies $\mu < \mu_c = \frac{1}{2}(1 - \sqrt{69}/9) \approx 0.03852$. This condition is met in the Earth–Moon system, confirming the linear stability of L_4 and L_5 in that context.

3.2.3 Jacobi constant

The equations of motion (3.1) admit one integral of motion known as the Jacobi constant, J. This constant is associated with the conservation of energy, representing the sum of the kinetic and potential energy of the tertiary:

$$J = \frac{\dot{x}^2 + \dot{y}^2 + \dot{z}^2}{2} - \frac{1}{2}(x^2 + y^2) - \frac{1-\mu}{r_1} - \frac{\mu}{r_2} - \frac{\mu(1-\mu)}{2} \tag{3.19}$$

This constant value is determined by the characteristics and geometry of the orbits, serving as a valuable tool for distinguishing between them. However, this conservation property is strictly preserved in numerical solutions obtained through direct time integration. For periodic orbits computed using the HBM, small oscillations in the Jacobi constant are typically observed along the orbit. These oscillations arise due to the inherent approximation in HBM, which represents the solution as a truncated Fourier series. Specifically, the state variables (position and velocity) are approximated as sums of harmonics up to a prescribed order, N_H. Because the Jacobi constant depends nonlinearly on both position and velocity, any approximation error in these quantities translates into deviations from perfect conservation. The presence of oscillations in the Jacobi constant is therefore a direct consequence of the truncation of the harmonic expansion. The HBM solution satisfies the governing equations in an averaged sense, rather than pointwise over time. As such, the method does not enforce conservation laws exactly at each point in time, and this leads to slight periodic variations in the computed Jacobi constant. The amplitude of these oscillations decreases as the number of harmonics included in the approximation is increased. A higher number of harmonics enables the HBM to better capture the nonlinearities present in the system dynamics, leading to a more accurate reconstruction of the periodic orbit. Consequently, the approximation of the Jacobi constant improves, and the oscillations diminish in amplitude.

The global features of the periodic orbit, such as its geometry, stability type, and position in phase space, remain in good agreement with those obtained via time inte-

gration. When only a few harmonics are retained, the method primarily captures the dominant frequency content of the orbit. For many low- to moderate-amplitude periodic orbits in the CRTBP, a large proportion of the solution energy is contained in the first few harmonics. As a result, even a low-order HBM approximation can represent the general shape and timing of the orbit reasonably well. In contrast, the Jacobi constant involves nonlinear combinations of velocity and position, which are sensitive to small inaccuracies in the higher-frequency components. Consequently, even small truncation errors in the harmonic expansion, negligible in terms of trajectory shape, can result in perceptible deviations in the computed Jacobi constant. This is presented in Figure 3.3 where the trajectories and the evolution of the Jacobi constant over time for 5 and 25 harmonics are compared with the results of time integration.

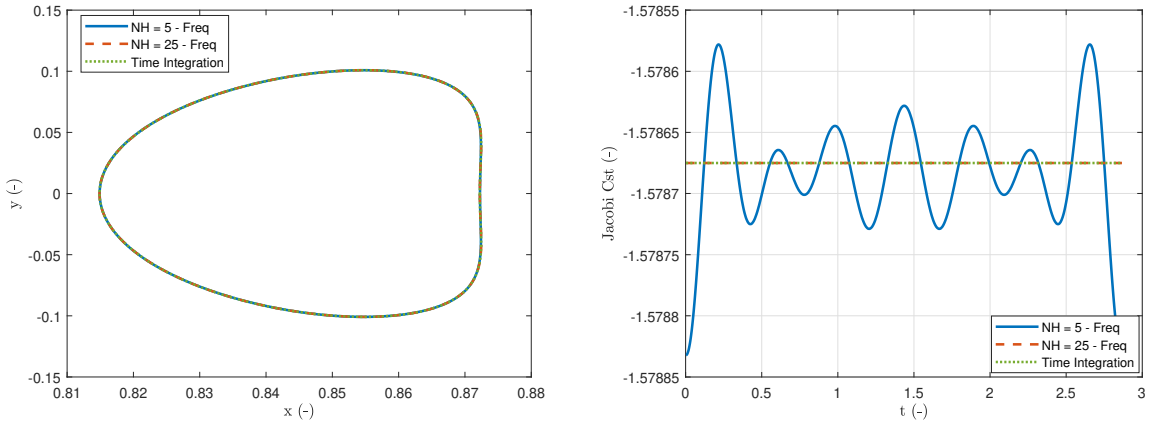

(a) (b)

Figure 3.3: Comparison of periodic orbit shape obtained with HBM and time integration (a); Evolution of the Jacobi constant showing oscillations in HBM results and their reduction with increasing harmonic order (b).

To compensate for the oscillations observed in the Jacobi constant when using the HBM, the median value of the Jacobi constant over one orbit period is used as a reference. This approach provides a robust and representative estimate of the true constant, minimizing the influence of transient numerical artifacts that can disproportionately affect the mean. The median is particularly well-suited in this context due to the symmetric nature of the oscillations around the underlying value, especially when a sufficient number of harmonics is included. This reference value enables consistent comparison with time integration results.

3.3 Periodic families around Lagrange points

The search for three-dimensional periodic orbits around equilibrium points dates back over a century to Moulton [85], who introduced the concept of *oscillating satellites*. This work led to the discovery of the first periodic vertical orbits near collinear Lagrange points. However, progress in computing periodic orbits within the CRTBP was initially limited by the lack of numerical tools. In the 1960s, Goudas extended Moulton's work, calculating 19 periodic orbits [53]. Today, advanced numerical methods enable the efficient computation of numerous periodic orbits around Lagrange points.

One potential tool for this purpose is the software AUTO, which employs piecewise polynomial collocation with Gauss–Legendre collocation points and adaptive mesh refinement. Additionally, AUTO calculates Floquet multipliers, essential for analyzing the asymptotic stability and bifurcation characteristics of periodic orbits. Frequent applications of AUTO are found in various domains of nonlinear dynamics and control theory [86, 87, 88].

The harmonic balance method (HBM), combined with Hill's method for bifurcation detection and branch-following algorithms, facilitates mapping entire families of periodic orbits from a single initial solution. Figure 3.4 illustrates a subset of periodic orbit families around the first Lagrange point, interconnected through bifurcations, plotted against their periods and associated Jacobi constants. The results derived using the HBM are compared with those obtained from AUTO, serving as a validation of the HBM's accuracy. The different families are connected via branch points represented with blue squares. All the orbits presented in this chapter have been computed with a maximum of 30 harmonics ($N_H = 30$), a time discretization $N = 512$, and a tolerance for the HBM $\epsilon = 1e^{-10}$.

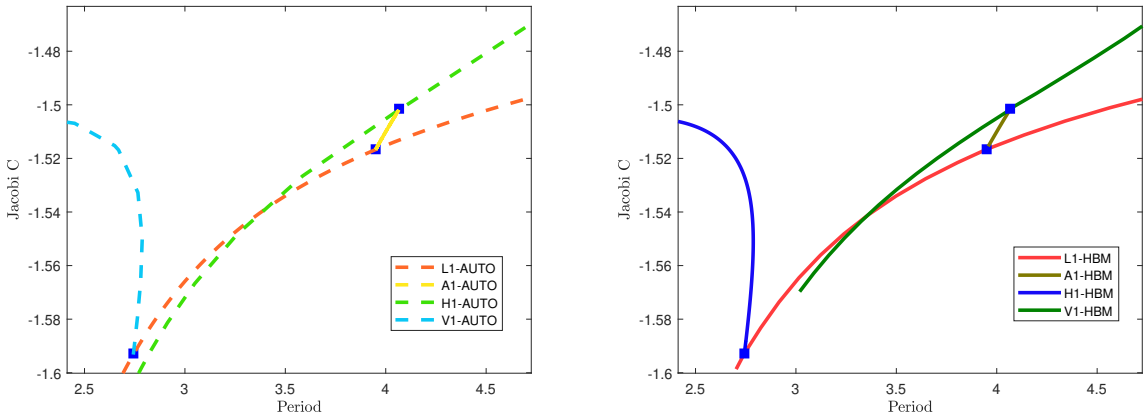

(a) (b)

Figure 3.4: Sample branches of periodic orbits around the first Lagrange point in the Earth-Moon CRTBP, illustrating connections through bifurcations. Results obtained with AUTO software (a) and Harmonic Balance method (b).

To aid interpretation, a schematic bifurcation diagram inspired by the 3D representation of Doedel [89] is shown in Figure 3.5. Additional branches originating from period-doubling bifurcations are included. Each colored line represents a family of periodic orbits associated with specific Lagrange points. In the diagram, Earth is denoted by a blue circle, the Moon by a green circle, and the five Lagrange points by red squares. Line intersections indicate bifurcations between orbit families, while dashed lines do not represent intersections. Collisions and non-converged orbits are marked by small red circles. Notably, collisions are not algorithmic limitations but rather an intentional criterion to terminate continuation.

Table 3.1: Abbreviations and colors on the schematic bifurcation map of periodic orbit families in Figure 3.5.

Symbols	**Family**	**Color**
$L1, L2, L3$	Lyapunov	Red
$H1, H2, H3$	Halo	Dark Blue
$A1, A2, A3$	Axial	Yellow
$V1, V2, V3, V4, V5$	Vertical	Green
$S3$	Short-period	Orange
$L4, L5$	Long-period	Grey
$B1, B2, B3$	Backflip	Purple
$Y4, Y5$	Long-axial	Black
$R2$	L2-vertical	Green-blue
$W4, W5$	Halo-vertical transition	Light Blue
$C1, C2$	Circular	Brown
$L1_{PD}, L2_{PD1}, L2_{PD2}, L3_{PD}$	Lyapunov period doubling	Violet
$H1_{PD1}, H2_{PD2}$	Halo period doubling	Pink

This analysis focuses on orbits directly connected to Lagrange points and their bifurcated branches. However, many additional periodic orbits can be computed using these methods. The names, abbreviations, and associated colors of the different families are detailed in Table 3.1.

The following sections provide a comprehensive description of the different families of periodic orbits. For each family, a detailed analysis includes:

1. **Three-dimensional representations:** Visualization of selected orbits in 3D space, highlighting their relationship to the primaries and equilibrium points.

2. **Stability analysis:** Assessment of stability characteristics based on Floquet multipliers, offering insight into the dynamic behavior of the orbits.

3. **Bifurcation identification:** Identification and classification of bifurcations, revealing connections between orbit families and the emergence of new periodic solutions.

This systematic approach aims to offer a deeper understanding of the structural and dynamical properties of periodic orbits within the Earth-Moon CRTBP framework.

3.3.1 Lyapunov families

The Lyapunov families consist of planar orbits originating from the three collinear Lagrange points, L_1, L_2 and L_3. As depicted in Figure 3.5, these families terminate in collisions with one of the primaries. Graphical representations of the Lyapunov orbits for $L1$, $L2$ and $L3$ are provided in Figures 3.6a, 3.6b and 3.6c respectively.

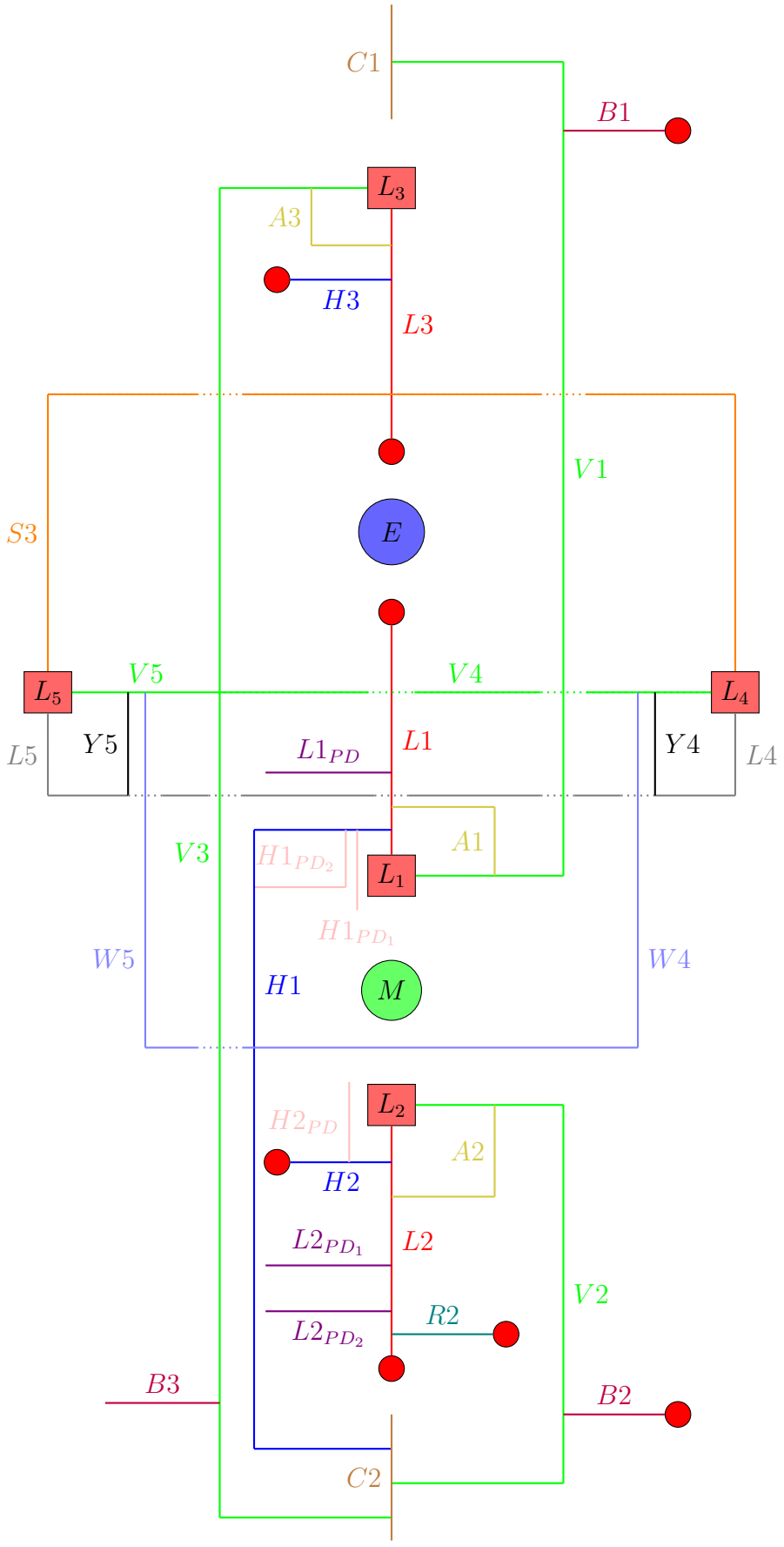

Figure 3.5: Schematic bifurcation map for the Earth-Moon CRTBP ($\mu = 0.0121508$).

Branch point bifurcations, which are represented by colored dashed lines, connect the Lyapunov families with other periodic orbit families. Period-doubling bifurcations, marked by dotted lines, lead to the creation of new families, such as $L1_{PD}$ or $L2_{PD1,2}$. The orbits shared between the Lyapunov and halo families ($H1, H2, H3$), are depicted in blue, while the orbits that connect to the axial families ($A1, A2, A3$) are shown in yellow. In Figure 3.6b, the green-blue orbit represents the bifurcation with the $R2$ family, and in Figure 3.6c, the orange orbit corresponds to the short-period bifurcation $S3$. Purple orbits are the result of period-doubling bifurcations of $L1$ and $L2$, leading to unnamed families labeled $L1_{PD}$ or $L2_{PD1,2}$. While these Lyapunov orbits give rise to additional periodic families through further bifurcations, this work focuses only on the families directly connected to the Lyapunov orbits. All three Lyapunov families ($L1, L2, L3$) are inherently unstable.

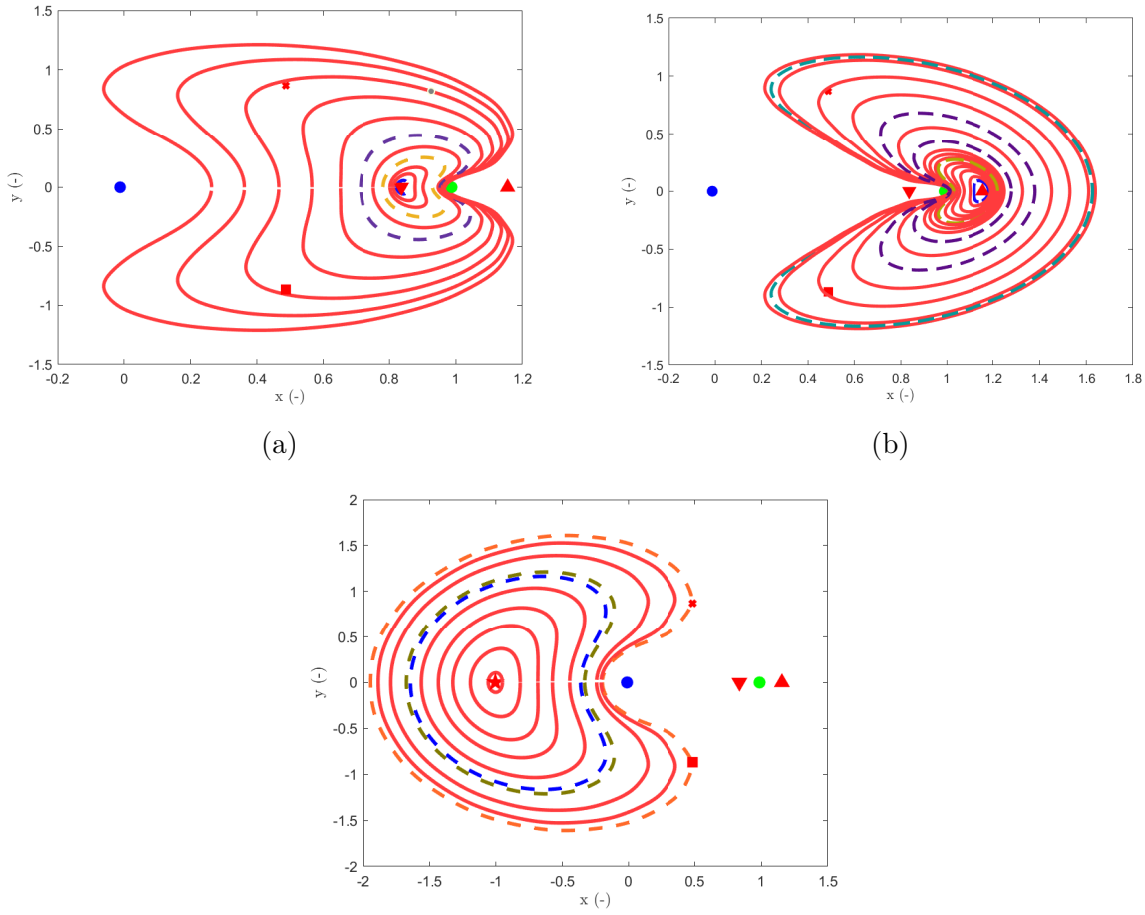

(a) (b)

(c)

Figure 3.6: 3D representation of orbits of (a) $L1$ family; (b) $L2$ family; (c) $L3$ family; relative to the primaries and Lagrange points.

3.3.2 Vertical families

The vertical families arise from all five Lagrange points and are labeled $V1$, $V2$, $V3$, $V4$ and $V5$, as depicted by the green lines in Figure 3.5. The families $V4$ and $V5$ are directly connected, without a bifurcation, and can be considered as a single family ($V4/V5$) even though they originate from different Lagrange points. All four Vertical families are unstable. Sample 3D representations of orbits from these families are shown in Figure 3.7.

The bifurcations encountered by the Vertical families $V1$, $V2$ and $V3$ follow a similar pattern. Starting from the equilibrium points, the orbits initially share common paths with the Axial families $A1$, $A2$ and $A3$. As the families continue, an additional bifurcation with the Backflip orbits $B1$, $B2$ and $B3$ occurs. Eventually, the vertical families transform into planar, circular orbits via a period-doubling bifurcation, which connects the circular families $C1$ and $C2$. The period of the circular orbits is half the period of the Vertical family at the bifurcation point.

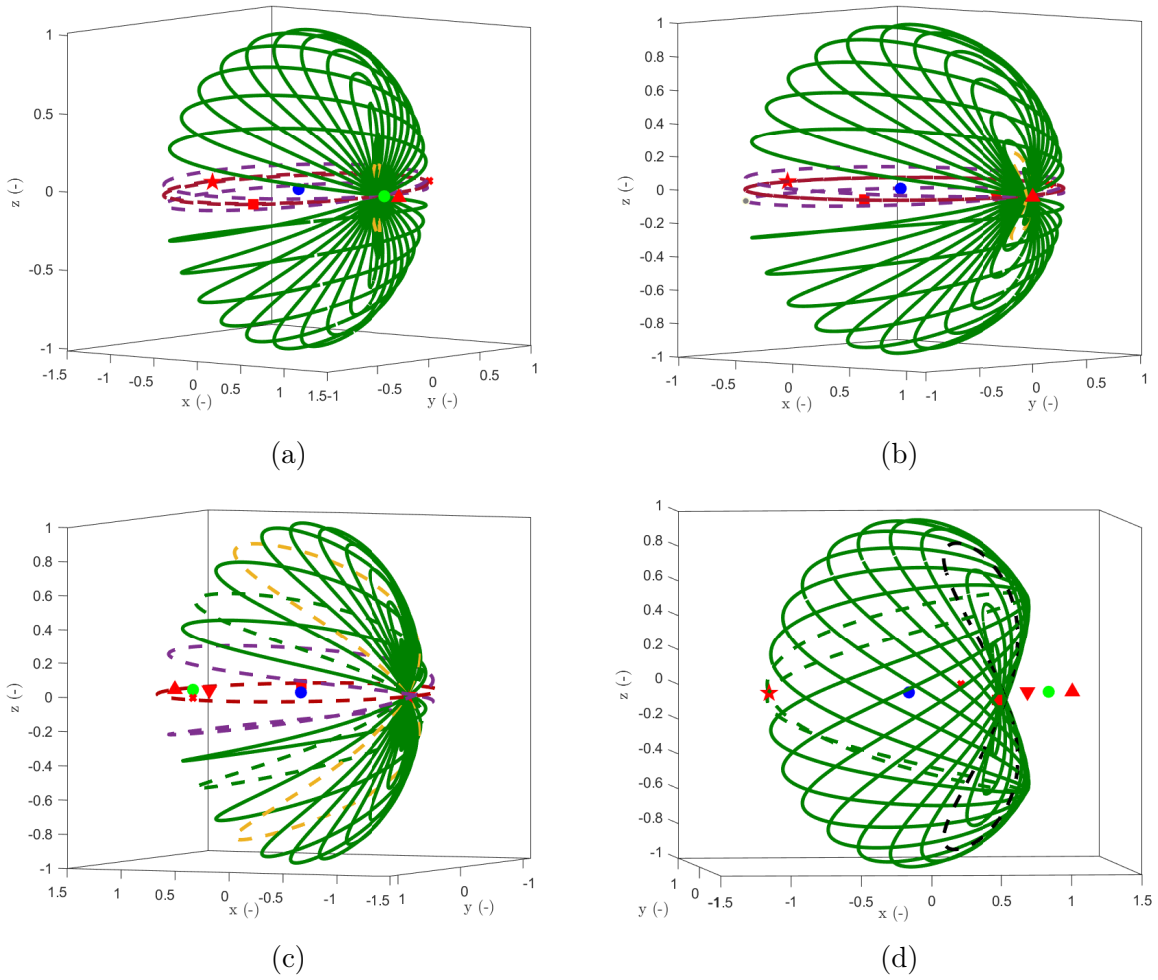

Figure 3.7: 3D representation of orbits of (a) $V1$ family; (b) $V2$ family; (c) $V3$ family; (d) $V4$ family; relative to the primaries and Lagrange points.

The family $V3$ experiences an additional bifurcation compared to $V1$ and $V2$. At a certain point during the continuation, one of the periodic orbits of $V3$ is shared with the

$V4/V5$ family. The $V4/V5$ family starts from either of the triangular equilibrium points, with five bifurcation points during its continuation, specifically with respect to frequency. Starting from L_4, the first bifurcation is a period-quadrupling with the $Y4$ family where the members have a period 4 times greater than the bifurcating orbit of $V4$ bifurcates. Further along the continuation, the family undergoes a pitchfork bifurcation with the $W4$ family, where orbits can grow in either the northern or southern part. Once the orbits from $V4$ reach the symmetry axis formed by the collinear Lagrange points, a bifurcation with $V3$ occurs. Due to symmetry, a similar behavior is observed starting from L_5.

3.3.3 Halo families

The halo families, labeled $H1, H2$ and $H3$, result from branch point bifurcations of the Lyapunov families $L1$, $L2$ and $L3$. In these families, the orbits grow out of the plane in either the northern or southern direction, and they are represented by the color blue in Figure 3.5. Due to the configuration of the CRTBP, the periods and Jacobi constants of the Northern Halo and Southern Halo are identical. Sample 3D representations of orbits from these families are shown in Figure 3.8.

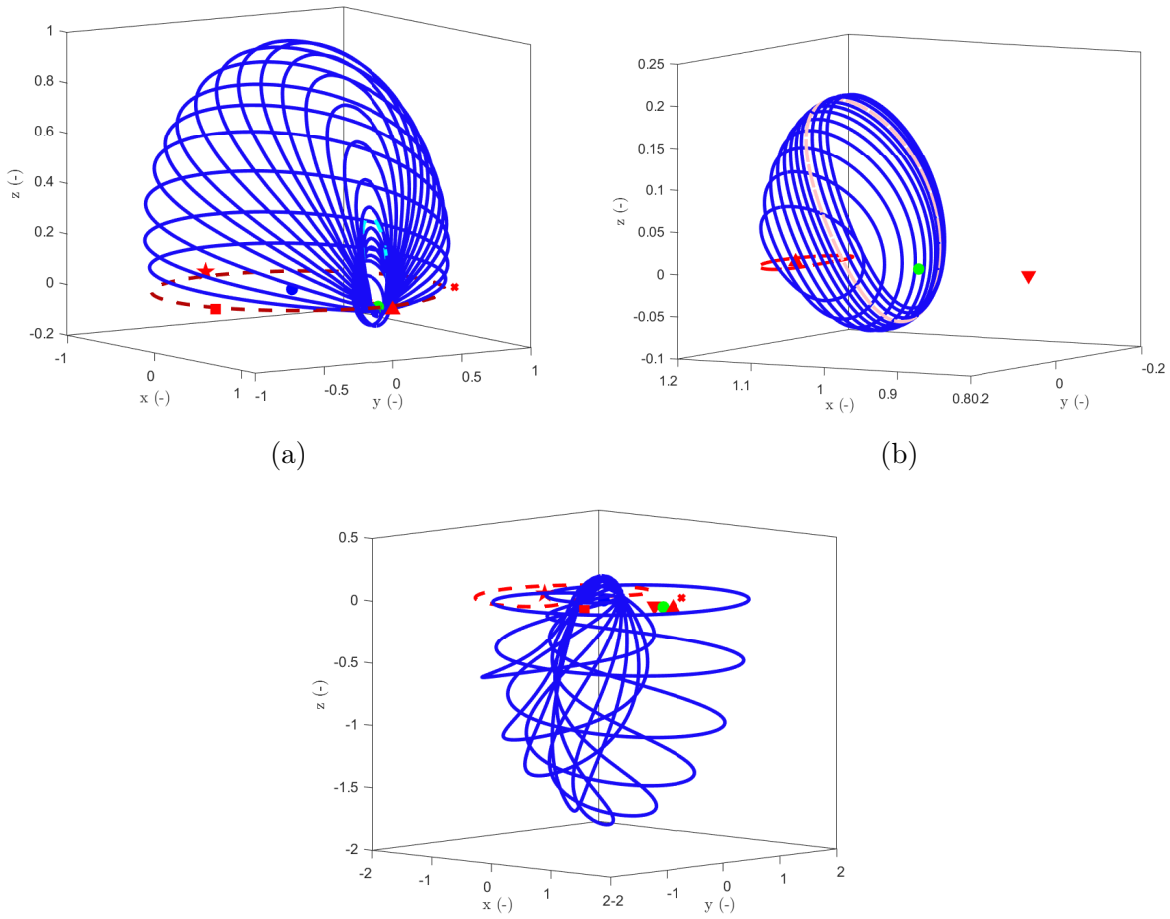

(a) (b)

(c)

Figure 3.8: 3D representation of orbits of (a) $H1$ family; (b) $H2$ family; (c) $H3$ family; relative to the primaries and Lagrange points.

The halo family $H1$ is unique among the three in that it bifurcates with another family through branch points. First, there are two period-doubling bifurcations that result in the families $H1_{PD_1}$ and $H1_{PD_2}$. Then, a branch point bifurcation occurs with the $W4/W5$ family (light blue), followed by a period doubling bifurcation with the circular family $C2$ (brown). The other two halo families, $H2$ and $H3$ ultimately collide with the primaries, though $H2$ undergo a period-doubling bifurcation leading to the $H2_{PD}$ family before that. All three halo families, $H1, H2$ and $H3$ are unstable.

3.3.4 Axial families

The axial families $A1, A2$ and $A3$ also bifurcate from the Lyapunov families $L1$, $L2$ and $L3$. These three-dimensional orbits connect the vertical families $V1$, $V2$ and $V3$. and are represented in yellow on Figure 3.5. Apart from the starting and ending points, none of the three families experiences bifurcations. There is no stability change during the continuation, and the families remain unstable throughout.

Figure 3.9 shows the 3D orbits with respect to the primaries and Lagrange points.

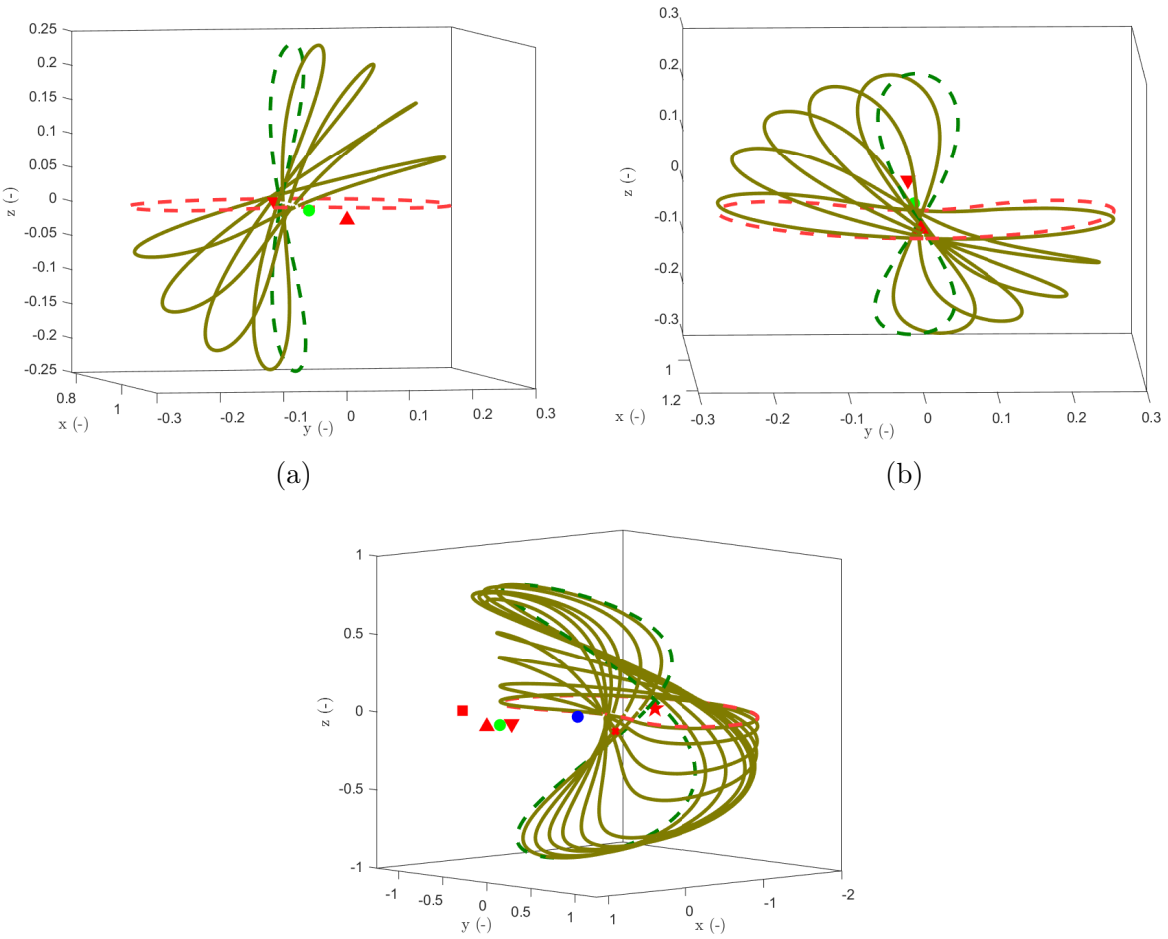

Figure 3.9: 3D representation of orbits of (a) $A1$ family; (b) $A2$ family; (c) $A3$ family; relative to the primaries and Lagrange points.

3.3.5 Short and long period families

The short-period family $S3$ is a planar family emanating from either of the triangular Lagrange points L_4 or L_5. It is named in contrast to the Long-Period family that also originates from these points. The short-period family is represented in orange in Figure 3.5, while the long-period family is in gray. The short-period family connects with the $L3$ family, while the long-period family has one bifurcation with the $Y4/5$ family. Due to symmetry with respect to the x-z axis, the same behavior is observed regardless of whether the continuation starts from L_4 or L_5 The short-period family is stable, while the long-period family shows stable orbits near the equilibrium points L_4 and L_5 until the branch point bifurcation with the $Y4/5$ family is encountered, after which the orbits become unstable.

The short-period family is represented in Figure 3.10a, while the long-period family is shown in Figures 3.10b, where the 3D orbits with respect to the primaries and Lagrange points are displayed.

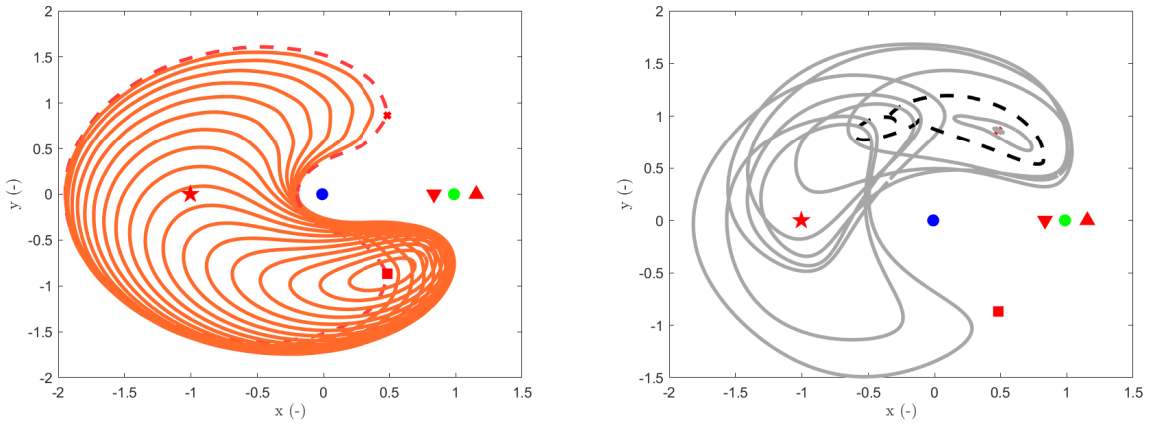

(a) (b)

Figure 3.10: 3D representation of orbits of (a) $S3$ family; (b) $L4$ family; relative to the primaries and Lagrange points.

3.3.6 Backflip families

Each of the three vertical families $V1$, $V2$ and $V3$ exhibits a bifurcation that leads to the backflip families $B1$, $B2$ and $B3$. The $B1$ and $B2$ families ultimately end with a collision with the primaries, while the $B3$ family bifurcates into other periodic families, which are not discussed in the scope of this thesis. These periodic orbits are associated with the color purple in Figure 3.5.

All three backflip families are unstable. The 3D representations of some of the periodic orbits of each family are shown in Figures 3.11a, 3.11b, and 3.11c.

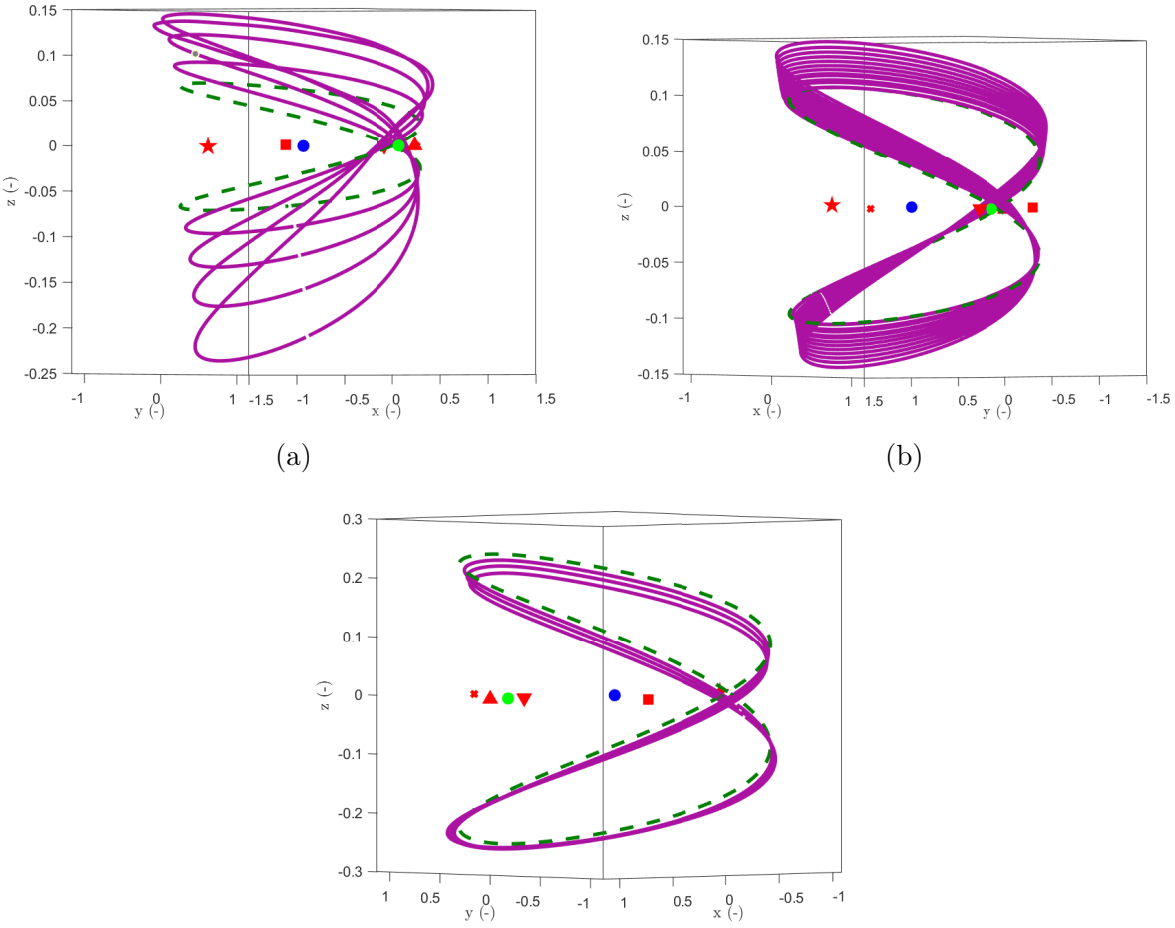

Figure 3.11: 3D representation of orbits of (a) $B1$ family; (b) $B2$ family; (c) $B3$ family; relative to the primaries and Lagrange points.

3.3.7 Long-axial families

The long-axial families, labeled $Y4/5$ and depicted in black in Figure 3.5, originate from a bifurcation point in the long-period family $L4/5$ and end with a period-quadrupling bifurcation in the vertical family $V4/5$. Similar to the axial families $A1$, $A2$ and $A3$, the orbits of the $Y4/5$ families serve as a bridge between a planar and a vertical orbit, with the key difference being that the vertical termination has a period four times smaller than the starting period. This family is unstable.

A sample of the $Y4/5$ families is shown in Figure 3.12.

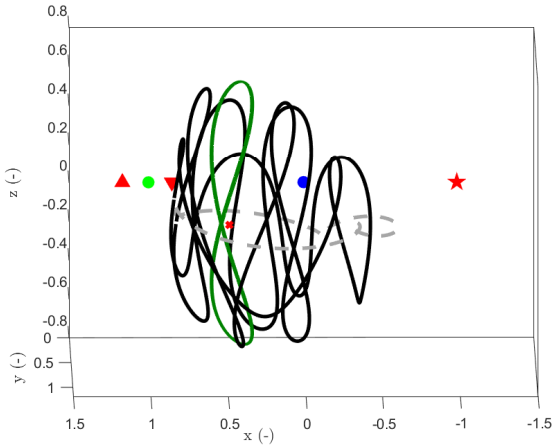

Figure 3.12: 3D representation of orbits of $W4/W5$ family relative to the primaries and Lagrange points.

3.3.8 L2-vertical family

This family of periodic orbits results from a bifurcation of the $L2$ family just before it collides with the Moon. It consists of several orbits that depart from the orbital plane and eventually end in a collision with the Moon. In Figure 3.5, it is labeled $R2$ and corresponds to the green-blue color. Figure 3.13 shows a few orbits of the family. The $R2$ family is unstable as well.

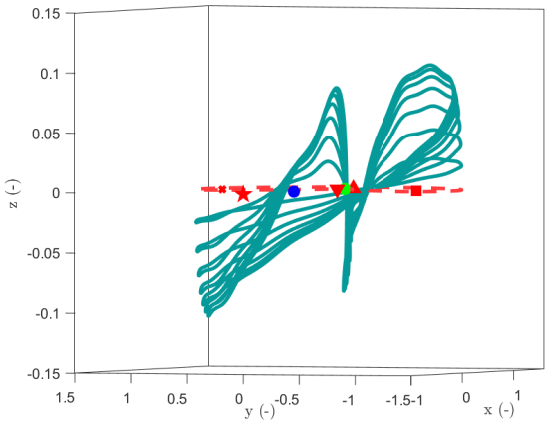

Figure 3.13: 3D representation of orbits of $R2$ family relative to the primaries and Lagrange points.

3.3.9 Halo-vertical transition families

The halo-vertical transition families share some similarities with the short-period family, as they can be associated with a single family due to symmetry along the x-z plane and the fact that one can be reached from the other without any bifurcations. The $W4/5$ families begin with a pitchfork bifurcation from the vertical families $V4/V5$, with $W4$ and $W5$ branching off in either the northern or southern direction. The northern parts of $W4$ and $W5$ eventually merge in a bifurcation with the northern part of $H1$ in the middle. Similarly, the southern parts of $W4$ and $W5$ merge with the southern part of

$H1$. These families are depicted in pale blue in Figure 3.5. The halo-vertical transition families are unstable.

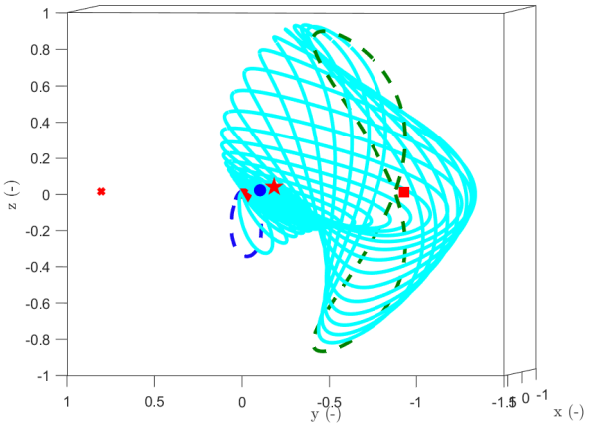

Figure 3.14: 3D representation of orbits of $W4/W5$ family relative to the primaries and Lagrange points.

3.3.10 Circular families

The circular families $C1$ and $C2$ are named for their circular shape. The $C1$ family results from a period-doubling bifurcation from the vertical family $V1$, where the two vertical branches collapse onto one another, forming a circle with half the period of the $V1$ orbit at the connection. The $C2$ family can be reached in multiple ways. One path involves a connection with the $H1$ family at its end, while another mirrors the case of $C1$ involving period-doubling bifurcations from the collapsing orbits of $V2$ and $V3$.Both $C1$ and $C2$ are represented by the brown color in Figure 3.5.

Figures 3.15a and 3.15b display samples of periodic orbits from these families. Additional bifurcations exist, such as the one shown by the dashed line in Figure 3.15a. The emerging branches of these bifurcations are not considered in this work. The circular family $C1$ is mostly stable, though it becomes unstable between the two bifurcation points while the $C2$ family is unstable.

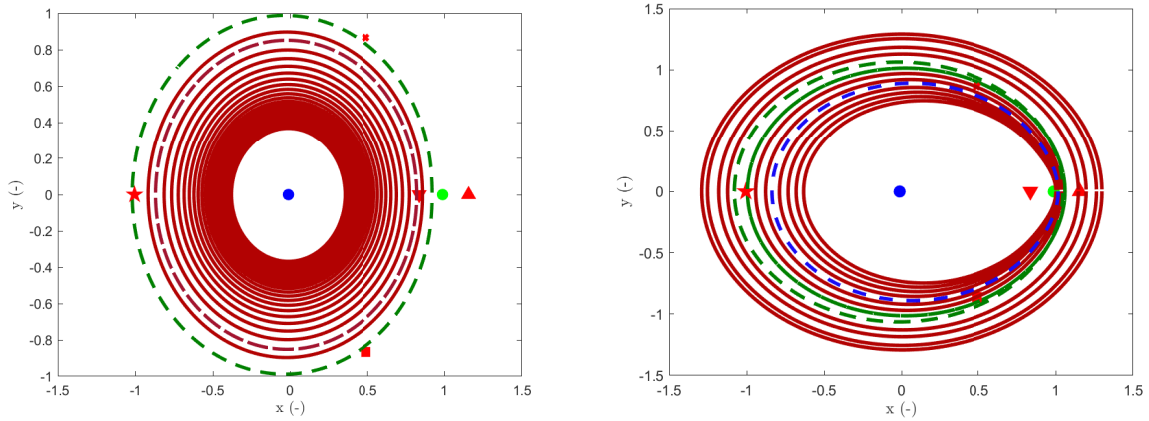

(a) (b)

Figure 3.15: 3D representation of orbits of (a) $C1$ family; (b) $C2$ family; relative to the primaries and Lagrange points.

3.3.11 Halo period-doubling families

The halo period-doubling families result from period-doubling bifurcations along the halo families $H1$ and $H2$, and are labeled $H1_{PD_1}$, $H1_{PD_2}$, $H2_{PD}$ associated with the color pink in Figure 3.5. Three distinctive period-doubling bifurcations are detected during the continuation process of the $H1$ family, some of which are discussed in [90]. The first, $H1_{PD_1}$, is continued until the algorithm can no longer converge toward a new solution. The two other period-doubling bifurcations form a loop emanating from the main branch of solution $H1$. Both of these families, along with the family bifurcated from $H2$ are unstable. Samples of these bifurcated branches are shown in Figures 3.16a, 3.16b, and 3.16c. The families $H1_{PD_1}$ and $H2_{PD}$ are also known as the *dragonfly* families [91]. All three of these families, $H1_{PD_1}$, $H1_{PD_2}$, $H2_{PD}$ are unstable.

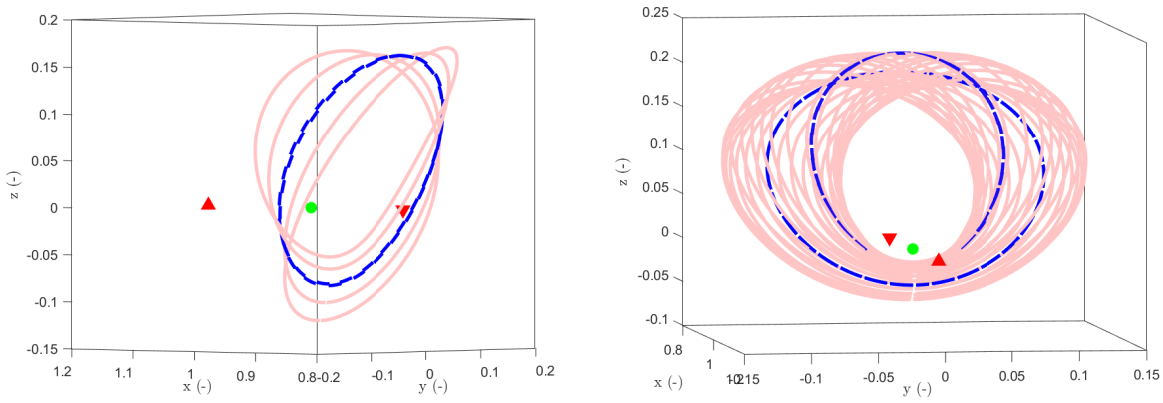

(a) (b)

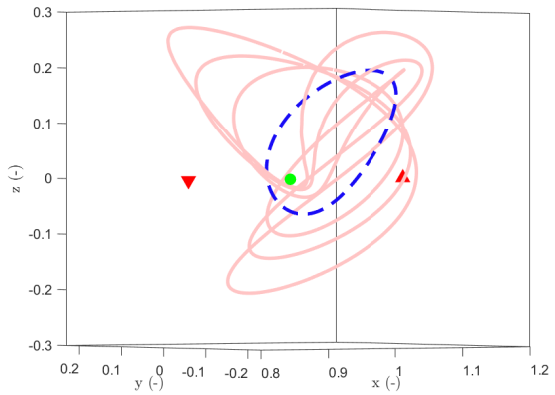

(c)

Figure 3.16: 3D representation of orbits of (a) $H1_{PD_1}$ family; (b) $H1_{PD_2}$ family; (c) $H2_{PD}$ family; relative to the primaries and Lagrange points.

3.3.12 Lyapunov period-doubling families

Along the Lyapunov families, various period-doubling bifurcations are encountered. These periodic orbits are grouped under the labels $L1_{PD}$, $L2_{PD}$ and $L3_{PD}$, and are colored in violet in Figure 3.5. They are out-of-plane orbits with an X shape. Bifurcations occur during the continuation process, which are highlighted in Figure 3.17a, though the emerging branches are not followed in this work. These period-doubled families are unstable.

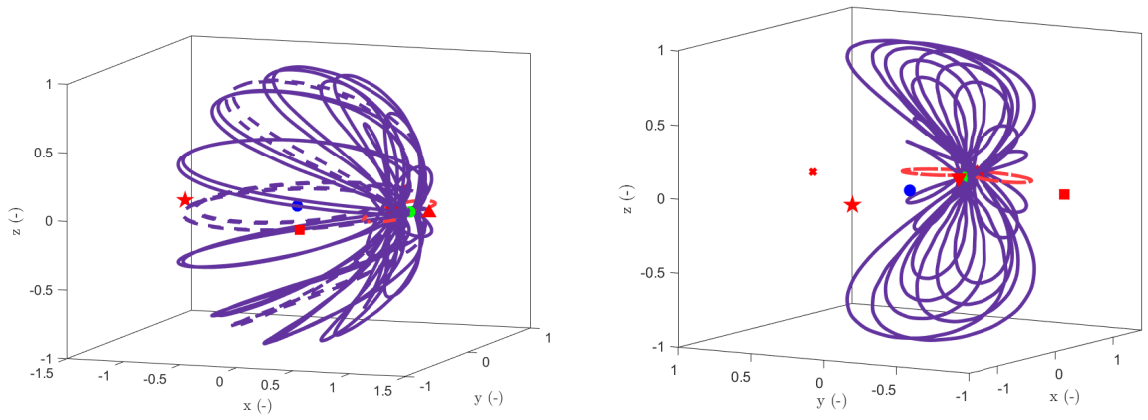

(a) (b)

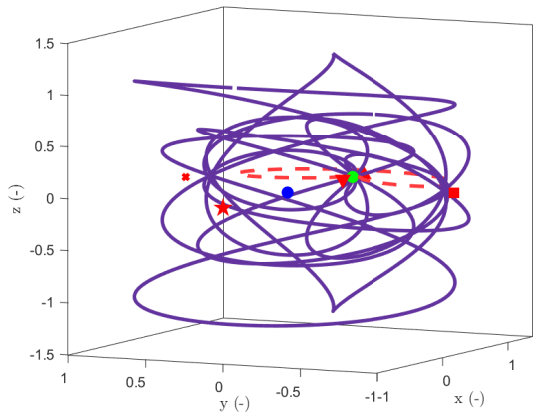

(c)

Figure 3.17: 3D representation of orbits of (a) $L1_{PD}$ family; (b) $L2_{PD_1}$ family; (c) $L2_{PD_2}$ family; relative to the primaries and Lagrange points.

3.4 Resonant periodic families

In the previous section, the importance of Lagrange points for the emergence of periodic families was highlighted. However, periodic solutions can exist outside of these equilibrium points. In this section, resonant periodic orbits are explored using the harmonic balance method. A resonant orbit is defined by the ratio m:n, where m is the period of the spacecraft's motion and n is the period of rotation of the secondary around the center of mass. In the CRTBP, the ratio is not exactly equal to the ratio of two integers due to the gravitational influence of the secondary primary body [92]. In other words, the spacecraft completes m orbits while the secondary body completes approximately n revolutions [93]. If $m>n$ the resonant families are labeled interior, if $n>m$ the families are called exterior.

Unlike the families around Lagrange points, families of resonant periodic orbits are not interconnected in the Earth-Moon configuration. However, for lower mass ratios, the families are linked together by near-circular families. In his work, Pan [75] explored the breaking points and the recombination of these connections with respect to the mass ratio. He covered the interior and exterior planar resonant families and discussed some of the limitations he encountered, such as having to stop his algorithm when the solutions were too close to the primaries. HBM does not have issues with orbits close to the primaries, making it a useful tool for the propagation and continuation of resonant families. In addition, the HBM combined with the Hill's method allows the detection of bifurcation and the construction of new paths of solutions. Examples of resonant periodic orbits for different ratios are presented in Figure 3.18.

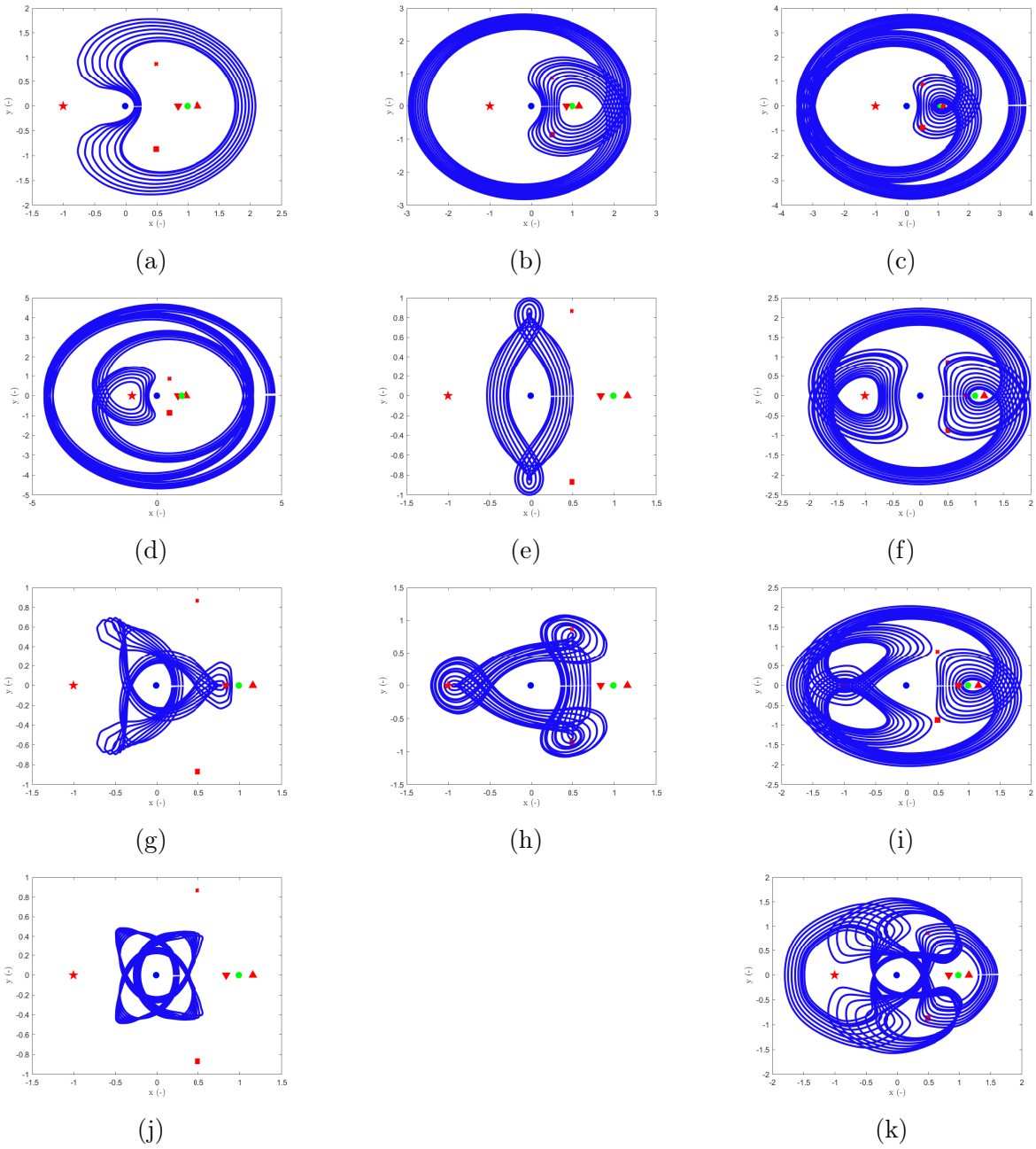

Figure 3.18: Example of resonant periodic orbits in the Earth-Moon system : (a) 1:1 Resonance; (b) 1:2 Resonance; (c) 1:3 Resonance; (d) 1:4 Resonance; (e) 2:1 Resonance; (f) 2:3 Resonance; (g) 3:1 Resonance; (h) 3:2 Resonance; (i) 3:4 Resonance; (j) 4:1 Resonance; (k) 4:3 Resonance

Figure 3.18 provides a few samples from the continuation processes. Over a broader range of frequencies, orbits within the same families undergo numerous bifurcations, leading to increasingly complex orbital paths. For instance, Figure 3.19 illustrates the continuation of the 1:1 resonant family with respect to the frequency. In this figure, blue squares denote bifurcations, where new solutions could potentially emerge. Following each of these branches is a meticulous task, and the decision not to trace the emerging branches reflects the author's choice rather than a limitation of the algorithm.

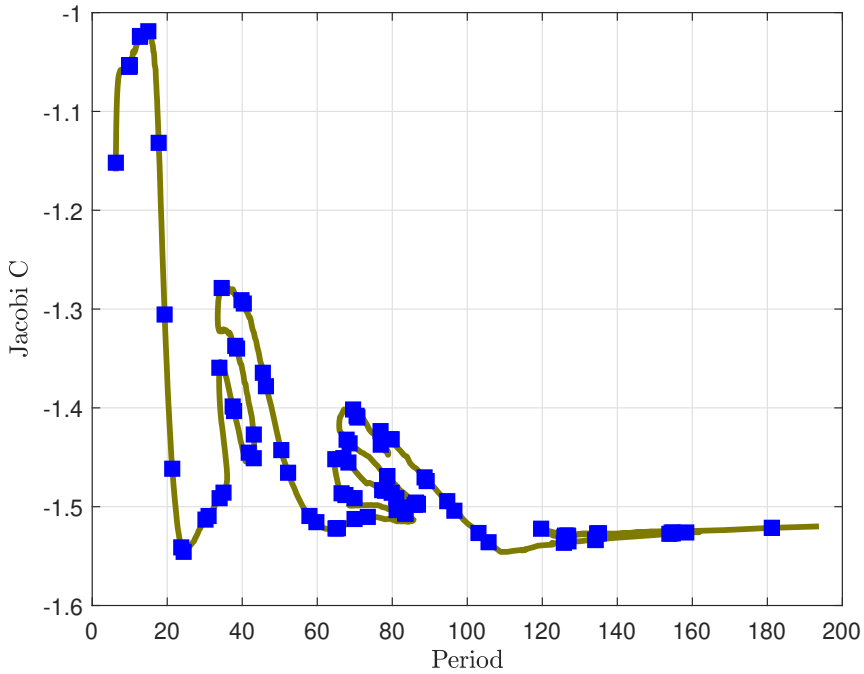

Figure 3.19: Continuation process with HB for 1:1 resonant family in the Earth-Moon CRTBP.

The potential branches are not confined to the case of the 1:1 resonant family; numerous solutions exist for various resonant ratios. Building on the observations of Pan [75], the focus is directed toward a closed loop of solutions, particularly examining the interior first-order 3:2 resonance and its connection to the 2:1 resonance.

3.4.1 3:2 Resonant periodic family

The interior 3:2 resonant family (Figure 3.18h) serves as an ideal case study due to the regular shape of its continuation loop and the presence of both branch points, marked by blue squares, and period-doubling bifurcations, denoted by green diamonds. The continuation process, represented in Figure 3.20, illustrates the evolution of the solutions with respect to their period, where stable portions are shown as solid black lines and unstable portions as dotted red lines.

The continuation loop initiates at the smallest dimensionless period, approximately 10.5, along the lower branch, which is initially unstable. As the loop progresses, it transitions into a primarily stable branch, disrupted by a segment of instability flanked by two period-doubling bifurcations. Along this stable segment, two branch-point bifurcations are encountered. Following these branch points, the loop enters another unstable region, also constrained by two period-doubling bifurcations. Beyond this, a brief stable segment appears between the final period-doubling bifurcation and the loop's fold-back point around a period of 13. Ultimately, the continuation forms a closed loop, exhibiting instability exclusively in regions where two distinct branch points are present.

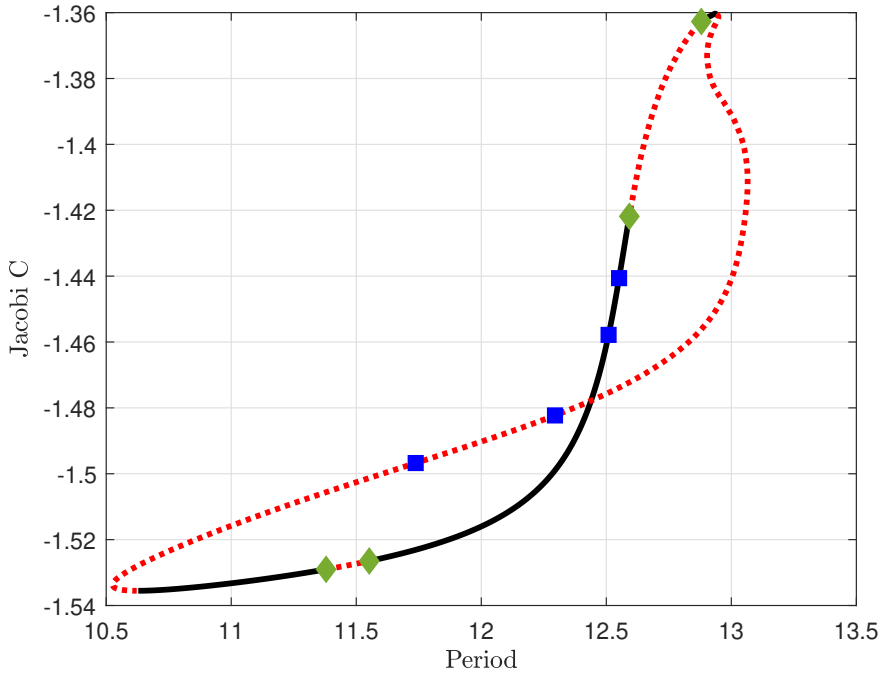

Figure 3.20: Continuation process with HB for 3:2 resonant family in the Earth-Moon CRTBP.

The periods and Jacobi constants associated with the bifurcations are summarized in Table 3.2. These bifurcations include four period-doubling events (PD_1, PD_2, PD_3, PD_4) and four branch points (B_1, B_2, B_3, B_4).

The four period-doubling bifurcations form two connected pairs: PD_1 links to PD_3, and PD_2 links to PD_4. To highlight this relationship, the periods of the bifurcated branches are halved, and the solutions are overlaid onto Figure 3.20. Figure 3.21 showcases the resulting bifurcations, while Figure 3.22 presents 3D visualizations of the orbits for these period-doubled branches, with stable orbits in black and unstable ones in red.

Table 3.2: Period and Jacobi constant of the orbits at the bifurcations of the periodic 3:2 resonant family in the Earth-Moon CRTBP associated to Figure 3.20

Bifurcation	**Period**	**Jacobi Cst**
PD_1	11.379	-1.457
PD_2	11.551	-1.440
B_1	12.509	-1.529
B_2	12.551	-1.526
PD_3	12.592	-1.421
PD_4	12.880	-1.362
B_3	12.294	-1.482
B_4	11.737	-1.496

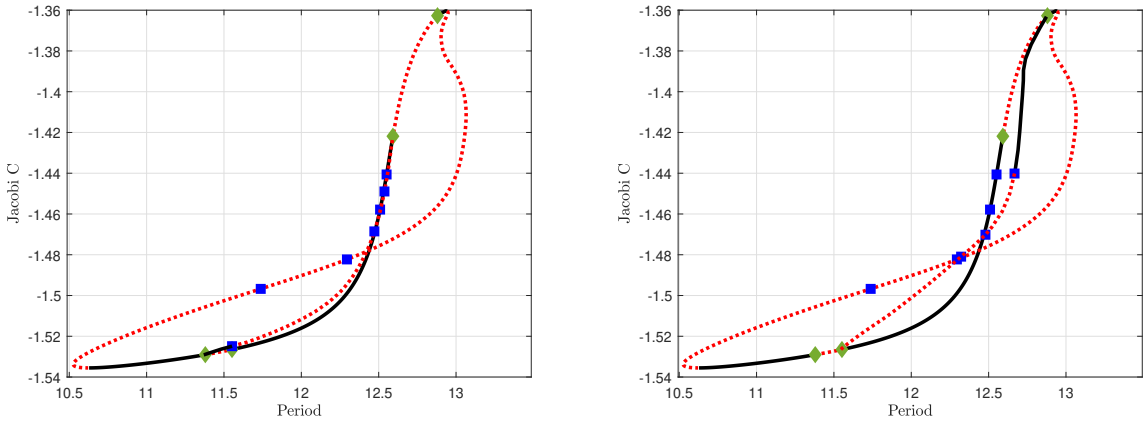

(a) (b)

Figure 3.21: Continuation process with HB for 3:2 resonant family supperposed with the period doubling connection between (a) PD_1 and PD_3;(b) PD_2 and PD_4; in the Earth-Moon CRTBP.

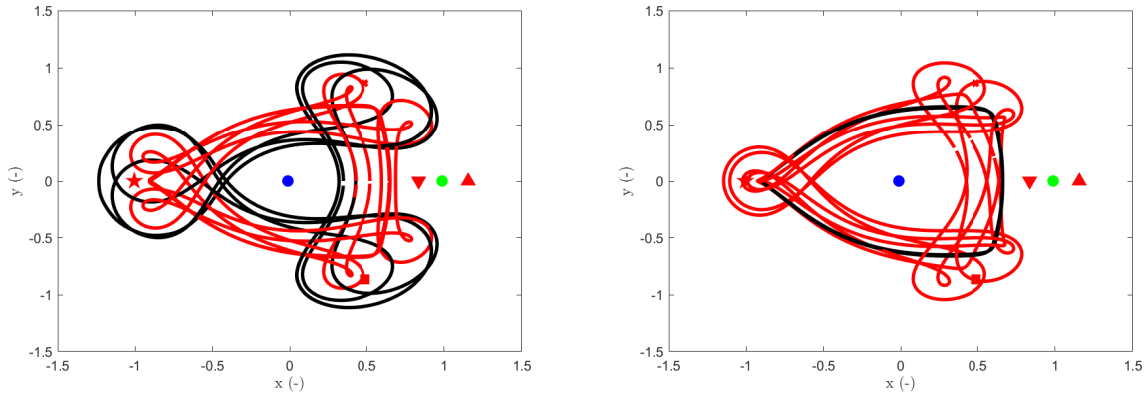

(a) (b)

Figure 3.22: 3D representation of (a) the period doubled orbits between PD_1 and PD_3; (b) the period doubled orbits between PD_2 and PD_4; relative to the primaries and Lagrange points.

This loop structure is not universal for all CRTBP configurations. Pan [75] demonstrated that for smaller mass ratios (μ), the loop opens and connects to the 2:1 resonance branch via quasi-circular orbits. Figure 3.23 shows the evolution of the continuation process for different μ values, ranging from the Sun-Earth system (small μ) to the Earth-Moon system (large μ).

For $\mu < 4.09019\text{e}{-3}$, the 2:1 resonant orbits are unstable and directly connected to the stable 3:2 resonant orbits via quasi-circular orbits. As μ increases, two period-doubling bifurcations emerge, introducing an unstable segment that grows as μ increases further. For $\mu > 4.09019\text{e}{-3}$, the 3:2 branch becomes a closed loop, separate from the 2:1 resonance. To clarify, Figures 3.24 and 3.25 isolate the continuation processes for the 3:2 and 2:1 families, respectively, across different mass ratios.

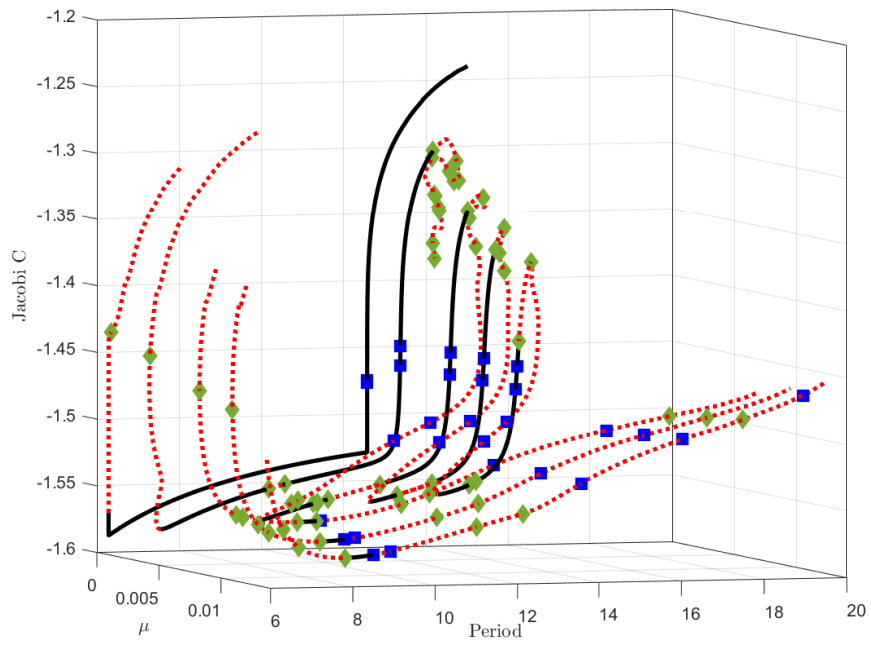

Figure 3.23: Continuation along the frequency ω with HB of the 2:1 and 3:2 resonant families with respect to the mass ratio μ.

With increasing values of μ, both the period and the Jacobi constant ranges for the solutions shrink, leading to the disappearance of certain bifurcations at specific μ values. Across all solutions, stable portions exist, separated by unstable segments bounded by two period-doubling bifurcations. As μ increases, the unstable portion decreases. On the stable branch, two branch point bifurcations consistently occur regardless of μ. The stable branch terminates at a period-doubling bifurcation.

For larger values of μ, as seen in the Earth-Moon CRTBP, the number of period-doubling bifurcations on the unstable branch following the stable segment reduces. For $\mu > 8\text{e}{-3}$, a small stable portion of solutions emerges, ending at the maximum value of the Jacobi constant. This stable portion loops back onto itself with unstable orbits until it reaches the minimum Jacobi constant, with two branch points located along this unstable segment. For $\mu < 8\text{e}{-3}$, additional period-doubling bifurcations appear after the branch points on the unstable portion.

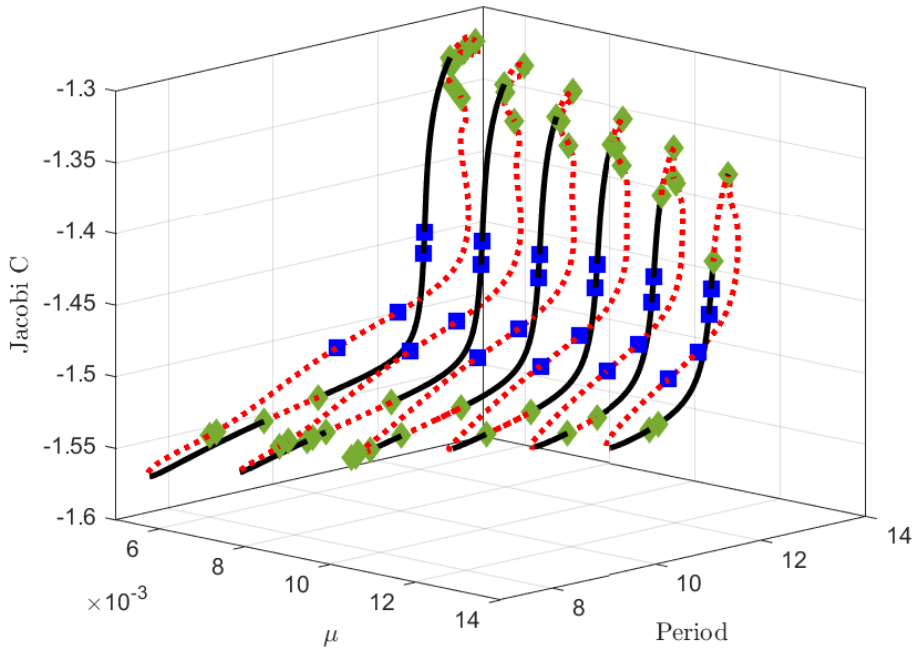

Figure 3.24: Continuation along the frequency ω with HB of the 3:2 resonant family with respect to the mass ratio μ.

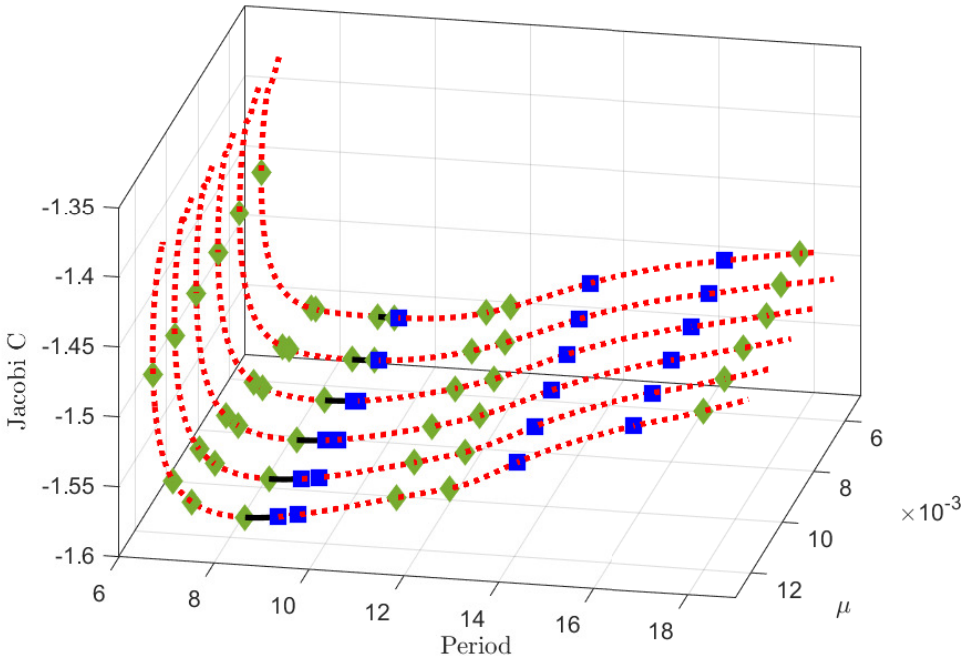

Figure 3.25: Continuation process with HB of the 2:1 family with respect to the mass ratio μ.

On the continuation branch of the 2:1 resonance after its separation from the 3:2 branch, the bifurcations remain consistent across nearly all branches. The branch starts with a drop in the Jacobi constant and encounters four period-doubling bifurcations. At

the fourth period-doubling, the unstable branch transitions into a stable segment that quickly ends with a branch point, closely followed by another branch point. Five additional bifurcations are observed before the continuation process halts at a dimensionless period of approximately 18. These include two period-doubling bifurcations, two branch points, and a final period-doubling bifurcation.

These numerous bifurcations can be followed to construct new connecting paths, similar to what has been accomplished with the orbits around the Lagrange points (Figure 3.5). To reconnect the two resonant families, the new bifurcations that emerge at high μ values can be utilized. In the specific case of the Earth-Moon CRTBP, attention is focused on the emerging branch points after the stable portion of the 2:1 resonant family. Two distinct bifurcation pathways can be identified to connect the 2:1 and 3:2 families.

Figures 3.26a and 3.26b illustrate these connections, with branches after the bifurcations in the connecting paths highlighted in pale red. A 3D visualization of the transition orbits along both new pathways between the two families is shown in Figures 3.27a and 3.27b, with a color gradient applied to distinguish individual orbits.

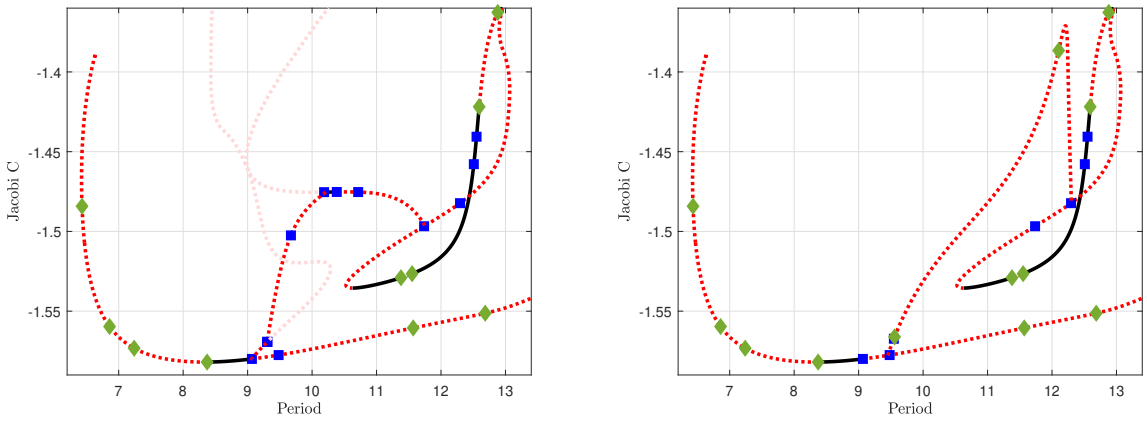

(a) (b)

Figure 3.26: Connecting paths between the 2:1 and 3:2 families for the Earth-Moon CRTBP.

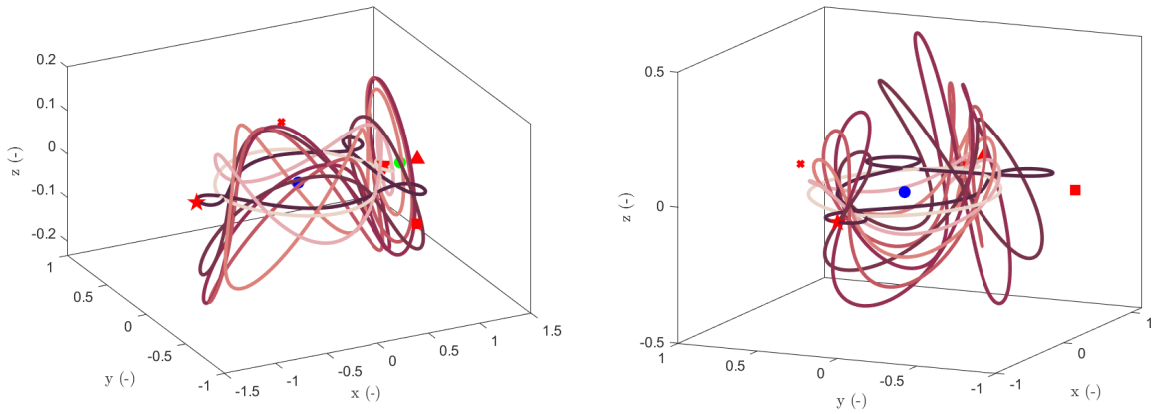

(a) (b)

Figure 3.27: 3D representation of (a) the first path of connection between the 2:1 and the 3:2 resonant periodic families; (b) the second path of connection between the 2:1 and the 3:2 resonant periodic families; relative to the primaries and Lagrange points for the Earth-Moon CRTBP.

This result highlights the robustness of the harmonic balance method in constructing complex periodic orbit transitions through bifurcation detection and stability tracking. Despite the separation of the 2:1 and 3:2 resonant families at lower mass ratios, new connecting paths are discovered and explored for mass ratios up to the Earth-Moon case.

In addition, the investigation of several period-doubling bifurcations along the 2:1 resonant family revealed a connection to the circular family $C1$ through a period-octupling bifurcation. This result further demonstrates the effectiveness of the HBM as a powerful tool for uncovering complex networks of periodic orbits and their interconnections. While it is likely that many other connections remain undetected, the HBM provides a robust framework for systematically exploring such pathways. The identified connection and the associated periodic orbits are illustrated in Figure 3.28.

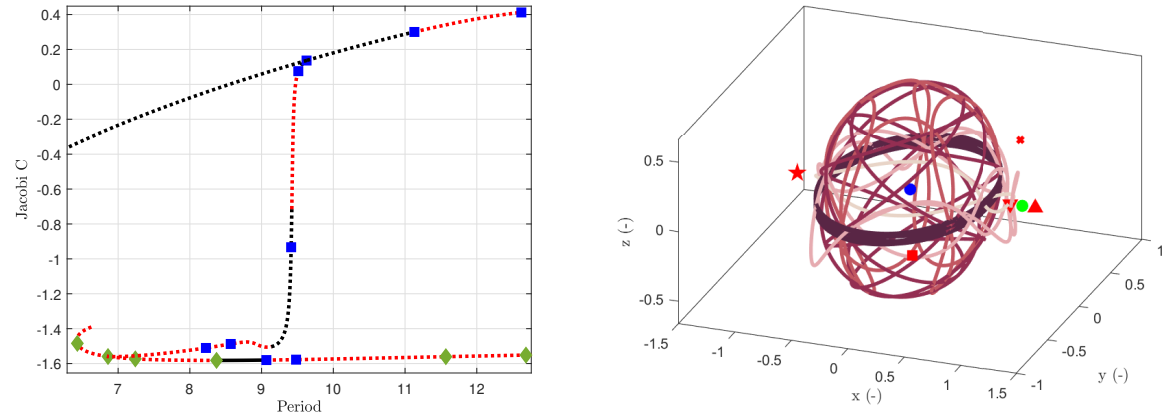

(a) (b)

Figure 3.28: Connecting paths between the 2:1 and $C1$ families for the Earth-Moon CRTBP (a) and the corresponding orbits (b).

The bifurcated path to reconnect resonant families is not exclusive to the 3:2 resonant

family. For the sake of completeness, the analysis of reconnection through bifurcations is extended to another resonant family, the 4:3 family. A brief description of the evolution of bifurcations within this family is also provided.

3.4.2 4:3 Resonant periodic family

Similarly to the 3:2 case, at low mass ratios, such as in the Sun-Earth system, the 4:3 resonant family is connected to the 3:2 family. These two families disconnect at a critical mass ratio, $\mu \approx 6.508\text{e}{-4}$. A comparison of the continuation process, similar to Figure 3.20, is presented in Figure 3.25. A similar pattern emerges, featuring an unstable left branch with one period-doubling bifurcation that transitions to a stable branch. This stable branch maintains an almost constant Jacobi constant until a period of approximately 8π, corresponding to the 4:3 resonant family. Two branch-point bifurcations are also located on this branch.

Increasing the mass ratio μ to $4.050\text{e}{-3}$ results in a large unstable branch emanating from the 3:2 family, featuring four period-doubling bifurcations and one branch-point bifurcation. The isolated 4:3 family exhibits similarities with the solutions discussed in the previous section (Figure 3.20). Four branch points are identified, along with two period-doubling bifurcations instead of four. The solutions are predominantly unstable, with two portions of stable orbits detected between the period-doubling bifurcations and the fold of the loop at both extremities of the closed branch.

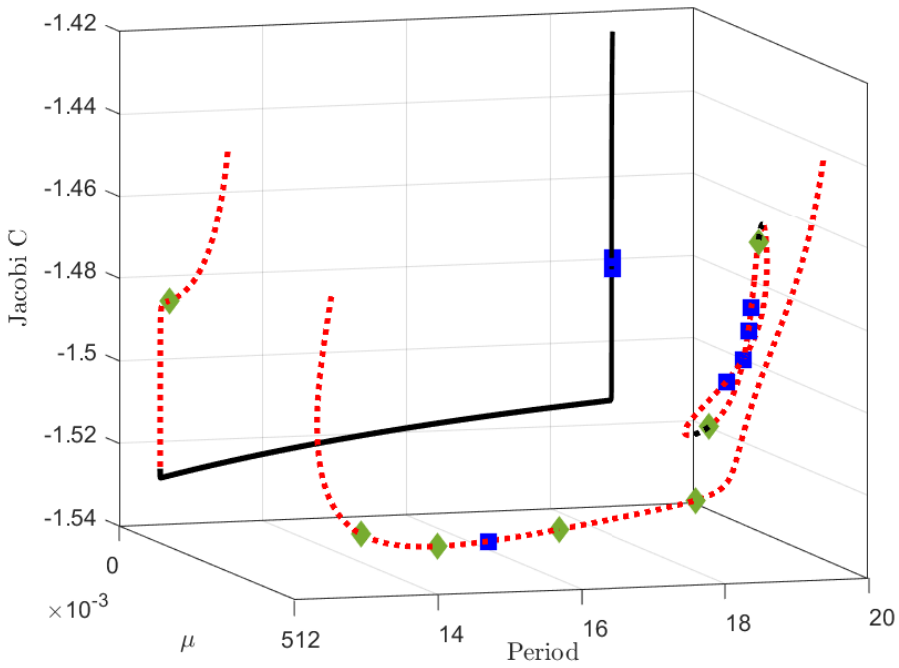

Figure 3.29: Continuation process with HB of the 3:2 and 4:3 resonant families with respect to the mass ratio μ.

The focus is placed on the branch point that appears on the lower part of the 3:2

continuation. By applying the harmonic balance method for branch switching, a path of periodic orbits reconnecting the two families is constructed, mirroring the results found in the previous section. Figures 3.30a-b depict the connecting branch and the corresponding 3D representation of the orbits along this connection, respectively.

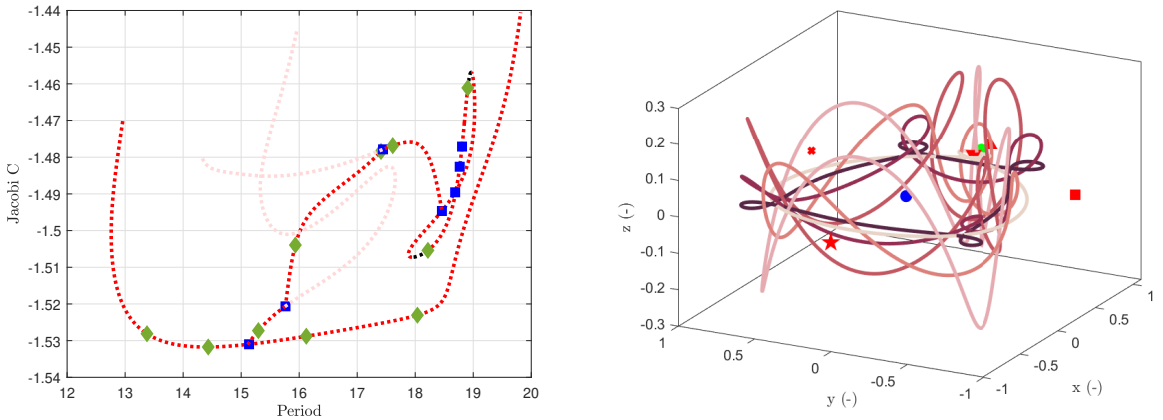

(a) (b)

Figure 3.30: (a) Connecting path between the 3:2 and 4:3 families for the Earth-Moon CRTBP;(b) 3D representation of the path of connection between the 3:2 and the 4:3 resonant periodic families relative to the primaries and Lagrange points for $\mu = 0.004050$.

3.5 Continuation with respect to the mass ratio μ

As introduced in the previous chapter, the continuation in HBM is not restricted to the frequency of the solution. Instead of differentiating Eq. (2.31) with respect to ω, it can be differentiated with respect to the mass ratio μ. In this case, the Jacobian of the HBM system takes the form $\mathbf{J}(\mathbf{y}_i) = \begin{bmatrix}\mathbf{h_z} & \mathbf{h}_\mu & \mathbf{h}_\eta\end{bmatrix}$ where

$$\mathbf{h}_\mu = -\frac{\partial \mathbf{b}(\mathbf{z},\mu)}{\partial \mu} \tag{3.20}$$

and

$$\frac{\partial \mathbf{b}(\mathbf{z},\mu)}{\partial \mu} = (\mathbf{\Gamma}(\omega))^+ \frac{\partial \tilde{\mathbf{f}}(\mathbf{z},\mu)}{\partial \mu} \tag{3.21}$$

The derivative of the force with respect to μ across the three degrees of freedom is $\frac{\partial \tilde{\mathbf{f}}(\mathbf{z},\mu)}{\partial \mu} = (\frac{\partial f_x}{\partial \mu}, \frac{\partial f_y}{\partial \mu}, \frac{\partial f_z}{\partial \mu})$. The explicit expressions of these components are given by

$$\frac{\partial f_x}{\partial \mu} = \frac{1-2\mu-x}{\|\mathbf{r}_1\|^3} - 3(1-\mu)\frac{(x+\mu)^2}{\|\mathbf{r}_1\|^5} + \frac{x-1+2\mu}{\|\mathbf{r}_2\|^3} - 3\mu\frac{(x-1+\mu)^2}{\|\mathbf{r}_2\|^5}, \tag{3.22}$$

$$\frac{\partial f_y}{\partial \mu} = -\frac{y}{\|\mathbf{r}_1\|^3} - 3(1-\mu)\frac{y(x+\mu)}{\|\mathbf{r}_1\|^5} + \frac{y}{\|\mathbf{r}_2\|^3} - 3\mu\frac{y(x-1+\mu)}{\|\mathbf{r}_2\|^5}, \tag{3.23}$$

$$\frac{\partial f_z}{\partial \mu} = -\frac{z}{\|\mathbf{r}_1\|^3} - 3(1-\mu)\frac{z(x+\mu)}{\|\mathbf{r}_1\|^5} + \frac{z}{\|\mathbf{r}_2\|^3} - 3\mu\frac{z(x-1+\mu)}{\|\mathbf{r}_2\|^5}. \tag{3.24}$$

with $\|\mathbf{r}_1\| = \sqrt{(x+\mu)^2+y^2+z^2}$ and $\|\mathbf{r}_2\| = \sqrt{(x-(1-\mu))^2+y^2+z^2}$. This adapted HBM formulation makes it possible to explore periodic orbits from a different perspective. For a fixed period, one can follow the evolution of the families introduced earlier as μ varies. For example, Figure 3.31 shows the continuation of the vertical family $V1$ for a period T = 3242 as μ increases from 0 up to approximately 0.25.

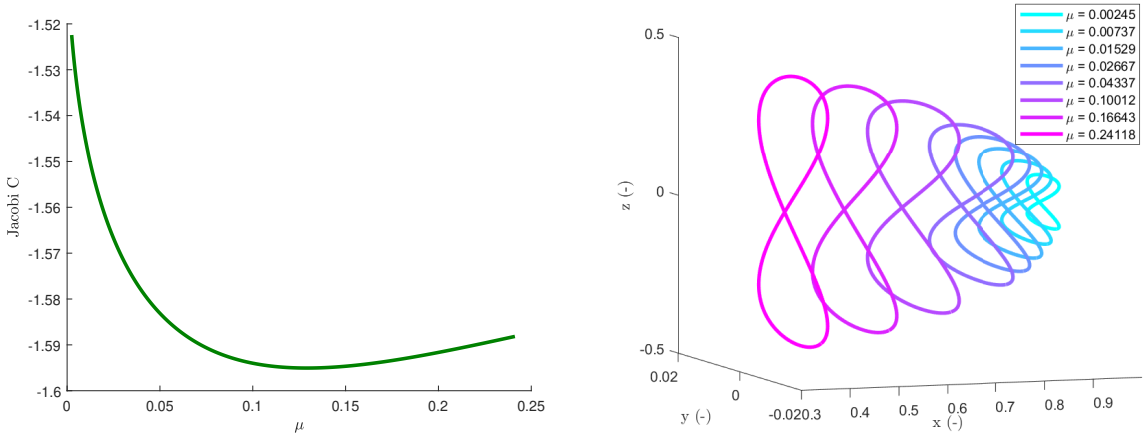

(a) (b)

Figure 3.31: (a) Continuation of the V1 family with respect to the mass ratio μ; (b) Evolution of the V1 orbits with respect to the mass ratio μ.

As shown in Figure 3.31a, the Jacobi constant decreases with increasing μ up to $\mu \approx 0.12$ after which it rises again. The overall orbital geometry remains the characteristic "8" shape. As μ grows, the orbits expand both vertically and horizontally until the minimum Jacobi constant is reached; beyond this point, the width decreases while the vertical extent continues to increase. The instability of these solutions persists for all values of μ.

In the previous section, continuation with respect to the frequency ω was applied to resonant families (2:1, 3:2) for various mass ratios, as illustrated in Figure 3.20. Using μ as the continuation parameter instead provides additional insight into the dynamics, especially in connection with bifurcations and changes in stability. Figure 3.32 shows the evolution of solutions for a fixed period T = 10.5629.

The associated orbits are displayed in Figure 3.33. For small values of μ, the orbit is nearly circular and stable. As μ increases, the 3:2 resonant features become more pronounced. The transition from stability to instability in Figure 3.32 is explained by the period-doubling bifurcations listed in Table 3.2 and illustrated in Figure 3.24. As the unstable region shifts toward higher periods, the orbits regain stability. The branch eventually folds back around $\mu = 0.012324$, giving rise to unstable solutions associated with the upper part of the 3:2 resonant loop. Another fold at low μ reveals unstable periodic orbits at higher Jacobi constants, whose geometry corresponds to the last orbit shown in Figure 3.33.

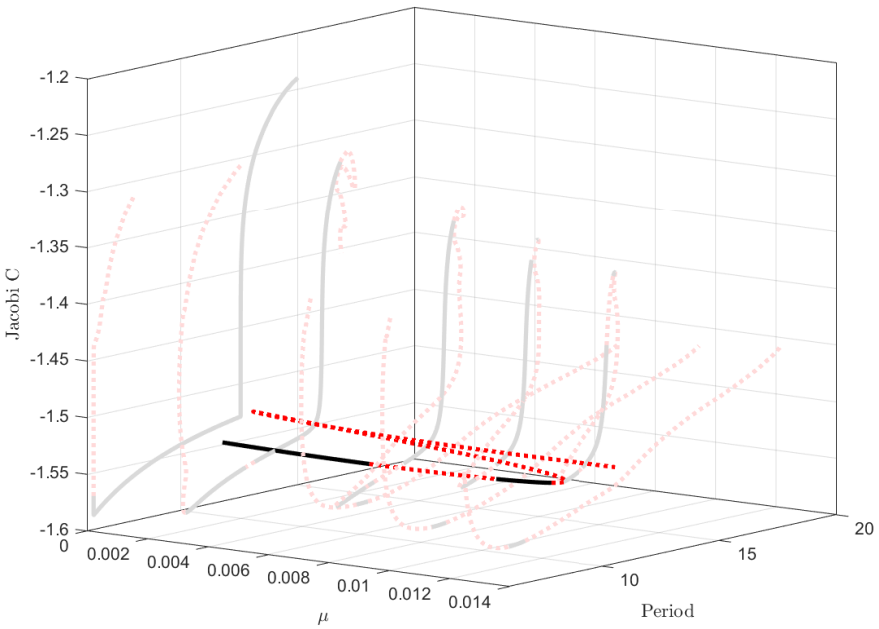

Figure 3.32: Continuation along the mass ratio μ with HB of the 2:1 and 3:2 resonant families for a period T = 10.5629

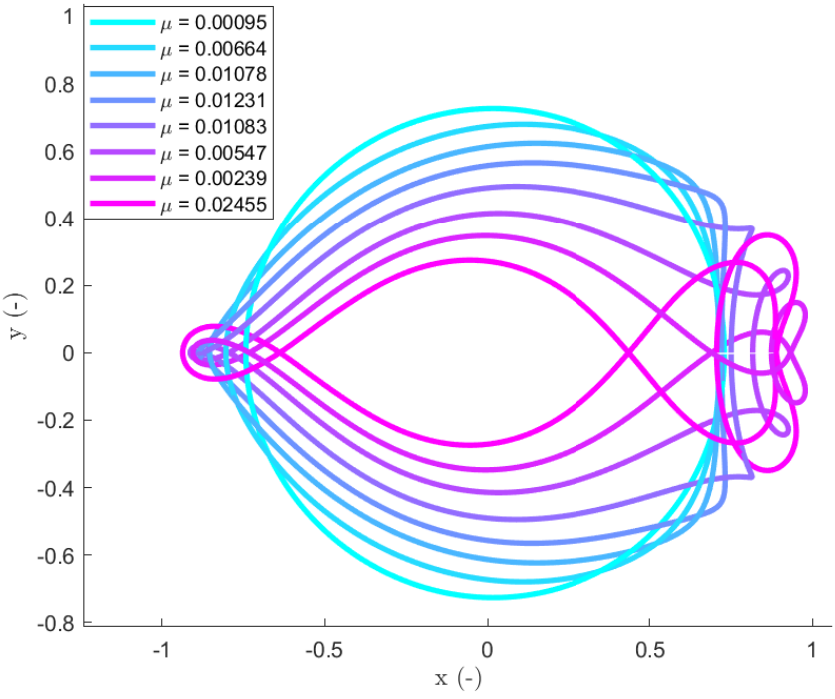

Figure 3.33: Evolution of the resonant orbits with respect to the mass ratio μ.

3.6 Conclusion

This chapter introduced the equations of motion governing the Circular Restricted Three-Body Problem (CRTBP) and explicitly presented its equilibrium points. The application of the Harmonic Balance Method (HBM) offers several distinct advantages over conventional time integration or collocation-based continuation methods. By working directly in the frequency domain, HBM enforces periodicity naturally and avoids issues related to accumulated integration errors. Unlike time-domain methods, it is inherently suited for the analysis and continuation of families of periodic solutions, making it particularly effective in mapping complex bifurcation structures. Furthermore, HBM demonstrates robust behavior even near sensitive regions, such as close approaches to the primaries, where traditional methods may fail or require special handling. These characteristics make HBM not only a competitive alternative but also a complementary tool to established techniques like `AUTO`, enabling richer exploration of the CRTBP landscape. Beginning from a single periodic orbit, the approach generated a vast interconnected map of solutions emanating from different types of bifurcations.

A particular emphasis was placed on the 3:2 periodic resonant orbits and their connection to the 2:1 resonant family as a function of the mass ratio in the CRTBP. By following the branches emanating from multiple bifurcations within the 3:2 family, variations in stability with respect to the orbital period were revealed, confirming the persistent existence of stable solutions across the entire range of periods. The bifurcation tracking capabilities of the harmonic balance method further enabled the construction of previously unreported connecting paths within the 4:3 resonant family, thereby uncovering a new reconnection pattern between the $n+1$:n and n:$n-1$ resonant families for mass ratios up to that of the Earth–Moon system. To the author's knowledge, this is the first time such connections have been explicitly identified and characterized using a frequency-domain formulation.

The last part of this chapter explored an alternative continuation approach, highlighting the versatility of the HBM for periodic solutions. Instead of using the frequency, the continuation parameter was set to the mass ratio μ, allowing the method to track the evolution of the $V1$ and 3:2 resonant families for selected periods. This change of perspective not only uncovers periodic orbits that might otherwise remain hidden but also provides valuable insight into the behavior of bifurcations and stability across different CRTBP systems.

Despite the intrinsic complexity of this autonomous dynamical system, the results clearly demonstrate the effectiveness of the HBM in reproducing and extending the known structure of periodic orbits in the circular restricted three-body problem. The method successfully recovered the classical periodic families around the equilibrium points and accurately captured their bifurcations and stability transitions. Its continuation and branching capabilities enabled the systematic exploration of resonant families such as the 3:2 and 4:3 orbits, including the identification of new connecting paths between resonant branches. The close agreement with reference results obtained using `AUTO` confirms the accuracy and reliability of the frequency-domain formulation. These achievements demonstrate that the harmonic balance framework provides not only a computationally efficient alternative to time-domain integration but also a powerful tool for uncovering previously unreported dynamical connections. This success establishes a solid foundation

for its extension to more complex gravitational environments, such as those surrounding irregular asteroids, addressed in the following chapter.

Chapter 4

Periodic and quasiperiodic propagation around the asteroid 433 Eros

4.1 Introduction

Interest in small celestial bodies has reached unprecedented levels in recent years, with numerous recent and upcoming space missions targeting asteroids and comets. Notable examples include ESA's Rosetta mission, which successfully landed on comet 67P/Churyumov-Gerasimenko in 2014 [94]; NASA's Psyche mission, launched in 2023, which will be the first to orbit a metal-rich asteroid, 16 Psyche [95]; and Lucy, launched in 2021, which has already encountered two asteroids and is scheduled to visit nine additional Trojan asteroids trapped at Jupiter's Lagrangian points [96]. Other landmark missions include OSIRIS-REx, which collected and returned samples from asteroid 101955 Bennu after a successful surface contact in 2020 [97]; Hayabusa2, a Japanese mission that recovered samples from asteroid Ryugu in 2019 and returned them to Earth in 2020 [98]; and DART, the first planetary defense test mission, which altered the trajectory of the asteroid Dimorphos in 2022 [99]. The Hera mission will follow up on DART by analyzing the impact's aftermath in 2026 [100].

Planning and executing such missions requires a precise understanding of the dynamical environment surrounding these small bodies. Various methods exist to approximate gravitational attraction, including the mascon method [101], the polyhedron method [102] and the hybrid tetrahedron approach [103]. The mascon method discretizes the body into a set of point masses (mascons) to approximate its mass distribution. Although simple to implement, it suffers from reduced accuracy due to voids between discrete mass elements. The tetrahedron method improves accuracy by representing the volume with tetrahedral elements of specified mass, eliminating such voids. However, the method primarily serves in numerical modeling. The primary method employed in this work is the polyhedron model [104, 105], which assumes a uniform density and uses a surface mesh to represent the shape of the asteroid. This approach provides high precision in gravitational modeling but can be computationally demanding, particularly as mesh resolution increases. However, computational efficiency can be greatly improved by using parallel processing techniques.

The identification of periodic orbits plays a central role in designing spacecraft trajectories. Early work by Riaguas et al. (1999) demonstrated the existence of periodic orbits

around a linear segment [106]. Scheeres computed multiple periodic orbits around the asteroid 4769 Castalia using the Newton-Raphson method in combination with Poincaré maps [107]. Additional studies investigated periodic orbits around the asteroids 216 Kleopatra and 4179 Toutatis, led by Yu [4] and Scheeres [108], respectively. Yu also developed a hierarchical grid search technique, later applied by Jiang to compute near-surface periodic orbits for asteroids 216 Kleopatra and 101955 Bennu [109]. However, these grid-based approaches tend to be computationally expensive, particularly when coupled with the polyhedron method. To address this, Shang proposed a modified approach that uses mascons with global optimization and local refinement [110].

The complex dynamical environment near asteroids can also give rise to quasi-periodic orbits. Recent efforts have focused on identifying such orbits, especially near slowly rotating asteroids and small planetary moons, leading to the concept of quasi-frozen orbits [111, 112, 113]. In 2018, Baresi introduced a numerical method for continuing quasi-periodic orbit families in the time domain [114]. In 2023, he extended this work to compute two-dimensional quasi-periodic tori around planetary satellites such as Io and Phobos [115].

The search for periodic and quasi-periodic orbits typically relies on time-integration techniques and is inherently computationally intensive. In this chapter, we apply the harmonic balance method (HBM) to asteroid 433 Eros to identify periodic orbits, assess their stability, and construct a comprehensive bifurcation map. Unlike time-marching approaches such as multiple shooting or collocation, which rely on integrating the equations of motion over many steps or segments, HBM tackles the problem directly in the frequency domain. This not only avoids cumulative integration errors but also provides a global view of the solution from the outset. Particularly for smooth, closed orbits, HBM can deliver accurate results with relatively few harmonics, making it well-suited for preliminary analyses or continuation studies. Its capacity to handle strong nonlinearities and compute stability properties without resorting to time integration offers a significant benefit, especially in the complex dynamical environment near an asteroid. The first section details the implementation of the polyhedron model to compute the gravitational field of 433 Eros. Section 4.3 presents a catalog of more than 100 bifurcations and a bifurcation map, with periodic orbits classified by their geometrical properties. Section 4.4 focuses on resonant orbits, particularly near equilibrium points. In Section 4.5, the focus is put on the amplitude of the Fourier coefficients to provide a spectral analysis of the transitions between different bifurcations. Finally, Section 4.6 applies the multi-harmonic balance method (MHBM) to compute and analyze quasi-periodic orbits and their stability around 433 Eros.

4.2 Polyhedron method

A polyhedron is a three-dimensional solid whose surface consists of flat polygonal faces that intersect along straight edges and meet at vertices. Each edge is shared by exactly two faces, and each vertex is the meeting point of three or more edges and, correspondingly, three or more faces. It is important to emphasize that the vertex coordinates alone are insufficient to fully define a polyhedron. A complete description also requires its connectivity topology, specifying which pairs of vertices are connected by edges and how

these edges define the boundaries of the faces [102].

Each face f, of the polyhedron is associated with an outward-pointing unit normal vector $\hat{\mathbf{n}}_f$, which is essential in the computation of the matrix $\mathbf{F}_f$:

$$\mathbf{F}_f = \hat{\mathbf{n}}_f \otimes \hat{\mathbf{n}}_f \tag{4.1}$$

Each edge e, also has an associated unit normal vector, $\hat{\mathbf{n}}_e^f$, defined with respect to a given face f. This vector points outward from the polyhedron and is perpendicular to both the normal face $\hat{\mathbf{n}}_f$ and the direction of the edge. It is used to define the contribution of the edge to the overall gravitational potential. The matrix associated with an edge defined by vertices P_1 and P_2, which lies between faces A and B, is given by:

$$\mathbf{E}_{12} = \hat{\mathbf{n}}_A \otimes \hat{\mathbf{n}}_{12}^A + \hat{\mathbf{n}}_B \otimes \hat{\mathbf{n}}_{21}^B \tag{4.2}$$

Figure 4.1 provides a graphical representation of the various normal vectors, including face and edge normals, to aid in visualizing their geometric relationships.

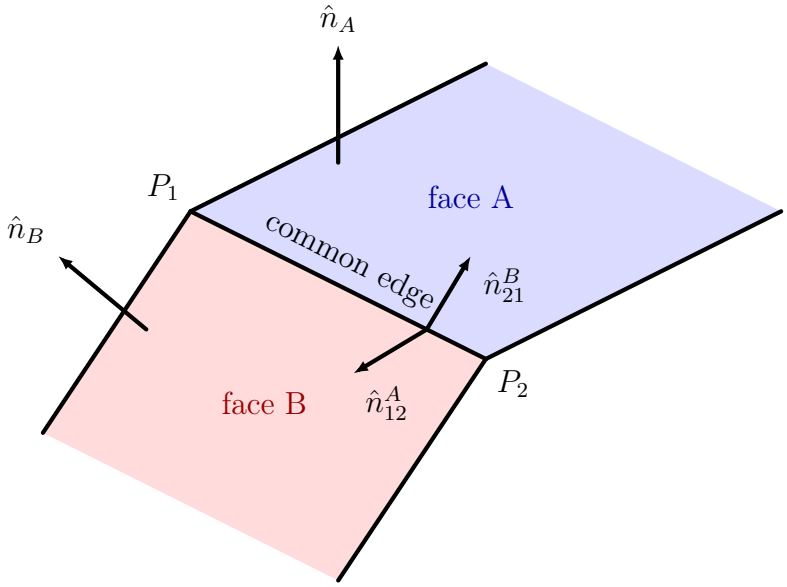

Figure 4.1: Face and edge normal vectors.

The gravitational potential U of a polyhedron is expressed as

$$U = \frac{1}{2} G\sigma \sum_{e \in \text{edges}} \mathbf{r}_e \cdot \mathbf{E}_e \mathbf{r}_e \cdot L_e - \frac{1}{2} G\sigma \sum_{f \in \text{faces}} \mathbf{r}_f \cdot \mathbf{F}_f \mathbf{r}_f \cdot \omega_f \tag{4.3}$$

where G is the gravitational constant, with a value of $6.67430 \times 10^{-11} \text{m}^3\text{kg}^{-1}\text{s}^{-2}$ and σ denotes the constant density of the polyhedron. The dimensionless scalars L_e and ω_f are associated with the geometric properties of the edges and faces, respectively.

$$L_e \equiv \int_e \frac{1}{r}\, ds = \int_{P_i}^{P_j} \frac{1}{r}\, ds = \ln \frac{r_i + r_j + e_{ij}}{r_i + r_j - e_{ij}} \tag{4.4}$$

$$\omega_f = \iint_{\text{triangle}} \frac{\Delta z}{r^3}\, dS = 2 \arctan \frac{\mathbf{r}_i \cdot (\mathbf{r}_j \times \mathbf{r}_k)}{r_i r_j r_k + r_i(\mathbf{r}_j \cdot \mathbf{r}_k) + r_j(\mathbf{r}_k \cdot \mathbf{r}_i) + r_k(\mathbf{r}_i \cdot \mathbf{r}_j)} \tag{4.5}$$

Considering a field point located at position O, the vector $\mathbf{r}_i$ connects O to the vertex P_i, and its magnitude is denoted r_i. The quantity e_{ij} represents the length of the edge connecting vertices P_i to P_j. A graphical representation illustrating this configuration for the specific case of a single triangular face is provided in Figure 4.2.

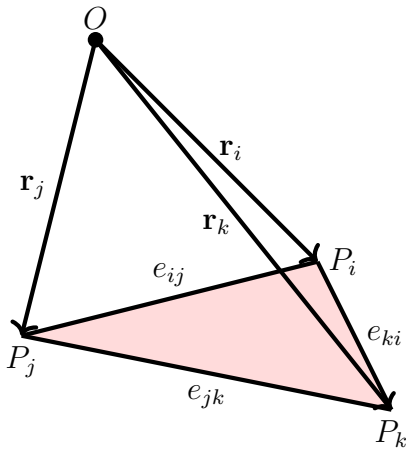

Figure 4.2: Graphical representation of the field-point to polyhedron vertices vectors.

The gravitational attraction force—defined as the gradient of the potential—as well as its gradient and Laplacian, corresponding to equations (4.6)–(4.8), can be directly derived from the expression of the potential.

$$\nabla U = -G\sigma \sum_{e \in \text{edges}} \mathbf{E}_e \mathbf{r}_e \cdot L_e + G\sigma \sum_{f \in \text{faces}} \mathbf{F}_f \mathbf{r}_f \cdot \omega_f \tag{4.6}$$

$$\nabla\nabla \mathbf{U} = G\sigma \sum_{e \in \text{edges}} \mathbf{E}_e \cdot L_e - G\sigma \sum_{f \in \text{faces}} \mathbf{F}_f \cdot \omega_f \tag{4.7}$$

$$\nabla^2 U = -G\sigma \sum_{f \in \text{faces}} \omega_f \tag{4.8}$$

The Laplacian of the gravitational potential vanishes when the field point lies outside the polyhedron, as the summation term $\sum_f \omega_f$, evaluates to zero in this case. However, when the field point is located inside the polyhedron, the sum equals 4π. This fundamental result serves as a straightforward criterion for detecting potential orbit penetration or collision. The full derivation of these expressions is presented in [102] for readers seeking further detail.

4.2.1 Application to the asteroid 433 Eros

Eros is one of the largest near-Earth objects, making it one of the most extensively studied asteroids to date. Figure 4.3 presents images captured by the NEAR Shoemaker probe during its mission in 2000. This mission provided a wealth of data on the asteroid, including detailed measurements of its topography [116] and physical characteristics [117], which have been instrumental in generating high-resolution shape models. The total mass of 433 Eros is estimated at 6.69×10^{15}kg with a bulk density, ρ, of 2.67 ± 0.03 g cm^{-3}. Its dimensions were measured as $34.4 \times 11.2 \times 11.2$ km and the rotation period is approximately 5.27 hours [118]. When combined with the polyhedron method, these parameters allow

for an accurate modeling of the gravitational environment surrounding Eros. Figure 4.4 displays the polyhedron model constructed from a mesh consisting of 856 edges and 1708 faces [119].

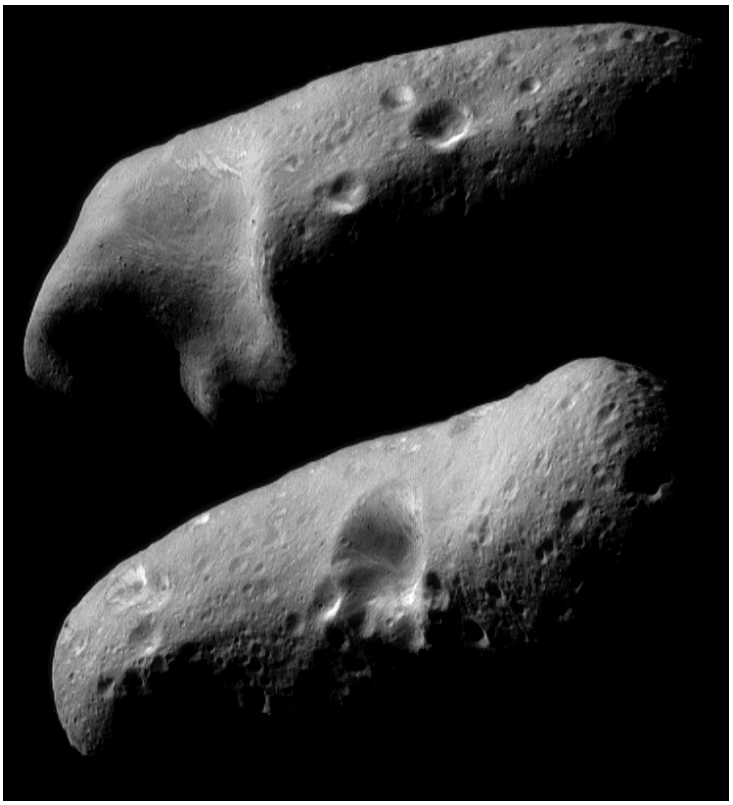

Figure 4.3: Eastern and western hemispheres of asteroid 433 Eros. Pictures were taken by NEAR-Shoemaker on 23 February 2000 [120].

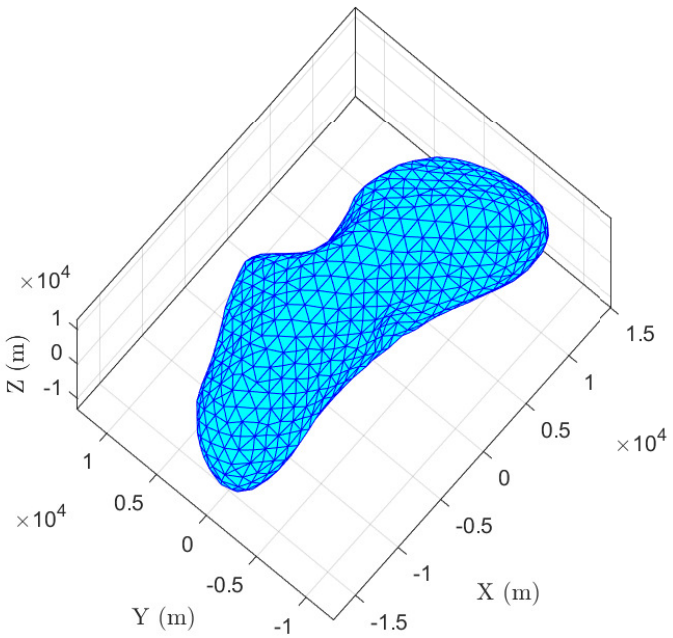

Figure 4.4: 3D surface mesh of asteroid 433 Eros with 856 edges and 1708 faces.

The equations of motion governing the dynamics of a massless body in orbit around an asteroid are given by:

$$\ddot{\mathbf{x}} + 2\omega_{\mathbf{a}} \times \dot{\mathbf{x}} + \omega_{\mathbf{a}} \times (\omega_{\mathbf{a}} \times \mathbf{x}) - \nabla U(\mathbf{x}) = 0 \tag{4.9}$$

where $\mathbf{x}$ denotes the position vector of the massless body, $\omega_{\mathbf{a}} = [0, 0, \omega_a]$ is the angular velocity of the asteroid about its principal axis of inertia, and $\nabla U(\mathbf{x})$ corresponds to the gravitational acceleration derived from equation (4.6). The distribution of the gravitational potential on the surface of asteroid 433 Eros is illustrated in Figure 4.5.

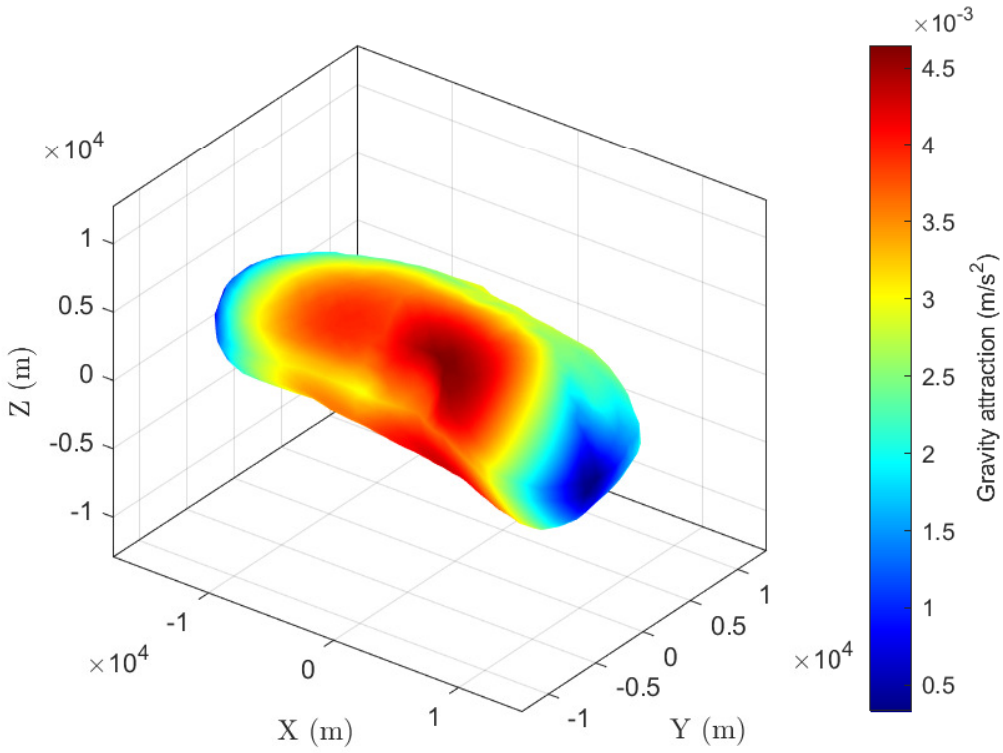

Figure 4.5: Intensity of the gravitational potential on the surface of 433 Eros.

Equation (5.1) can be recast in the HBM formalism with the matrices $\mathbf{M} = \begin{bmatrix} 1 & 0 & 0 \\ 0 & 1 & 0 \\ 0 & 0 & 1 \end{bmatrix}$, $\mathbf{C} = \begin{bmatrix} 0 & -2\omega_a & 0 \\ 2\omega_a & 0 & 0 \\ 0 & 0 & 0 \end{bmatrix}$, $\mathbf{K} = \begin{bmatrix} -\omega_a^2 & 0 & 0 \\ 0 & -\omega_a^2 & 0 \\ 0 & 0 & 0 \end{bmatrix}$ and $\mathbf{f}_{nl} = \begin{bmatrix} \frac{\partial \mathbf{U}(\mathbf{x})}{\partial x} \\ \frac{\partial \mathbf{U}(\mathbf{x})}{\partial y} \\ \frac{\partial \mathbf{U}(\mathbf{x})}{\partial z} \end{bmatrix}$.

Similar to the Circular Restricted Three-Body Problem (CRTBP), the time invariance of equation (5.1) implies the existence of a conserved quantity: the Jacobi constant. In the rotating frame of the asteroid, it is expressed as:

$$J = \frac{1}{2}\dot{\mathbf{x}} \cdot \dot{\mathbf{x}} - \frac{1}{2}(\omega_{\mathbf{a}} \times \mathbf{x}) \cdot (\omega_{\mathbf{a}} \times \mathbf{x}) - U(\mathbf{x}) \tag{4.10}$$

The Jacobi constant offers valuable insight into the structure of zero-velocity surfaces and the location of equilibrium points. These surfaces represent the boundaries beyond

which a body, given its specific energy level, cannot travel, as doing so would require negative kinetic energy. In other words, all available kinetic energy would be converted into potential energy, leaving the body with zero velocity. Mathematically, this corresponds to rewriting equation (4.10) in terms of the modified potential V, such that:

$$V = -\frac{1}{2}(\omega_{\mathbf{a}} \times \mathbf{x}) \cdot (\omega_{\mathbf{a}} \times \mathbf{x}) - U(\mathbf{x}) \tag{4.11}$$

There are four critical values of V for the particular case of 433 Eros, corresponding to the four equilibrium points. Notably, two of these points, E_1 and E_2, are saddle points, while E_3 and E_4 are center points; all are linearly unstable [121]. The positions of the equilibrium points are obtained by solving $\nabla V = 0$, their coordinates are listed in Table 4.1 and are displayed in Figure 4.6.

Table 4.1: Position of the four equilibrium points around 433 Eros.

Equilibrium point	**x** (km)	**y** (km)	**z** (km)
E_1	18.444	-5.68	0.193
E_2	-19.993	-0.075	0.162
E_3	2.886	14.428	-0.015
E_4	-2.7	-13.697	-0.027

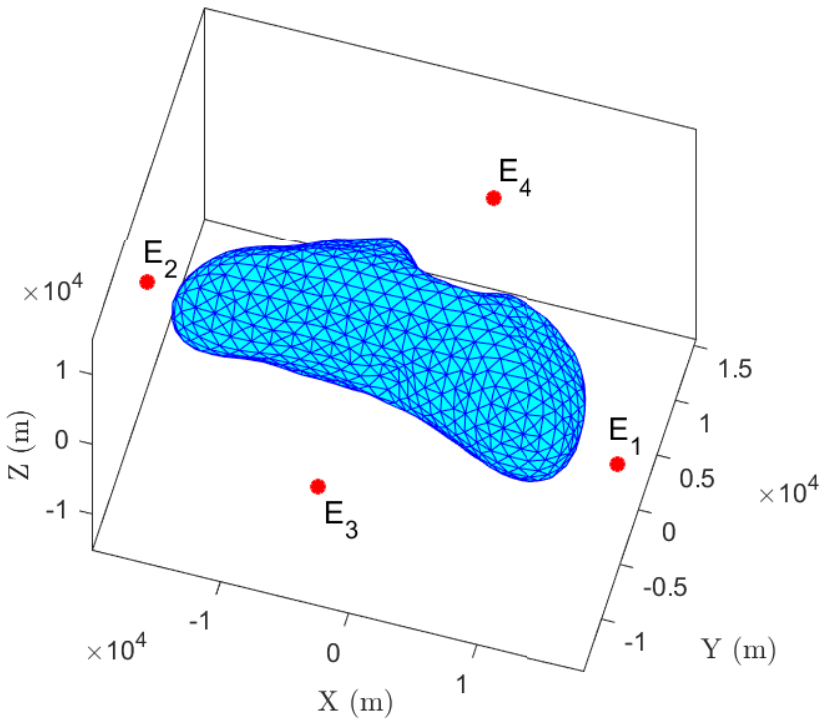

Figure 4.6: Position of the equilibrium points with respect to 433 Eros.

The influence of the number of harmonics on the accuracy of the solutions was already discussed in the previous chapter. Similar conclusions hold for the case of periodic orbits around 433 Eros. Therefore, in the results that follow, a total of 30 harmonics ($N_h = 30$)

are retained in the Fourier decomposition in order to reduce the errors associated with the Jacobi constant. In addition, the time discretization is kept equal to one in the previous chapter, $N = 512$. To ensure the periodicity of the computed solutions, the accuracy of the HBM is enforced by requiring that the residual of Eq. (2.16) remains below $\epsilon = 10^{-12}$.

Impact of the mesh refinement

The HBM is compatible with asteroid models represented by meshes of various densities and shapes. However, the resolution of the mesh directly affects computational cost; denser meshes significantly increase the time required to construct families of periodic orbits. When the goal is to identify general orbit shapes rather than highly precise trajectories, reducing the number of faces in the mesh can greatly speed up the computation, albeit at the expense of accuracy. Since HBM requires an initial guess for the orbit to begin the correction process, the ability to explore a wide range of orbit types at lower computational cost is a notable advantage. To illustrate how mesh simplification affects both CPU time and solution accuracy, four different mesh resolutions are considered in this study. The original model contains 1708 faces [91], and three progressively coarser versions are generated with 1200, 298, and 30 faces, respectively (see Figure 4.7).

Two distinct orbits are analyzed: one primarily confined to the equatorial plane, and another exhibiting a more complex three-dimensional structure with a noticeable vertical component. The results of orbit propagation using the four mesh resolutions are compared in Figure 4.8. For the planar orbit, all four meshes produce converged solutions that are extremely close to one another. The solution obtained with the coarsest mesh shows a slight deviation but still captures the essential dynamics. In contrast, for the orbit with vertical motion, discrepancies become more evident in the results from the two lower-resolution meshes. Nevertheless, even these coarser meshes manage to reproduce the overall orbit shape, making them suitable for generating initial guesses that can be refined with higher-resolution models. Initial guesses are obtained either from the literature [122], or by adjusting the initial Fourier coefficients. For example, a simple circular orbit can be readily expressed in terms of Fourier coefficients, which, after a few corrective steps, provides a suitable starting point for continuation.

Computation time is largely insensitive to the orbit type but is strongly influenced by the mesh resolution. Table 4.2 summarizes the average time per correction step and per full iteration leading to convergence. These two metrics are reported separately, as mesh resolution also affects tasks such as stability analysis and continuation prediction, which contribute to the total iteration time. All computations were carried out using `MATLAB` R2020a on a Intel(R) Core(TM) i9-9900K CPU at 3.60GHz, with 32Go RAM. From Table 4.2, it is evident that reduced-resolution meshes significantly improve performance. The 30- and 298-face meshes yield speedups of approximately 3.84× and 2.74×, respectively, compared to the full 1708-face mesh. A smaller but still notable difference is observed between the 1200- and 1708-face meshes, with negligible differences in the resulting orbits. This demonstrates that combining HBM with mesh simplification offers an effective strategy for quickly exploring families of periodic orbits. Promising candidates identified using coarse meshes can then be used as initial conditions for higher-resolution refinement.

To improve the generality and numerical conditioning of the problem, the equations of motion are adimensionalized using characteristic units of length, time, and mass. It

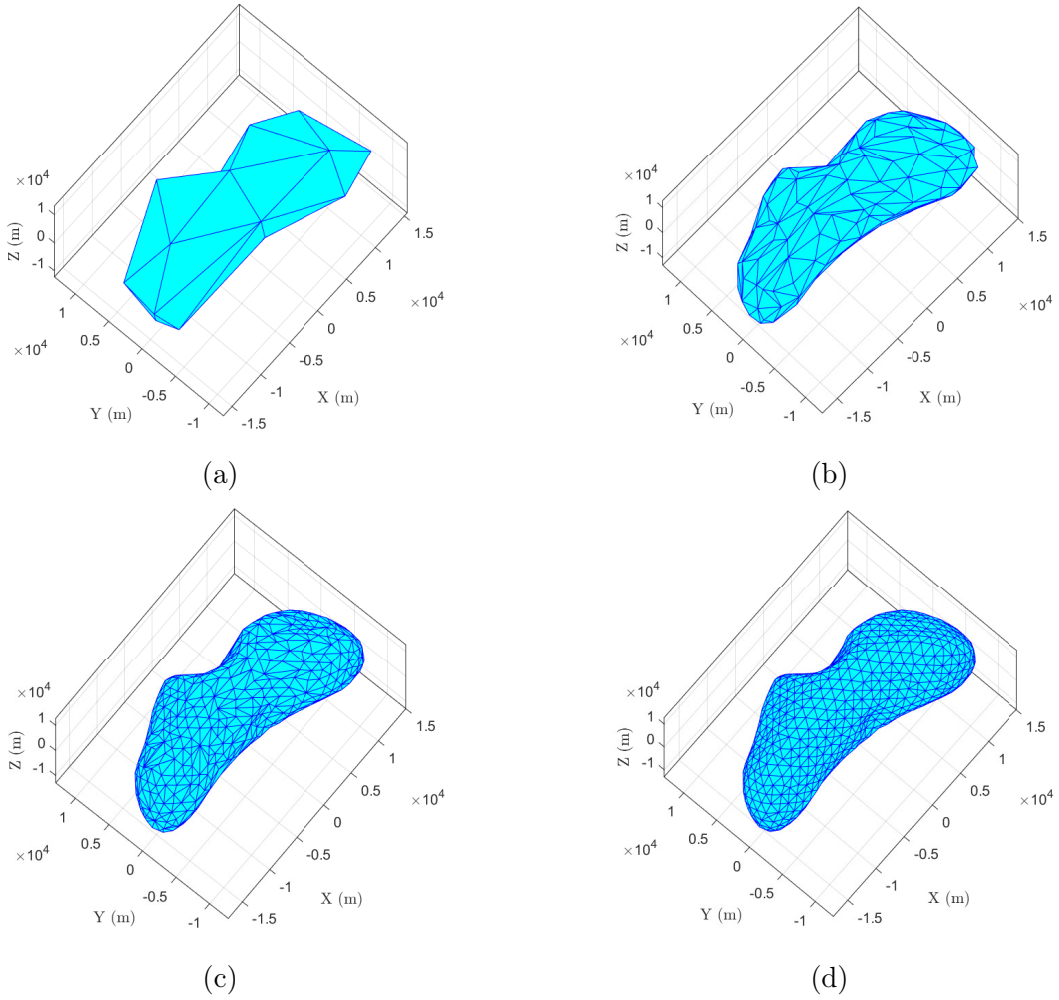

(a) (b)

(c) (d)

Figure 4.7: 3D surface mesh of asteroid 433 Eros with 17 vertices and 30 faces (a), with 151 vertices and 298 faces (b), with 602 vertices and 1200 faces (c), with 856 vertices and 1708 faces (d).

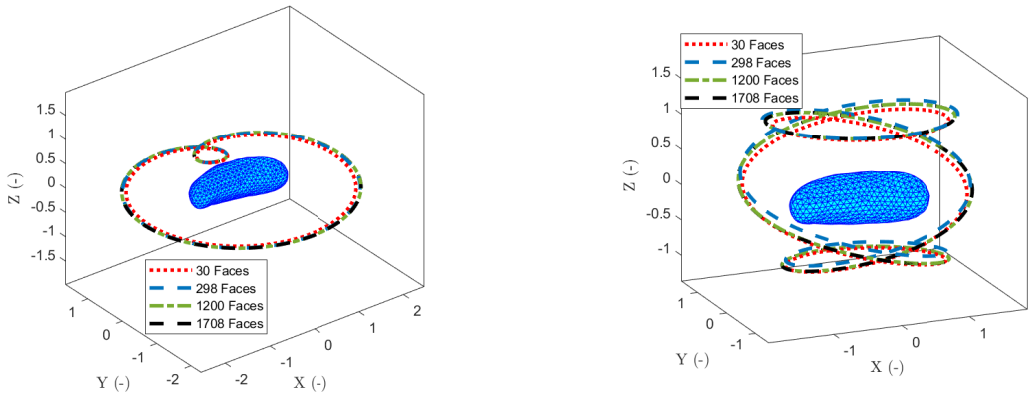

(a) (b)

Figure 4.8: Comparison of planar orbit computed with the four different meshes (a). Comparison of 3D orbit computed with the four different meshes (b).

Table 4.2: Computation time per correction and iteration for the different mesh refinements.

Mesh	CPU time/correction (s)	CPU time/iteration (s)
30 Faces	≈ 1.27	≈ 3.69
298 Faces	≈ 1.72	≈ 5.17
1200 Faces	≈ 3.35	≈ 9.95
1708 Faces	≈ 4.56	≈ 14.2

improves numerical stability and precision by minimizing the risk of floating-point errors arising from very large or small dimensional quantities. The unit of time is chosen as the asteroid's rotation period, $t_u = 5.27 \times 3600$s, the unit length $l_u = 16.84e^3$ m and the unit mass $m_u = 6.69 \times 10^{15}$kg. It is also worth noting that the mass term cancels out due to the presence of the product $G\rho$ in equation (4.6).

4.3 Main periodic families

A wide variety of periodic orbits coexist in the vicinity of irregular celestial bodies. The Harmonic Balance Method (HBM) provides a powerful framework for identifying these solutions and constructing a comprehensive bifurcation map. Figure 4.9 illustrates such a map, where the Jacobi constant is plotted against the orbital period. This representation reveals the presence of all three primary bifurcation types, with corresponding branches tracked across the diagram. Notably, while multiple period-doubling bifurcations are identified, only a single branch point is observed. The majority of periodic orbits around 433 Eros are found to be unstable. Several examples presented in this section have also been reported in prior studies using time-domain approaches [123]. Let's note that 30 harmonics were considered in order to fully capture the dynamics of the different periodic orbits.

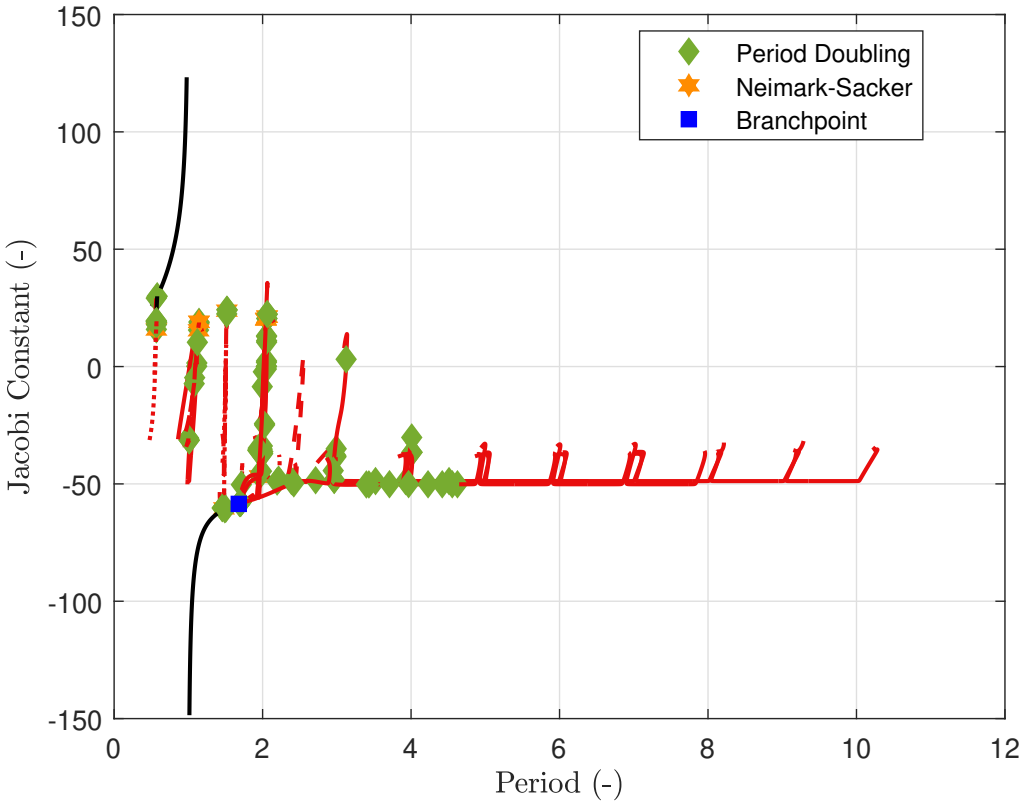

Figure 4.9: Continuation of stable (in black) and unstable (in red) periodic orbits around 433 Eros.

Given the large number of periodic solutions identified through the HBM, all bifurcations that give rise to new branches are listed in Table 4.3, sorted by increasing period. To enhance the visualization of the connections between these branches, a deconstructed version of Figure 4.9 is provided in Figure 4.10. This schematic representation highlights the structure of the bifurcation network: dashed lines indicate branches emerging from period-doubling bifurcations, while dotted lines represent secondary branches that originate from bifurcations on already period-doubled solutions. The color coding follows the convention established in the previous chapter, where black lines denote stable orbits and

red lines correspond to unstable ones.

The symbol "//" is used to indicate gaps in the continuation between pairs of branches with nearly identical Jacobi constants and orbital periods, suggesting similar orbital geometries, either around different equilibrium points or shifted in space but not connected with bifurcations. It is worth noting that the initial conditions for branches beyond a gap are obtained by deliberately overshooting the prediction of a solution from the preceding branch. The bifurcations are denoted as period doubling (PD), Neimark–Sacker (NS), or branch point (BP). Table 4.3 specifies the type of each bifurcation along with the associated dimensionless period, Jacobi constant, and the corresponding label as marked in Figure 4.10.

Table 4.3: Bifurcations encountered around asteroid 433 Eros.

Type	Period (-)	Jacobi cst (-)	Label
PD	0.56761	29.1465	PD_1
PD	0.58041	29.9525	PD_2
PD	1.0022	-30.5076	PD_{11}
PD	1.0028	-30.5476	PD_{12}
PD	1.0098	-31.3439	PD_{16}
PD	1.0121	-31.41	PD_{15}
PD	1.0785	-7.28	PD_{10}
PD	1.0848	-4.7402	PD_9
PD	1.1124	0.1313	PD_{17}
PD	1.1141	1.5178	PD_{18}
PD	1.1335	19.5227	PD_3
PD	1.1368	15.5393	PD_8
PD	1.1374	15.8453	PD_4
PD	1.1418	19.3767	PD_6
PD	1.1431	19.045	PD_{19}
PD	1.1453	18.7585	PD_5
PD	1.1458	18.6409	PD_7
PD	1.4972	-60.6822	PD_{21}
PD	1.5037	-60.5872	PD_{22}
BP	1.6793	-58.5165	BP_1
PD	1.6896	-58.1206	PD_{23}
PD	1.6972	-58.1397	PD_{24}
PD	1.9414	-34.7775	PD_{37}
PD	1.9424	-35.3276	PD_{38}
PD	1.9606	-46.4628	PD_{53}
NS	1.962	-46.8412	NS_7
NS	1.9641	-46.9332	NS_8
PD	1.9866	-37.573	PD_{54}
PD	2.0256	-24.3058	PD_{28}
PD	2.0271	-24.8698	PD_{39}
PD	2.0532	13.0937	PD_{27}
PD	2.0538	10.3995	PD_{55}

Type	Period (-)	Jacobi cst (-)	Label
PD	2.0538	10.9927	PD_{40}
PD	2.0612	22.2521	PD_{26}
PD	2.06268	22.3411	PD_{25}
NS	2.0442	20.0458	NS_{9}
NS	2.045	20.4044	NS_{10}
PD	2.2424	10.3421	PD_{20}
PD	2.264	19.0591	PD_{13}
NS	2.2748	15.4504	NS_{2}
NS	2.2753	15.7825	NS_{1}
PD	2.2796	17.9082	PD_{14}
NS	2.2848	19.0131	NS_{3}
NS	2.2853	19.079	NS_{4}
PD	2.41	-49.105	PD_{29}
PD	2.4204	-49.7634	PD_{41}
PD	2.913	-60.2813	PD_{56}
PD	2.951	-44.3426	PD_{43}
NS	2.9593	-60.4317	NS_{5}
PD	2.9644	-48.3188	PD_{30}
PD	2.9889	-38.419	PD_{31}
PD	2.9913	-35.0437	PD_{32}
PD	3.0362	24.2222	PD_{58}
PD	3.1251	3.0993	PD_{42}
PD	3.3979	-50.2375	PD_{44}
PD	3.4013	-58.0013	PD_{61}
PD	3.404	-57.9008	PD_{70}
PD	3.4122	-57.9225	PD_{62}
PD	3.4162	-57.8066	PD_{71}
PD	3.4172	-57.8857	PD_{63}
PD	3.4318	-50.2157	PD_{45}
PD	3.521	-48.8105	PD_{33}
PD	3.7093	-50.1298	PD_{46}
PD	3.8754	-35.7693	PD_{74}
PD	3.8767	-35.6124	PD_{73}
PD	3.9265	-48.7963	PD_{34}
PD	3.9666	-50.1044	PD_{48}
PD	3.9906	-8.5624	PD_{65}
PD	4.0021	-37.1016	PD_{83}
PD	4.0047	-36.238	PD_{75}
PD	4.0088	-30.2116	PD_{47}
PD	4.0136	-36.5268	PD_{35}
PD	4.0199	-2.2442	PD_{64}
PD	4.1002	-1.0565	PD_{82}
PD	4.1028	0.154	PD_{80}
PD	4.1037	1.8092	PD_{79}
PD	4.1051	2.3871	PD_{78}
NS	4.1191	21.1983	NS_{11}

Type	Period (-)	Jacobi cst (-)	Label
NS	4.1199	21.3195	NS_{12}
PD	4.1152	20.4362	PD_{67}
PD	4.1157	20.522	PD_{56}
PD	4.2286	-50.1687	PD_{49}
PD	4.3909	-49.0063	PD_{84}
PD	4.4198	-50.1687	PD_{50}
PD	4.4247	-48.9668	PD_{85}
PD	4.5113	-48.8044	PD_{36}
PD	4.5548	-50.1661	PD_{51}
PD	4.6247	-50.1646	PD_{52}
PD	5.8322	-60.2284	PD_{57}
PD	5.9303	-48.1999	PD_{68}
PD	5.9699	-37.853	PD_{69}
NS	6.072	23.8063	NS_{6}
PD	6.0678	22.4285	PD_{59}
PD	6.0953	24.1038	PD_{60}
PD	6.8555	-50.324	PD_{72}
PD	7.94	-44.5928	PD_{77}
PD	7.9742	-35.1899	PD_{86}
PD	7.9853	-33.8403	PD_{76}
PD	8.2038	-0.2622	PD_{81}
PD	8.8607	-48.1787	PD_{87}

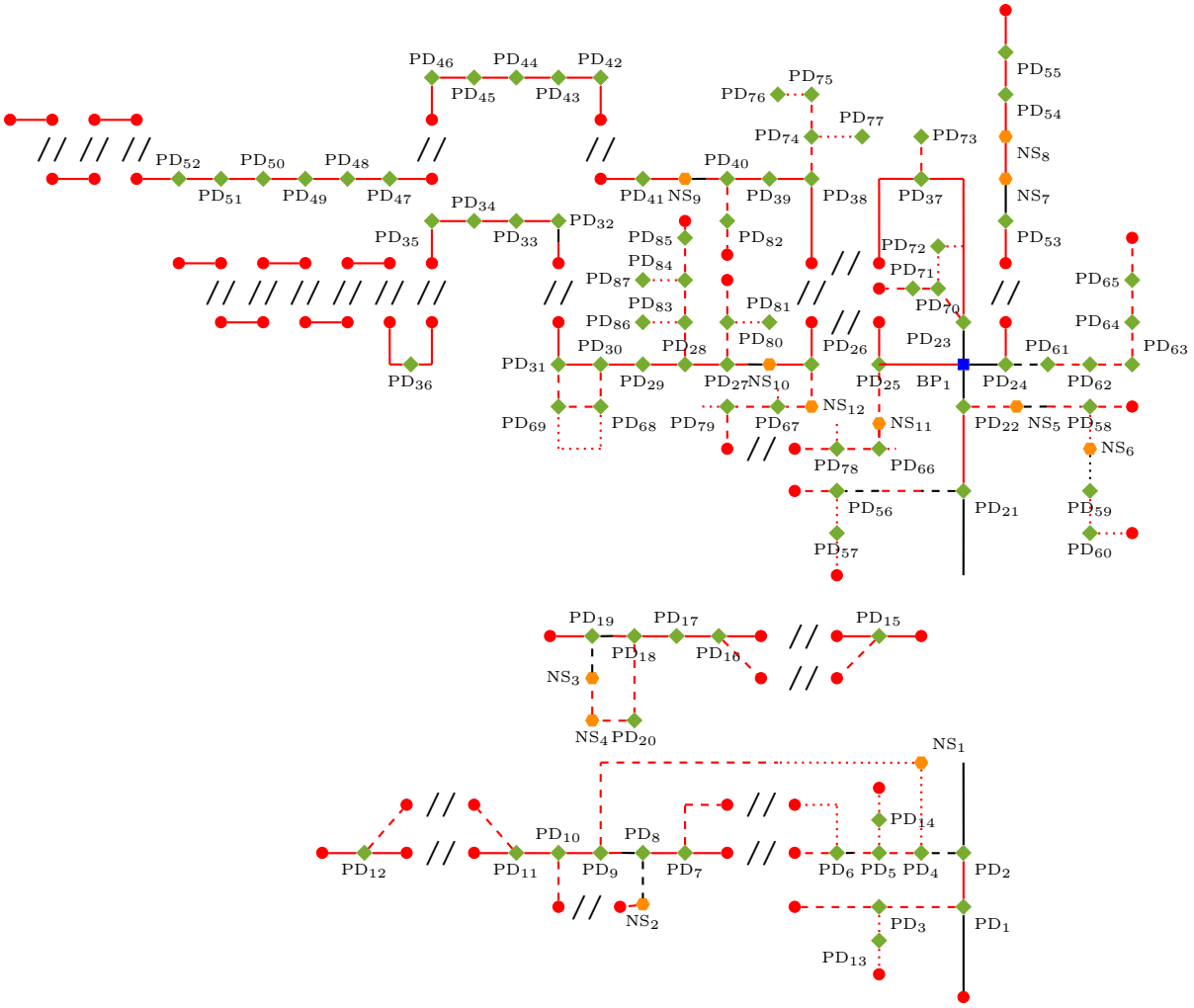

Figure 4.10: Schematic bifurcation map for 433 Eros.

In contrast to the results presented in the previous chapter for the CRTBP, the irregular shape of asteroid 433 Eros results in a highly non-uniform gravitational field, making the classification of well-defined orbital families more challenging. In 2019, Jiang presented few families around the equilibrium points of irregular bodies [124]. The simplest class of orbits is the planar circular orbit. However, even this basic configuration exhibits two distinct variants around 433 Eros. Since the asteroid rotates counterclockwise, circular orbits may rotate either in the opposite direction (clockwise), called *retrograde*, or in the same direction (counterclockwise), called *prograde*. It is important to note that in the rotating frame fixed to Eros, both orbit families appear as prograde. The NEAR-Shoemaker probe was placed in particular on a near-circular polar orbit [125]. All subsequent three-dimensional representations of the orbits are presented in this rotating reference frame.

4.3.1 Retrograde

The circular retrograde family predominantly consists of stable orbits. A narrow segment of instability is bounded by two period-doubling bifurcations, labeled PD_1 and PD_2 in Figure 4.10. These bifurcations are represented as dashed lines in Figure 4.11, which illustrates several representative orbits from this family. The branches that emerge from PD_1

and PD_2 are shown in Figures 4.12a and 4.12b, respectively. Orbits with shorter periods lie closer to the surface of Eros, while those farther away exhibit periods approaching unity, corresponding to a synchronous rotation with the asteroid. The color gradient used in Figure 4.11 serves solely to visually distinguish the individual orbits within the family.

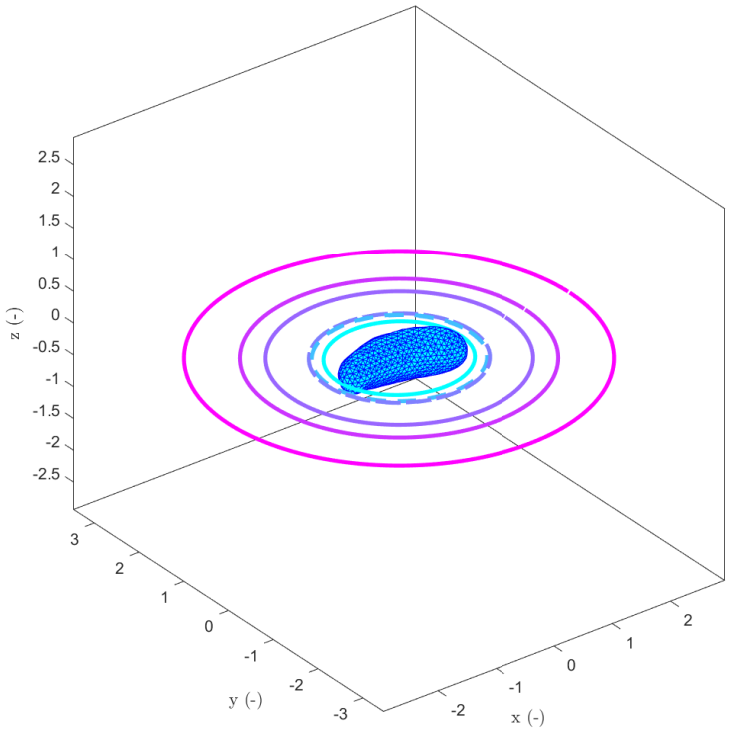

Figure 4.11: Retrograde family around 433 Eros

4.3.2 Vertical

The first period-doubling bifurcation encountered along the circular retrograde family initiates a transition toward vertical motion around the equilibrium point E_2. Additional vertical-like periodic orbits, often exhibiting a characteristic "figure-eight" shape, are found in the vicinity of the remaining three equilibrium points. Representative examples of these orbits are shown in Figures 4.12a, 4.12b, 4.12c, 4.12d, 4.12e, and 4.12f.

On the bifurcation diagram, the branch emerging from PD1, illustrated in Figure 4.12a, is entirely unstable. Figure 4.12b is the partially stable branch emerging from PD2 that includes 3 period-doubling bifurcations from PD4 to PD6. Figure 4.12c corresponds to the family containing period-doubling bifurcations PD_7 through PD_{11}. This family exhibits predominantly unstable behavior, except for a narrow stable segment near PD_8. The geometric evolution of these orbits reflects a smooth transition between vertical librations around equilibrium point E_4 and E_1. For clarity, individual bifurcations are intentionally omitted from the 3D visualizations.

Figures 4.12e and 4.12d depict two short branches containing bifurcations PD_{12} and PD_{15}, respectively. These branches follow a similar pattern on opposite hemispheres of 433 Eros: each begins with vertical motion about an equilibrium point, followed by a gradual tilting of the orbit plane until the trajectory ultimately collides with the asteroid. Both families are entirely unstable.

The final vertical-related family is shown in Figure 4.12f. This set of orbits originates near equilibrium point E_3 and follows a similar vertical-to-collision transition. It includes the bifurcations PD_{16} through PD_{19} and is mostly unstable, with the exception of a small stable region near PD_{19}.

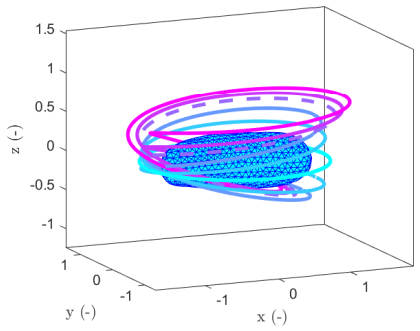

(a)

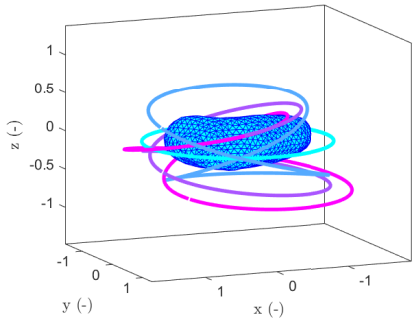

(b)

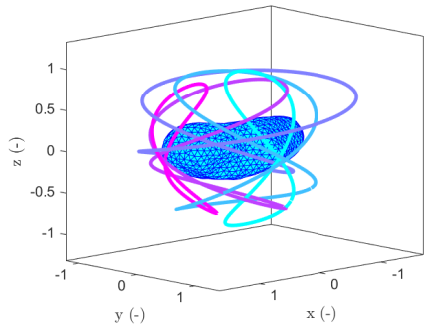

(c)

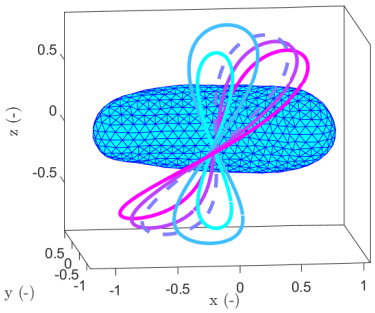

(d)

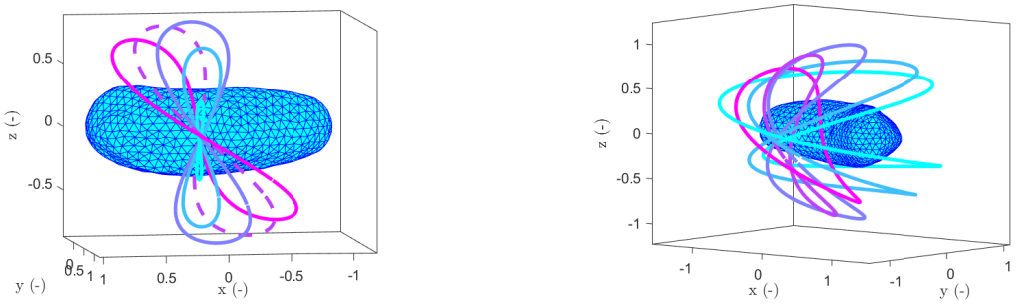

(e) (f)

Figure 4.12: Vertical families around 433 Eros.

4.3.3 Vertical period doubling

Along the various branches of vertical solutions, several period-doubling bifurcations are encountered, each associated with distinct dynamical behaviors. Figure 4.13a illustrates the result of the bifurcation labeled PD3. Another period-doubling event, PD_{13}, is encountered along a continuation path but was not followed further. Figure 4.13b shows the transition of orbit geometries between PD_4 and PD_9; notably, a Neimark–Sacker bifurcation, NS_1, is detected within this segment.

The family of orbits originating from PD_5 and depicted in Figure 4.13c exhibits morphological similarities with those of Figure 4.13a, including the presence of one period-doubling bifurcation, PD_{14}, and a comparable global structure. Orbits represented in Figure 4.13d, which emerge from PD_7, also share visual characteristics with these branches. All four of these branches are fully unstable.

Additionally, the branch that loops between PD_{18} and PD_{19} is part of the family of period-doubled vertical orbits. This loop includes three bifurcations: one period doubling (PD20) and two Neimark–Sacker bifurcations (NS_3 and NS_4). Most of this branch remains unstable, except for a narrow stable region between NS_3 and PD_{19}.

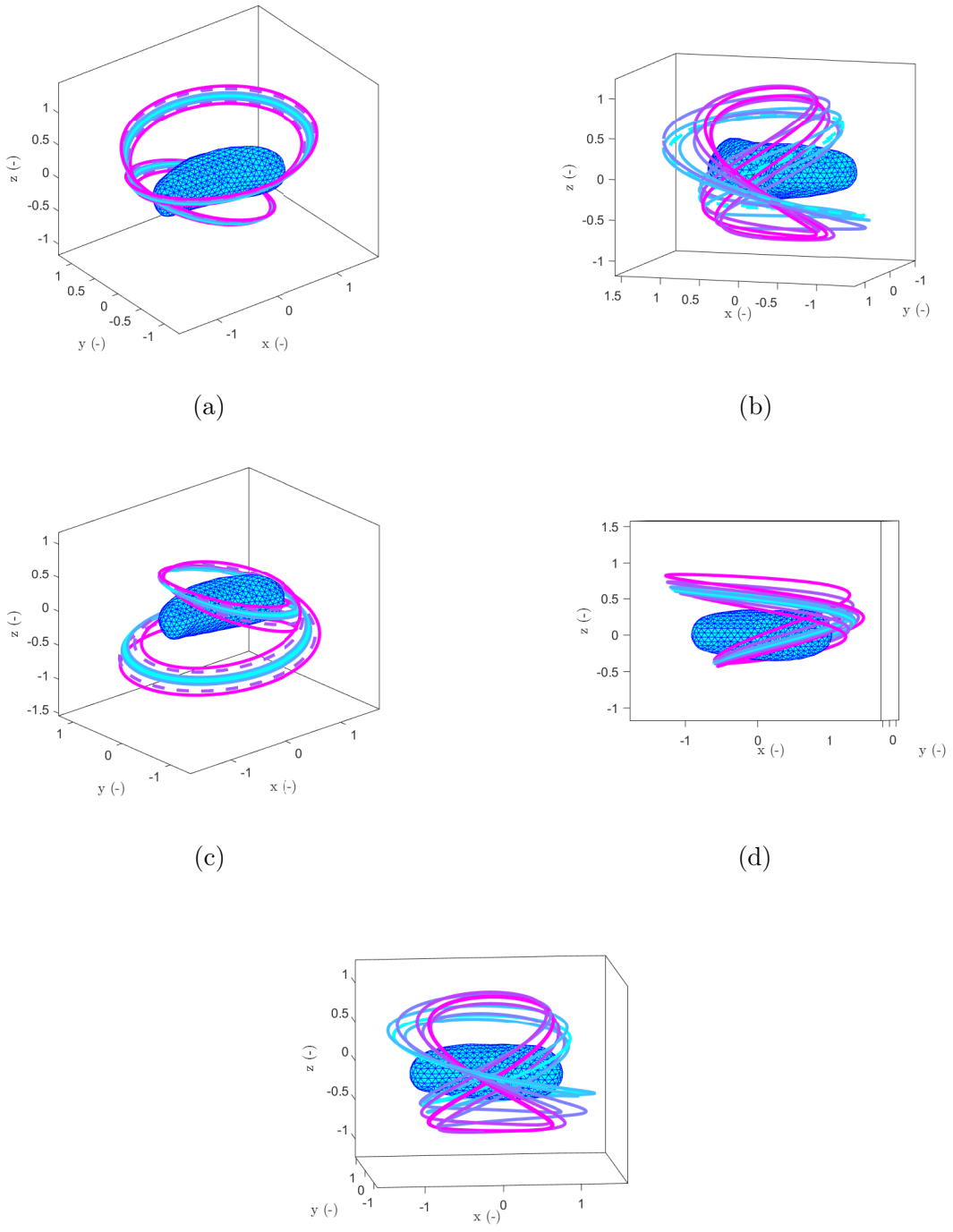

(a) (b) (c) (d) (e)

Figure 4.13: Vertical period doubling families around 433 Eros.

4.3.4 Heart-like

Another distinct family of orbits arising from a period-doubling bifurcation is referred to as the heartlike family, named for the heart-shaped appearance exhibited by some of its members. Figure 4.14a shows the unstable branch that emerges from PD_6, where the terminal orbit displays a heart shape oriented downward on the face of equilibrium point

E_3.

On the opposite side of the asteroid, also oriented downward, lie the orbits presented in Figure 4.14b, which belong to the unstable branch originating from PD_8. Still on this same face, the orbits in Figure 4.14c are oriented upward and belong to the unstable family emerging from the period-doubling bifurcation PD_{10}.

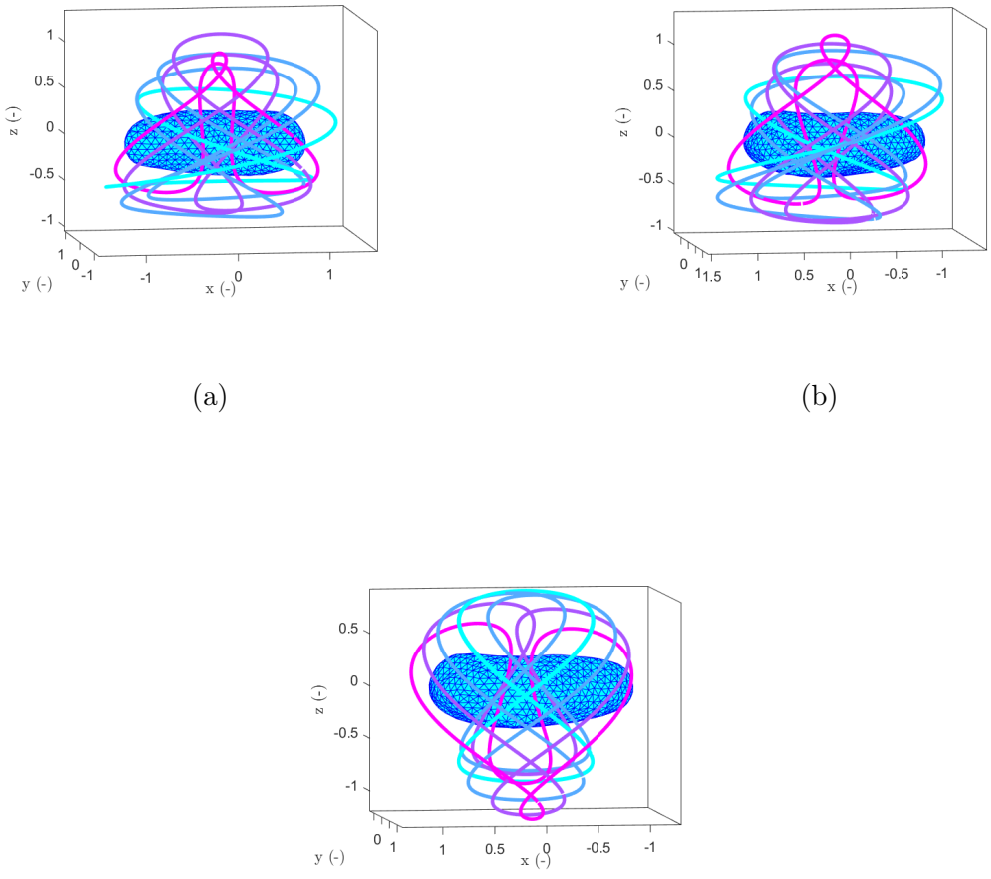

(a) (b)

(c)

Figure 4.14: Heart-like period doubling families around 433 Eros.

4.3.5 Double axial

Double axial families refer to orbit families that emerge from a period-doubling bifurcation associated with an axial orbit. Four distinct configurations are identified within this category: the orbits may lie on either side of equilibrium points E_3 or E_4, and they may exhibit a leftward or rightward tilt. Figures 4.15a through 4.15d illustrate these four scenarios, corresponding respectively to the branches bifurcating from PD_{11}, PD_{12}, PD_{15}, and PD_{16}. All of these families are characterized by instability.

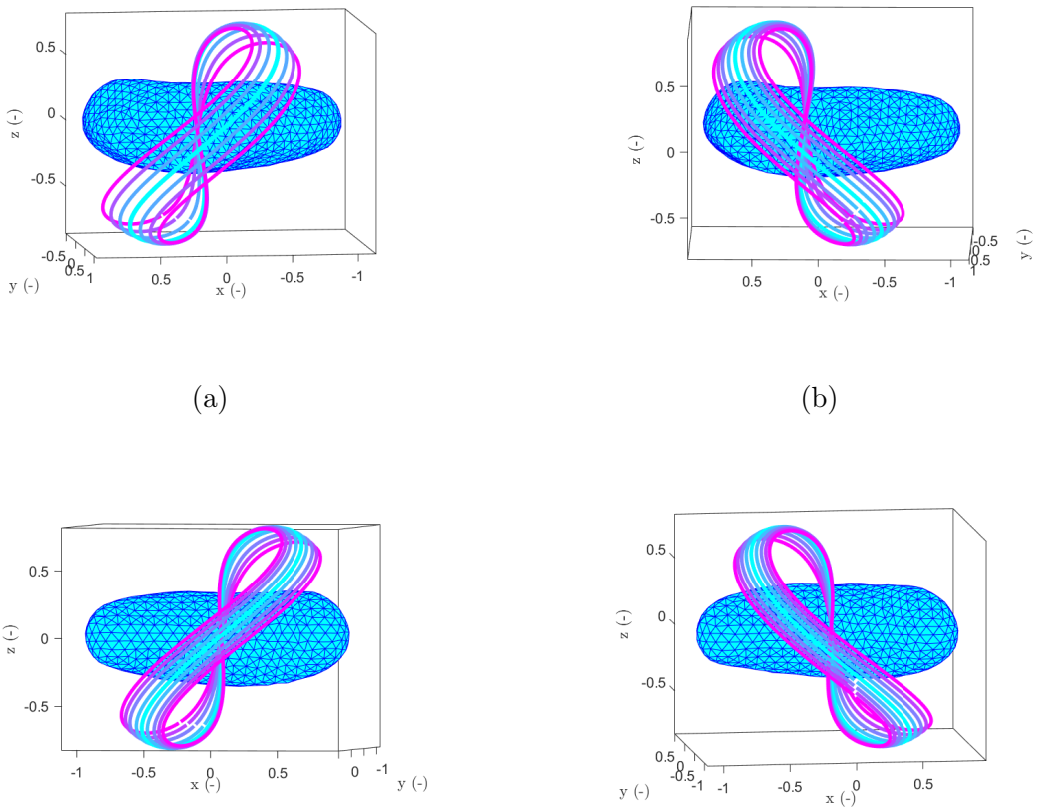

Figure 4.15: Double Axial families around 433 Eros.

4.3.6 Prograde

As illustrated in the bifurcation maps (Figures 4.9 and 4.10), the retrograde and prograde orbit families are clearly distinct. The prograde family consists of circular orbits that rotate in the same direction as asteroid 433 Eros. This family is predominantly stable, with the exception of a narrow segment of unstable orbits located between the two period-doubling bifurcations PD_{21} and PD_{22}. The stable portion terminates at BP_1, the only branch point detected by the HBM in the vicinity of Eros. These three bifurcations are marked by dashed lines in Figure 4.16. Notably, in contrast to the retrograde family, the orbital period increases as the orbit approaches the asteroid.

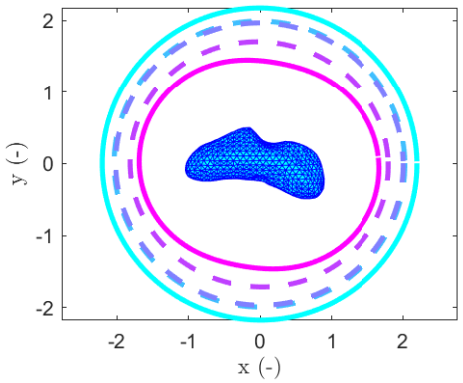

Figure 4.16: Prograde families around 433 Eros.

4.3.7 Pretzel-like

Following the branch point BP1, the prograde family either continues as an unstable extension or splits into two partially stable branches. The first branch, shown to the left of BP_1 in Figure 4.10, remains stable up to the period-doubling bifurcation PD_{24}, with its 3D representation provided in Figure 4.17a. The second branch, leading up to BP_1 in the same figure, is stable until PD_{23}, with an additional period-doubling bifurcation encountered along the continuation at PD_{37}. Its corresponding 3D view is shown in Figure 4.17d. Figures 4.17b and 4.17c represent the counterparts of these two branches, with the key difference being that the orbits tilt in the opposite direction. Another notable distinction is that the horizontal sections of these families are not strictly circular but form loop-like structures around the equilibrium points—resembling a "pretzel"—which gives the family its name.

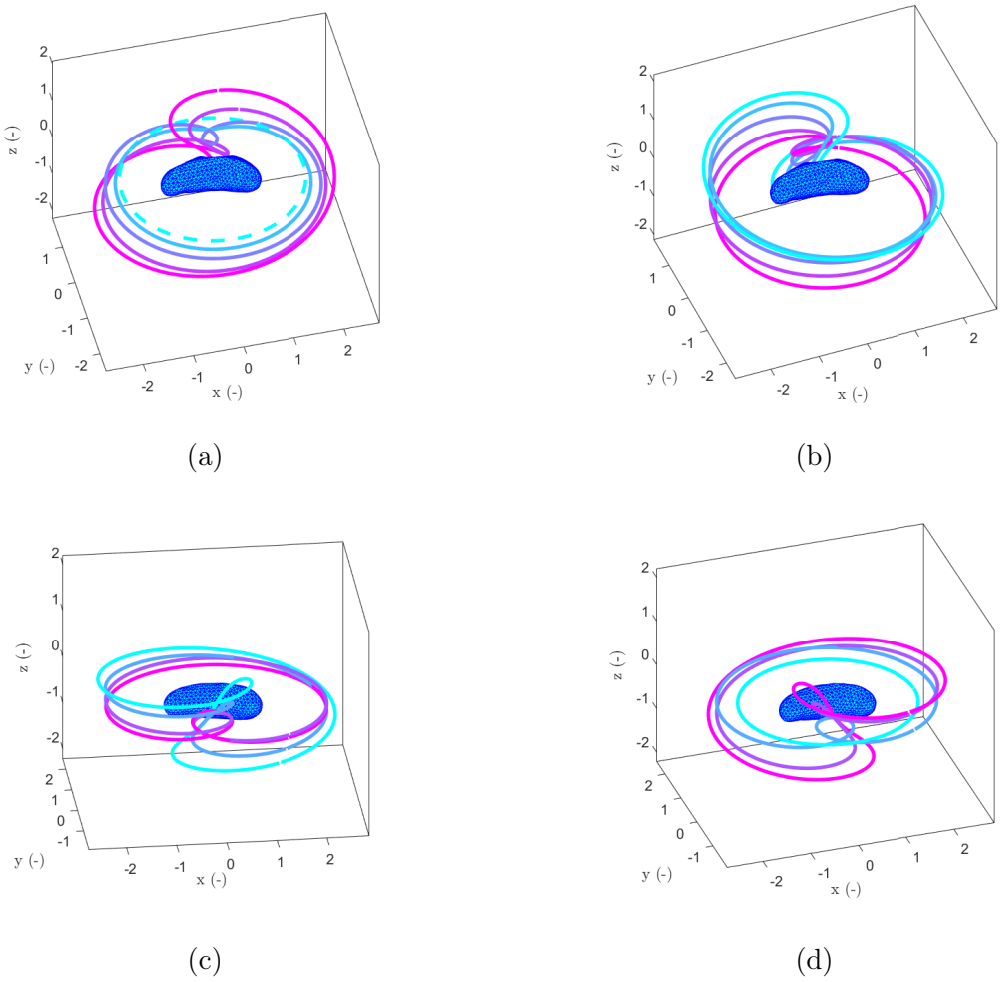

(a) (b)

(c) (d)

Figure 4.17: Pretzel-like families around 433 Eros.

4.3.8 Vertical circular

The family referred to as "Vertical circular" is characterized by large circular trajectories around the asteroid, with the orbit remaining close to either of the equilibrium points E_3 or E_4 Figures 4.18a and 4.18b display the orbits arising from the two period-doubling bifurcations detected within the prograde family, PD_{21} and PD_{22}, respectively. Both families initially emerge as doubled planar circular orbits. The family from PD_{21} begins with stable orbits, transitions briefly to unstable ones, then returns to stability until it reaches period-doubling PD_{56}, beyond which it remains unstable. In contrast, the family from PD_{22} starts as unstable, becomes temporarily stable after the Neimark-Sacker bifurcation NS_5, and then reverts to instability. Along this path, an additional period-doubling bifurcation, PD_{58}, is also encountered.

The family represented in Figure 4.18c originates as the unstable continuation following the branch point BP_1, where planar orbits begin to tilt vertically as the period increases. This branch contains one period-doubling bifurcation, PD_{25}. Its symmetrical counterpart on the opposite side of 433 Eros is shown in Figure A.1, which corresponds to the unstable branch containing bifurcation PD_{26}. It's worth noting that this family terminates before reaching the Neimark-Sacker bifurcation NS_{10}, at the point where the

orbit becomes planar once again.

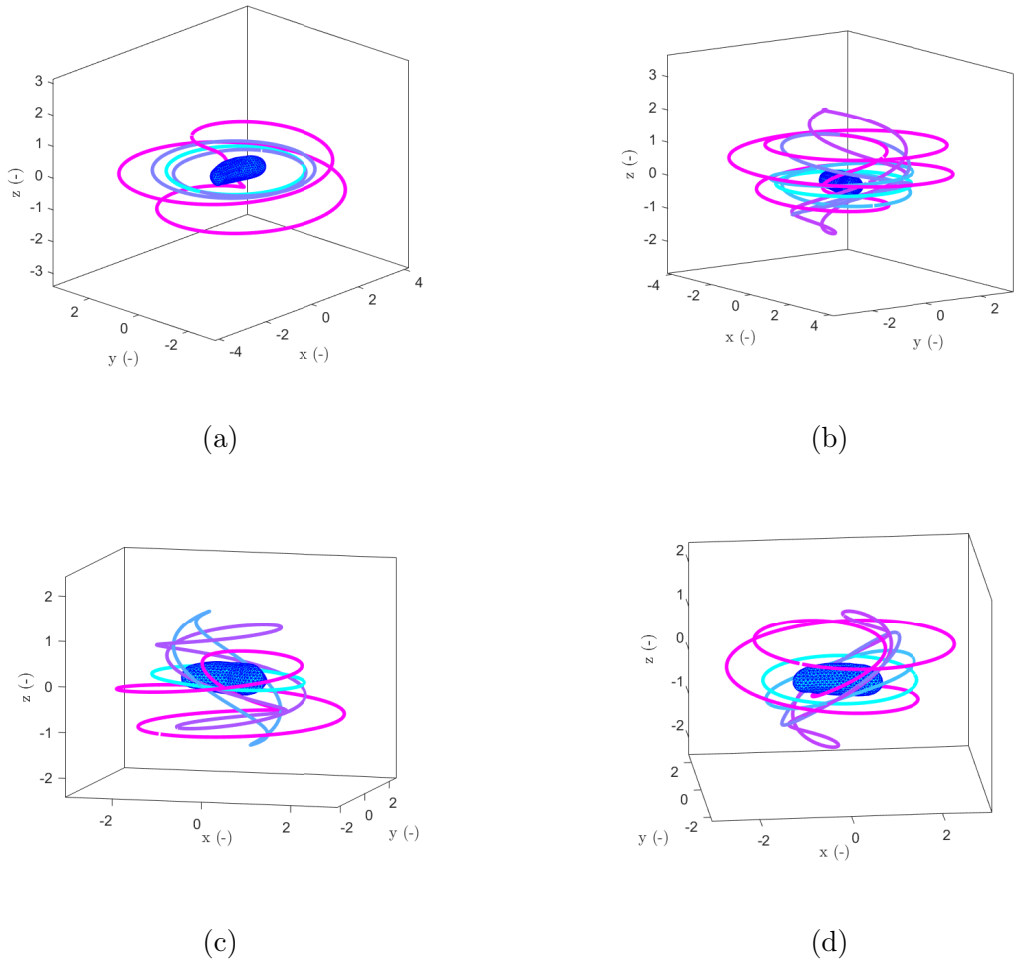

Figure 4.18: Vertical circular families around 433 Eros.

4.3.9 S-shaped vertical

The final family described in this chapter is referred to as 'S-shaped vertical', named after the distinct shape of its orbits, which loop above and below 433 Eros in opposite directions, forming an S-like configuration. Figures 4.19a and 4.19b belong to the same branch of solutions, which includes the bifurcations NS_{10}, PD_{27}, PD_{28}, and PD_{29}. These two figures represent orbits located on either side of the Neimark-Sacker bifurcation: Figure 4.19a lies to the right, and Figure 4.19b to the left. Most of the orbits within this family are unstable. Additionally, Figures 4.19c and 4.19d correspond to other unstable orbits arising after Neimark-Sacker bifurcations NS_9 and NS_8, respectively.

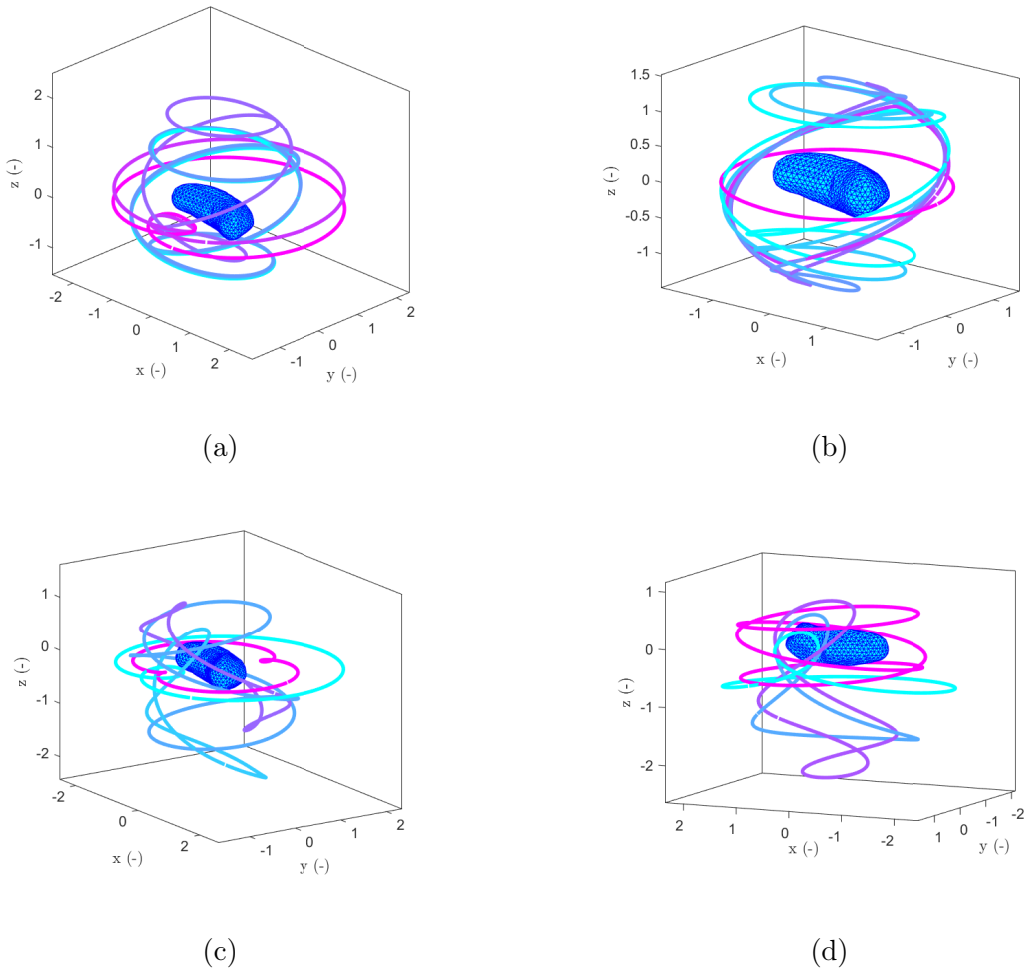

(a) (b)

(c) (d)

Figure 4.19: S-shaped vertical families around 433 Eros.

4.4 Resonance

As in the case of the CRTBP discussed in the previous chapter, resonances are also observed in the dynamics around 433 Eros. This phenomenon is clearly visible in Figure 4.9, where the Jacobi constant exhibits distinct increases at integer dimensionless period values, and the associated orbital shapes tend to deviate from the equatorial plane. It is worth noting that the dashed lines, representing period doubling bifurcations, have their period halved for visualization purposes; their actual periods correspond to integer values in Figure 4.9. Since most of the orbits with period ratios below 3 were extensively described in the previous section, the focus here shifts to those with period ratios greater than 3. On the bifurcation map, Figure 4.10, these orbits correspond to a series of parallel branches, beginning with those associated with PD32 and PD42. Although the bifurcations encountered along these branches are labeled, they are not analyzed in detail, as the efficacy of the HBM in tracking bifurcations has already been demonstrated. Generally, each of these branches originates at a resonant orbit. As the period increases, the orbits tend to align with the equatorial plane. However, when the period approaches another integer value, the Jacobi constant increases and a vertical component emerges in the orbit. These vertically extended resonant orbits are the focus of this section.

Figure 4.20 shows several examples of resonant orbits corresponding to different period ratios: 1:4, 1:6, 1:8, and 1:10. For a resonance of the form n:m, the asteroid completes m rotations about its principal axis of inertia while the massless particle completes n revolutions around it. Several key observations arise from the morphology of these resonant orbits. First, their similarity to the Heart-like family introduced in the previous section is evident, with the addition of vertical loops near the equilibrium point E_3. Second, despite the variety of period ratios, the overall shape of these resonant orbits remains qualitatively similar. The difference in period between them is largely due to the number of vertical loops: the higher the period, the greater the number of loops.

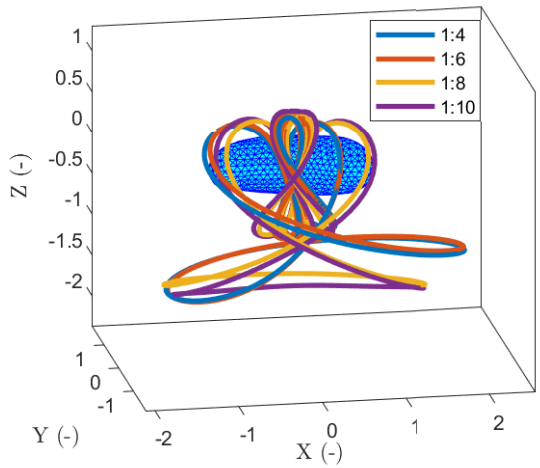

Figure 4.20: Resonant orbits of the southern Heart-like family around 433 Eros.

A similar pattern is observed for various combinations of the previously introduced families, which consistently interact with the vertical family to form resonance loops. Figure 4.21 presents resonant ratios of 1:3, 1:4, 1:5, 1:6, and 1:7, all associated with the northern branch of the Heart-like family. Other orbit families also combine with the vertical family to generate resonant structures. For instance, the Pretzel-like family gives rise to resonant orbits with ratios of 1:8 and 1:9, as shown in Figure 4.22.

In addition, resonance is not confined to a single equilibrium point. Figure 4.23 illustrates resonant orbits around equilibrium point E_4, formed by a combination of axial motion and vertical loops, for resonant ratios ranging from 1:4 to 1:8. Similarly, Figure 4.24 displays resonant orbits belonging to a previously unpresented family, yet exhibiting comparable resonant dynamics.

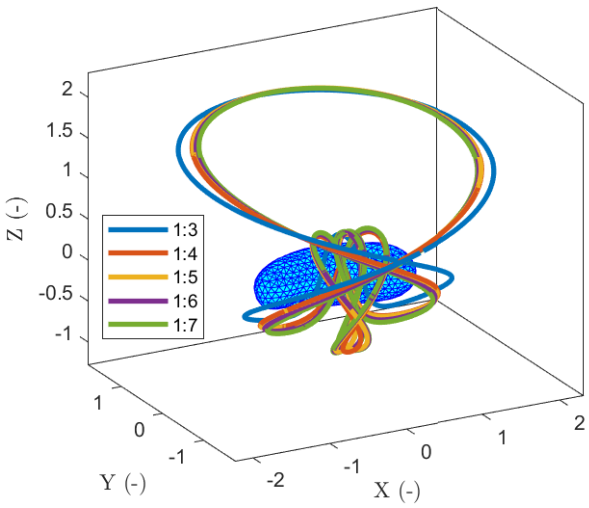

Figure 4.21: Resonant orbits of the northern Heart-like family around 433 Eros.

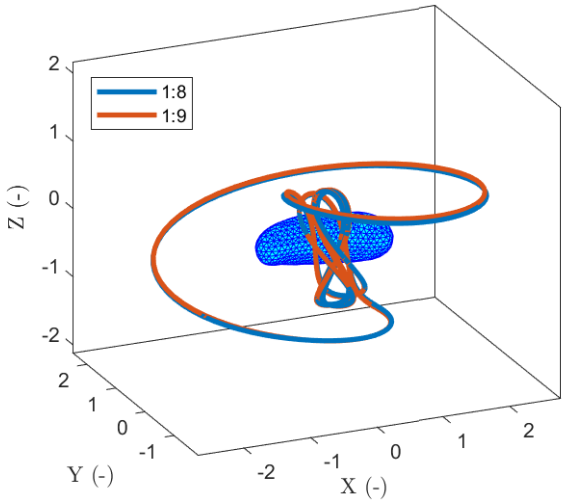

Figure 4.22: Resonant orbits of the Pretzel-like family around 433 Eros.

A considerable number of periodic orbits have been identified through the continuation process combined with branch switching using the HBM. However, this collection is far from exhaustive; many more periodic orbits exist around 433 Eros. Additional computations with the HBM have led to the discovery of more intricately shaped periodic orbits. These advanced results are presented in Appendix A for the interested reader.

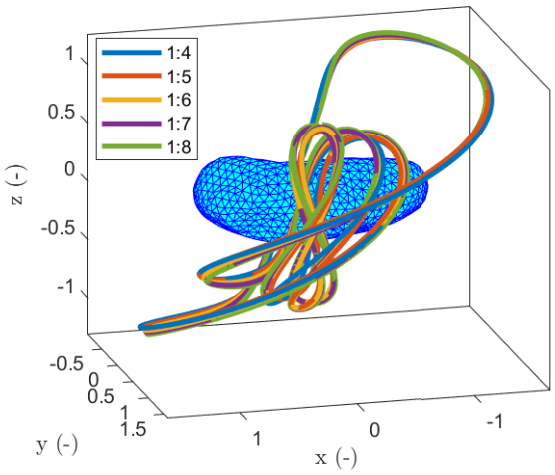

Figure 4.23: Resonant orbits of the axial family around 433 Eros.

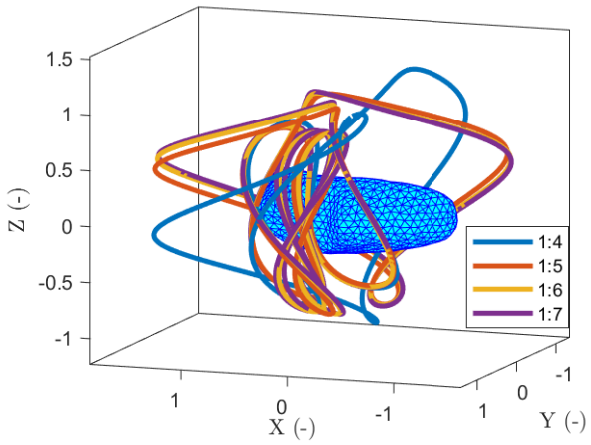

Figure 4.24: Resonant orbits of an unlabeled family around 433 Eros.

4.5 HBM spectral analysis

Compared to classical time integration methods, the HBM offers a powerful additional perspective for analyzing the dynamics of orbit families. In particular, it enables the study of how bifurcations influence the evolution of solutions during continuation by examining the behavior of the normalized Fourier coefficients, denoted σ_i^j:

$$\sigma_i^j = \frac{\Phi_i^j}{\sum_{i=0}^{N_H} \Phi_i^j}$$

with

$$\Phi_i^j = \sqrt{\left(s_i^{f_{xj}}\right)^2 + \left(c_i^{f_{xj}}\right)^2} \quad (j = 1, ..., n; i = 0, ..., N_H)$$

where $\Phi^j i$ represents the amplitude of the i-th harmonic in the j-th degree of freedom, and $\sigma^j i$ expresses its normalized contribution relative to the total harmonic content. The analysis focuses on a particular circular orbit family that exhibits two period-doubling bifurcations, PD_1 and PD_2, each marking a change in stability along the continuation path. The secondary branch that emerges from PD_1, which includes another bifurcation (PD_3), is also investigated, along with the new branch that arises from PD_3. These bifurcating branches are compared with the main circular family to highlight the changes in harmonic content and dynamics. Figure 4.25 shows the three sets of orbits in the spatial context of asteroid 433 Eros. Figure 4.26 presents a heat map of the normalized Fourier coefficients σ_i^j for the first 10 harmonics in the X and Y directions across the entire continuation. The positions of the period-doubling bifurcations are indicated by green lines, clearly marking where changes in harmonic structure and orbital stability occur.

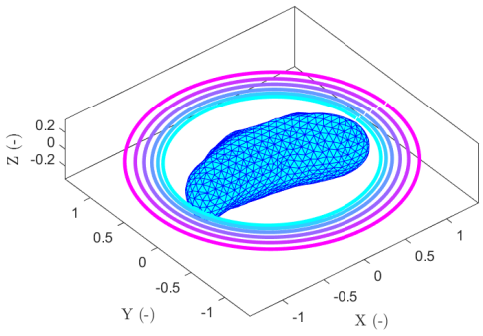

(a)

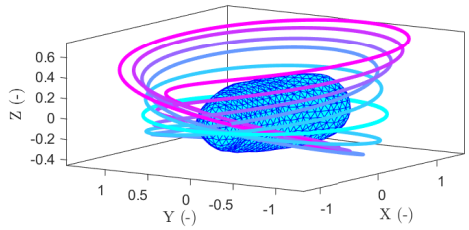

(b)

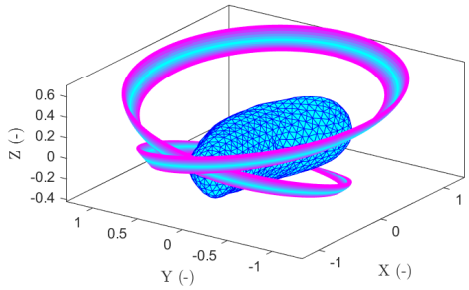

(c)

Figure 4.25: Quasi-circular orbits, including the period doubling bifurcations PD_1 and PD_2 (a). Vertical orbits resulting from PD_1 including the period doubling bifurcation PD_3 (b). Vertical orbits resulting from PD_3 (c).

As expected, the Fourier coefficients for the circular orbit family show dominant activ-

ity in the first harmonic for both the X and Y degrees of freedom. A smaller contribution from the third harmonic in the X direction is also observed. Given that the bifurcated orbits in Figure 4.25(b) exhibit vertical deviations from the circular family, it is particularly relevant to examine the harmonic content in the Z direction, as shown in Figure 4.27. This heat map reveals a clear signature of the period-doubling bifurcation, marked by a noticeable change of the dominant harmonic near the PD bifurcations.

Concerning the orbits in Figure 4.25(b), the dominant harmonic is the second one, around the 60th orbit in the continuation, the third harmonic begins to show increased activity, and shortly after PD_3, the fourth harmonic becomes significant as well. Figure 4.28 offers a comparison of the orbits in Figure 4.25(b) before and after the 60th orbit. Prior to this point, the orbits primarily show increasing vertical excursion along the Z axis. Beyond the 60th orbit, however, the vertical growth is accompanied by noticeable deviations in the X and Y directions, suggesting a shift in the orbit structure.

The final family of orbits emerging after PD_3, represented in Figure 4.25(c), is predominantly governed by the fourth harmonic. Nonetheless, the second harmonic retains a non-negligible presence, indicating that these orbits share certain dynamical features with those just prior to the bifurcation. This evolution of the harmonic structure underscores the power of HBM in capturing subtle qualitative transitions in orbital dynamics.

Figures 4.9 and 4.10 reveal that two consecutive resonant peaks are connected through a transition involving planar orbits. The HBM facilitates a spectral analysis of these transitions by examining the evolution of the normalized Fourier coefficients. The transitions between the 5:1 and 6:1 resonances, as well as between the 1:9 and 1:10 resonances, are shown in Figures 4.29 and 4.31, with their corresponding spectral decompositions illustrated in Figures 4.30 and 4.32.

From these analyses, several patterns emerge. First, the transition between the 1:9 and 1:10 resonances involves a broader and more complex spectrum of harmonics than the 1:5 to 1:6 case, which reflects the increasing geometrical intricacy of higher-order resonant orbits. In both transitions, the z-component of the motion exhibits a clear shift in the dominant harmonic, moving from the 5th to the 6th and from the 9th to the 10th harmonic respectively, demonstrating the spectral signature of the change in resonance. As the orbits pass through the equatorial plane during the transition, the contribution of the lower-order harmonics becomes more prominent in all three degrees of freedom, especially in the x and y directions. Additionally, the x and y components show noticeable activation of higher harmonics, particularly the 10th and 12th during the 1:5–1:6 transition and the 18th and 20th during the 1:9–1:10 transition. These contributions further emphasize the increased harmonic richness associated with more complex orbital geometries near higher-order resonances.

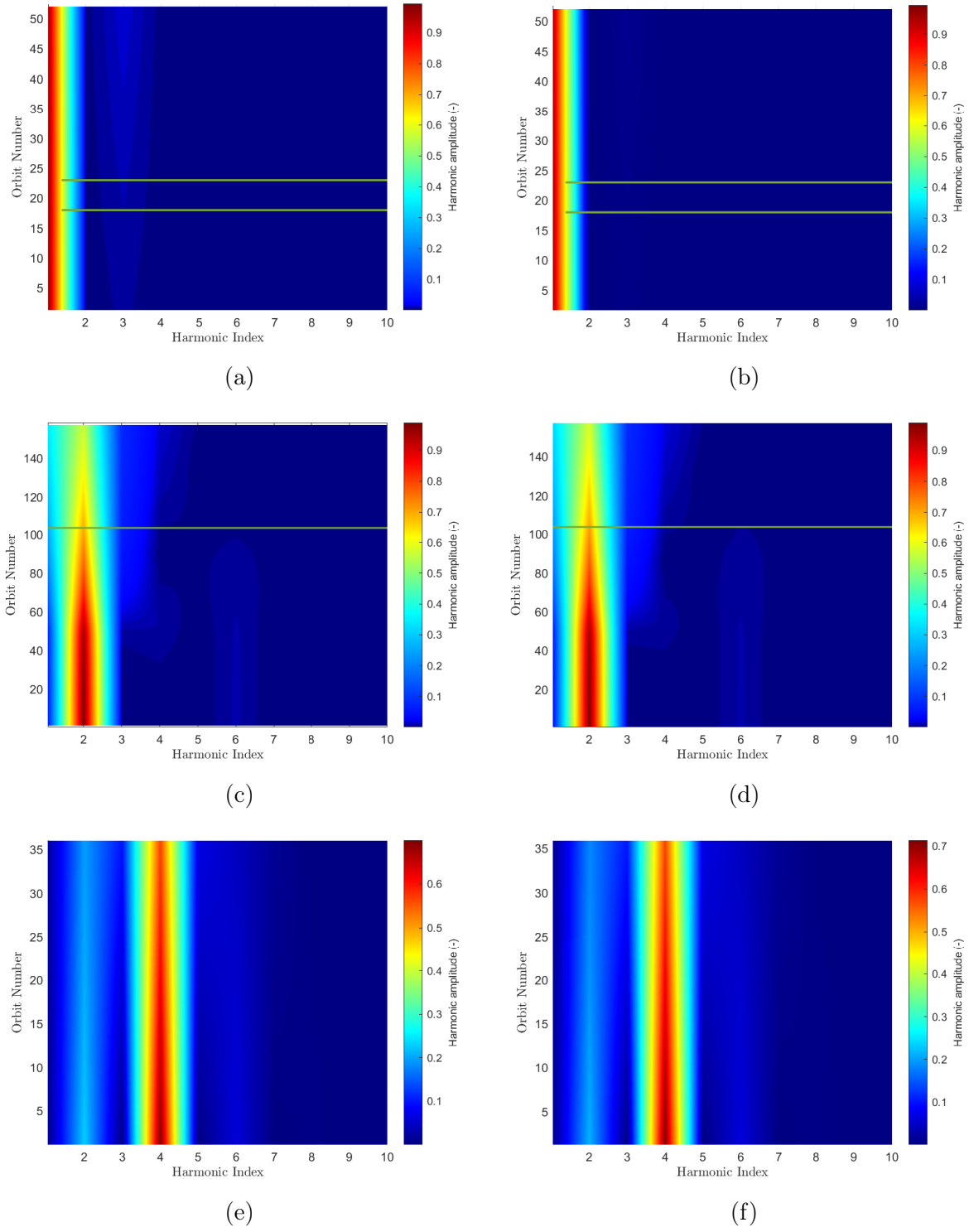

Figure 4.26: Normalized Fourier coefficients of the quasi-circular orbits, including the period doubling bifurcations PD_1 and PD_2 of x (a) and y (b). Normalized Fourier coefficients of the vertical orbits resulting from PD_1 including the period doubling bifurcation PD_3 of x (c) and y (d). Normalized Fourier coefficients of the vertical orbits resulting from PD_3 of x (e) and y (f).

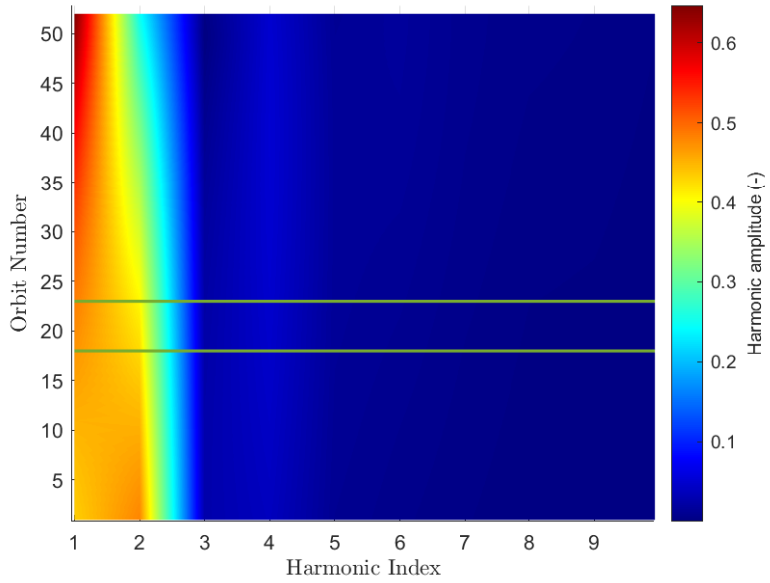

Figure 4.27: Normalized Fourier coefficients of the quasi-circular orbits, including the period doubling bifurcations PD_1 and PD_2 of z

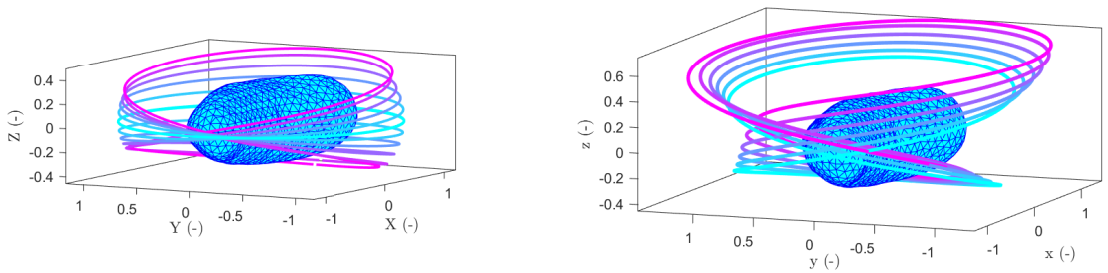

(a) (b)

Figure 4.28: Decomposition of the vertical orbits resulting from PD_1 including the period doubling bifurcation PD_3. Before orbit 60 (a), after orbit 60 (b).

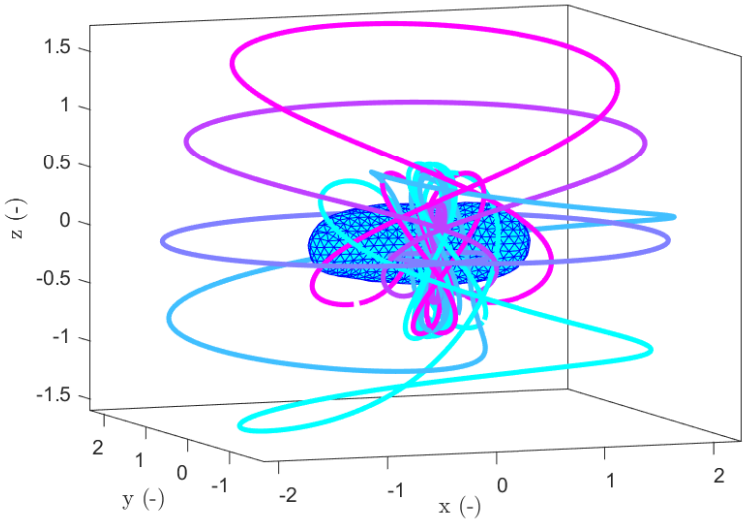

Figure 4.29: Transition of 1:5 resonant orbits to the 1:6 resonant orbits.

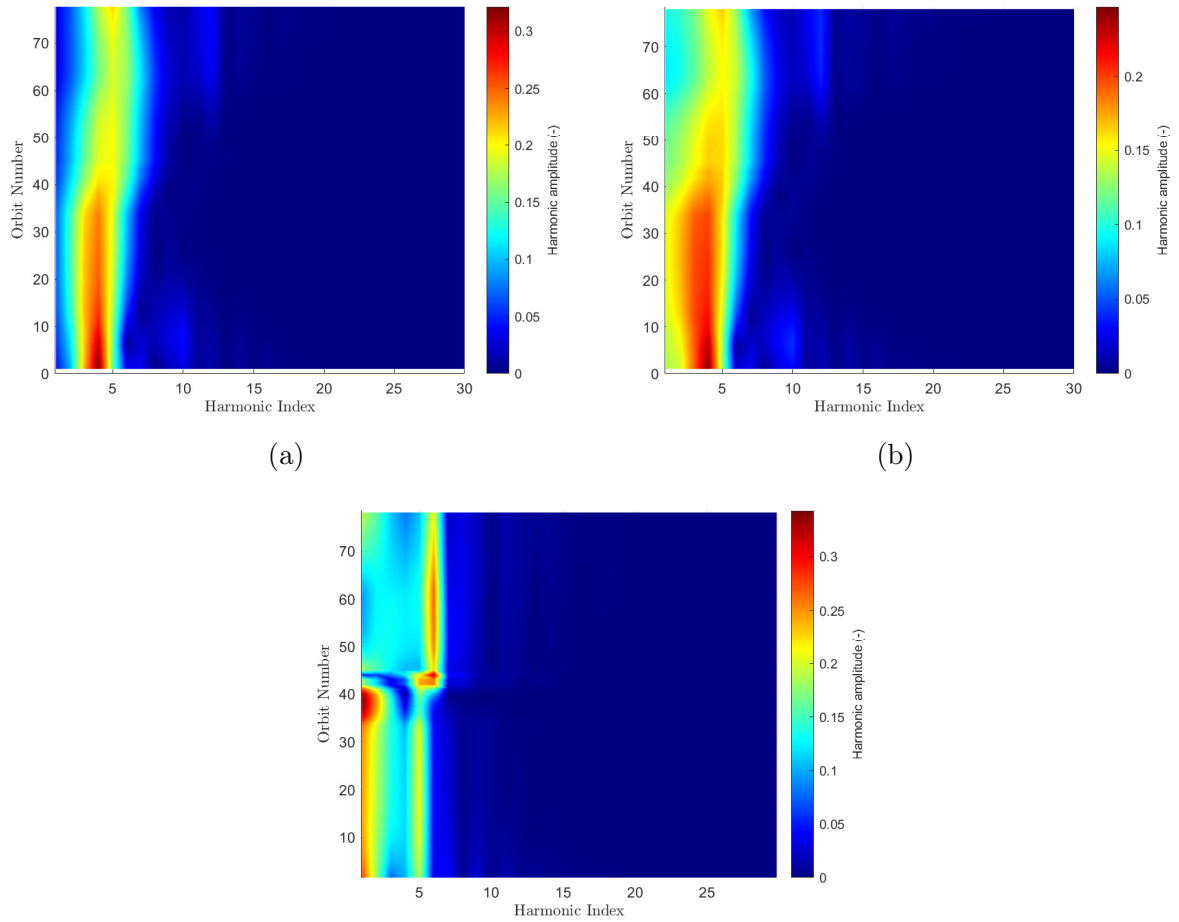

Figure 4.30: Normalized Fourier coefficients of the transition of the resonances 1:5 to the 1:6 of x (a), y (b) and z (c).

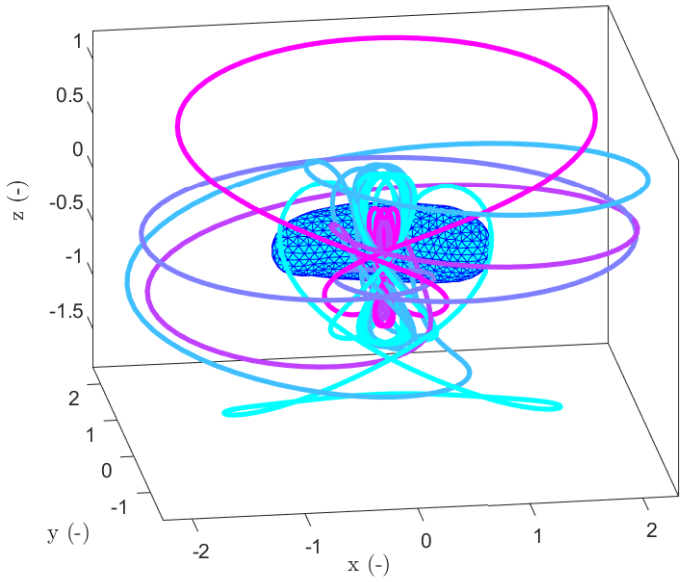

Figure 4.31: Transition of 1:9 resonant orbits to the 1:10 resonant orbits.

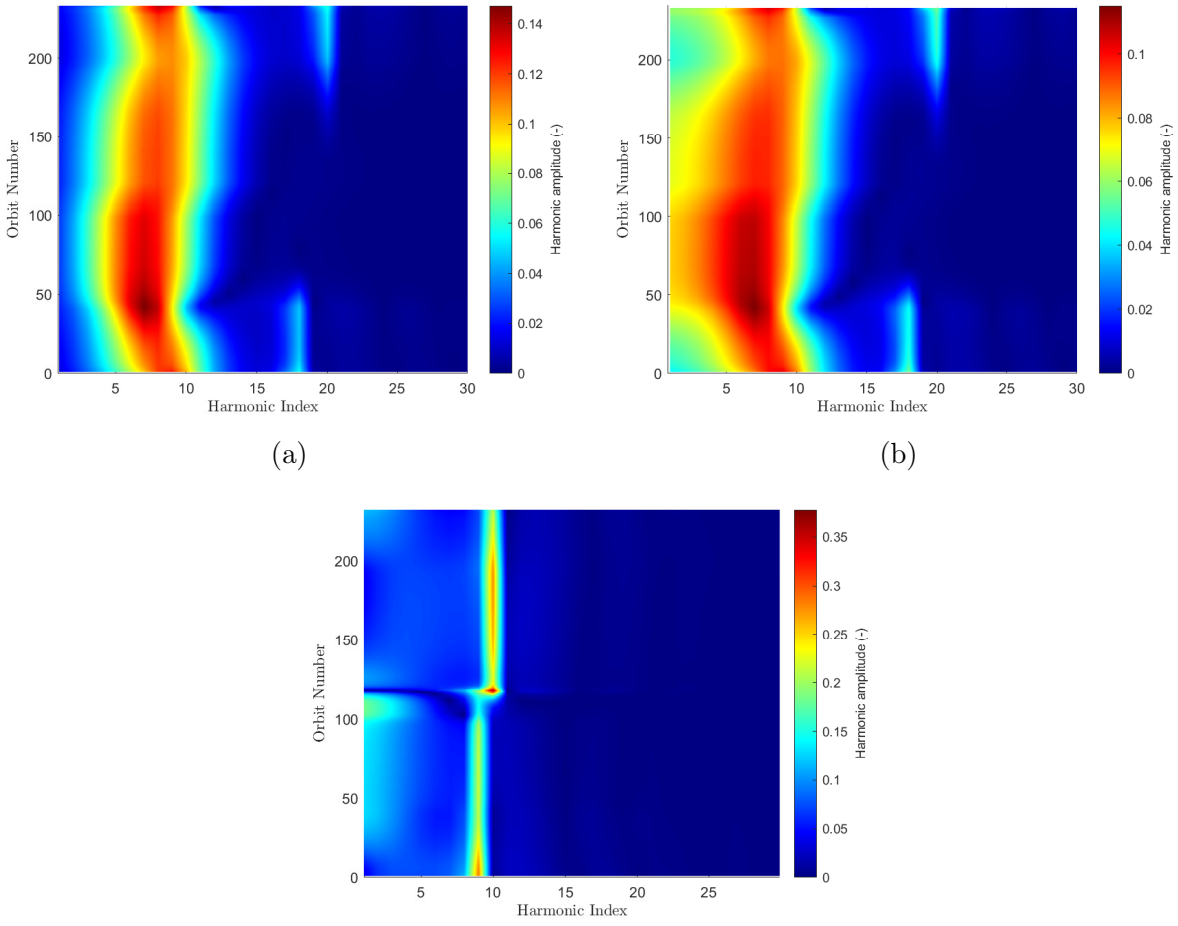

Figure 4.32: Normalized Fourier coefficients of the transition of the resonances 1:9 to the 1:10 of x (a), y (b) and z (c).

4.6 Quasi-periodic solutions

Up to this point, only the branches emerging from branch points and period-doubling bifurcations have been followed, while Neimark–Sacker bifurcations have been left aside. The branches associated with Neimark–Sacker bifurcations correspond to quasi-periodic solutions. Tracking these solutions requires adapting the HBM to account for an additional frequency. The Multi-Harmonic Balance Method (MHBM), presented in the first chapter, allows the computation of those emerging quasi-periodic solutions.

To obtain quasi-periodic orbits, complex and time-consuming computations are necessary. While 12 different Neimark-Sacker bifurcations have been detected and are listed in Table 4.3, not all of them were followed. The focus has been placed on one Neimark-Sacker bifurcation that is not a result of a period doubling bifurcation, specifically NS_{10}. The quasi-periodic orbit resulting from this bifurcation is depicted around 433 Eros in Figure 4.33.

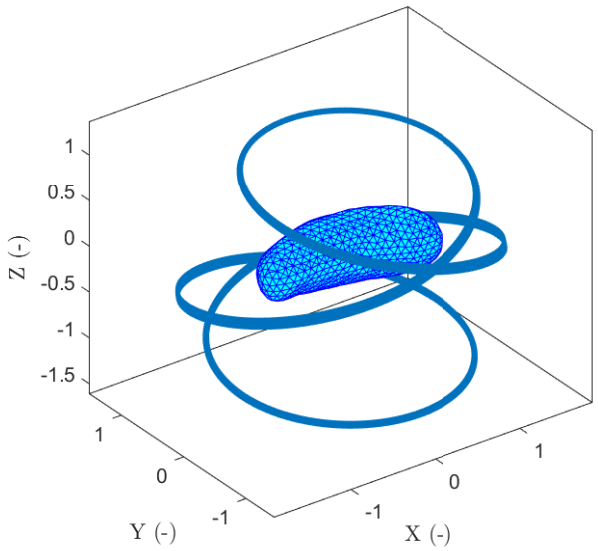

Figure 4.33: Quasi-periodic orbit resulting from Neimark-Sacker bifurcation NS_{10}.

The continuation of these solutions reveals how the quasi-periodic orbits evolve and interact with their periodic counterparts. Figure 4.34 provides a more detailed view, focusing on the region around NS_{10} as shown in Figure 3.5, where the secondary period of the quasi-periodic orbits is represented along a third axis.

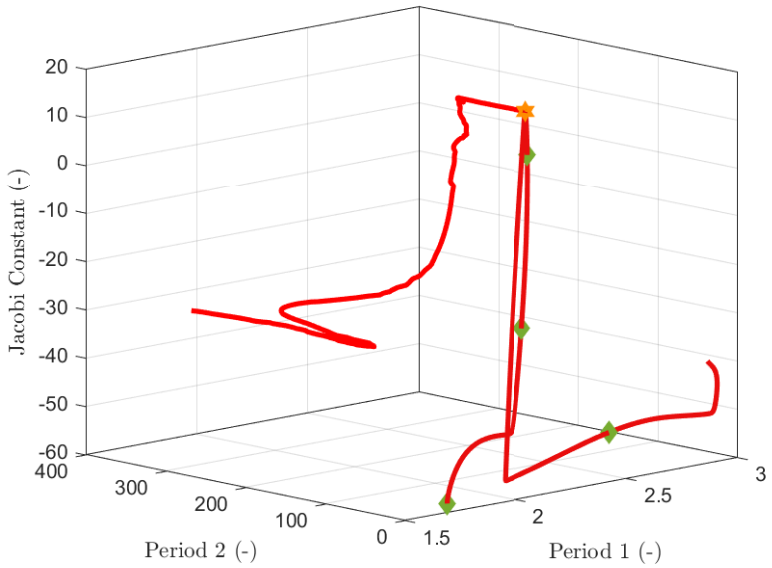

Figure 4.34: Jacobi constant with respect to the period for periodic and quasi-periodic orbits around the Neimark-Sacker bifurcation NS_{10}.

To validate the result obtained via MHBM, the decomposed motion along the x, y, and z directions is compared to a time integration performed using MATLAB's `ode113` solver over one period of the second frequency, $\frac{2\pi}{\omega_2}$ (see Figure 4.35). The two solutions are in excellent agreement, confirming the accuracy of the MHBM. The quasi-periodic nature of the orbit is especially evident in the x and y directions. It is worth noting that this particular orbit is unstable. The solution was computed using 20 harmonics for the first frequency and 10 for the second. As previously mentioned, obtaining quasi-periodic solutions with MHBM is computationally intensive: in this case, the solution required approximately 30 minutes[1] to converge and have its stability determined.

To illustrate the sensitivity of time-domain numerical integration for quasi-periodic solutions, two different sets of initial conditions, listed in Table 4.4, are considered. These sets are derived from quasi-periodic orbits computed with different harmonic resolutions. The first corresponds to a solution obtained using 20 harmonics on the first frequency and 5 on the second, while the second (taken as the reference for relative error computation) results from a higher-resolution solution using 80 harmonics on the first frequency and 5 on the second.

Despite the difference in harmonic content, the solutions computed in the frequency domain using MHBM are nearly identical, as the method enforces quasi-periodicity by construction. However, when these initial conditions are propagated in time using a classical numerical integrator (Figure 4.36), the solution derived from the lower-harmonic approximation gradually diverges from the reference over several periods. This divergence highlights the sensitivity of traditional time-domain methods to small discrepancies in initial conditions, especially for unstable orbits. In contrast, the frequency-domain framework provided by HBM and MHBM offers a much more robust and reliable environment for studying such solutions.

[1]Intel(R) Core(TM) i9-9900K CPU at 3.60GHz, with 32GB RAM, MATLAB R2020a

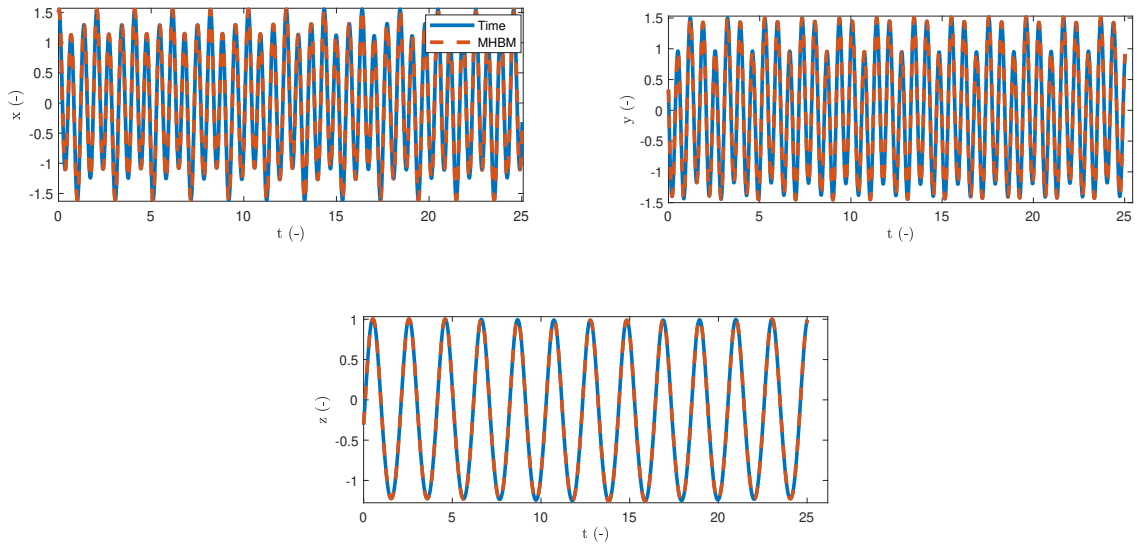

Figure 4.35: Comparision of the evolution of the three degrees of freedom over time computed with MHBM ($NH_1 = 20$ and $NH_2 = 5$) and time integration with `ode113` for x (a), y (b) and z (c)

Table 4.4: Initials conditions for 20 and 80 harmonics on the first frequency and 5 on the second and the associated relative error.

Coordinate	Initial condition 1 (-)	Initial condition 2 (-)	Relative error (%)
$\mathbf{x}_0$	1.5106	1.5073	0.2184
$\mathbf{y}_0$	0.3153	0.3361	6.1702
$\mathbf{z}_0$	-0.2842	-0.30602	7.1171
$\mathbf{v}_{x0}$	2.9441	3.1102	5.3397
$\mathbf{v}_{y0}$	-12.6162	-12.5755	0.3235
$\mathbf{v}_{z0}$	3.3842	3.3571	0.8073

To accelerate the computation of quasi-periodic solutions using the MHBM, the total number of harmonics can be reduced, allowing the exploration of the solution space at a lower resolution. However, this approach has limitations: if the number of harmonics is too small, the solution may fail to converge. The main sources of computational cost when solving for quasi-periodic solutions are directly linked to the number of harmonics and to the asteroid's mesh resolution, since orbits with more sampling points require a greater number of potential evaluations.

Both factors can be adjusted to significantly reduce computation time. One effective approach is the adaptive harmonic selection strategy, previously introduced for the periodic case and extended here to filter out negligible harmonic components. This method relies on evaluating the amplitude of the forcing vector $\mathbf{b}$ and retaining only the harmonics whose magnitude exceeds a prescribed threshold ϵ_{AHBM}. Figure 4.37 illustrates the effect of ϵ_{AHBM} on the average computation time per iteration, the number of iterations, and

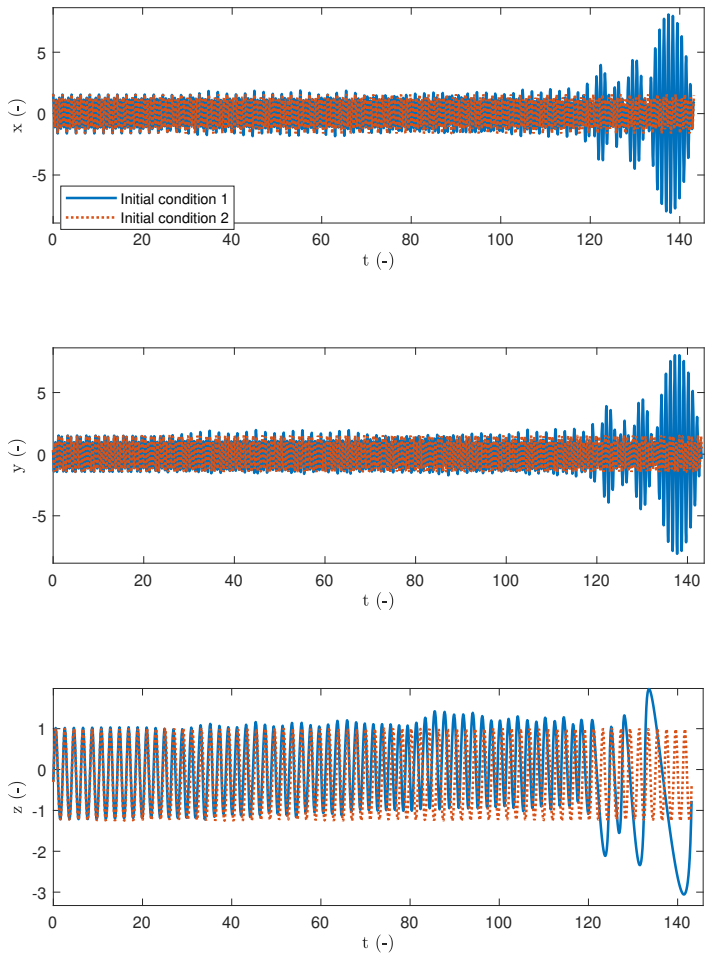

Figure 4.36: Comparison of the evolution of the three degrees of freedom over time for two different set of initial conditions propagated with `ode113` for x (a), y (b) and z (c)

the total convergence time for three consecutive continuation points. The example orbit considered here includes 15 harmonics on the first frequency and 5 on the second.

As ϵ_{AHBM} decreases, more harmonics are preserved, which increases both the computational load per iteration and the overall time required for convergence. Conversely, higher values of ϵ_{AHBM}, shown on the left side of the plot, filter out more harmonic components. This leads to faster computations, though with a slightly coarser approximation of the solution. The blue curves illustrate that the correction time per iteration decreases as more harmonics are filtered out. However, the dotted blue line, representing the average time to reach convergence, shows a minimum around $\epsilon_{AHBM} = 10^{-6}$. This behavior correlates directly with the orange curve, which indicates the number of corrections needed for convergence.

When fewer harmonics are retained, each correction step is faster, but more corrections are required overall. As a result, the total computation time increases despite the shorter individual steps. The horizontal dashed blue lines indicate reference times for the case where all harmonics are kept. It is worth noting that if ϵ_{AHBM} is set too high, too few harmonics are considered, and the solution may fail to converge. On average,

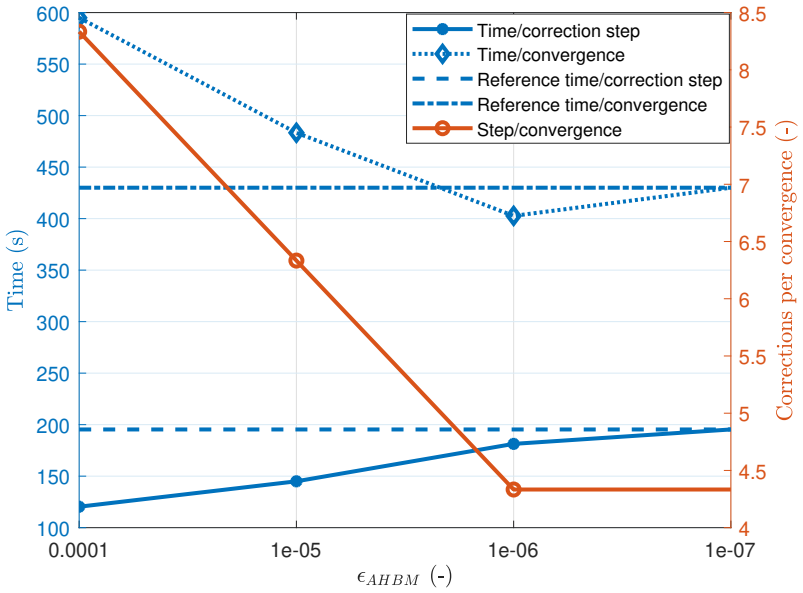

Figure 4.37: Influence of ϵ_{AHBM} on the computation time per iteration, the number of iterations and the total time required for convergence with 15 harmonics on the first frequency and 5 on the second.

the total time for the reference solution is about 7 minutes, substantially higher than for $\epsilon_{AHBM} = 10^{-6}$, which achieves roughly a 30 seconds reduction per solution.

Figure 4.38 illustrates the effect of the AHBM when 20 harmonics are used on the first frequency and 10 on the second. As expected, the influence of filtering becomes more noticeable as the number of harmonics increases. Even with $\epsilon_{AHBM} = 10^{-7}$, some harmonic components are filtered, leading to a reduction in total computation time compared to the reference case. Both the correction time per iteration and the overall time decrease as ϵ_{AHBM} increases. Between the reference case and $\epsilon_{AHBM} = 10^{-5}$, approximately 300 seconds are saved, a significant improvement in computational efficiency.

To assess the influence of the mesh on the computation time of quasi-periodic solutions, the same meshes shown previously in Figure 4.7 are considered. To isolate the mesh effect, the solutions are selected close to each other so that the number of correction steps remains roughly constant. Figure 4.39 clearly shows that coarser meshes yield faster computations. With a simple mesh of 30 faces, the computation time is reduced by about a factor of five. As in the classical HBM case, this makes coarse meshes a valuable tool for rapid exploration at low resolution before refining the solution around a specific orbit.

Combining both methods the evolution of the solutions along this quasi-periodic branch emerging from NS_{10} can be built and corresponds to the one represented in Figure 4.40. It appears that, at first, the orbits path gets slightly thicker as the second period grows

Figure 4.41 presents two additional unstable quasi-periodic orbits that arise from two distinct Neimark-Sacker bifurcations, NS_1 and NS_2. It's worth mentioning that despite the more intricate shape of the orbit in Figure 4.41b, the dimensionless period of the

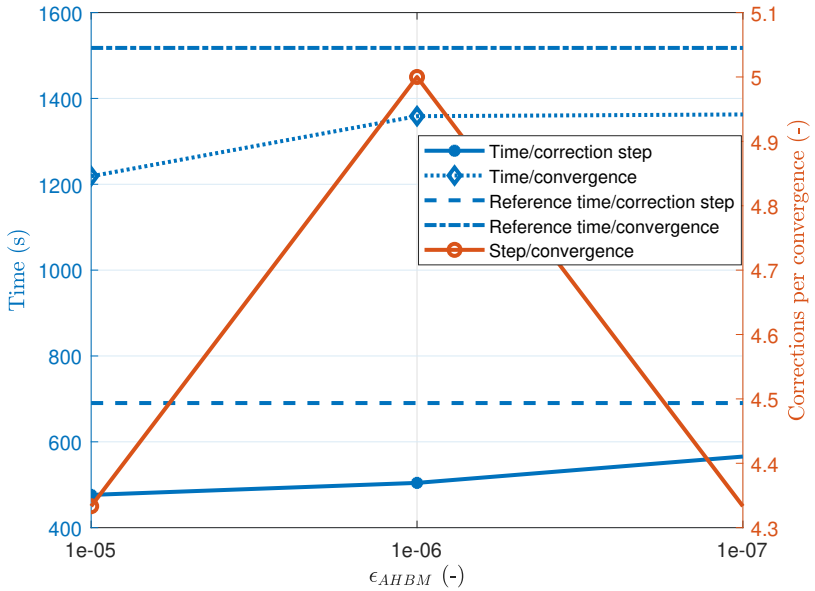

Figure 4.38: Influence of ϵ_{AHBM} on the computation time per iteration, the number of iterations and the total time required for convergence with 20 harmonics on the first frequency and 10 on the second.

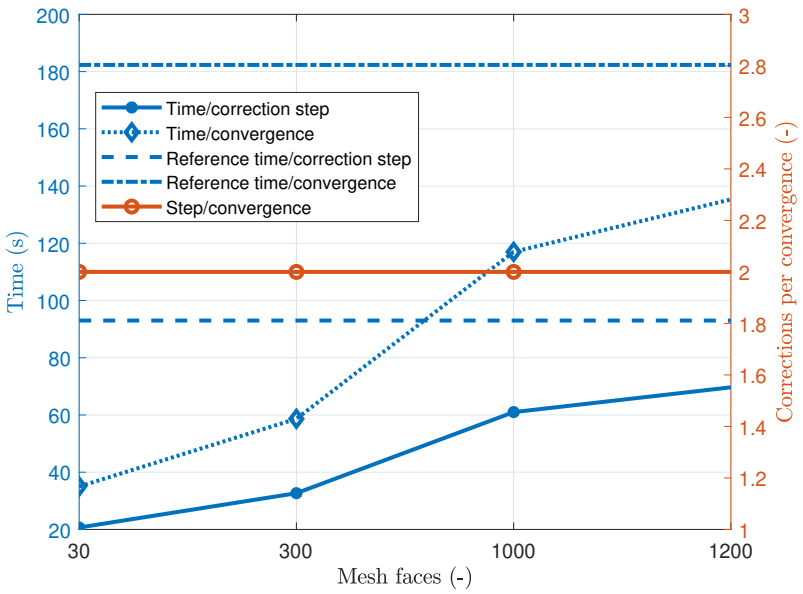

Figure 4.39: Influence of the polyhedron mesh on the computation time per iteration, the number of iterations and the total time required for convergence with 15 harmonics on the first frequency and 5 on the second.

orbits is 23.998, whereas the orbit in Figure 4.41a has a period of 76.152.

Despite attempting to reproduce the quasi-periodic solutions reported by Baresi et al. [114] using the MHBM formulation, convergence could not be achieved. The absence of Neimark-Sacker bifurcations to guide the first prediction to the quasi-periodic branch leads to diverging corrections. Nonetheless, each correction step required approximately

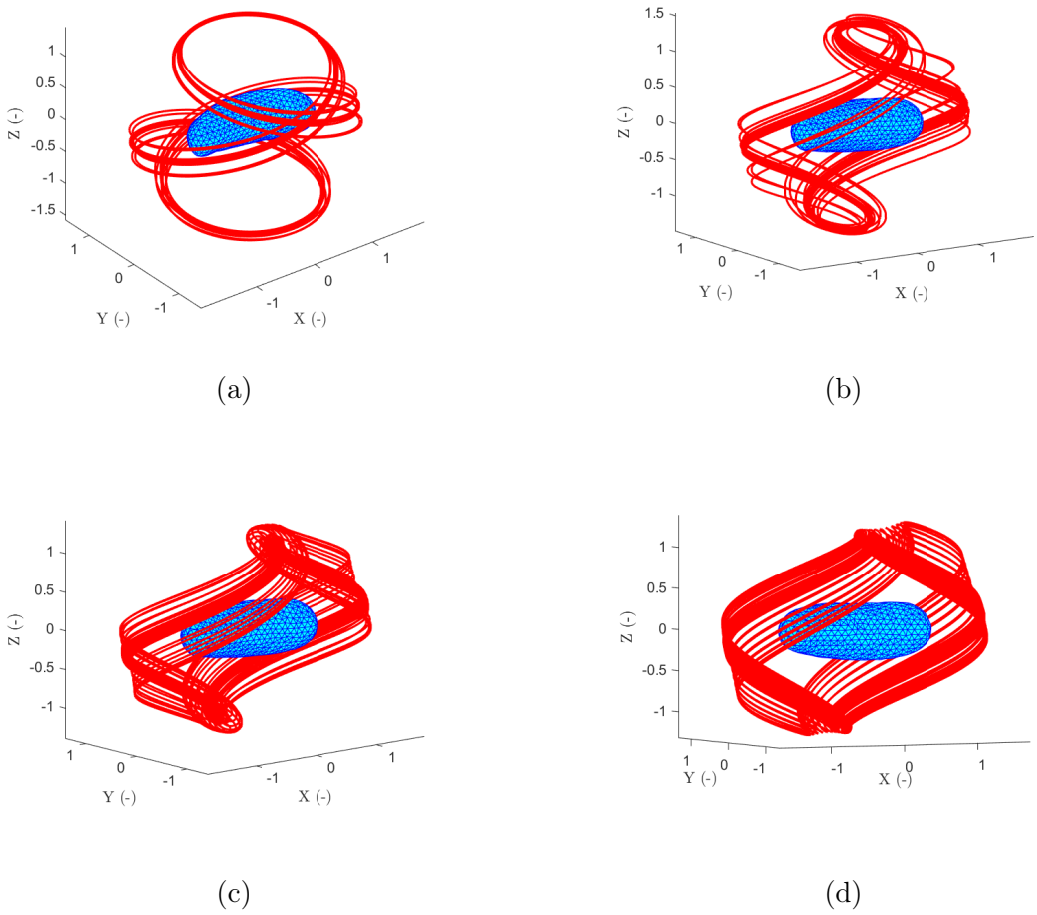

(a) (b)

(c) (d)

Figure 4.40: Evolution of the quasi-periodic orbits resulting from Neimark-Sacker bifurcation NS_{10}.

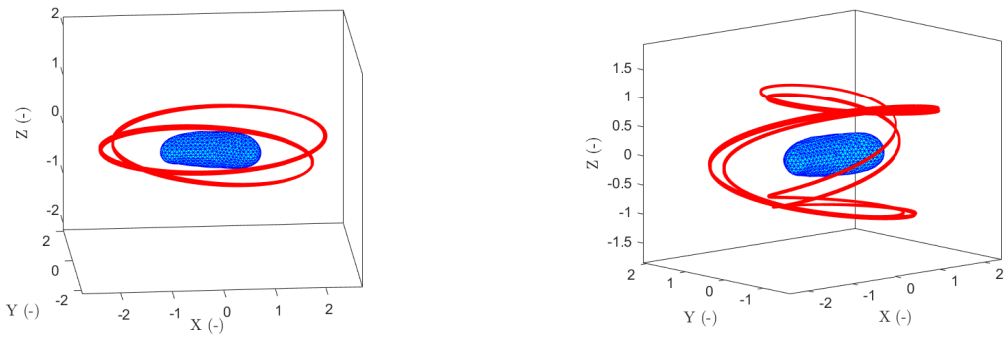

(a) (b)

Figure 4.41: Quasi-periodic orbits resulting from Neimark-Sacker bifurcation NS_1 (a) and NS_2 (b).

10 seconds, indicating that, had convergence been reached, the total computational cost per solution would likely have been comparable to that obtained with the numerical continuation methods reported in the reference study. Combined with the AHBM the method may even outperform them.

4.7 Conclusion

In this chapter, the polyhedron method was introduced to model the gravitational field around an irregularly shaped celestial body, specifically applied to the asteroid 433 Eros. This approach enabled the identification of equilibrium points, which are crucial for understanding the orbital environment of the asteroid.

The harmonic balance method (HBM) was then extended from the CRTBP to accommodate the complex dynamics of 433 Eros, which is characterized by low gravity and an irregular shape. Approximately one hundred bifurcations of three distinct types were encountered. Both branchpoint and period-doubling bifurcations were tracked, resulting in a dense bifurcation map. The stability of the different branches was evaluated using Hill's method. For the first time, a classification of orbits based on their general shape, similar to the CRTBP, was proposed. Despite the complexity of the system, the application of the HBM revealed patterns in the orbits, particularly with respect to resonant orbits. Several cases of resonant ratios in different shapes were presented through HBM applications.

Furthermore, the application of the multi-harmonic balance method (MHBM) and the detection of Neimark-Sacker bifurcations allowed for the smooth computation and continuation of quasi-periodic orbits. The extension of Hill's method provided insights into the stability of these quasi-periodic orbits. Additionally, the harmonic selection algorithm, previously discussed, was successfully extended, which reduced the computational burden associated with quasi-periodic orbits. The impact of the meshes on the computation time was also discussed.

To conclude, this chapter has established the HBM and its multi-frequency extension as effective and reliable tools for exploring the complex dynamical environment around irregular celestial bodies. Through their application to asteroid 433 Eros, the methods proved capable of revealing the global organization of periodic and quasi-periodic orbits, their bifurcations, and stability transitions within a highly nonlinear gravitational field. Beyond the quantitative results obtained, such as the mapping of over a hundred bifurcations and the identification of multiple resonant connections, the frequency-domain approach demonstrated its efficiency and interpretive power through the spectral characterization of the solutions.

Building on these achievements, the next chapter extends the analysis to more realistic dynamical scenarios, incorporating external perturbations such as solar radiation pressure and the mutual gravitational coupling within binary systems. This progression aims to assess the robustness and adaptability of the harmonic balance framework under conditions representative of actual mission environments.

Chapter 5

Major perturbations

5.1 Introduction

The relatively small size of asteroids induces a weak gravity field, small perturbations can have a large impact on the overall dynamic of orbital motion around an asteroid. The first source of external perturbation is the solar radiation pressure (SRP), especially for orbits that grow away from the asteroid. When carefully exploited, the SRP can become a valuable asset in space exploration. Solar sails directly harness this pressure to provide continuous propulsion for spacecraft [126, 127]. The influence of SRP on motion around asteroids was investigated in the context of hovering orbits [128, 129, 130] as well as periodic orbits within the Hill model [131, 132, 133]. To further enhance hovering capabilities, alternating SRP-assisted orbiter trajectories were studied by García [134]. Later, Xin [135] analyzed SRP-forced periodic orbits around asteroids modeled with an ellipsoidal gravity field combined with a cylindrical eclipse model projected by the ellipsoidal body. This eclipse model was subsequently extended to asteroid 101955 Bennu, represented with a polyhedral shape model, for the study of equatorial orbits [136]. Recently, the search for forced periodic motions by SRP with the polyhedron method has been conducted by Pedros-Faura [137], where the periodic orbits are corrected using Melnikov-like functions.

The second major source of perturbation arises from the presence of one or more smaller bodies gravitationally bound to a larger asteroid. Such systems, commonly referred to as binaries or triples, are more frequent than one might expect [138]. The most well-known example is the binary asteroid (65803) Didymos, the target of NASA's DART mission. The mission aimed to demonstrate planetary defense by intentionally impacting the secondary body, Dimorphos, in order to alter its orbit around the primary [139, 140]. The impact successfully shortened the orbital period by approximately 33 minutes [141]. A follow-up mission, Hera, led by ESA, is currently en route to the system and is expected to arrive in December 2026 [142].

The simplest dynamical model for such systems is the CRTBP, introduced in Chapter 3, where both Didymos and Dimorphos are approximated as point masses without additional perturbations. To improve the quality of the numerical analysis, numerous studies investigated the dynamical environment around Didymos under various influences, including solar radiation pressure, stability analyses, and planar periodic orbits [143, 144, 145, 146, 147]. More recently, Voyatzis [148] examined the evolution of planar orbits within the Didymos system by progressively increasing the model's fidelity, from

the classical CRTBP to more realistic representations incorporating the asteroid's actual shape and rotation.

In this chapter, the solar radiation pressure is introduced as a perturbation within the HBM, with asteroid 433 Eros approximated by an ellipsoid to construct the eclipse model. The influence of SRP on the orbital dynamics is examined by comparing periodic solutions computed with the HBM against direct time integrations. To further assess stability, these orbits are propagated over multiple periods, highlighting how prolonged exposure to radiation pressure affects their long-term behavior.

The second part of the chapter shifts focus on the binary system Didymos–Dimorphos, in order to demonstrate the capability of the HBM to account for third-body perturbations. Initial families of periodic orbits are identified in a complexified version of the CRTBP, where Didymos is modeled as a non-rotating polyhedron and Dimorphos as an ellipsoid. Building on these solutions, the analysis is then refined to incorporate the rotation of the primary asteroid, further illustrating the method's robustness in increasingly realistic dynamical environments.

5.2 Solar radiation pressure

Solar radiation pressure (SRP) is an antisunward force acting on a spacecraft directly exposed to sunlight. Since the rotation period of an asteroid about its spin axis is typically much shorter than its orbital period around the Sun, the Sun can be considered *frozen* in the inertial frame. This approximation is valid for short-period motions, such as the orbits computed with the HBM.

In the body-fixed frame, rotating with a constant angular velocity ω_a, the Sun follows a circular trajectory perpendicular to the spin axis at a constant latitude θ. The orientation of the asteroid with respect to the Sun is then described by a time-varying longitude,

$$\psi = -\omega_a t + \psi_0,$$

where ψ_0 is the initial longitude of the Sun. As this orientation is generally unknown, ψ_0 is conventionally set to 0°. A schematic representation of the Sun's apparent motion around the asteroid is shown in Figure 5.1.

The equations of motion including SRP are written as

$$\ddot{\mathbf{x}} + 2\omega_\mathbf{a} \times \dot{\mathbf{x}} + \omega_\mathbf{a} \times (\omega_\mathbf{a} \times \mathbf{x}) - \nabla U(\mathbf{x}) + \mathbf{f}_{\text{SRP}} = 0, \tag{5.1}$$

with the SRP force expressed in the antisunward direction as

$$\mathbf{f}_{\text{SRP}} = \begin{bmatrix} \nu g \cos\theta \cos\psi \\ \nu g \cos\theta \sin\psi \\ \nu g \sin\theta \end{bmatrix}, \tag{5.2}$$

where ν denotes the eclipse factor, and the SRP magnitude g is defined by

$$g = \frac{\beta}{D^2}, \tag{5.3}$$

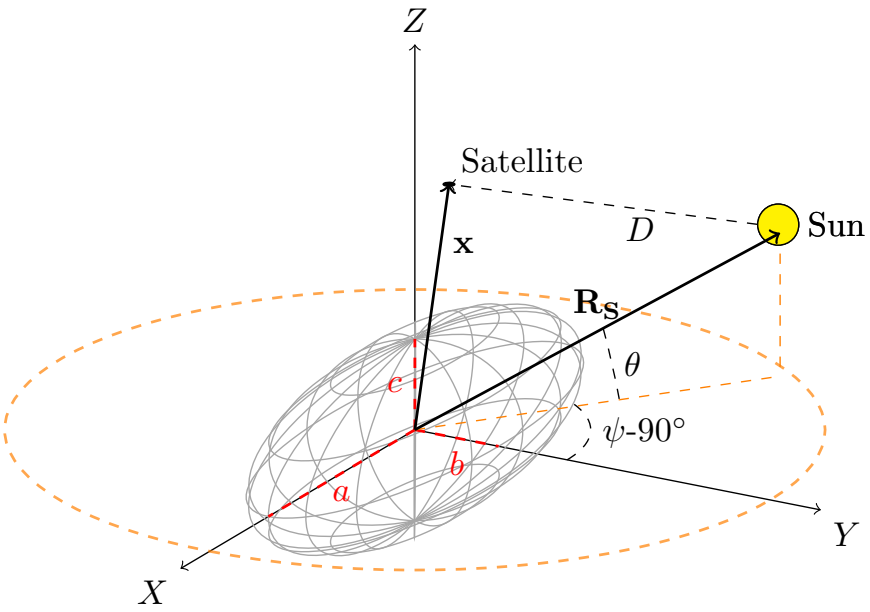

Figure 5.1: Schematic representation of the Sun's apparent motion in the body-fixed frame.

with

$$\beta = (1+\eta)\,\frac{G_1}{B}. \tag{5.4}$$

Here, $G_1 = 10^8$ kg km^3 s^{-2} m^{-2} is a solar constant, B is the spacecraft mass-to-area ratio in kg m^{-2}, and η is the reflectance coefficient of the spacecraft. Following the Osiris-Rex mission around Bennu [103], η is set to 0.2. The distance from the Sun to the spacecraft is denoted by D (in km). For nondimensionalization, the unit length is taken as the mean radius of asteroid 433 Eros, $l_u = 16.84$ km, and the time unit as its rotation period, $t_u = 5.27$ h.

5.2.1 Eclipse

When the spacecraft enters the shadow of the asteroid, the SRP no longer reaches its surface, effectively canceling the forcing term. Owing to the elongated shape of asteroid 433 Eros, the shadow it casts is best approximated by an ellipsoid combined with a cylindrical solar eclipse model [135]. The differences between cylindrical and conical eclipse models are generally negligible [133]. The ellipsoid semi-axes α, β, and γ are nondimensionalized such that $\alpha = 1$, $\beta = 0.3325$, and $\gamma = 0.3088$. A comparison between the ellipsoidal approximation (in red) and the actual shape of 433 Eros (in gray) is shown in Figure 5.2.

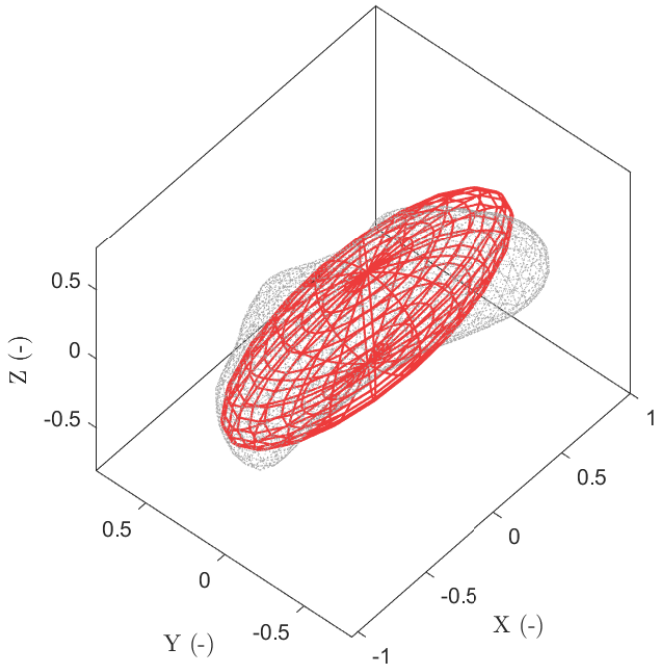

Figure 5.2: Ellipsoidal approximation of asteroid 433 Eros with nondimensional semi-axes $\alpha = 1$, $\beta = 0.3325$, and $\gamma = 0.3088$.

The direction vector of the Sun is expressed as

$$\hat{\mathbf{R}}_\mathbf{s} = \frac{\mathbf{R_s}}{R_s} = \begin{pmatrix} l_x \\ l_y \\ l_z \end{pmatrix} = \begin{pmatrix} \cos\theta\cos\psi \\ \cos\theta\sin\psi \\ \sin\theta \end{pmatrix}, \tag{5.5}$$

where $\mathbf{R_s}$ is the Sun's position vector and R_s its norm.

The line of sight between the spacecraft (x, y, z) and the Sun is modeled as a half-line (or ray) that originates at the spacecraft and extends indefinitely toward the Sun. Any point along this ray is given by

$$\begin{cases} x' = x + l_x s, \\ y' = y + l_y s, \\ z' = z + l_z s, \end{cases} \tag{5.6}$$

with $s \in [0, +\infty)$. The purpose of introducing this half-line is to test whether the spacecraft's view of the Sun is obstructed by the asteroid.

The ellipsoid is defined by

$$\frac{x'^2}{\alpha^2} + \frac{y'^2}{\beta^2} + \frac{z'^2}{\gamma^2} = 1. \tag{5.7}$$

Substituting Eq. (5.6) into Eq. (5.7) yields a quadratic equation in s:

$$As^2 + 2Bs + C = 0, \tag{5.8}$$

with coefficients

$$\begin{cases} A = \dfrac{l_x^2}{\alpha^2} + \dfrac{l_y^2}{\beta^2} + \dfrac{l_z^2}{\gamma^2}, \\ B = \dfrac{l_x X}{\alpha^2} + \dfrac{l_y Y}{\beta^2} + \dfrac{l_z Z}{\gamma^2}, \\ C = \dfrac{X^2}{\alpha^2} + \dfrac{Y^2}{\beta^2} + \dfrac{Z^2}{\gamma^2} - 1. \end{cases} \tag{5.9}$$

If the quadratic admits real, positive solutions, the ray intersects the ellipsoid, implying that the Sun is occluded by the asteroid and the spacecraft lies in eclipse. If no such solution exists, the spacecraft remains illuminated.

The eclipse factor ν is then defined as

$$\nu = \begin{cases} 0, & D > 0 \text{ and } B < 0, \\ 1, & \text{otherwise}, \end{cases} \tag{5.10}$$

where

$$D = B^2 - AC. \tag{5.11}$$

This condition can be expressed more compactly using a two-dimensional Heaviside function:

$$\nu = 1 - \mathrm{H}(D, -B), \tag{5.12}$$

where H is equal to 0 for negative arguments and 1 otherwise. However, the sudden passage in the shadow of the asteroid immediately induces a change in the forcing term. In the HBM formalism it may result in the appearance of Gibbs phenomenon. To prevent it, the transition must be smoothed to improve it representation with the Fourier decomposition. For this reason, the eclipse is overlooked in this work and ν is set to 1.

5.2.2 Results

Because SRP acts as a periodic forcing term with frequency 2π, only resonant periodic orbits can be obtained. Several resonant cases are therefore revisited from the previous chapter, where purely gravitational solutions were used as initial guesses for the computation with SRP included. An example of such a resonant orbit, is shown in Figure 5.3.

The introduction of SRP removes the autonomous character of the equations of motion, owing to the explicit time dependence in the longitude ψ. In principle, this implies that the phase condition introduced in the previous chapter, together with the fictitious energy used to regularize the equations, are no longer strictly necessary. However, since the influence of SRP is significantly weaker than the gravitational attraction of 433 Eros, the system may still be regarded as perturbed autonomous, or *quasi-autonomous*. In practice, omitting the phase condition leads to greater divergence of the algorithm, whereas retaining it does not compromise the accuracy of the results and, in fact, contributes to numerical stability. For the orbit shown in Figure 5.3, the Jacobian with the phase condition has $\mathrm{cond}(J) \approx 1.28 \times 10^5$ and $\sigma_{\min} \approx 0.519$, whereas without it $\mathrm{cond}(J) \approx 3.89 \times 10^9$

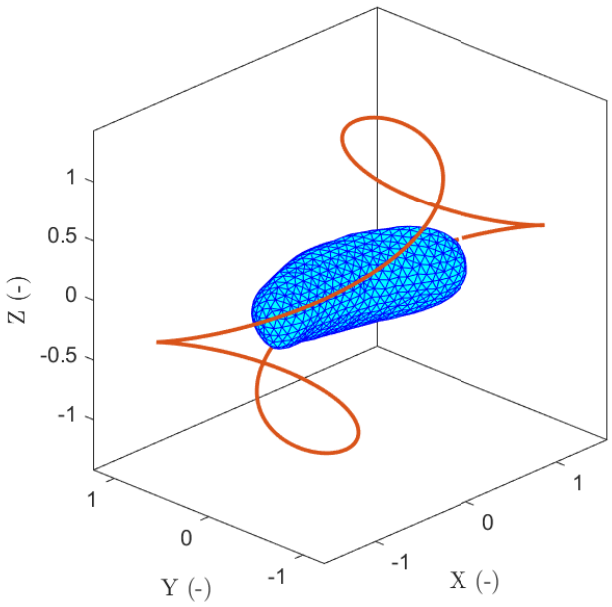

Figure 5.3: Periodic orbit around 433 Eros computed with SRP taken into account.

and $\sigma_{\min} \approx 1.71 \times 10^{-5}$. As highlighted in Figure 5.4, the discrepancy is entirely concentrated at the small end of the spectrum. Retaining the phase condition therefore reduces sensitivity by several orders of magnitude, stabilizing Newton iterations without altering the underlying orbit.

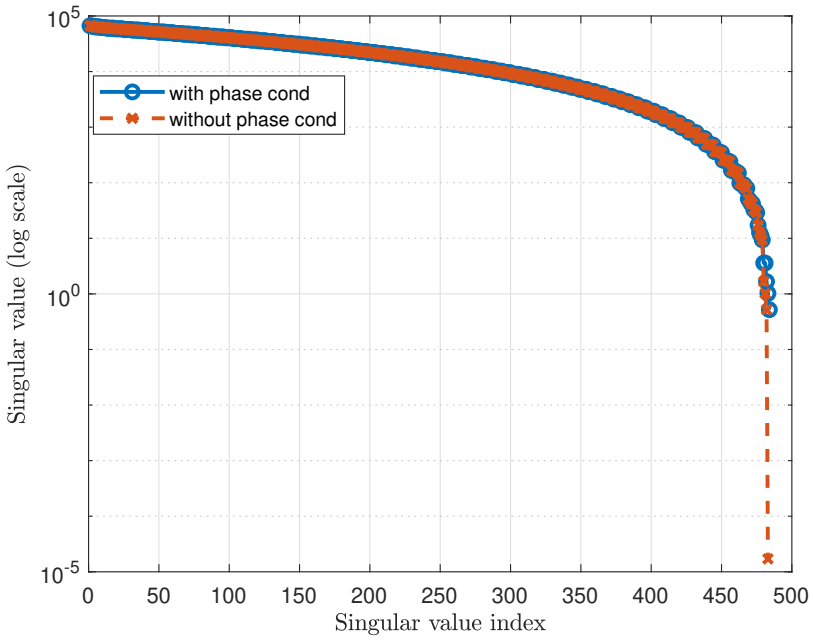

Figure 5.4: Singular value spectrum of HBM Jacobian with and wihtout a phase condition.

Incorporating SRP into the HBM requires modifying the forcing term $\mathbf{b}$, which is

computed as

$$\mathbf{b}(\mathbf{z}) = (\mathbf{\Gamma}(\omega))^{+} \left(\nabla U - \mathbf{f}_{SRP}\right). \tag{5.13}$$

Since the position of the spacecraft, $\mathbf{x}$, with respect to the center of mass of the asteroid is significantly smaller than the distance between the asteroid and the Sun, D, the distance between the spacecraft and the Sun is assumed constant and equal to D. Therefore, the SRP does not explicitly depend on $\mathbf{x}$, the derivative of the force with respect to position is not required. No further modifications to the HBM formulation presented in earlier chapters are necessary.

To quantify the influence of SRP on this periodic orbit, the gravitational and SRP contributions are decoupled and compared along the X, Y, and Z axes in Figure 5.5. Several observations can be drawn. First, the amplitude of SRP is approximately four orders of magnitude smaller than the gravitational attraction of 433 Eros. Second, the orbit does not intersect the asteroid's shadow at any point, and thus the spacecraft remains continuously exposed to SRP throughout its motion. Finally, the SRP component along the Z axis vanishes because the latitude is fixed at $\theta = 0°$.

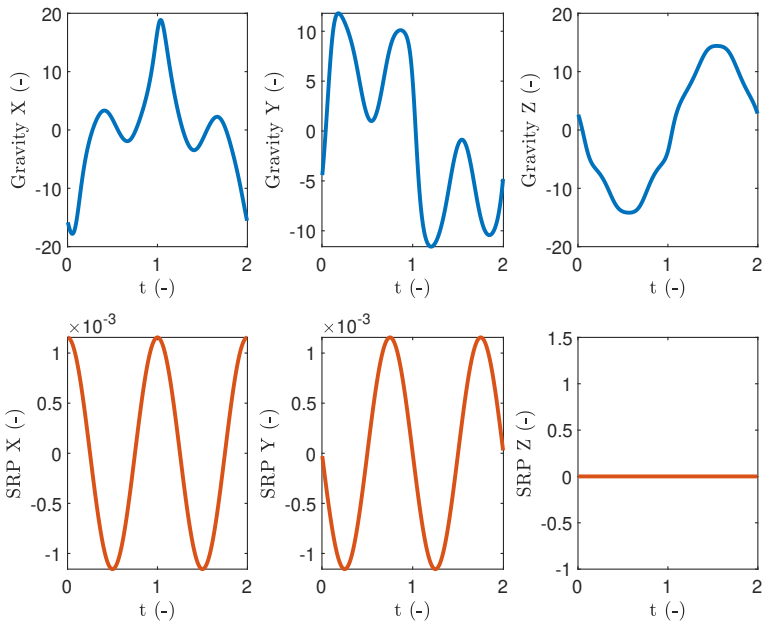

Figure 5.5: Comparison of the X, Y, and Z components of the gravitational attraction of 433 Eros and the solar radiation pressure.

Although the SRP is small in magnitude compared to gravity, its inclusion has a direct effect on the evaluation of the Jacobi constant and the equilibrium points. Because SRP is explicitly time dependent, the Jacobi constant is no longer conserved; instead, it oscillates at the forcing frequency of the SRP. Over longer timescales, these oscillations lead to a secular drift. For consistency with the earlier chapters, the term "Jacobi constant" is retained here as a comparative diagnostic, rather than adopting the more precise term "pseudo-Jacobi constant."

This effect is illustrated in Figure 5.6, where the orbit from Figure 5.3 is shown with and without SRP, along with the corresponding Jacobi constant evolution. The three-dimensional orbit shapes overlap closely in both cases, while the oscillatory behavior induced by SRP is clearly visible in the Jacobi constant.

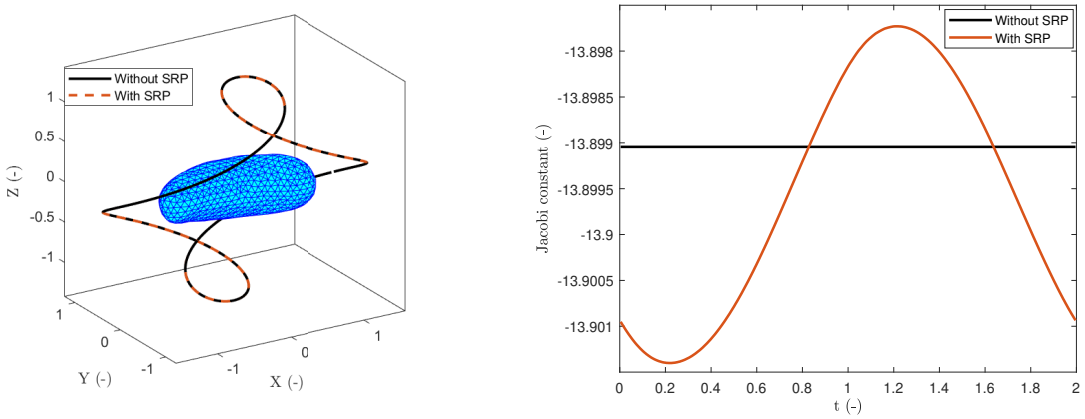

(a) (b)

Figure 5.6: Comparison of the periodic orbit around 433 Eros computed using the HBM with and without the SRP effect (a); Comparison of the Jacobi constant with and without the SRP (b).

The equilibrium points found in the previous chapter are no longer equilibrium positions. Figure 5.7 shows the evolution of a spacecraft left at the position of the previous equilibrium points with no velocity. The propagation was terminated upon collision with the asteroid.

To further quantify the differences between the cases with and without SRP, the variation in the amplitudes of the harmonic components is examined. The differences along the X, Y, and Z directions are shown in Figure 5.8. As expected from the three-dimensional orbit comparison, the amplitude differences are small, yet they remain sufficient to affect the long-term propagation. The predominance of the second harmonic can be traced to a geometric frequency-mixing effect. The direction of the SRP force rotates with the Sun at the fundamental frequency, but its action on the spacecraft is not felt directly, it is always projected onto the orbital coordinates. Along a nearly symmetric orbit, the projection of the SRP vector repeats twice during one SRP cycle, because the spacecraft encounters geometrically similar configurations on opposite sides of the asteroid. In other words, the scalar product between the once-per-cycle SRP direction and the orbital position vector introduces a modulation with a two-per-cycle character. From a Fourier point of view, this corresponds to the product of two periodic functions with different periodicities; the convolution of their spectra transfers energy from the fundamental into higher harmonics, with the second harmonic being the strongest. As a result, even though SRP itself is a simple sinusoidal forcing at the Sun's frequency, its geometric projection onto the orbit naturally amplifies the second harmonic component of the response.

As discussed earlier, the inclusion of SRP introduces an explicit time dependence into

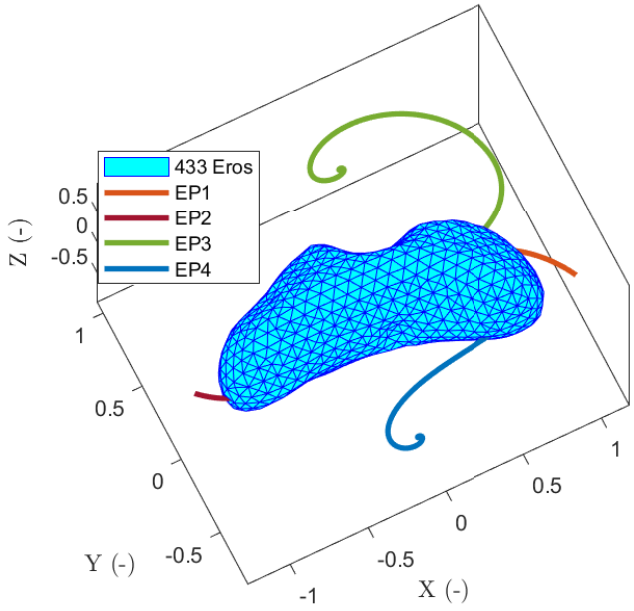

Figure 5.7: Evolution of the position of the equilibrium points under SRP.

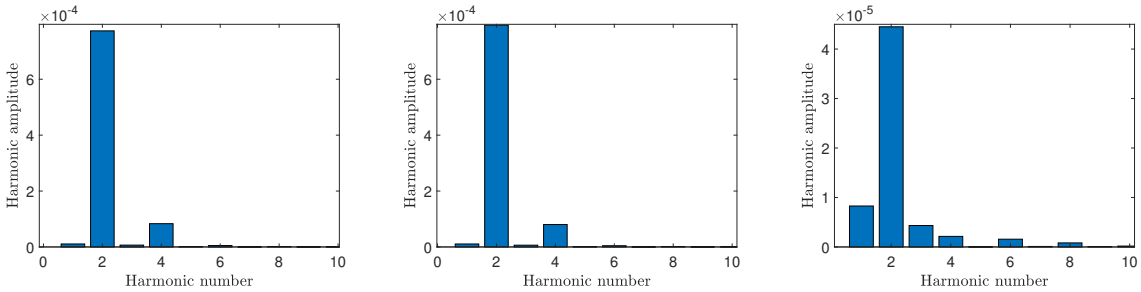

(a) (b) (c)

Figure 5.8: Differences in harmonic amplitudes along X (a); Y (b); Z (c) between the cases with and without SRP.

the system. As a result, periodic solutions can only exist when the orbital motion is resonant with the SRP forcing period. Several resonance orders are identified with the HBM and compared against direct time integration, first over a single period and then over multiple periods. The resonance notation $m : n$ is used, where m denotes the rotation period of the asteroid (and thus of the SRP), and n corresponds to the orbital period. For this analysis, the latitude is fixed at $\theta = 10.827°$, equal to the inclination of Eros with respect to the ecliptic plane. This angle only serves to provide a vertical component to the force. As in the previous chapter, a total of 30 harmonics ($N_H = 30$) are retained, with a tolerance of $\epsilon = 10^{-10}$ imposed for convergence and a time discretization of $N = 512$.

Resonance 1:1 - T = 1

The orbit investigated at the 1:1 resonance corresponds to a low-amplitude, vertically unstable trajectory. Figure 5.9a compares the time-integrated solution with the result obtained through the HBM over a single period, T = 1. The associated evolution of the

Jacobi constant is presented in Figure 5.9b. This comparison illustrates the ability of the HBM to efficiently capture periodic solutions while accounting for the effect of SRP. The SRP acts as a continuous perturbation, which gradually amplifies the instability of the trajectory.

It is nevertheless instructive to examine how this solution behaves when propagated forward in time, as this provides insight into the robustness of the initial conditions supplied by the HBM. Figures 5.9c–5.9d show the trajectory extended over four orbital periods. The orbit maintains its overall shape for approximately three periods before gradually diverging from the original path, reflecting its intrinsic instability.

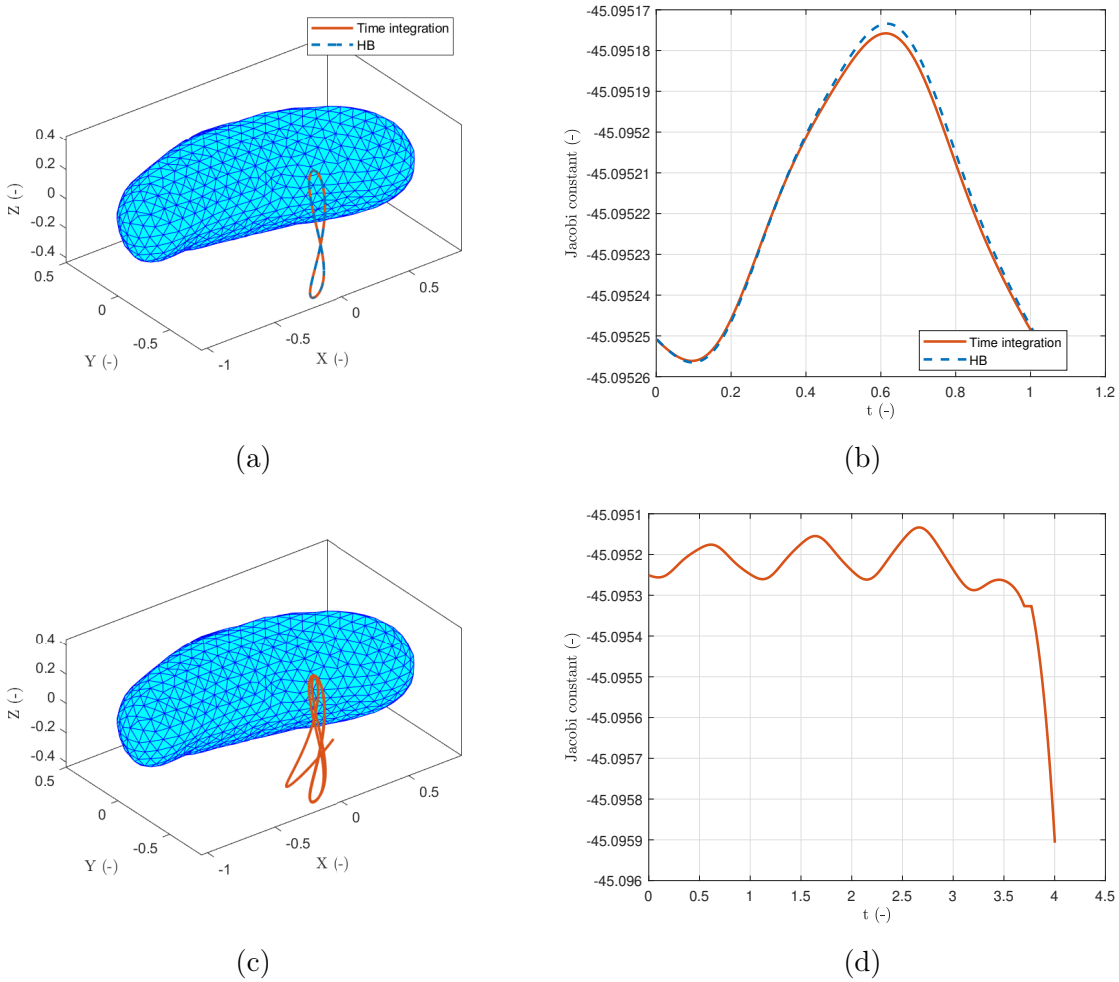

(a) (b)

(c) (d)

Figure 5.9: Periodic orbit at the 1:1 resonance under SRP: (a) short-term HBM vs time integration; (b) Jacobi constant evolution; (c-d) multi-period propagation.

Resonance 2:1 - T = 2

At the 2:1 resonance, the computed solution corresponds to a periodic orbit with period T = 2. Figure 5.10a compares the trajectory obtained with the HBM to the time-integrated solution over one full period, and the agreement between the two is again verified. The evolution of the Jacobi constant, shown in Figure 5.10b, highlights the same oscillatory

behavior observed in the 1:1 case, confirming that the presence of SRP prevents strict conservation of the quantity.

When the orbit is propagated for several successive periods, as shown in Figures 5.10c–5.10d for 10 periods, the solution initially maintains its periodic structure before exhibiting a gradual divergence from the original trajectory. This deviation appears after a few cycles and is consistent with the expected unstable nature of the orbit. The HBM nonetheless provides highly accurate initial conditions, as evidenced by the excellent short-term agreement. The orbital shape is kept for more than 10 times the period despite being constantly exposed to the perturbation of the SRP.

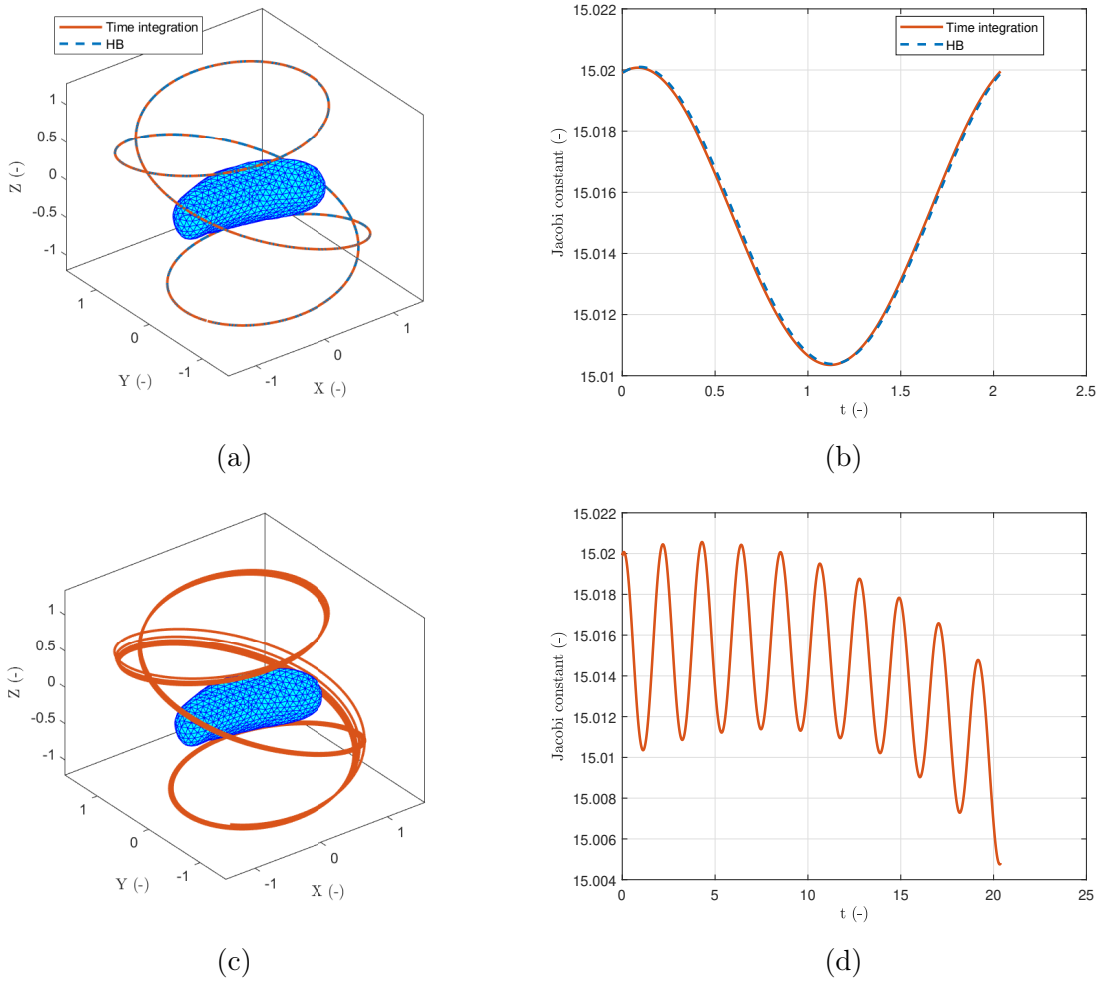

Figure 5.10: Periodic orbit at the 2:1 resonance under SRP: (a) short-term HBM vs time integration; (b) Jacobi constant evolution; (c-d) multi-period propagation.

Resonance 3:1 - T = 3

At the 3:1 resonance, the HBM again identifies a periodic orbit of period T=3, however the solution is stable under the SRP. The comparison in Figure 5.11a shows that the HBM solution and the time-integrated trajectory are nearly indistinguishable over a single orbital cycle. The corresponding Jacobi constant evolution in Figure 5.11b follows the

familiar oscillatory pattern, reflecting the time-dependent forcing introduced by SRP.

Extending the propagation across multiple periods (Figures 5.11c–5.11d) demonstrates that the orbit retains its global structure for the 10 additional periods which is in agreement with the stability of the orbit. This reflects as well in the evolution of the Jacobi constant which solely displays a slow drift over time compared to the sudden deviation observed in the previous cases.

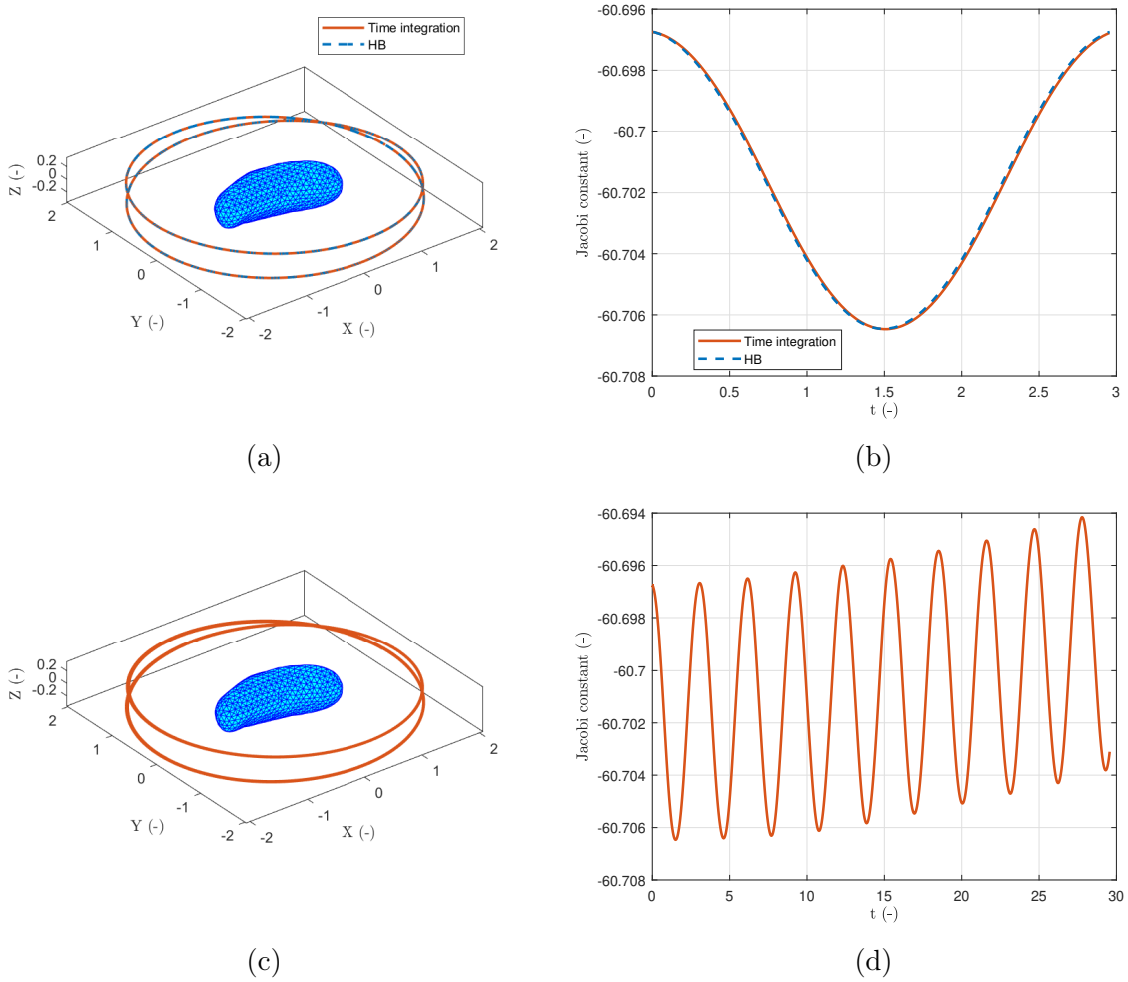

Figure 5.11: Periodic orbit at the 3:1 resonance under SRP: (a) short-term HBM vs time integration; (b) Jacobi constant evolution; (c-d) multi-period propagation.

Resonance 4:1 - T = 4

The unstable periodic orbit at the 4:1 resonance exhibits the same general characteristics as the lower-order resonances. As seen in Figure 5.12a, the short-term match between HBM and time integration is excellent. However, the Jacobi constant, illustrated in Figure 5.12b, exhibits larger oscillations for the results obtained with the HBM. Due to the complex shape of the orbit, the effect on the Jacobi constant has to be mitigated with a large amount of harmonics, as portrayed in previous chapters. The impact on the orbit shape is negligible, and the global trend of the time integration Jacobi constant is still

followed; hence, the number of harmonics is kept equal to 30 and this oscillatory behavior is disregarded.

The long-term propagation in Figures 5.12c–5.12d shows that the orbit barely maintains its coherence for two periods but even if the orbit loses its periodicity, it remains bounded to the asteroid for multiple periods. This is directly linked to the initial conditions given by the HBM, which reflects that the more complex the orbit, the more harmonics are required to better capture the periodicity of the orbit. In addition, the longer the period, the more the solution is subject to small deviations and numerical errors, which add up over time and eventually set the orbit off its original path.

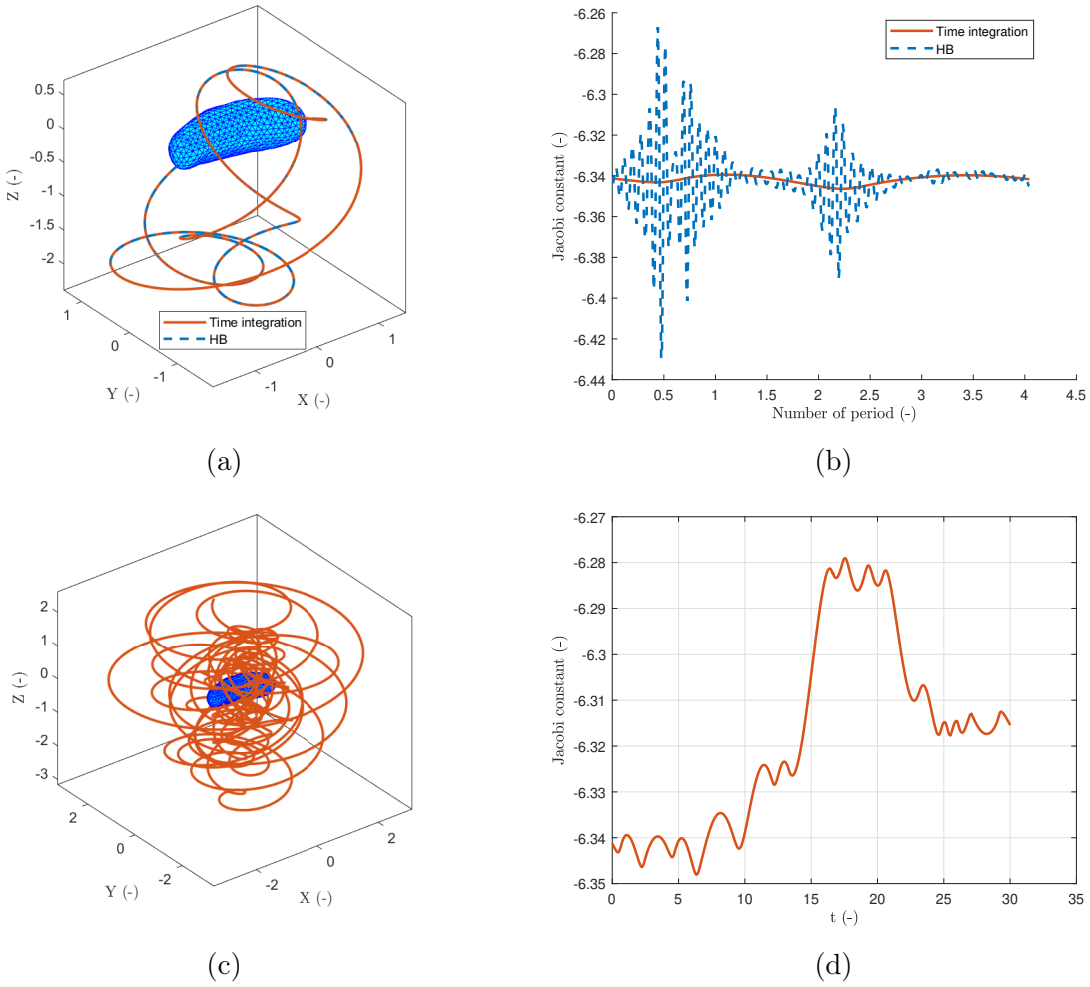

Figure 5.12: Periodic orbit at the 4:1 resonance under SRP: (a) short-term HBM vs time integration; (b) Jacobi constant evolution; (c-d) multi-period propagation.

Resonance 5:1 - T = 5

Lastly, the 5:1 resonance provides the longest-period orbit examined in this study. Figure 5.13a illustrates that the HBM prediction and the time-integration remain in close agreement during a single orbital cycle. The Jacobi constant variation in Figure 5.13b confirms the persistence of oscillatory, non-conservative behavior due to SRP with one more os-

cillation associated with the HBM resolution. The trend of the Jacobi constant is followed.

Similar results as the ones shown for the 4:1 resonance are retrieved for the propagation over multiple periods. The orbit keeps its periodic shape for few orbits before diverging from its path.

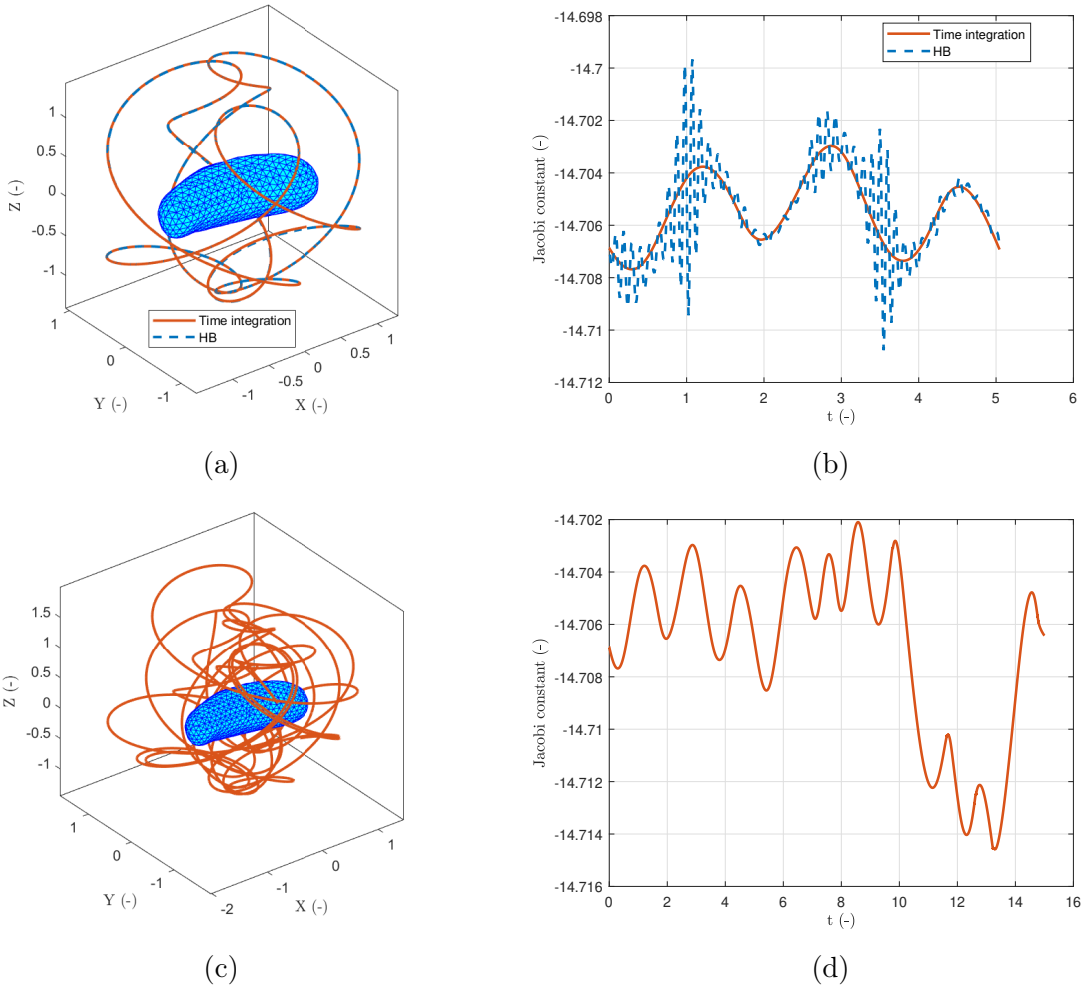

Figure 5.13: Periodic orbit at the 5:1 resonance under SRP: (a) short-term HBM vs time integration; (b) Jacobi constant evolution; (c-d) multi-period propagation.

5.3 Binary system — The case of Didymos and Dimorphos

A second major source of perturbation in orbital propagation around irregular bodies arises from the presence of a secondary companion orbiting the primary. This is the case of the binary asteroid system composed of Didymos and its moon Dimorphos.

Didymos is a quasi-spherical asteroid with an effective diameter of approximately 850 m. For this study, it is represented by a polyhedral shape model consisting of 1000 vertices and 1996 faces (Figure 5.14) [149]. Dimorphos, by contrast, is modeled as a tri-axial ellipsoid with a longest axis of about 180 m. The primary rotates about its principal axis of inertia with a period of 2.26 h, while the secondary follows a nearly circular orbit of radius 1.19 km around Didymos with a period of 11.37 h. These values correspond to the post-impact configuration measured after the DART mission [150].

As in the CRTBP, the two bodies of mass m_1 and m_2 revolve in circular motion around their barycenter O with angular velocity n and separation distance r_{12} [148]. Figure 5.15 illustrates the Didymos–Dimorphos system, showing both the inertial frame centered at O and the body-fixed frame attached to Didymos (in blue). The latter rotates with angular velocity ω and is oriented at an angle ϕ_D with respect to the inertial frame. The difference between the two angular velocities defines the synodic frequency,

$$\omega_{\text{synodic}} = \omega - n.$$

The relevant physical parameters are summarized in Table 5.1, where the semi-axes of the ellipsoid representing Dimorphos are denoted a, b, and c.

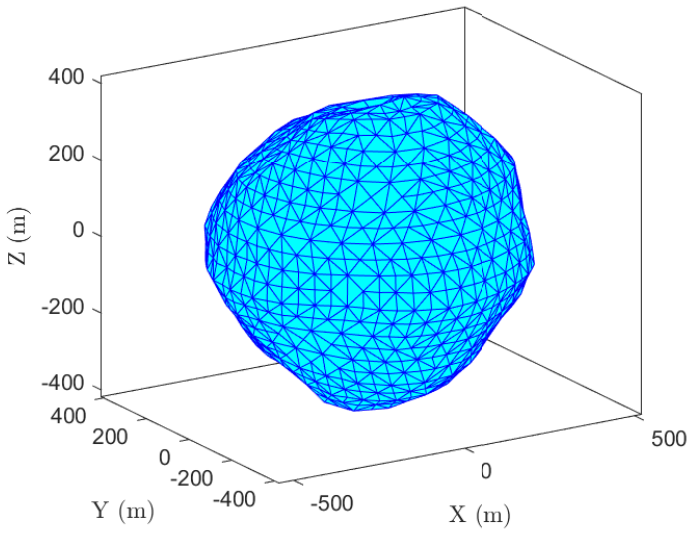

Figure 5.14: Dydimos mesh made of 1000 edges and 1996 faces.

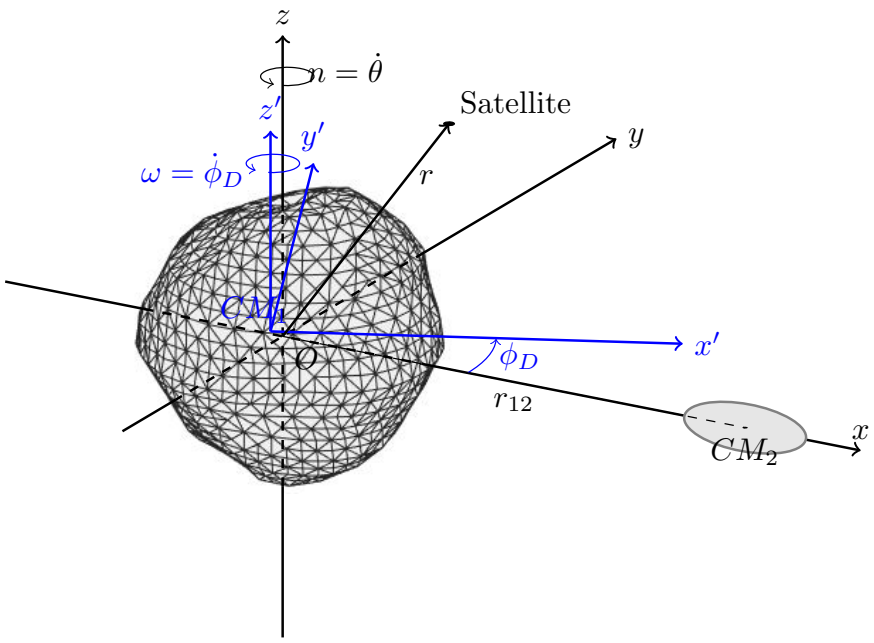

Figure 5.15: Dydimos and Dimorphos frames.

Table 5.1: Physical values of Didymos and Dimorphos.

Parameter	**Physical values**
m_1	5.32×10^{11} kg
m_2	4.94×10^{9} kg
r_{12}	1.19 km
a	0.088 km
b	0.087 km
c	0.058 km
$\mathrm{T}_{\mathrm{system}}$	11.37 h
$\mathrm{T}_{\mathrm{Didymos}}$	2.26 h
$\mathrm{T}_{\mathrm{synodic}}$	2.82 h

The nondimensionalization of the physical parameters is carried out by defining the unit time as

$$t_u = \frac{11.37}{2\pi} \text{ h},$$

such that the nondimensional angular velocity is $n = 1$. The unit length is taken as $l_u = 1.19$ km, and the unit mass as $m_u = m_1 + m_2$.

With these definitions, the nondimensional equations of motion become

$$\begin{cases} \ddot{x} = 2n\dot{y} + n^2 x + \nabla U_x - \mu \nabla U_{x_{\mathrm{ell}}}, \\ \ddot{y} = -2n\dot{x} + n^2 y + \nabla U_y - \mu \nabla U_{y_{\mathrm{ell}}}, \\ \ddot{z} = \nabla U_z - \mu \nabla U_{z_{\mathrm{ell}}}, \end{cases} \tag{5.14}$$

where $\mu = 0.0092535$ is the mass ratio, and ∇U is the gradient of the potential of a point

mass. The potential of the ellipsoidal secondary is written as

$$U_{\text{ell}} = -\frac{1}{r} - \frac{I_x + I_y + I_z}{2r^3} + \frac{3}{2}\frac{I_x x^2 + I_y y^2 + I_z z^2}{r^5}, \tag{5.15}$$

where the gradient is evaluated at the position

$$R = (x - 1 + \mu,\, y,\, z),$$

and the distance is

$$r = \sqrt{(x - 1 + \mu)^2 + y^2 + z^2}.$$

The nondimensional semi-axes of Dimorphos are $\alpha = 0.0739$, $\beta = 0.0731$, and $\gamma = 0.0487$, leading to the expressions for the principal moments of inertia:

$$\begin{cases} I_x = \frac{1}{5}\,\mu(\beta^2 + \gamma^2), \\ I_y = \frac{1}{5}\,\mu(\alpha^2 + \gamma^2), \\ I_z = \frac{1}{5}\,\mu(\alpha^2 + \beta^2). \end{cases} \tag{5.16}$$

The gradient of the ellipsoidal potential in each coordinate direction is then given by

$$\begin{cases} \nabla U_{x_{\text{ell}}} = \dfrac{x}{r^3} + \dfrac{3}{2}\dfrac{(I_x + I_y + I_z)x}{r^5} + \dfrac{3I_x x}{r^5} - \dfrac{15}{2}\dfrac{(I_x x^2 + I_y y^2 + I_z z^2)x}{r^7}, \\ \nabla U_{y_{\text{ell}}} = \dfrac{y}{r^3} + \dfrac{3}{2}\dfrac{(I_x + I_y + I_z)y}{r^5} + \dfrac{3I_y y}{r^5} - \dfrac{15}{2}\dfrac{(I_x x^2 + I_y y^2 + I_z z^2)y}{r^7}, \\ \nabla U_{z_{\text{ell}}} = \dfrac{z}{r^3} + \dfrac{3}{2}\dfrac{(I_x + I_y + I_z)z}{r^5} + \dfrac{3I_z z}{r^5} - \dfrac{15}{2}\dfrac{(I_x x^2 + I_y y^2 + I_z z^2)z}{r^7}. \end{cases} \tag{5.17}$$

Unlike the perturbation induced by SRP, the forcing term due to the presence of the secondary body depends explicitly on the spacecraft's position. Consequently, the Hessian matrix is required for the HBM implementation. Its expression is provided in Eq. (5.18), where the indices i and j can be replaced with x, y, or z with $i \neq j$.

$$\begin{cases} \nabla\nabla U_{ii_{ell}} = \dfrac{r^2 - 3i^2}{r^5} + \dfrac{3}{2}(I_x + I_y + I_z)\left(\dfrac{1}{r^5} - \dfrac{5i^2}{r^7}\right) \\ \qquad\qquad + 3I_i\left(\dfrac{1}{r^5} - \dfrac{5i^2}{r^7}\right) - \dfrac{15}{2}\,\dfrac{I_x x^2 + I_y y^2 + I_z z^2}{r^7} \\ \qquad\qquad + \dfrac{105}{2}\,\dfrac{(I_x x^2 + I_y y^2 + I_z z^2)\,i^2}{r^9} \\ \nabla\nabla U_{ij_{ell}} = \dfrac{-3ij}{r^5} - \dfrac{15}{2}(I_x + I_y + I_z)\left(\dfrac{ij}{r^7}\right) \\ \qquad\qquad - 15(I_i + I_j)\left(\dfrac{ij}{r^7}\right) + \dfrac{105}{2}\,\dfrac{(I_x x^2 + I_y y^2 + I_z z^2)\,ij}{r^9} \end{cases} \tag{5.18}$$

The HBM algorithm itself remains unchanged, except for updates to the forcing vector $\mathbf{b}$ and the expression of the Jacobian $\mathbf{h_z}$, which are now written as

$$\mathbf{b}(\mathbf{z}) = (\mathbf{\Gamma}(\omega))^{+} \left(\nabla \mathbf{U} - \mu \nabla \mathbf{U}_{\text{ell}}\right) \tag{5.19}$$

$$\mathbf{h}_{\mathbf{z}} = \mathbf{A} - \mathbf{\Gamma}^{+} \left(\nabla\nabla \mathbf{U}\text{Didy} - \mu \nabla\nabla \mathbf{U}\text{ell}\right) \mathbf{\Gamma}. \tag{5.20}$$

5.3.1 Non-rotating Didymos

When the polyhedral model of Didymos is considered fixed in the frame connecting Didymos to Dimorphos, the angular velocity ω is set equal to the orbital angular velocity n. This choice results in a synodic angular velocity ω_{Synodic} of zero, meaning that Dimorphos constantly observes the same face of Didymos. Under these conditions, the system remains autonomous and behaves analogously to the CRTBP, with the addition of an irregular gravitational field from Didymos and the possibility of collisions with either body.

Building on the periodic orbit families introduced in the CRTBP chapter, analogous families are identified in the non-rotating Didymos–Dimorphos system. These include, for example, the vertical family around the first Lagrange point shown in Figure 5.16, and the W4 family that connects the vertical family near the fourth Lagrange point, L4, with the halo family around Dimorphos (Figure 5.17). Circular families are also recovered across the system, as illustrated in Figure 5.18, together with the halo family located opposite Dimorphos near the third Lagrange point, L3.

In addition, families of orbits in resonance with the system's rotation are detected. The 1:1 and 1:2 resonant families are displayed in Figures 5.20 and 5.21, respectively. The perturbations introduced by the irregular gravity field of Didymos become more pronounced for orbits closer to the asteroid, as illustrated by the 2:1 resonant family in Figure 5.23 and the 2:3 resonant family in Figure 5.24.

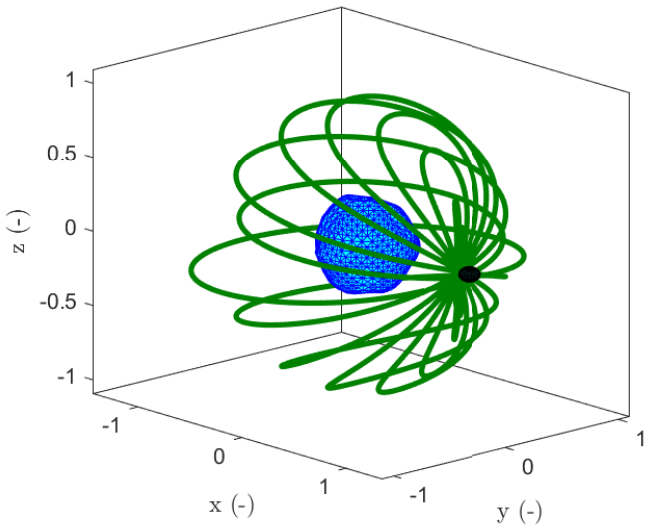

Figure 5.16: V1 orbit family around Didymos-Dimorphos.

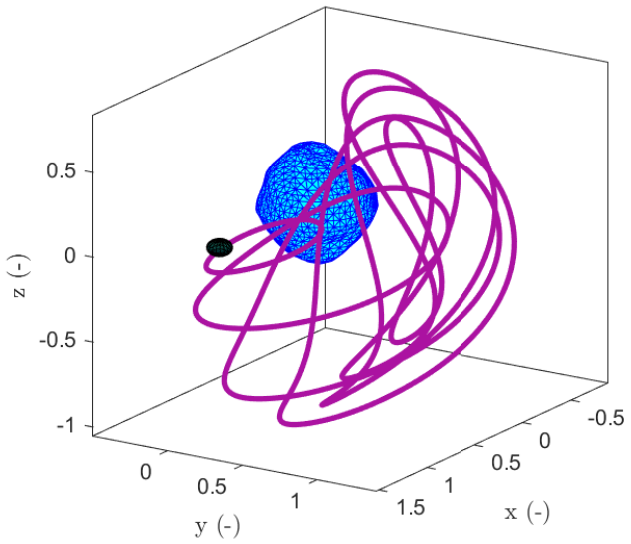

Figure 5.17: W4 orbit family around Didymos-Dimorphos.

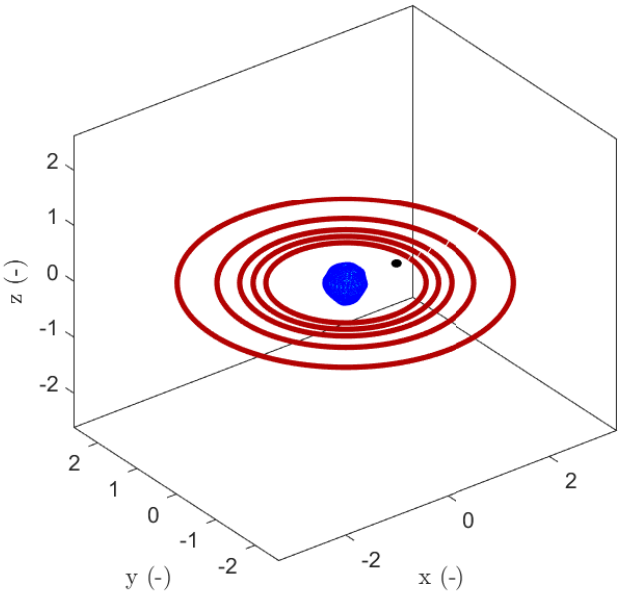

Figure 5.18: Circular orbit family around Didymos-Dimorphos.

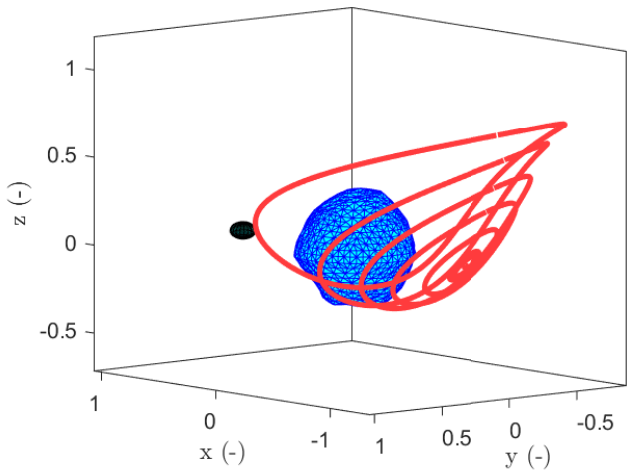

Figure 5.19: H3 orbit family around Didymos-Dimorphos.

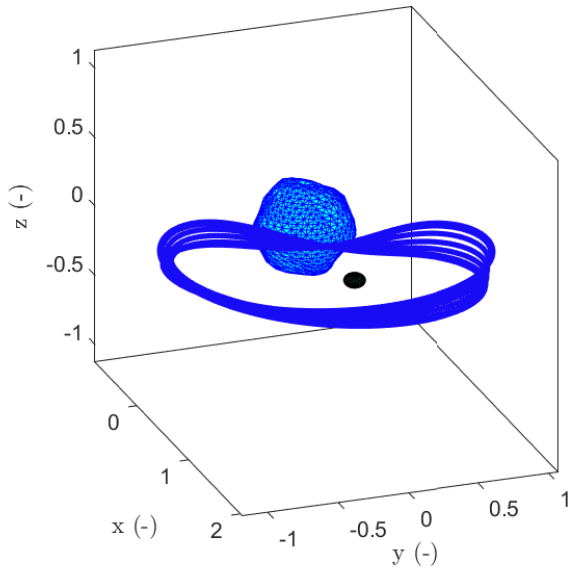

Figure 5.20: Resonant 1:1 orbit family around Didymos-Dimorphos.

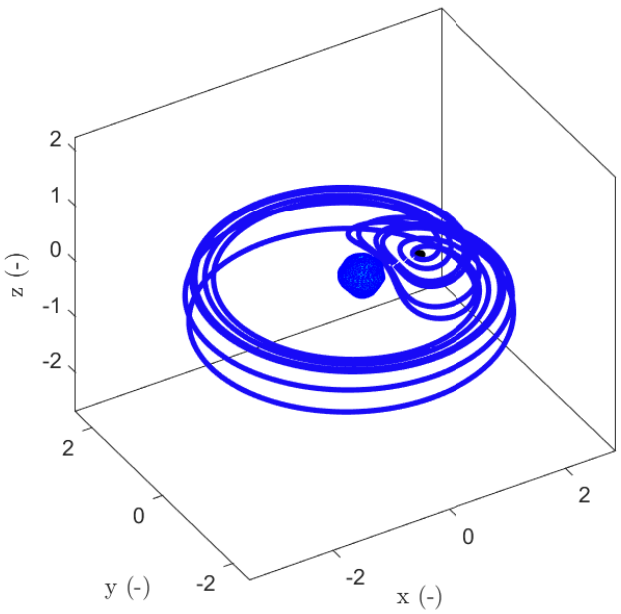

Figure 5.21: Resonant 1:2 orbit family around Didymos-Dimorphos.

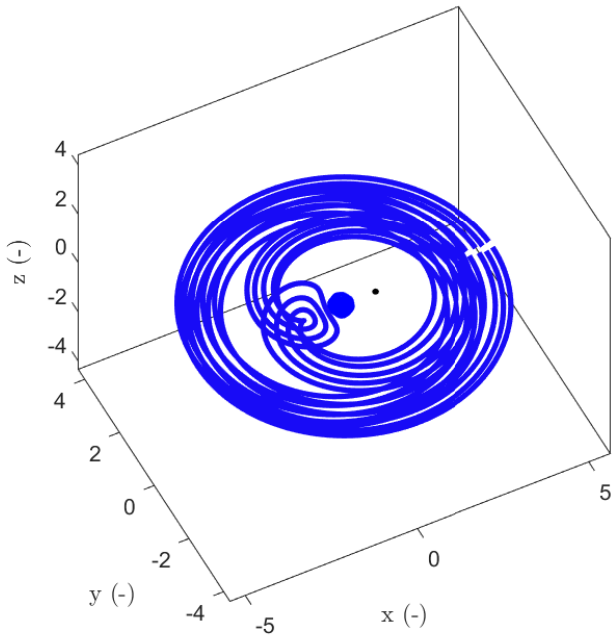

Figure 5.22: Resonant 1:4 orbit family around Didymos-Dimorphos.

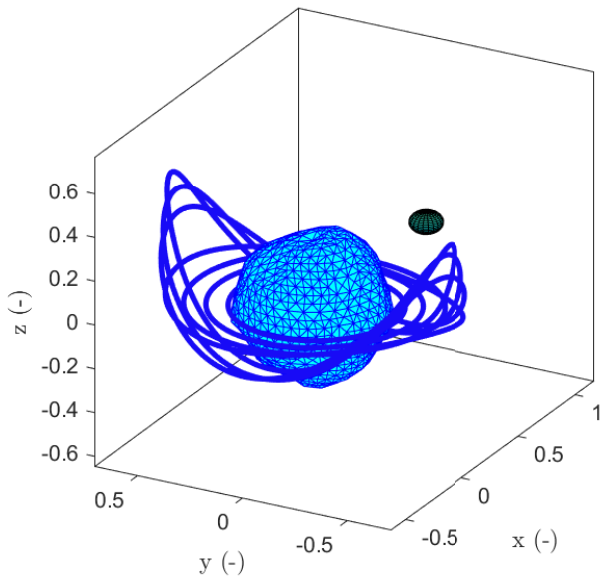

Figure 5.23: Resonant 2:1 orbit family around Didymos-Dimorphos.

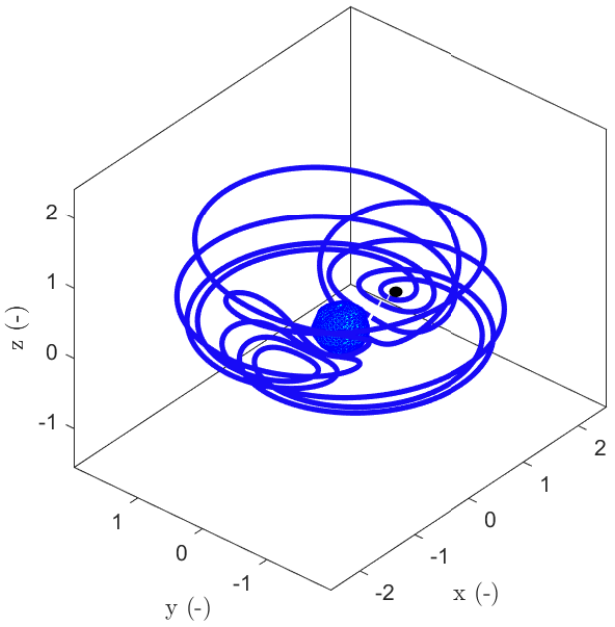

Figure 5.24: Resonant 2:3 orbit family around Didymos-Dimorphos.

5.3.2 Rotating Didymos

Introducing the rotation of Didymos induces a time dependence in the system of equations, as the angle between the two frames, ϕ_D, evolves according to

$$\phi_D(t) = \omega_{\text{Synodic}} t + \phi_D(0), \tag{5.21}$$

thereby removing the autonomous character of the system.

There are two approaches to account for the rotation of Didymos in the primary rotating frame. One option is to rotate the entire polyhedral mesh at each time step before evaluating the gradient, however, this method is computationally expensive. An alternative, more efficient approach is to project the predicted orbit into the body-attached frame of Didymos, compute the gradient and Hessian matrix there, and then project the results back into the main frame. This method is less costly and straightforward to implement. The initial orientation is set as $\phi_D(0) = 0$, and the rotation matrix is defined as

$$\mathbf{R}(t) = \begin{bmatrix} \cos(\omega_{\text{Syn}} t) & \sin(\omega_{\text{Syn}} t) & 0 \\ -\sin(\omega_{\text{Syn}} t) & \cos(\omega_{\text{Syn}} t) & 0 \\ 0 & 0 & 1 \end{bmatrix}. \tag{5.22}$$

The transformation from the body-attached frame to the main frame is then given by

$$\nabla \mathbf{U}_{\text{main}} = \mathbf{R}^T(t) \nabla \mathbf{U}_{\text{body}}, \tag{5.23}$$

and analogously for the Hessian matrix

$$\nabla\nabla \mathbf{U}\text{main} = \mathbf{R}^T(t) \nabla\nabla \mathbf{U}_{\text{body}} \mathbf{R}(t). \tag{5.24}$$

Since the rotation introduces a time-dependent perturbation in the main frame, isolated periodic solutions can only exist when in resonance with the synodic period, similar to the effect of the SRP discussed earlier in this chapter. When SRP is considered in addition to Didymos' rotation, the system loses its periodicity because the SRP period and the rotation period are generally incommensurate [148].

Based on the periodic families obtained in the non-rotating case, a few resonant orbits of various shape and resonance ratio are represented and compared with the solution computed with the initial conditions given by the HBM and integrated over one period in Figure 5.25. Figure 5.25a is a vertical orbit, found near the second Lagrange point of the autonomous system, in a 2:1 resonance with the synodic period, its period of rotation is twice the synodic period. Figure 5.25b corresponds to a retrograde planar circular orbit in a 3:1 resonance. The third orbit, in Figure 5.25c is an halo orbit mainly orbiting Dimorphos that extends toward a side of Didymos. This orbit is in a 3:1 ratio as well. The final orbit represented in Figure 5.25d is part of the 1:3 resonance orbit presented in the previous section. It is, however, in a 11:1 resonance ratio with the synodic period. This orbit exhibits a verticalization in the vicinity of Dimorphos.

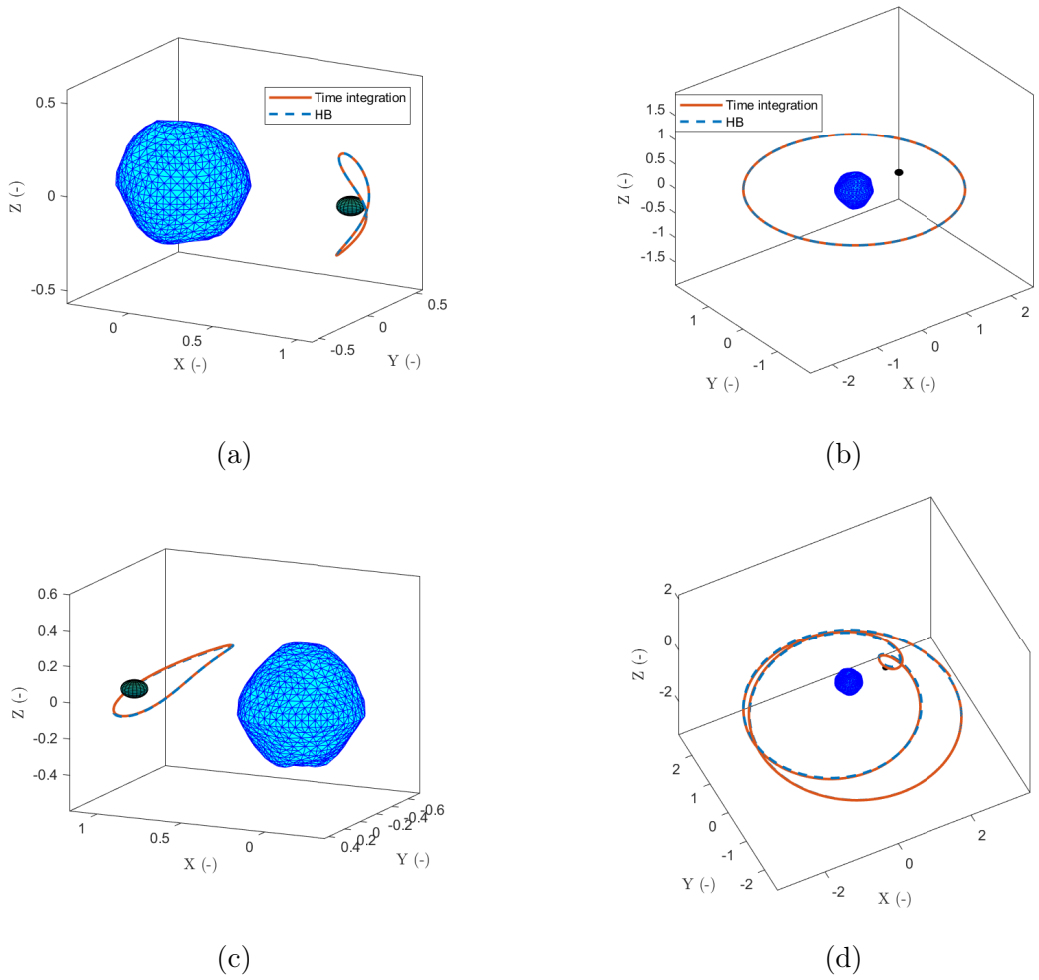

Figure 5.25: (a) Vertical synodic resonant (2:1) orbit around Dimorphos; (b) Circular synodic resonant (3:1) orbit; (c) Long-period synodic resonant (3:1) orbit around Dimorphos; (d) Resonant orbit (1:3) in the CRTBP and synodic resonant (11:1) orbit around Didymos-Dimorphos taking the rotation of Didymos into account.

5.4 Conclusion

In this chapter, the primary sources of perturbations in the vicinity of asteroids are investigated. Periodic orbits, under the influence of either solar radiation pressure or within the binary system Didymos–Dimorphos, are studied using the HBM.

Solar radiation pressure is modeled as a periodic force acting on a body when exposed to direct sunlight. A shadow model was introduced to account for eclipses during propagation around asteroid 433 Eros. Despite the approximations, this simple representation of SRP directly influences the system's dynamics; only minor modifications to the HBM are required, and the method remains highly effective for obtaining periodic orbits at different resonance ratios. To validate the results, they are compared with classical time-integration methods, with orbits propagated over multiple periods. A brief analysis of the effect of orbit passages through the shadow is also presented.

The binary system Didymos–Dimorphos is first considered as a generalized CRTBP, comprising a non-rotating polyhedral mesh for Didymos and an ellipsoid for Dimorphos. This approach allows the continuation of solutions obtained via the HBM and provides a partial map of periodic orbits in the vicinity of Didymos. Building on these branches, the rotation of Didymos is then introduced to enhance the model's fidelity. The analysis focuses on a selection of resonant orbits with the synodic angular velocity, enabling the identification of periodic solutions that are subsequently validated through time integration. Overall, the HBM proves to be an efficient and reliable tool for computing periodic solutions under the major perturbative forces, highlighting its value in astrodynamics.

Chapter 6

Conclusions and perspectives

This thesis set out to explore the use of the harmonic balance method (HBM) and its multi-frequency extension (MHBM) for the computation and analysis of periodic and quasi-periodic orbits in astrodynamics. The central objective was to demonstrate that this frequency-domain approach, originally rooted in nonlinear electrical circuits, could provide an efficient, accurate, and insightful framework for studying orbital motion around irregular celestial bodies. Through successive levels of model complexity, from academic examples to realistic asteroid environments, this work has shown that HBM not only reproduces known families of solutions but also reveals new dynamical features with exceptional clarity.

The first part of the thesis established the theoretical foundations of the method. The formulation of HBM for autonomous and conservative systems was revisited, with special attention given to stability analysis via Floquet theory and the detection of bifurcations. The proposed adaptive harmonic selection and branching strategies proved essential for exploring large solution sets efficiently. The theory of the MHBM was also presented in detail. This framework was then validated on a simple two-degree-of-freedom nonlinear oscillator, providing a clear demonstration of the method's robustness and extensibility.

In the second stage, the method was applied to the classical circular restricted three-body problem (CRTBP), a cornerstone of celestial mechanics. Here, HBM offered a fresh perspective on a well-established model. By enforcing periodicity directly in the frequency domain, the method allowed the systematic mapping of resonant families and bifurcation structures without relying on time integration. The comparison with established tools such as `AUTO` confirmed the accuracy of the approach, while the continuation across mass ratios and resonance connections showcased its versatility. This stage validated HBM as a reliable continuation tool capable of reproducing and extending known results in nonlinear orbital dynamics.

Building on this foundation, the third part of the work addressed the highly irregular gravitational environment of asteroid 433 Eros. Using a polyhedral representation of the asteroid's shape, a dense bifurcation map, comprising over one hundred detected bifurcations, was constructed. This analysis revealed rich transitions between resonant families and provided an unprecedented spectral view of the dynamics. Furthermore, the introduction of the MHBM enabled the computation and continuation of quasi-periodic orbits, marking one of the first applications of this technique in celestial mechanics. The detec-

tion of Neimark–Sacker bifurcations and the subsequent continuation of quasi-periodic branches demonstrated the method's ability to capture multi-frequency motion in a fully nonlinear gravitational field.

Finally, the scope of the HBM was extended to more realistic dynamical scenarios, including external perturbations such as solar radiation pressure and binary gravitational coupling. Around asteroid Eros, the SRP was modeled alongside an eclipse function, and the results were directly validated by time integration. In the case of the Didymos–Dimorphos binary system, the HBM successfully handled the complexity of a rotating polyhedral primary coupled with an ellipsoidal secondary. In both cases, the method proved remarkably adaptable, requiring only minor modifications to accommodate additional forces and couplings. These applications highlight its potential for future mission design and long-term stability analysis around small celestial bodies.

Taken together, the results confirm that the harmonic balance method constitutes a powerful alternative to classical time-domain approaches for studying periodic and quasi-periodic orbits in astrodynamics. By enforcing periodicity intrinsically, it avoids the accumulation of integration errors, offers direct access to stability information, and facilitates the global exploration of solution families. Beyond its computational advantages, the spectral interpretation of the solutions provides a new lens through which resonance interactions and bifurcations can be understood.

Perspectives

Several directions naturally emerge from this work. First, the MHBM formulation could be further generalized to handle higher-dimensional quasi-periodic tori, allowing the study of systems with three or more interacting frequencies. Such an extension would open the door to exploring chaotic transitions and the onset of instability in more detail.

Second, coupling HBM with optimization and control design could provide a systematic framework for identifying stable orbits, transfer trajectories, or resonant pathways in multi-body systems, particularly relevant for asteroid exploration missions.

Third, extending the frequency-domain framework to include weakly non-conservative effects, such as solar tides, low-intensity thrust, or thermal forces, would broaden its applicability to realistic mission scenarios. While strict periodicity is generally lost in the presence of such perturbations, the harmonic balance formulation could still provide valuable approximate solutions by capturing near-periodic or slowly varying dynamics. This would make it a useful diagnostic or predictive tool for studying the long-term behavior and stability of trajectories in environments where classical time integration is limited by stiffness or sensitivity.

In a broader sense, the work presented here bridges two traditionally distinct communities: nonlinear dynamics and celestial mechanics. By transferring concepts such as harmonic balance, stability maps, and bifurcation tracking into orbital mechanics, this thesis contributes to building a unified methodology for analyzing complex gravitational systems. The results achieved, from the Earth–Moon system to Eros and Didymos–Dimorphos, demonstrate the maturity of this approach and its promise for future

applications in astrodynamics and space mission design.

Bibliography

[1] A. Blondel, "Amplitude du courant oscillant produit par les audions générateurs," *Comptes rendus hebdomadaires des séances de l'Académie des sciences*, vol. 169, no. 17, pp. 943–948, 1919.

[2] J.-P. Noël and G. Kerschen, "Nonlinear system identification in structural dynamics: 10 more years of progress," *Mechanical Systems and Signal Processing*, vol. 83, pp. 2–35, 2017.

[3] T. Detroux, L. Renson, L. Masset, and G. Kerschen, "The harmonic balance method for bifurcation analysis of large-scale nonlinear mechanical systems," *Computer Methods in Applied Mechanics and Engineering*, vol. 296, pp. 18–38, 2015.

[4] Y. Yu and H. Baoyin, "Generating families of 3d periodic orbits about asteroids," *Monthly Notices of the Royal Astronomical Society*, vol. 427, no. 1, pp. 872–881, 2012.

[5] S. Stoykov and S. Margenov, "Numerical computation of periodic responses of nonlinear large-scale systems by shooting method," *Computers Mathematics with Applications*, vol. 67, 07 2014.

[6] F. Wang, "Bifurcations of nonlinear normal modes via the configuration domain and the time domain shooting methods," *Communications in Nonlinear Science and Numerical Simulation*, vol. 20, no. 2, pp. 614–628, 2015.

[7] H. Dai, X. Yue, and J.-P. Yuan, "A time domain collocation method for obtaining the third superharmonic solutions to the duffing oscillator," *Nonlinear Dynamics*, vol. 73, 07 2013.

[8] A. Dhooge, W. Govaerts, and Y. A. Kuznetsov, "Matcont: A matlab package for numerical bifurcation analysis of odes," *ACM Trans. Math. Softw.*, vol. 29, p. 141–164, June 2003.

[9] E. Doedel, A. Champneys, T. Fairgrieve, Y. Kuznetsov, B. Sandstede, and X. Wang, "Auto 97: Continuation and bifurcation software for ordinary differential equations (with homcont)," 06 1999.

[10] H. Dankowicz and F. Schilder, "An extended continuation problem for bifurcation analysis in the presence of constraints," *Journal of Computational and Nonlinear Dynamics*, vol. 6, 01 2009.

[11] S. Karkar, B. Cochelin, and C. Vergez, "A comparative study of the harmonic balance method and the orthogonal collocation method on stiff nonlinear systems," *Journal of Sound and Vibration*, vol. 333, no. 12, pp. 2554–2567, 2014.

[12] Z. Yan, H. Dai, Q. Wang, and S. N. Atluri, "Harmonic balance methods: A review and recent developments," *CMES - Computer Modeling in Engineering and Sciences*, vol. 137, no. 2, pp. 1419–1459, 2023.

[13] A. Leung and Z. Guo, "Forward residue harmonic balance for autonomous and non-autonomous systems with fractional derivative damping," *Communications in Nonlinear Science and Numerical Simulation*, vol. 16, no. 4, pp. 2169–2183, 2011.

[14] C. Grenat, S. Baguet, R. Dufour, and C.-H. Lamarque, "Generalization of conservative nonlinear normal modes to the non-conservative equation of motion," in *ASME IDETC/CIE 2018 Conference, International Design Engineering Technical Conferences & Computers and Information in Engineering Conference*, pp. DETC2018–85799, 2018.

[15] L. Renson, G. Kerschen, and B. Cochelin, "Numerical computation of nonlinear normal modes in mechanical engineering," *Journal of Sound and Vibration*, vol. 364, pp. 177–206, 2016.

[16] R. Seydel, *Practical bifurcation and stability analysis*, vol. 5. Springer Science & Business Media, 2009.

[17] F. Muñoz-Almaraz, E. Freire, J. Galán, E. Doedel, and A. Vanderbauwhede, "Continuation of periodic orbits in conservative and hamiltonian systems," *Physica D: Nonlinear Phenomena*, vol. 181, no. 1, pp. 1–38, 2003.

[18] G. W. Hill, "On the part of the motion of the lunar perigee which is a function of the mean motions of the sun and moon," 1886.

[19] L. Chua and A. Ushida, "Algorithms for computing almost periodic steady-state response of nonlinear systems to multiple input frequencies," *IEEE Transactions on circuits and systems*, vol. 28, no. 10, pp. 953–971, 1981.

[20] Y.-B. Kim and S. Noah, "Quasi-periodic response and stability analysis for a nonlinear jeffcott rotor," *Journal of Sound and Vibration*, vol. 190, no. 2, pp. 239–253, 1996.

[21] L. Guillot, P. Vigué, C. Vergez, and B. Cochelin, "Continuation of quasi-periodic solutions with two-frequency harmonic balance method," *Journal of Sound and Vibration*, vol. 394, pp. 434–450, 2017.

[22] Q. Wang, Z. Yan, and H. Dai, "An efficient multiple harmonic balance method for computing quasi-periodic responses of nonlinear systems," *Journal of Sound and Vibration*, vol. 554, p. 117700, 2023.

[23] H. Liao, Q. Zhao, and D. Fang, "The continuation and stability analysis methods for quasi-periodic solutions of nonlinear systems," *Nonlinear Dynamics*, vol. 100, pp. 1469–1496, 2020.

[24] S. Nacivet, C. Pierre, F. Thouverez, and L. Jezequel, "A dynamic lagrangian frequency–time method for the vibration of dry-friction-damped systems," *Journal of Sound and Vibration*, vol. 265, no. 1, pp. 201–219, 2003.

[25] M. J. Powell, "A hybrid method for nonlinear equations," *Numerical methods for nonlinear algebraic equations*, pp. 87–161, 1970.

[26] A. Cardona, A. Lerusse, and M. Géradin, "Fast fourier nonlinear vibration analysis," *Computational Mechanics*, vol. 22, no. 2, pp. 128–142, 1998.

[27] E. Doedel, A. Champneys, T. Fairgrieve, Y. A. Kuznetsov, B. Sandstede, and X. Wang, "Continuation and bifurcation software for ordinary differential equations," *FTP from pub/doedel/auto*, 1997.

[28] M. Peeters, R. Viguié, G. Sérandour, G. Kerschen, and J.-C. Golinval, "Nonlinear normal modes, part ii: Toward a practical computation using numerical continuation techniques," *Mechanical Systems and Signal Processing*, vol. 23, no. 1, pp. 195–216, 2009. Special Issue: Non-linear Structural Dynamics.

[29] G. Von Groll and D. Ewins, "The harmonic balance method with arc-length continuation in rotor/stator contact problems," *Journal of Sound and Vibration*, vol. 241, no. 2, pp. 223–233, 2001.

[30] L. Woiwode, N. N. Balaji, J. Kappauf, F. Tubita, L. Guillot, C. Vergez, B. Cochelin, A. Grolet, and M. Krack, "Comparison of two algorithms for harmonic balance and path continuation," *Mechanical Systems and Signal Processing*, vol. 136, p. 106503, 2020.

[31] J. Wu, L. Hong, and J. Jiang, "A robust and efficient stability analysis of periodic solutions based on harmonic balance method and floquet-hill formulation," *Mechanical Systems and Signal Processing*, vol. 173, p. 109057, 2022.

[32] A. Grolet and F. Thouverez, "On a new harmonic selection technique for harmonic balance method," *Mechanical Systems and Signal Processing*, vol. 30, pp. 43–60, 2012.

[33] R. Lin, L. Hou, Y. Chen, J. Yuhong, N. Saeed, and Y. Chen, "A novel adaptive harmonic balance method with an asymptotic harmonic selection," *Applied Mathematics and Mechanics*, vol. 44, pp. 1887–1910, 10 2023.

[34] C. Grenat, *Nonlinear Normal Modes and multi-parametric continuation of bifurcations : Application to vibration absorbers and architectured MEMS sensors for mass detection.* Theses, Université de Lyon, Oct. 2018.

[35] A. Lazarus, "A harmonic-based method for computing the stability of periodic solutions of dynamical systems," *Comptes Rendus Mecanique - C R MEC*, vol. 338, pp. 510–517, 09 2010.

[36] G. Moore, "Floquet theory as a computational tool," *SIAM Journal on Numerical Analysis*, vol. 42, no. 6, pp. 2522–2568, 2005.

[37] B. Meini, "A "shift-and-deflate" technique for quadratic matrix polynomials," *Linear Algebra and its Applications*, vol. 438, p. 1946–1961, 02 2013.

[38] Y. A. Kuznetsov, I. A. Kuznetsov, and Y. Kuznetsov, *Elements of applied bifurcation theory*, vol. 112. Springer, 1998.

[39] W. Govaerts, Y. Kuznetsov, V. De Witte, A. Dhooge, H. Meijer, W. Mestrom, A. Riet, and B. Sautois, "MATCONT and CL MATCONT: Continuation toolboxes in MATLAB," technical report, Gent University and Utrecht University, 2011.

[40] R. Alcorta, S. Baguet, B. Prabel, P. Piteau, and G. Jacquet-Richardet, "Period doubling bifurcation analysis and isolated sub-harmonic resonances in an oscillator with asymmetric clearances," *Nonlinear Dynamics*, vol. 98, 12 2019.

[41] L. Xie, S. Baguet, B. Prabel, and R. Dufour, "Bifurcation tracking by Harmonic Balance Method for performance tuning of nonlinear dynamical systems," *Mechanical Systems and Signal Processing*, vol. 88, pp. 445–461, May 2017.

[42] G. Hurel, S. Baguet, and C.-H. Lamarque, "Neimark sacker bifurcations and nonlinear energy exchange in chains of non-linear oscillators," *International Journal of Non-Linear Mechanics*, vol. 144, p. 104057, 2022.

[43] A. M. Samoilenko, *Elements of the mathematical theory of multi-frequency oscillations*, vol. 71. Springer Science & Business Media, 2012.

[44] F. Schilder, W. Vogt, S. Schreiber, and H. Osinga, "Fourier methods for quasi-periodic oscillations," *International Journal for Numerical Methods in Engineering*, vol. 67(5), pp. 629 – 671, July 2006. Publisher: John Wiley Sons Ltd.

[45] M. Guskov and F. Thouverez, "Harmonic balance-based approach for quasi-periodic motions and stability analysis," *Journal of Vibration and Acoustics*, vol. 134, p. 031003, 04 2012.

[46] B. Zhou, F. Thouverez, and D. Lenoir, "A variable-coefficient harmonic balance method for the prediction of quasi-periodic response in nonlinear systems," *Mechanical Systems and Signal Processing*, vol. 64-65, pp. 233–244, 2015.

[47] G. Kerschen, M. Peeters, J.-C. Golinval, and A. Vakakis, "Nonlinear normal modes, part i: A useful framework for the structural dynamicist," *Mechanical Systems and Signal Processing - MECH SYST SIGNAL PROCESS*, vol. 23, 05 2008.

[48] J. Barrow-Green, "Poincare and the three body problem," 1996.

[49] K. R. Lang, "Soho reveals the secrets of the sun," *Scientific American*, vol. 276, no. 3, pp. 40–47, 1997.

[50] D. Grebow, M. Ozimek, K. Howell, and D. Folta, "Multibody orbit architectures for lunar south pole coverage," *Journal of Spacecraft and Rockets - J SPACECRAFT ROCKET*, vol. 45, pp. 344–358, 03 2008.

[51] M. Hénon, "Exploration numérique du problème restreint. II. Masses égales, stabilité des orbites périodiques," *Annales d'Astrophysique*, vol. 28, p. 992, Feb. 1965.

[52] M. Henon, "Numerical exploration of the restricted problem. VI. Hill's case: Non-periodic orbits.," , vol. 9, pp. 24–36, Nov. 1970.

[53] C. Goudas, "Three-dimensional periodic orbits and their stability," *Icarus*, vol. 2, pp. 1–18, 1963.

[54] T. BRAY and C. GOUDAS, "Three-dimensional periodic oscillations about l1, l2, and l3," vol. 5 of *Advances in Astronomy and Astrophysics*, pp. 71–130, Elsevier, 1967.

[55] V. G. Szebehely and F. T. Geyling, "Theory of orbits: The restricted problem of three bodies," 1967.

[56] R. Zhang, "A review of periodic orbits in the circular restricted three-body problem," *Journal of Systems Engineering and Electronics*, vol. 33, no. 3, pp. 612–646, 2022.

[57] K. E. Papadakis and C. G. Zagouras, "Bifurcation points and intersections of families of periodic orbits in the three-dimensional restricted three-body problem," , vol. 199, pp. 241–256, Jan. 1993.

[58] K. Howell and E. Campbell, "Three-dimensional periodic solutions that bifurcate from halo families in the circular restricted three-body problem," *Advances in the Astronautical Sciences*, vol. 102, pp. 891–910, 01 1999.

[59] D. Dichmann, E. Doedel, and R. Paffenroth, "The computation of periodic solutions of the 3-body problem using the numerical continuation software auto," pp. 489–528, 05 2003.

[60] E. Doedel, R. Paffenroth, H. Keller, D. Dichmann, J. Galán, and A. Vanderbauwhede, "Computation of periodic solutions of conservative systems with application to the 3-body problem," *International Journal of Bifurcation and Chaos*, vol. 13, 06 2003.

[61] C. D. Murray and S. F. Dermott, *Solar System Dynamics*. Cambridge University Press, 2000.

[62] R. Anderson, S. Campagnola, and G. Lantoine, "Broad search for unstable resonant orbits in the planar circular restricted three-body problem," *Advances in the Astronautical Sciences*, vol. 150, 02 2016.

[63] B. M. Patel, N. M. Pathak, and E. I. Abouelmagd, "Stability analysis of first order resonant periodic orbit," *Icarus*, vol. 387, p. 115165, 2022.

[64] L.-B. Liu, Y. Qian, and X.-D. Yang, "Initial parameter analysis about resonant orbits in earth-moon system," *Advances in Astronomy*, vol. 2019, pp. 1–17, 01 2019.

[65] K. I. Antoniadou and G. Voyatzis, "2/1 resonant periodic orbits in three dimensional planetary systems," *Celestial Mechanics and Dynamical Astronomy*, vol. 115, p. 161–184, Jan. 2013.

[66] K. I. Antoniadou and A.-S. Libert, "Spatial resonant periodic orbits in the restricted three-body problem," *Monthly Notices of the Royal Astronomical Society*, vol. 483, pp. 2923–2940, 11 2018.

[67] J. S. Parker and M. W. Lo, "Unstable resonant orbits near Earth and their applications in planetary missions," 2004.

[68] M. Vaquero and K. C. Howell, "Leveraging resonant-orbit manifolds to design transfers between libration-point orbits," *Journal of Guidance, Control, and Dynamics*, vol. 37, no. 4, pp. 1143–1157, 2014.

[69] D. Canales, M. Gupta, B. Park, and K. C. Howell, "A transfer trajectory framework for the exploration of phobos and deimos leveraging resonant orbits," *Acta Astronautica*, vol. 194, pp. 263–276, 2022.

[70] D. Dichmann, R. Lebois, and J. Carrico, "Dynamics of orbits near 3:1 resonance in the earth-moon system," *The Journal of the Astronautical Sciences*, vol. 60, 03 2014.

[71] G. R. Ricker, "The Transiting Exoplanet Survey Satellite (TESS): Discovering New Earths and Super-Earths in the Solar Neighborhood," in *AAS/Division for Extreme Solar Systems Abstracts*, vol. 47 of *AAS/Division for Extreme Solar Systems Abstracts*, p. 503.01, Dec. 2015.

[72] M. Vaquero and K. C. Howell, "Design of transfer trajectories between resonant orbits in the earth–moon restricted problem," *Acta Astronautica*, vol. 94, no. 1, pp. 302–317, 2014.

[73] C. Peng, Y. Zhang, and S. He, "3:1/3:2 resonant orbits touring l3–l5 in cislunar space," *Advances in Space Research*, vol. 73, no. 5, pp. 2499–2514, 2024.

[74] S. Pan and X. Hou, "Review article: Resonant families of periodic orbits in the restricted three-body problem," *Research in Astronomy and Astrophysics*, vol. 22, July 2022. Publisher Copyright: © 2022. National Astronomical Observatories, CAS and IOP Publishing Ltd.

[75] S. Pan and X. Hou, "Analysis of resonance transition periodic orbits in the circular restricted three-body problem," *Applied Sciences (Switzerland)*, vol. 12, Sept. 2022. Publisher Copyright: © 2022 by the authors.

[76] X. Li, Y. Qian, X.-D. Yang, and W. Zhang, "Stability and bifurcation analyses for exterior resonant families in earth-moon system," *Results in Physics*, vol. 31, p. 104961, 11 2021.

[77] K. Antoniadou and A.-S. Libert, "Origin and continuation of 3/2, 5/2, 3/1, 4/1 and 5/1 resonant periodic orbits in the circular and elliptic restricted three-body problem," *Celestial Mechanics Dynamical Astronomy*, vol. 130, June 2018. Publisher Copyright: © 2018, Springer Science+Business Media B.V., part of Springer Nature.

[78] R. B. Barrar, "Existence of periodic orbits of the second kind in the restricted problems of three bodies," , vol. 70, p. 3, Feb. 1965.

[79] R. Broucke, "Periodic orbits in the restricted three body problem with earth-moon masses," 1968.

[80] R. Restrepo and R. Russell, "Aas 17-694 a database of planar axi-symmetric periodic orbits for the solar system," 08 2017.

[81] Y. Akiyama, M. Bando, and S. Hokamoto, "Periodic and quasi-periodic orbit design based on the center manifold theory," *Acta Astronautica*, vol. 160, pp. 672–682, 2019.

[82] [U+FFFD] Francisco Gil, W. Litteri, V. Rodriguez-Fernandez, D. Camacho, and M. Vasile, "Generative design of periodic orbits in the restricted three-body problem," 08 2024.

[83] J. Zhang, H. Dai, and Q. Wang, "Highly accurate reconstruction harmonic balance scheme for three-body libration point orbits," *Journal of Guidance, Control, and Dynamics*, vol. 48, no. 5, pp. 1148–1157, 2025.

[84] H. Dai, Z. Yan, X. Wang, X. Yue, and S. Atluri, "Collocation [U+2010] based harmonic balance framework for highly accurate periodic solution of nonlinear dynamical system," *International Journal for Numerical Methods in Engineering*, vol. 124, 09 2022.

[85] F. Moulton, *Periodic Orbits*. No. 161, Washington: Carnegie Institution of Washington Publications, 1920.

[86] R. C. Calleja, E. J. Doedel, A. R. Humphries, A. Lemus-Rodríguez, and E. Oldeman, "Boundary-value problem formulations for computing invariant manifolds and connecting orbits in the circular restricted three body problem," *Celestial Mechanics and Dynamical Astronomy*, vol. 114, pp. 77–106, 2012.

[87] M. Paak, M. Païdoussis, and A. Misra, "Nonlinear dynamics and stability of cantilevered circular cylindrical shells conveying fluid," *Journal of Sound and Vibration*, vol. 332, no. 14, pp. 3474–3498, 2013.

[88] R. Singh, O. Prakash, S. Joshi, and Y. Jeppu, *Bifurcation Analysis of Longitudinal Dynamics of Generic Air-Breathing Hypersonic Vehicle for Different Operating Flight Conditions*, pp. 1149–1158. 10 2022.

[89] E. Doedel, V. Romanov, R. Paffenroth, H. Keller, D. Dichmann, J. Galán, and A. Vanderbauwhede, "Elemental periodic orbits associated with the libration points in the circular restricted 3-body problem," *International Journal of Bifurcation and Chaos*, vol. 17, 08 2007.

[90] P. Verrier, T. Waters, and J. Sieber, "Evolution of the l1 halo family in the radial solar sail circular restricted three-body problem," *Celestial Mechanics and Dynamical Astronomy*, vol. 120, p. 373–400, Aug. 2014.

[91] N. J. P. Laboratory, "Three-body periodic orbits," 2024. https://ssd.jpl.nasa.gov/tools/periodic$_o$*rbits.html*/*intro*[*Accessed* : (11/12/2024)].

[92] M. Vaquero and K. C. Howell, "Design of transfer trajectories between resonant orbits in the earth–moon restricted problem," *Acta Astronautica*, vol. 94, no. 1, pp. 302–317, 2014.

[93] C. Petrovich, R. Malhotra, and S. Tremaine, "Planets near mean-motion resonances," *The Astrophysical Journal*, vol. 770, p. 24, May 2013.

[94] M. G. G. T. Taylor, N. Altobelli, B. Buratti, and M. Choukroun, "The rosetta mission orbiter science overview: the comet phase," *Philosophical Transactions of the Royal Society A: Mathematical, Physical and Engineering Sciences*, vol. 375, no. 2097, p. 20160262, 2017.

[95] D. Y. Oh, S. Collins, T. Drain, W. Hart, T. Imken, K. Larson, D. Marsh, D. Muthulingam, J. S. Snyder, D. Trofimov, *et al.*, "Development of the psyche mission for nasa's discovery program," 2019.

[96] H. F. Levison, C. B. Olkin, K. S. Noll, S. Marchi, J. F. Bell III, E. Bierhaus, R. Binzel, W. Bottke, D. Britt, M. Brown, M. Buie, P. Christensen, J. Emery, W. Grundy, V. E. Hamilton, C. Howett, S. Mottola, M. Pätzold, D. Reuter, J. Spencer, T. S. Statler, S. A. Stern, J. Sunshine, H. Weaver, and I. Wong, "Lucy mission to the trojan asteroids: Science goals," *The Planetary Science Journal*, vol. 2, p. 171, aug 2021.

[97] D. S. Lauretta, D. N. Dellagiustina, C. A. Bennett, D. R. Golish, K. J. Becker, S. S. Balram-Knutson, O. S. Barnouin, T. L. Becker, W. F. Bottke, W. V. Boynton, H. Campins, B. E. Clark, H. C. Connolly, C. Y. Drouet D'Aubigny, J. P. Dworkin, J. P. Emery, H. L. Enos, V. E. Hamilton, C. W. Hergenrother, E. S. Howell, M. R. M. Izawa, H. H. Kaplan, M. C. Nolan, B. Rizk, H. L. Roper, D. J. Scheeres, P. H. Smith, K. J. Walsh, C. W. V. Wolner, and Osiris-Rex Team, "The unexpected surface of asteroid (101955) Bennu," , vol. 568, pp. 55–60, Mar. 2019.

[98] Müller, T. G., Ďurech, J., Ishiguro, M., Mueller, M., Krühler, T., Yang, H., Kim, M.-J., O'Rourke, L., Usui, F., Kiss, C., Altieri, B., Carry, B., Choi, Y.-J., Delbo, M., Emery, J. P., Greiner, J., Hasegawa, S., Hora, J. L., Knust, F., Kuroda, D., Osip, D., Rau, A., Rivkin, A., Schady, P., Thomas-Osip, J., Trilling, D., Urakawa, S., Vilenius, E., Weissman, P., and Zeidler, P., "Hayabusa-2 mission target asteroid 162173 ryugu (1999 ju3): Searching for the object's spin-axis orientation⋆," *AA*, vol. 599, p. A103, 2017.

[99] P. Michel, M. Kueppers, H. Sierks, I. Carnelli, A. F. Cheng, K. Mellab, M. Granvik, A. Kestilä, T. Kohout, K. Muinonen, *et al.*, "European component of the aida mission to a binary asteroid: Characterization and interpretation of the impact of the dart mission," *Advances in Space Research*, vol. 62, no. 8, pp. 2261–2272, 2018.

[100] P. Michel, M. Küppers, A. C. Bagatin, B. Carry, S. Charnoz, J. De Leon, A. Fitzsimmons, P. Gordo, S. F. Green, A. Hérique, *et al.*, "The esa hera mission: detailed characterization of the dart impact outcome and of the binary asteroid (65803) didymos," *The planetary science journal*, vol. 3, no. 7, p. 160, 2022.

[101] P. Geissler, J.-M. Petit, D. D. Durda, R. Greenberg, W. Bottke, M. Nolan, and J. Moore, "Erosion and ejecta reaccretion on 243 ida and its moon," *Icarus*, vol. 120, no. 1, pp. 140–157, 1996.

[102] R. Werner and D. Scheeres, "Exterior gravitation of a polyhedron derived and compared with harmonic and mascon gravitation representations of asteroid 4769 castalia," *Celestial Mechanics and Dynamical Astronomy*, vol. 65, pp. 313–344, 09 1996.

[103] T. G. G. Chanut, S. Aljbaae, and V. Carruba, "Mascon gravitation model using a shaped polyhedral source," *Monthly Notices of the Royal Astronomical Society*, vol. 450, pp. 3742–3749, 05 2015.

[104] Y. Jiang and X. Liu, "Equilibria and orbits around asteroid using the polyhedral model," *New Astronomy*, vol. 69, pp. 8–20, 2019.

[105] W. Hu, T. Fu, and C. Liu, "Revisiting the numerical evaluation and visualization of the gravity fields of asteroid 4769 castalia using polyhedron and harmonic expansions models," *Applied Sciences*, vol. 14, no. 10, 2024.

[106] A. Riaguas, A. Elipe, and M. Lara, "Periodic orbits around a massive straight segment," *Celestial Mechanics and Dynamical Astronomy*, vol. 73, no. 1-4, pp. 169–178, 1999.

[107] D. Scheeres, S. Ostro, R. Hudson, and R. Werner, "Orbits close to asteroid 4769 castalia," *Icarus*, vol. 121, no. 1, pp. 67–87, 1996.

[108] D. Scheeres, "Orbital mechanics about small bodies," *Acta Astronautica*, vol. 72, pp. 1–14, 2012.

[109] Y. Jiang, H. Baoyin, and H. Li, "Periodic motion near the surface of asteroids," *Astrophysics and Space Science*, vol. 360, Nov. 2015.

[110] H. Shang, X. Wu, Y. Ren, and J. Shan, "An efficient algorithm for global periodic orbits generation near irregular-shaped asteroids," *Communications in Nonlinear Science and Numerical Simulation*, vol. 48, pp. 550–568, 2017.

[111] P. Llanos, J. Jordan, G. Hintz, M. Sanjurjo-Rivo, and P. Llanos de la Concha, "Trajectory analysis between quasi-periodic orbits and the lagrangian points around phobos," Aug. 2014. AIAA/AAS Astrodynamics Specialist Conference ; Conference date: 01-08-2014.

[112] H. Lei, C. Circi, E. Ortore, E. Condoleo, and B. Xu, "Quasi-frozen orbits around a slowly rotating asteroid," *Journal of Guidance, Control, and Dynamics*, vol. 42, no. 4, pp. 794–809, 2019.

[113] N. Baresi, D. J. Scheeres, and H. Schaub, "Bounded relative orbits about asteroids for formation flying and applications," *Acta Astronautica*, vol. 123, pp. 364–375, 2016.

[114] N. Baresi, Z. P. Olikara, and D. J. Scheeres, "Fully numerical methods for continuing families of quasi-periodic invariant tori in astrodynamics," *The Journal of the astronautical sciences*, vol. 65, pp. 157–182, 2018.

[115] N. Baresi and L. Dell'Elce, "Periodic and quasi-periodic orbits near close planetary moons," *Journal of Guidance, Control, and Dynamics*, vol. 46, no. 4, pp. 680–694, 2023.

[116] P. Thomas, J. Joseph, B. Carcich, J. Veverka, B. Clark, J. Bell, A. Byrd, R. Chomko, M. Robinson, S. Murchie, L. Prockter, A. Cheng, N. Izenberg, M. Malin, C. Chapman, L. McFadden, R. Kirk, M. Gaffey, and P. Lucey, "Eros: Shape, topography, and slope processes," *Icarus*, vol. 155, no. 1, pp. 18–37, 2002.

[117] J. Miller, A. Konopliv, P. Antreasian, J. Bordi, S. Chesley, C. Helfrich, W. Owen, T. Wang, B. Williams, D. Yeomans, and D. Scheeres, "Determination of shape, gravity, and rotational state of asteroid 433 eros," *Icarus*, vol. 155, no. 1, pp. 3–17, 2002.

[118] T. Chanut, O. Winter, and M. Tsuchida, "3d stability orbits close to 433 eros using an effective polyhedral model method," *Monthly Notices of the Royal Astronomical Society*, vol. 438, pp. 56–, 02 2014.

[119] M. Thompson, "Raugh, a., near collected target models v1.0, near-a-5-collected-models-v1.0, nasa planetary data system, 2002.," 2022. https://pds.nasa.gov/ds-view/pds/viewDataset.jsp?dsid=NEAR-A-5-COLLECTED-MODELS-V1.0.

[120] F. Williams, "Eros' eastern and western hemispheres," 2015. https://nssdc.gsfc.nasa.gov/imgcat/html/objectpage/nea0126712790mos.html.

[121] D. Scheeres, "Dynamics about uniformly rotating triaxial ellipsoids: Applications to asteroids," *Icarus*, vol. 110, no. 2, pp. 225–238, 1994.

[122] H. Kang, Y. Jiang, and H. Li, "Pseudo bifurcation and variety of periodic ratio for periodic orbit families close to asteroid (22) kalliope," *Planetary and Space Science*, vol. 158, pp. 69–86, 2018.

[123] Y. Ni, Y. Jiang, and H. Baoyin, "Multiple bifurcations in the periodic orbit around eros," *Astrophysics and Space Science*, vol. 361, Apr. 2016.

[124] Y. Jiang and H. Baoyin, "Periodic orbits related to the equilibrium points in the potential of irregular-shaped minor celestial bodies," *Results in Physics*, vol. 12, pp. 368–374, 2019.

[125] D. Yeomans, P. Antreasian, J.-P. Barriot, S. Chesley, D. Dunham, R. Farquhar, J. Giorgini, C. Helfrich, A. Konopliv, J. McAdams, J. Miller, W. Owen, D. Scheeres, P. Thomas, J. Veverka, and B. Williams, "Radio science results during the near-shoemaker spacecraft rendezvous with eros," *Science (New York, N.Y.)*, vol. 289, pp. 2085–8, 10 2000.

[126] J. Heiligers, M. Macdonald, and J. Parker, "Extension of earth-moon libration point orbits with solar sail propulsion," *Astrophysics and Space Science*, vol. 361, 06 2016.

[127] A. Herasimenka, L. Dell'Elce, J.-B. Caillau, and J.-B. Pomet, "Optimal control of a solar sail," *Optimal Control Applications and Methods*, vol. 45, pp. 2837–2855, July 2024.

[128] E. Morrow, D. Scheeres, and D. Lubin, "Solar sail orbit operations at asteroids," *JOURNAL OF SPACECRAFT AND ROCKETS*, vol. 38, 03 2001.

[129] S. Sawai, D. J. Scheeres, and S. Broschart, "Control of hovering spacecraft using altimetry," *Journal of Guidance, Control, and Dynamics*, vol. 25, no. 4, pp. 786–795, 2002.

[130] A. Quarta and G. Mengali, "Solar sail trajectories to earth's trojan asteroids," *Universe*, vol. 9, p. 186, 04 2023.

[131] A. Farrés, À. Jorba, J.-M. Mondelo, and B. Villac, *Periodic Motion for an Imperfect Solar Sail Near an Asteroid*, pp. 885–898. Berlin, Heidelberg: Springer Berlin Heidelberg, 2014.

[132] M. Giancotti, S. Campagnola, Y. Tsuda, and J. Kawaguchi, "Families of periodic orbits in Hill's problem with solar radiation pressure: application to Hayabusa 2," *Celestial Mechanics and Dynamical Astronomy*, vol. 120, pp. 269–286, Nov. 2014.

[133] D. García Yárnoz, D. J. Scheeres, and C. R. McInnes, "On the a and g families of orbits in the Hill problem with solar radiation pressure and their application to asteroid orbiters," *Celestial Mechanics and Dynamical Astronomy*, vol. 121, pp. 365–384, Apr. 2015.

[134] D. García Yárnoz, J.-P. Sánchez, and C. McInnes, "Alternating orbiter strategy for asteroid exploration," *Journal of Guidance, Control, and Dynamics*, vol. 38, pp. 280–291, 02 2015.

[135] X. Xin, D. J. Scheeres, and X. Hou, "Forced periodic motions by solar radiation pressure around uniformly rotating asteroids," *Celestial Mechanics and Dynamical Astronomy*, vol. 126, pp. 405–432, Nov. 2016.

[136] T. G. G. Chanut, S. Aljbaae, A. F. B. A. Prado, and V. Carruba, "Dynamics in the vicinity of (101955) bennu: solar radiation pressure effects in equatorial orbits," *Monthly Notices of the Royal Astronomical Society*, vol. 470, pp. 2687–2701, 05 2017.

[137] A. Pedros-Faura, G. Brown, J. Mcmahon, and D. Scheeres, "Forced periodic motion by solar radiation pressure in the polyhedral gravity model," *Celestial Mechanics and Dynamical Astronomy*, vol. 136, 08 2024.

[138] J.-L. Margot, P. Pravec, P. Taylor, B. Carry, and S. Jacobson, *Asteroid Systems: Binaries, Triples, and Pairs*. University of Arizona Press, 2015.

[139] S. Naidu, L. Benner, M. Brozovic, M. Nolan, S. Ostro, J. Margot, J. Giorgini, T. Hirabayashi, D. Scheeres, P. Pravec, P. Scheirich, C. Magri, and J. Jao, "Radar observations and a physical model of binary near-earth asteroid 65803 didymos, target of the dart mission," *Icarus*, vol. 348, p. 113777, 2020.

[140] D. C. Richardson, H. F. Agrusa, B. Barbee, R. H. Cueva, F. Ferrari, S. A. Jacobson, R. Makadia, A. J. Meyer, P. Michel, R. Nakano, Y. Zhang, P. Abell, C. C. Merrill, A. Campo Bagatin, O. Barnouin, N. L. Chabot, A. F. Cheng, S. R. Chesley, R. T. Daly, S. Eggl, C. M. Ernst, E. G. Fahnestock, T. L. Farnham, O. Fuentes-Muñoz, E. Gramigna, D. P. Hamilton, M. Hirabayashi, M. Jutzi, J. Lyzhoft, R. Lasagni Manghi, J. McMahon, F. Moreno, N. Murdoch, S. P. Naidu, E. E. Palmer, P. Panicucci, L. Pou, P. Pravec, S. D. Raducan, A. S. Rivkin, A. Rossi, P. Sánchez, D. J. Scheeres, P. Scheirich, S. R. Schwartz, D. Souami, G. Tancredi, P. Tanga, P. Tortora, J. M. Trigo-Rodríguez, K. Tsiganis, J. Wimarsson, and M. Zannoni, "The dynamical state of the didymos system before and after the dart impact," *The Planetary Science Journal*, vol. 5, p. 182, aug 2024.

[141] C. A. Thomas, S. P. Naidu, P. Scheirich, N. A. Moskovitz, P. Pravec, S. R. Chesley, A. S. Rivkin, D. J. Osip, T. A. Lister, L. A. M. Benner, M. Brozović, C. Contreras, N. Morrell, A. Rożek, P. Kušnirák, K. Hornoch, D. Mages, P. A. Taylor, A. D. Seymour, C. Snodgrass, U. G. Jørgensen, M. Dominik, B. Skiff, T. Polakis, M. M. Knight, T. L. Farnham, J. D. Giorgini, B. Rush, J. Bellerose, P. Salas, W. P.

Armentrout, G. Watts, M. W. Busch, J. Chatelain, E. Gomez, S. Greenstreet, L. Phillips, M. Bonavita, M. J. Burgdorf, E. Khalouei, P. Longa-Peña, M. Rabus, S. Sajadian, N. L. Chabot, A. F. Cheng, W. H. Ryan, E. V. Ryan, C. E. Holt, and H. F. Agrusa, "Orbital period change of dimorphos due to the dart kinetic impact," *Nature*, vol. 616, p. 448–451, Mar. 2023.

[142] P. Michel, M. Küppers, A. C. Bagatin, B. Carry, S. Charnoz, J. De Leon, A. Fitzsimmons, P. Gordo, S. F. Green, A. Hérique, *et al.*, "The esa hera mission: detailed characterization of the dart impact outcome and of the binary asteroid (65803) didymos," *The planetary science journal*, vol. 3, no. 7, p. 160, 2022.

[143] F. Damme, H. Hussmann, and J. Oberst, "Spacecraft orbit lifetime within two binary near-earth asteroid systems," *Planetary and Space Science*, vol. 146, pp. 1–9, 2017.

[144] L. Dell'Elce, N. Baresi, S. Naidu, L. Benner, and D. Scheeres, "Numerical investigation of the dynamical environment of 65803 didymos," *Advances in Space Research*, vol. 59, no. 5, pp. 1304–1320, 2017.

[145] A. Capannolo, F. Ferrari, and M. Lavagna, "Families of bounded orbits near binary asteroid 65803 didymos," *Journal of Guidance, Control, and Dynamics*, vol. 42, no. 1, pp. 189–198, 2019.

[146] R. Machado Oliveira, O. C. Winter, R. Sfair, G. Valvano, T. S. Moura, and G. Borderes-Motta, "Dynamics around the binary system (65803) didymos," *Proceedings of the International Astronomical Union*, vol. 15, no. S364, p. 197–202, 2019.

[147] I. Fodde, J. Feng, A. Riccardi, and M. Vasile, "Robust stability and mission performance of a cubesat orbiting the didymos binary asteroid system," *Acta Astronautica*, vol. 203, pp. 577–591, 2023.

[148] G. Voyatzis, D. Karydis, I. Gkolias, M. Gaitanas, and K. Tsiganis, "Planar spacecraft trajectories in the didymos–dimorphos binary asteroid system," *Planetary and Space Science*, vol. 240, p. 105825, 2024.

[149] "Dart - double asteroid redirection test." https://dart.jhuapl.edu/DART-Proposal-Reference/. Accessed: 2025-06-15.

[150] R. T. Daly, C. M. Ernst, O. S. Barnouin, N. L. Chabot, A. S. Rivkin, A. F. Cheng, E. Y. Adams, H. F. Agrusa, E. D. Abel, A. L. Alford, E. I. Asphaug, J. A. Atchison, A. R. Badger, P. Baki, R.-L. Ballouz, D. L. Bekker, J. Bellerose, S. Bhaskaran, B. J. Buratti, S. Cambioni, M. H. Chen, S. R. Chesley, G. Chiu, G. S. Collins, M. W. Cox, M. E. DeCoster, P. S. Ericksen, R. C. Espiritu, A. S. Faber, T. L. Farnham, F. Ferrari, Z. J. Fletcher, R. W. Gaskell, D. M. Graninger, M. A. Haque, P. A. Harrington-Duff, S. Hefter, I. Herreros, M. Hirabayashi, P. M. Huang, S.-Y. W. Hsieh, S. A. Jacobson, S. N. Jenkins, M. A. Jensenius, J. W. John, M. Jutzi, T. Kohout, T. O. Krueger, F. E. Laipert, N. R. Lopez, R. Luther, A. Lucchetti, D. M. Mages, S. Marchi, A. C. Martin, M. E. McQuaide, P. Michel, N. A. Moskovitz, I. W. Murphy, N. Murdoch, S. P. Naidu, H. Nair, M. C. Nolan, J. Ormö, M. Pajola, E. E. Palmer, J. M. Peachey, P. Pravec, S. D. Raducan, K. T. Ramesh, J. R.

Ramirez, E. L. Reynolds, J. E. Richman, C. Q. Robin, L. M. Rodriguez, L. M. Roufberg, B. P. Rush, C. A. Sawyer, D. J. Scheeres, P. Scheirich, S. R. Schwartz, M. P. Shannon, B. N. Shapiro, C. E. Shearer, E. J. Smith, R. J. Steele, J. K. Steckloff, A. M. Stickle, J. M. Sunshine, E. A. Superfin, Z. B. Tarzi, C. A. Thomas, J. R. Thomas, J. M. Trigo-Rodríguez, B. T. Tropf, A. T. Vaughan, D. Velez, C. D. Waller, D. S. Wilson, K. A. Wortman, and Y. Zhang, "Successful kinetic impact into an asteroid for planetary defence," *Nature*, vol. 616, p. 443–447, Mar. 2023.

Appendix A

Additional orbits around 433 Eros

The different labels of the bifurcations are found in Table 4.3 and Figure 4.10.

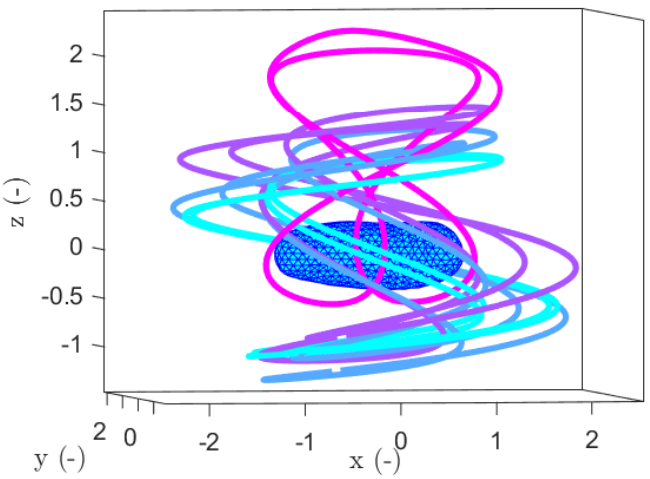

Figure A.1: Unstable branch emerging from PD_{26} with 3 bifurcations encountered: NS_{12}, PD_{67} and PD_{79}.

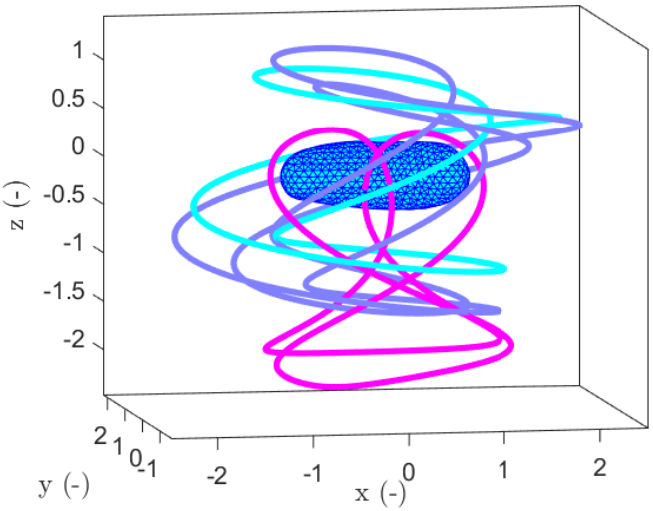

Figure A.2: Unstable branch emerging from PD_{25} with 3 bifurcations encountered: NS_{11}, PD_{66} and PD_{78}.

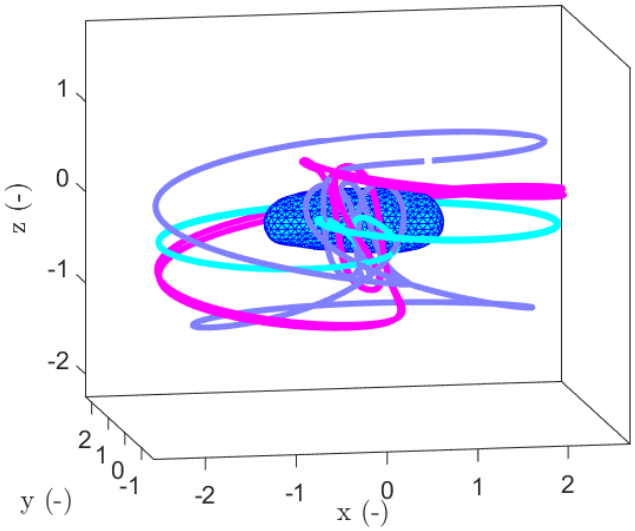

Figure A.3: Unstable branch emerging from PD_{30} looping back to PD_{31} with 2 bifurcations encountered: PD_{68} and PD_{69}.

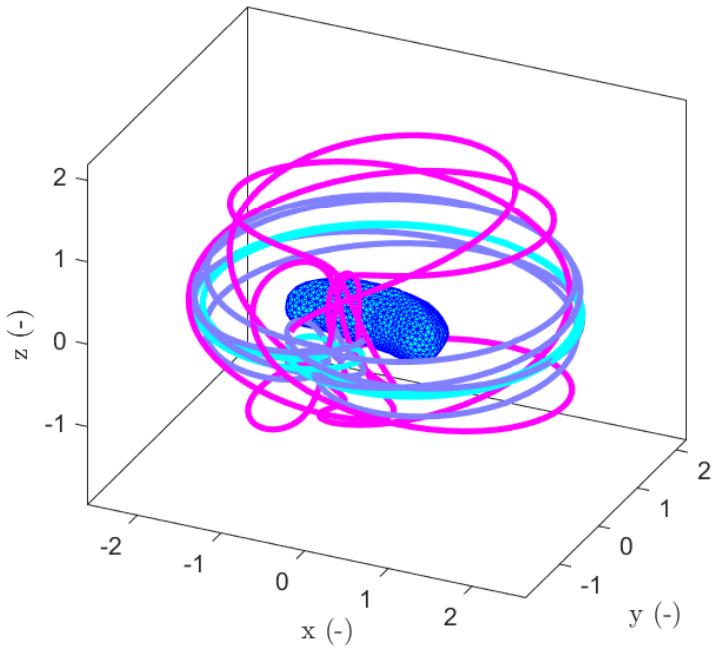

Figure A.4: Unstable branch emerging from PD_{84} with 1 bifurcation encountered: PD_{87}.

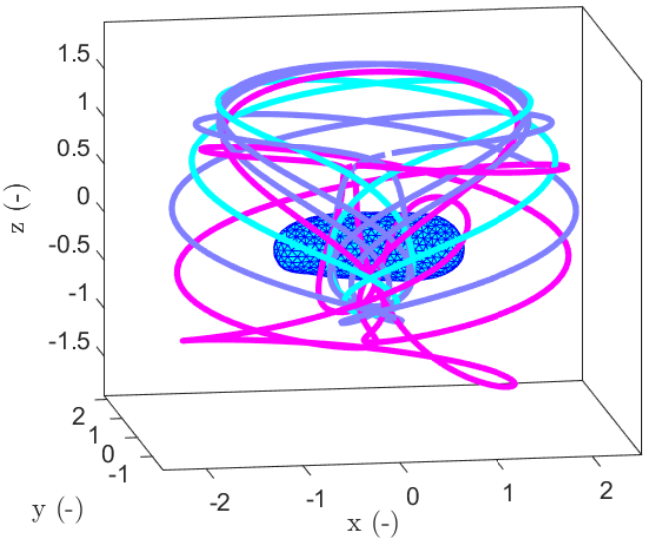

Figure A.5: Unstable branch emerging from PD_{83} with 1 bifurcation encountered: PD_{86}.

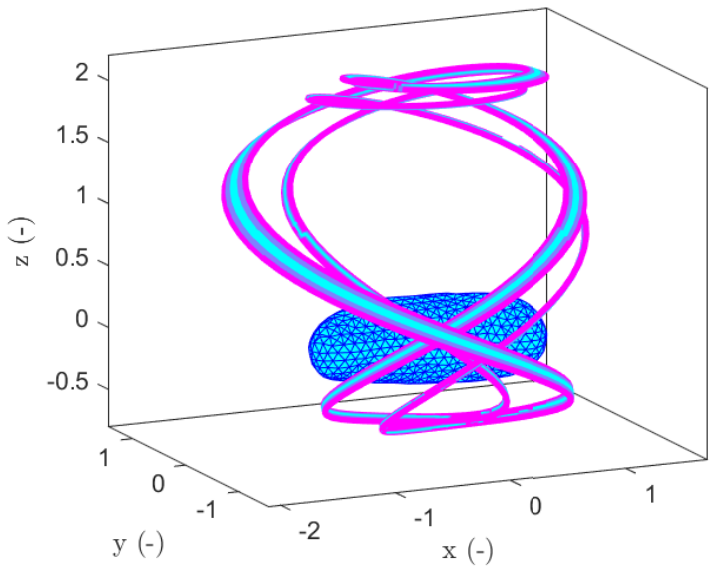

Figure A.6: Unstable branch emerging from PD_{80} with 1 bifurcation encountered: PD_{81}.

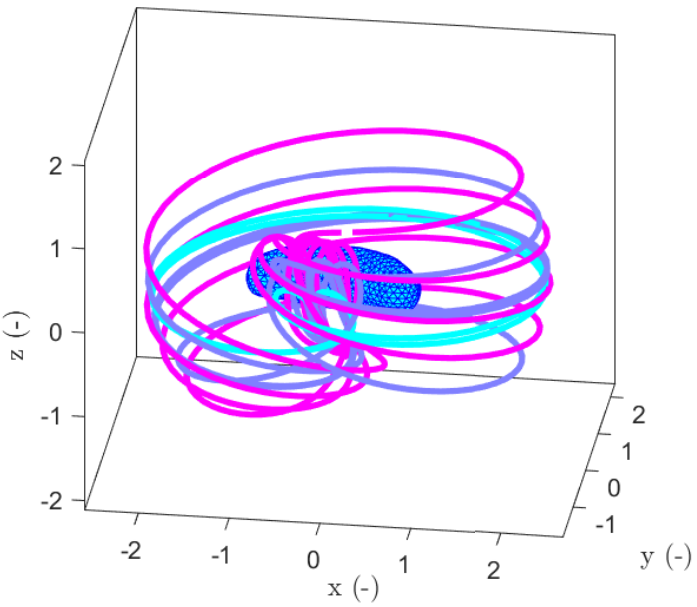

Figure A.7: Unstable branch emerging from PD_{68} looping back to PD_{69}.

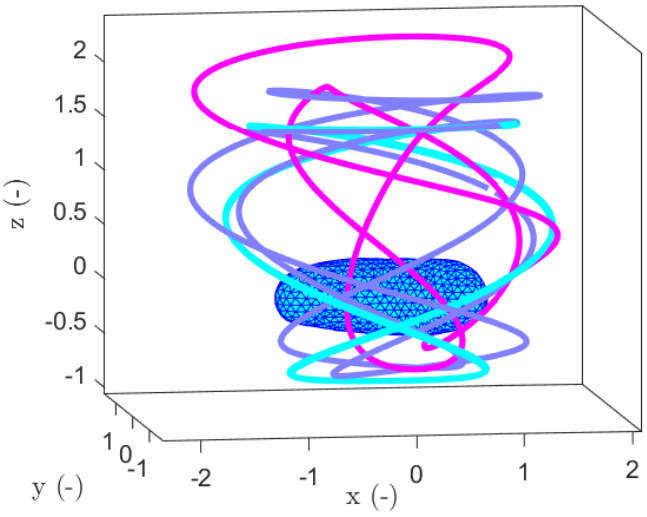

Figure A.8: Unstable branch emerging from PD_{80} with 1 bifurcation encountered: PD_{81}.

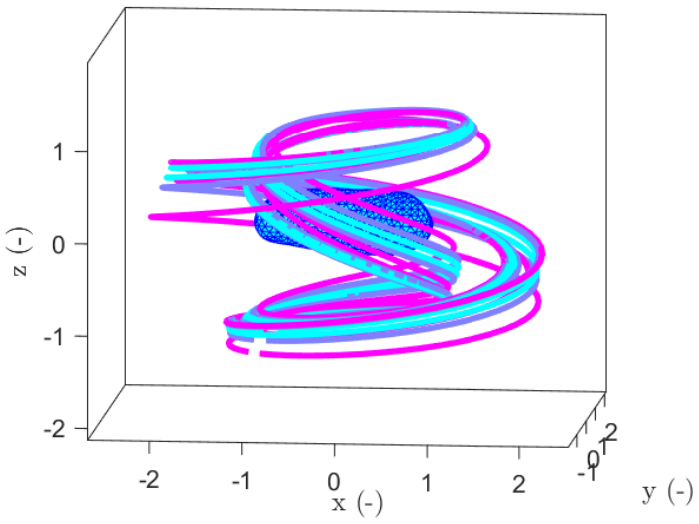

Figure A.9: Unstable branch emerging from PD_{66}.

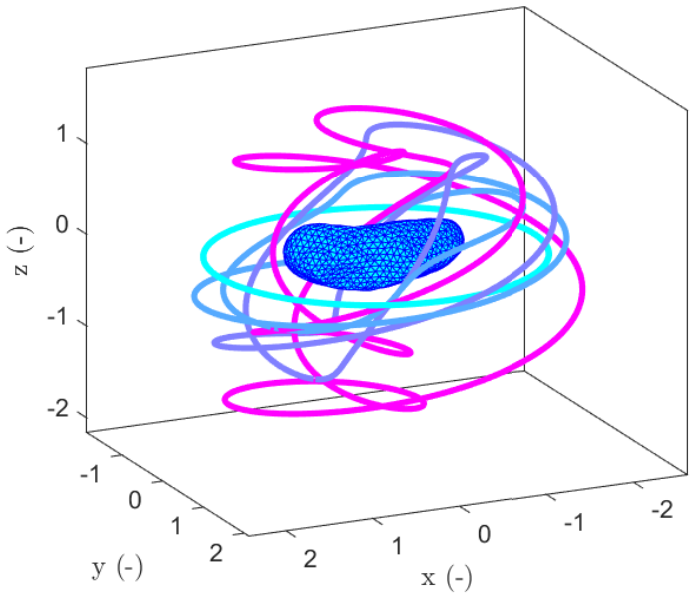

Figure A.10: Unstable branch emerging from PD_{23} with 2 bifurcations encountered: PD_{70} and PD_{71}.

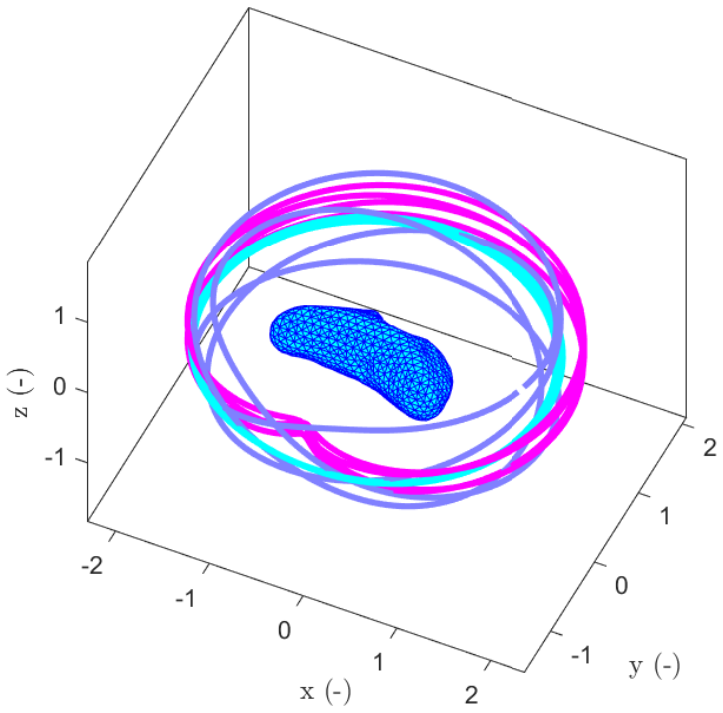

Figure A.11: Unstable branch emerging from PD_{71} with 1 bifurcation encountered: PD_{72}.

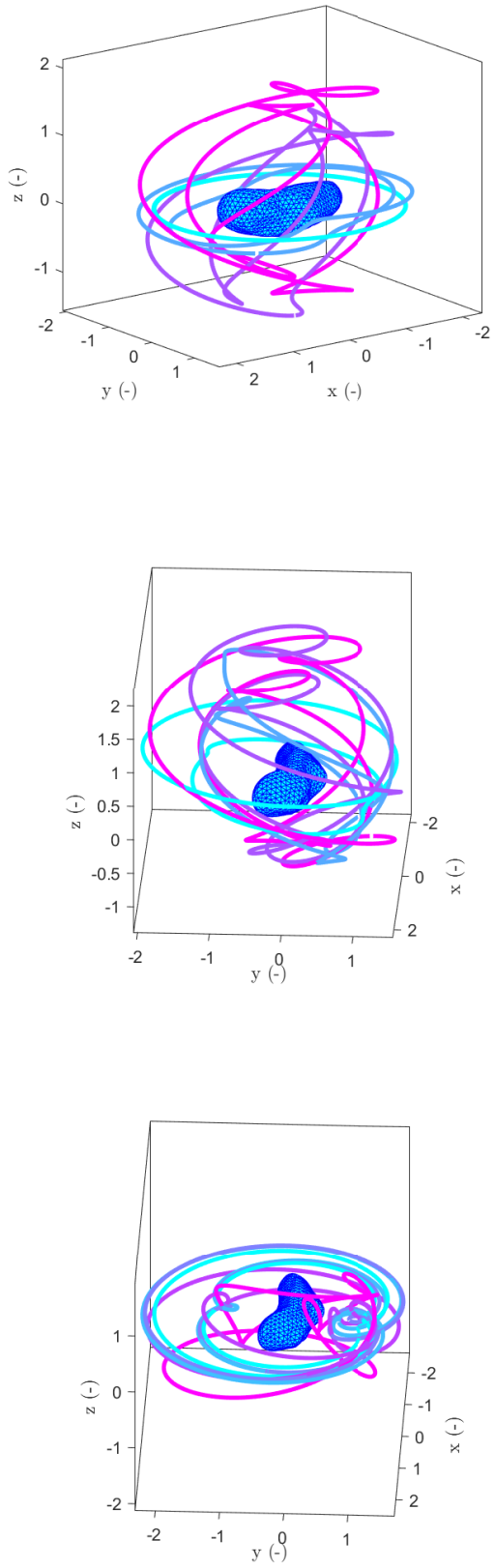

Figure A.12: Different orbits of the continuation branch emanating from PD_{24} with 5 bifurcations encountered: PD_{61}, PD_{62}, PD_{63}, PD_{64} and PD_{65}.

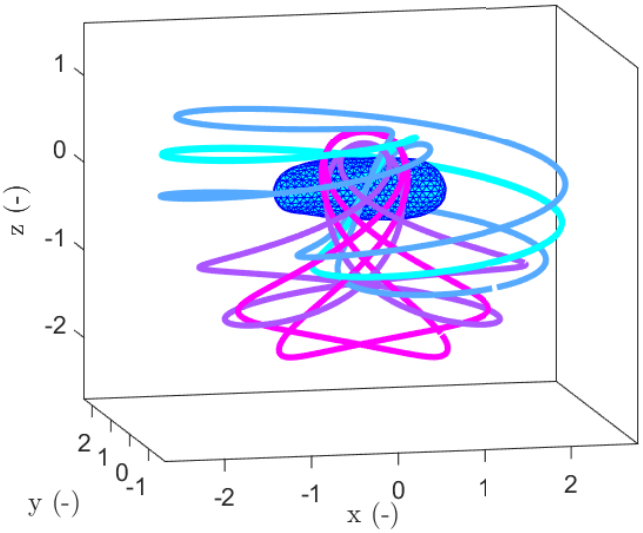

Figure A.13: Unstable branch emerging from PD_{38} with 2 bifurcations encountered: PD_{74} and PD_{75}.

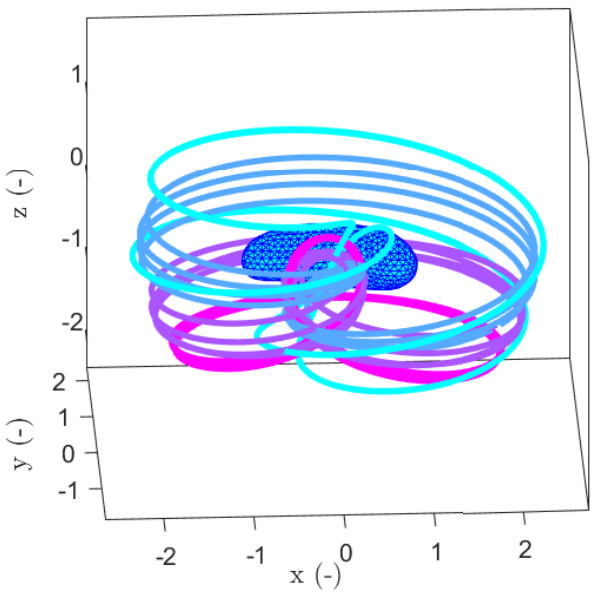

Figure A.14: Unstable branch emerging from PD_{74} with 1 bifurcation encountered: PD_{77}.

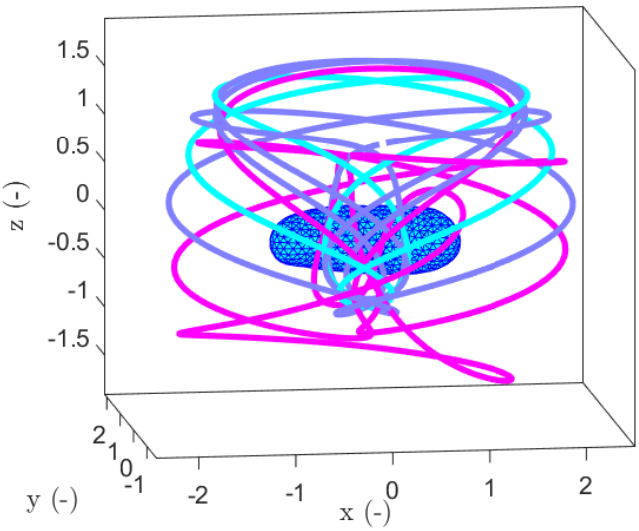

Figure A.15: Unstable branch emerging from PD_{75} with 1 bifurcation encountered: PD_{76}.

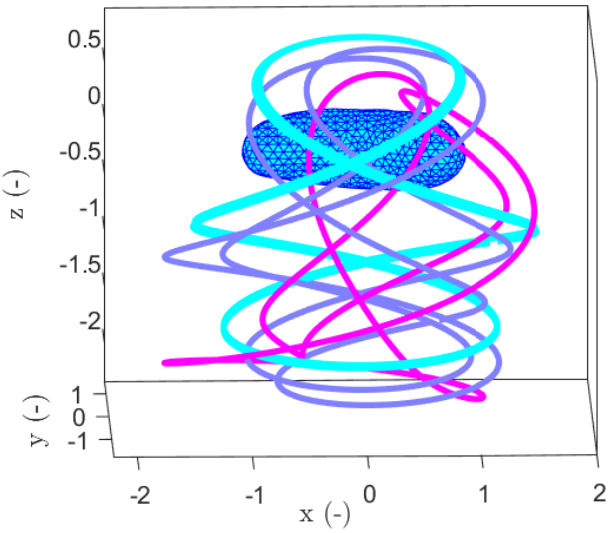

Figure A.16: Unstable branch emerging from PD_{40} with 1 bifurcation encountered: PD_{82}.

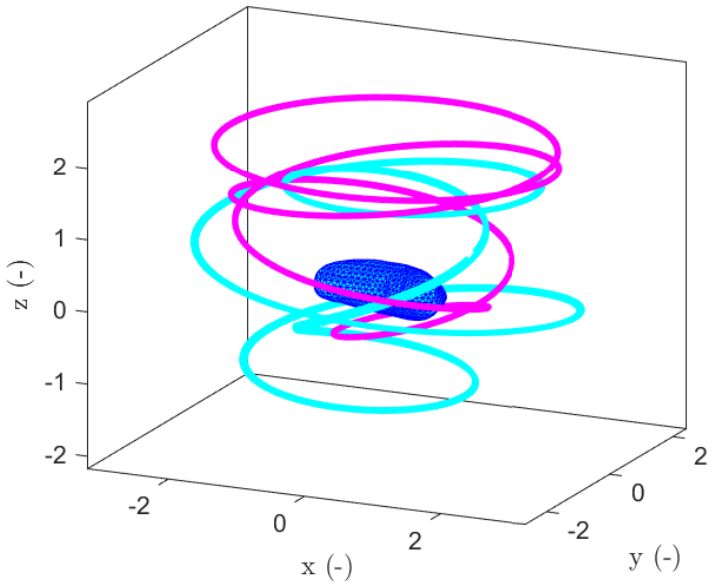

Figure A.17: Branch emerging from PD_{58} with 3 bifurcations encountered: NS_6, PD_{59} and PD_{60}. The branch is stable between NS_6 and PD_{59} otherwise it's unstable.

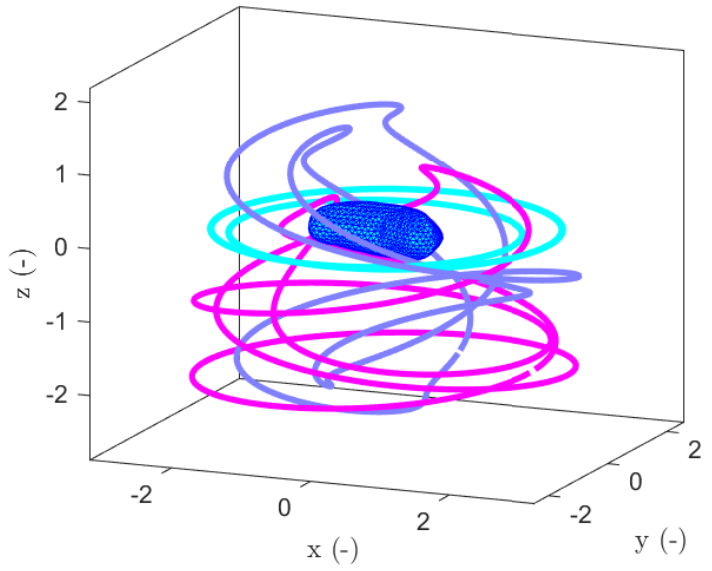

Figure A.18: Unstable branch emerging from PD_{56} with 1 bifurcation encountered: PD_{57}.